Computational Electrochemistry

Stephen Richard Belding

St John's College
University of Oxford

A thesis submitted for the degree of D.Phil.
in Physical and Theoretical Chemistry.

Michaelmas Term 2012

Computational Electrochemistry

Stephen Richard Belding
St John's College, University of Oxford
A thesis submitted for the degree of D.Phil. in Physical and Theoretical Chemistry
Michaelmas Term 2012

Abstract

Electrochemistry is the science of electron transfer. The subject is of great importance and appeal because detailed information can be obtained using relatively simple experimental techniques. In general, the raw data is sufficiently complicated to preclude direct interpretation, yet is readily rationalised using numerical procedures. Computational analysis is therefore central to electrochemistry and is the main topic of this thesis.
Chapters 1 and 2 provide an introductory account to electrochemistry and numerical analysis respectively. Chapter 1 explains the origin of the potential difference and describes its relevance to the thermodynamic and kinetic properties of a redox process. Voltammetry is introduced as an experimental means of studying electrode dynamics. Chapter 2 explains the numerical methods used in later chapters.
Chapter 3 presents a review of the use of nanoparticles in electrochemistry.
Chapter 4 presents the simulation of a random array of spherical nanoparticles. Conclusions obtained theoretically are experimentally confirmed using the Cr^{3+}/Cr^{2+} redox couple on a random array of silver nanoparticles.
Chapter 5 presents an investigation into the concentration of supporting electrolyte required to make a voltammetric experiment quantitatively diffusional. This study looks at a wide range of experimental conditions.
Chapter 6 presents an investigation into the deliberate addition of insufficient supporting electrolyte to an electrochemical experiment. It is shown that this technique can be used to fully study a stepwise two electron transfer. Conclusions obtained theoretically are experimentally confirmed using the reduction of anthracene in acetonitrile.
Chapter 7 presents a new method for simulating voltammetry at disc shaped electrodes in the presence of insufficient supporting electrolyte. It is shown that, under certain conditions, the results obtained from this complicated simulation can be quantitatively obtained by means of a much simpler 'hemispherical approximation'. Conclusions obtained theoretically are experimentally confirmed using the hexammineruthenium ($[Ru(NH_3)_6]^{3+}/[Ru(NH_3)_6]^{2+}$) and hexachloroiridate ($[IrCl_6]^{2-}/[IrCl_6]^{3-}$) redox couples.
Chapter 8 presents an investigation into the voltammetry of stepwise two electron processes using ionic liquids as solvents. It is shown that these solvents can be used to fully study a stepwise two electron transfer. Conclusions obtained theoretically are experimentally confirmed using the oxidation of N,N-dimethyl-p-phenylenediamine in the ionic liquid 1-butyl-3-methylimidazolium tetrafluoroborate ($[C_4$ mim$][BF_4]$).
The work presented in this thesis has been published as 7 scientific papers.

Acknowledgements

I am grateful to Professor Richard G. Compton for his commitment and inspiration as both a supervisor and a tutor throughout my 7 years at Oxford University. I especially appreciated the generous opportunities he gave me to teach undergraduate students.

I am indebted to my parents and to my sister, Rowena, for their love and encouragement.

Glossary

Where appropriate, symbols are defined in terms of the generic species X or the reduction $\mathrm{X} + \mathrm{e}^- \rightleftharpoons \mathrm{Y}$.

Roman Symbols

A	area / m^2
a_X	activity of species X
C_d	capacitance / F
c_X	concentration of species X / mol m^{-3}
c^*_X	bulk concentration of species X / mol m^{-3}
$c_{\mathrm{X},0}$	surface concentration of species X / mol m^{-3}
D_X	diffusion coefficient of species X / m^2 s^{-1}
E	potential difference
$E^\ominus_\mathrm{X/Y}$	standard potential difference of $\mathrm{X} + \mathrm{e}^- \rightleftharpoons \mathrm{Y}$ relative to the SHE / V
$E^\ominus_\mathrm{f,X/Y}$	formal potential difference of $\mathrm{X} + \mathrm{e}^- \rightleftharpoons \mathrm{Y}$ relative to the SHE / V
E_w	work done / J
F	faraday constant $\approx$ 96485 C mol^{-1}
$f(x)$	arbitrary function
$f'(x)$	1^st derivative of $f(x)$
$f''(x)$	2^nd derivative of $f(x)$
G	Gibb's energy / J mol^{-1}
$G_\mathrm{reactants}$	Gibb's energy of the reactants / J mol^{-1}
G_products	Gibb's energy of the products / J mol^{-1}
G_chem	chemical contribution to Gibb's energy / J mol^{-1}

G_{elec}	electrochemical contribution to Gibb's energy / J mol^{-1}
H	Enthalpy / J mol^{-1}
i	current / A
i_{faradaic}	faradaic current / A
$i_{\text{non-faradaic}}$	non-faradaic current / A
j	flux / mol m^{-2} s^{-1}
k^0	heterogeneous rate constant / m s^{-1}
k_{ox}	heterogeneous rate constant for oxidation / m s^{-1}
k_{red}	heterogeneous rate constant for reduction / m s^{-1}
n	number of moles of electrons transferred
p	pressure / N m^{-2}
Q	charge / C
q	heat / J
R	universal gas constant $\approx$ 8.314 J K^{-1} mol^{-1}
R	electrical resistance / Ω
r_{e}	electrode radius / m
r_{max}	radial limit of simulation space / m
r	radial coordinate / m
S	entropy / J K^{-1} mol^{-1}
T	absolute temperature / K
t	time / s
U	internal energy / J
V	volume / m^3
v	scan-rate / V s^{-1}

$\mathbf{v}$	vector of convection velocity / m s^{-1}
w	work
$w_{\text{mechanical}}$	mechanical work
$w_{\text{non-mechanical}}$	non-mechanical work
X	species X
x	linear coordinate / m
y	longitudinal coordinate / m
Z	Arrhenius pre-exponential factor / m s^{-1}
z	axial coordinate / m
z_{max}	axial limit of simulation space / m
z_{X}	charge of species X / e molec^{-1}

Greek Symbols

α	Butler-Volmer transfer coefficient (range: 0-1)
Δ	large difference in a quantity
ν_{X}	stoichiometric coefficient of species X
ϕ	potential / V
ϕ_{m}	electrode [metallic] potential / V
ϕ_{s}	solution potential / V
Θ	fractional surface coverage

Miscellaneous Symbols

∇	del operator
$\ddagger$	(as superscript) transition state
∇^2	Laplacian operator
$\sum$	sum of
$\ominus$	(as superscript) standard conditions
f	(as subscript) formal conditions
$\langle\rangle$	(as bracket) mean value of a quantity

Abbreviations

ADI	Alternating direction implicit
IHP	Inner Helmholtz plane
OHP	Outer Helmholtz plane
PDE	Potential determining equilibrium
ref	(as subscript) reference
SCE	saturated calomel electrode
SHE	standard hydrogen electrode
soln	solution
ss	(as subscript) steady-state

Normalised Parameters[i]

a	$\frac{c_\mathrm{A}}{c_\mathrm{A}^*}$
J	$\frac{jr_\mathrm{e}}{c_\mathrm{A}^* D_\mathrm{A}}$
K^0	$\frac{k^0 r_\mathrm{e}}{D_\mathrm{A}}$
K_comp	$\frac{k_\mathrm{comp} c_\mathrm{A}^* r_\mathrm{e}^2}{D_\mathrm{A}}$
K_disp	$\frac{k_\mathrm{disp} c_\mathrm{A}^* r_\mathrm{e}^2}{D_\mathrm{A}}$
θ	$\frac{F(E-E_\mathrm{f}^\ominus)}{RT}$
R	$\frac{r}{r_\mathrm{e}}$
R_d	$\frac{r_\mathrm{d}}{r_\mathrm{e}}$
σ	$\frac{r_\mathrm{e}^2}{D_\mathrm{A}} \frac{Fv}{RT}$
τ	$\frac{D_\mathrm{A} t}{r_\mathrm{e}^2}$
Z	$\frac{z}{r_\mathrm{e}}$

[i]It is traditional to normalise parameters using the first species in the mechanism (denoted 'A').

Contents

Chapter 1

Introduction to electrochemistry

Electrochemistry is divided into two parts: potentiometry and electrode dynamics. These are concerned, respectively, with the thermodynamic and kinetic properties of redox processes. This chapter provides an overview of each topic. The explanations are based on a simple one electron reduction ($A^{z_A} + e^- \rightleftharpoons B^{z_A - 1}$). More complicated many electron reactions ($A^{z_A} + ne^- \rightleftharpoons B^{z_A - n}$) are the sum of several one electron reductions.

1.1 Potentiometry[1–5]

1.1.1 The origin of the potential difference

The *potential* (ϕ) at a point is the work done by external forces (E_w) in bringing a unit positive 'test' charge from infinity to that point[i]:

$$\phi = E_w \text{ per unit positive 'test' charge} \tag{1.1.1}$$

[i]Potential is measured in units of volts (V). Equation 1.1.1 implies that 1 V = 1 J C^{-1}.

Equivalently, for a 'test' charge of arbitrary magnitude and sign (Q):

$$\phi = \frac{E_w}{Q} \tag{1.1.2}$$

The *potential difference* (E) between two arbitrary points labeled 1 and 2 is given by:

$$E = \phi_1 - \phi_2 \tag{1.1.3}$$

A non-zero potential difference arises from the separation of electrical charge. In an electrochemical context, charge separation can be brought about by a *potential determining equilibrium* (abbreviated as PDE). This is an equilibrium in which a charged species is exchanged across an interface[ii]. The most common example is one in which an electron is exchanged across the interface separating a metallic solid (metal) and a solution (soln):

$$\mathrm{A}^{z_\mathrm{A}}(\mathrm{soln}) + \mathrm{e}^-(\mathrm{metal}) \rightleftharpoons \mathrm{B}^{z_\mathrm{A}-1}(\mathrm{soln}) \tag{1.1.4}$$

This equilibrium can be established using a metallic solid, called an electrode, and a solution, containing dissolved species A and B. When separated, the electrode and the solution are each electrically neutral. When the electrode is immersed in the solution, the reversible reaction shown in equation 1.1.4 is established. As this reaction tends towards equilibrium, a net transfer of electrons occurs through the solid-liquid interface. Consequently, at equilibrium, the phases possess electrical

[ii]Chemical reactions involving two or more different phases are called heterogeneous reactions. Chemical reactions involving only one phase are called homogeneous reactions.

charges that are equal in magnitude but opposite in sign. A charge separation has been established. The potential difference between the metallic and solution phases is non-zero ($E = \phi_{\text{metal}} - \phi_{\text{soln}} \neq 0$ V).

1.1.2 Quantifying the potential difference

$$\mathrm{A}^{z_\mathrm{A}}(\text{soln}) + \mathrm{e}^-(\text{metal}) \rightleftharpoons \mathrm{B}^{z_\mathrm{A}-1}(\text{soln}) \tag{1.1.5}$$

For the PDE shown in equation 1.1.5, the potential difference across the interface is inextricably linked to the concentrations of species A and B. In this section, the relationship is quantified and its implications are explored.

From the first law of thermodynamics, at constant temperature and pressure, the internal energy change (ΔU) of the system is given by:

$$\Delta U = \Delta q + \Delta w \tag{1.1.6}$$

$$\Delta U = T\Delta S + \Delta\omega_{\text{mechanical}} + \Delta\omega_{\text{non-mechanical}} \tag{1.1.7}$$

where Δq is the heat taken in by the system; Δw is the work done on the system; T is the absolute temperature of the system; ΔS is the entropy change of the system; $\Delta\omega_{\text{mechanical}}$ is the mechanical work done on the system and $\Delta\omega_{\text{non-mechanical}}$ is the non-mechanical work done on the system.

By definition, at constant temperature and pressure, the enthalpy change (ΔH) and

the Gibb's energy change (ΔG) of the system are respectively given by:

$$\Delta H = \Delta U + p\Delta V \tag{1.1.8}$$

$$\Delta G = \Delta H - T\Delta S \tag{1.1.9}$$

where p is the pressure of the system and V is the volume of the system. Combining equations 1.1.7, 1.1.8 and 1.1.9 leads to:

$$\Delta G = \omega_{\text{non-mechanical}} \tag{1.1.10}$$

Therefore, at constant temperature and pressure, the Gibb's energy change of a system is equal to the non-mechanical work done on the system.

It follows from equation 1.1.2 that the work (E_{w}) required to move a charge through the potential difference ($E = \phi_{\text{metal}} - \phi_{\text{soln}}$) is given by:

$$E_{\text{w}} = QE \tag{1.1.11}$$

$$E_{\text{w}} \text{ per mole of electrons} = -\text{F}E \tag{1.1.12}$$

where F is the Faraday constant (= 96485 C mol^{-1}). The work referred to in equation 1.1.12 is non-mechanical. Therefore, combining equations 1.1.10 and 1.1.12 leads to:

$$\Delta G = -\text{F}E \tag{1.1.13}$$

It follows from equation 1.1.8, 1.1.9 and 1.1.13 that:

$$\Delta S = \mathrm{F}\left(\frac{\partial \Delta E}{\partial T}\right)_{p,T} \tag{1.1.14}$$

$$\Delta H = -\mathrm{F}E + \mathrm{F}T\left(\frac{\partial \Delta E}{\partial T}\right)_{p,T} \tag{1.1.15}$$

It can be shown[3] that the Gibb's energy change for the reaction in equation 1.1.5 is given by:

$$\Delta G = \Delta G_{\mathrm{f}}^{\ominus} + \mathrm{R}T \ln\left(\frac{c_{\mathrm{B}}}{c_{\mathrm{A}}}\right) \tag{1.1.16}$$

where $\Delta G_{\mathrm{f}}^{\ominus}$ is the Gibb's energy change under formal conditions[iii]; R is the universal gas constant ($= 8.314$ J K^{-1} mol^{-1}); c_{A} is the concentration of species A and c_{B} is the concentration of species B. Combining equations 1.1.13 and 1.1.16 leads to the Nernst equation[iv]:

$$E = E_{\mathrm{f}}^{\ominus} - \frac{\mathrm{R}T}{\mathrm{F}} \ln\left(\frac{c_{\mathrm{B}}}{c_{\mathrm{A}}}\right) \tag{1.1.17}$$

where $E_{\mathrm{f}}^{\ominus}$ is the potential difference under formal conditions. The Nernst equation is of central importance to field of potentiometry because it provides a *quantitative* relationship between the potential difference across an interface and the concentrations of the chemical species in the corresponding PDE.

In summary, the potential difference, or the potential difference as a function of

[iii] Formal conditions are as follows:

$$\begin{aligned} \text{temperature} &= 273.15 \text{ K} \\ \text{pressure} &= 1 \text{ bar} \\ \text{concentration} &= 1 \text{ mol dm}^{-3} \end{aligned}$$

[iv] The Nernst equation is named in honour of the German chemist Walther Nernst (1864-1941). He was the sole recipient of the 1920 Nobel prize for chemistry.

temperature, can be used as a tool with which to determine: the Gibb's energy change; the entropy change; the enthalpy change; and the chemical composition of the corresponding PDE.

1.1.3 Measuring the potential difference

The potential difference between two points is directly proportional to the rate at which an electric charge moves between them. This is expressed mathematically in Ohm's law:

$$E = \frac{\mathrm{d}Q}{\mathrm{d}t} R \tag{1.1.18}$$

where t is the time and R is a constant of proportionality called the resistance. The rate of movement of electric charge is called the *current*[v] (i). Therefore:

$$E = iR \tag{1.1.19}$$

The potential difference between two points is measured using a device called a *voltmeter*. A voltmeter possesses two electrodes which must be placed in electrical contact with each of the two points of interest. In order to avoid setting up a second PDE, these points of interest must *both* be in the solid phase. In sections 1.1.1 and 1.1.2, a PDE was used to establish a potential difference across two *different* phases. Therefore, it is *impossible* to measure the *absolute* potential difference established by the PDE of interest. However, it *is* possible to measure the potential difference of a PDE *relative* to a second PDE. These PDEs are combined to form an *electrochemical*

[v]Current is measured in units of amps (A). Equations 1.1.18 and 1.1.19 imply that 1 A = 1 C s^{-1}

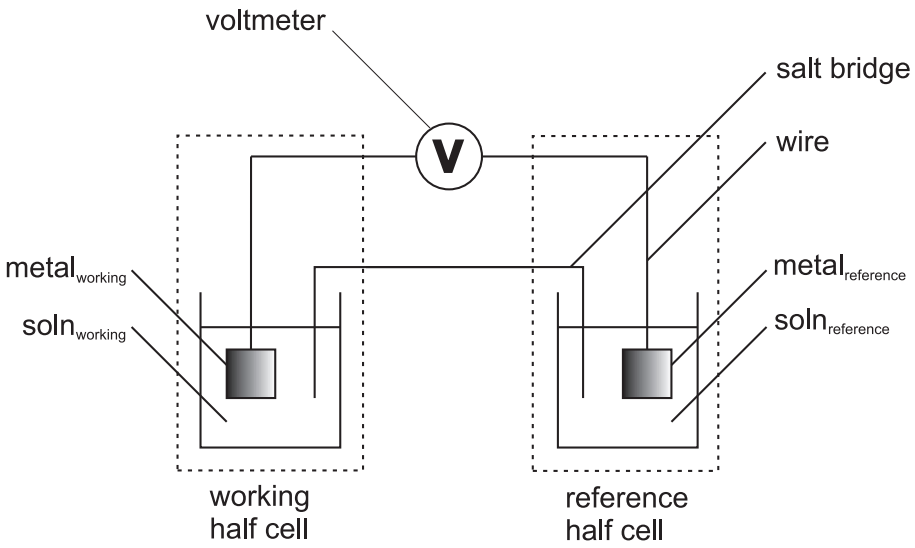

Figure 1.1.1: *Schematic electrochemical cell.*

cell as shown in figure 1.1.1. The PDE of interest is called the *working half cell* and the second PDE is called the *reference half cell*. The electrodes of the voltmeter are electrically connected to the electrodes in the working and reference half cells, as shown. The circuit is completed by electrically connecting the solutions by a *salt bridge*. This typically consists of a tube containing an electrolytic gel. The ions of the electrolyte must respond equally rapidly to current flowing through the cell in order to prevent an antagonistic *liquid junction potential* arising across the salt bridge. Potassium nitrate (KNO_3) is commonly used for this purpose. The potential difference (E) measured by the voltmeter is given by:

$$E = (\phi_{\text{metal}} - \phi_{\text{soln}})_{\text{working}} - (\phi_{\text{metal}} - \phi_{\text{soln}})_{\text{reference}} + iR \tag{1.1.20}$$

where the final term ('iR') is called the Ohmic drop[vi]. This quantifies the decrease in the measured potential difference derived from the inherent electrical resistance of the cell. As discussed at the beginning of this section, the potential difference be-

[vi] "Ohmic drop" is also commonly called "iR drop".

tween two points is directly proportional to the rate of movement of electric charge between them. Therefore, in order to measure the potential difference, a finite current must be permitted to flow through the cell. However, this can lead to two unwanted side effects: non-zero ohmic drop and perturbation of the equilibrium position (and hence potential difference) within each half cell[vii]. A compromise is effected through the use of a high resistance voltmeter that permits a very small (typically $\sim 10^{-12}$ A) current to pass through the cell. Therefore, to good approximation, the ohmic drop term can be neglected and the equilibrium position (and hence potential difference) of each half cell remains constant. The potential difference measured by the voltmeter (E) is therefore *directly* related to the potential difference across the working electrode:

$$E = (\phi_{\text{metal}} - \phi_{\text{soln}})_{\text{working}} + \text{constant} \tag{1.1.21}$$

Changes in the potential difference across the working electrode are therefore equal to *changes* in the measured potential difference of the cell.

1.1.4 Reference electrodes

A suitable reference electrode establishes a potential that is stable with respect to temperature, time and the passage of the small currents. By convention, the reference electrode used for potentiometric work is the *standard hydrogen electrode*

[vii] If current were allowed to flow freely through the cell, the equilibrium in each half cell would be lost and the *entire* cell would tend towards equilibrium. This is how a battery works.

(abbreviated as SHE). The corresponding PDE is:

$$\mathrm{H^+(aq)}(a_{\mathrm{H^+}} = 1) + \mathrm{e^-(metal)} \rightleftharpoons \frac{1}{2}\mathrm{H_2(g)(1\ bar)} \tag{1.1.22}$$

where $a_{\mathrm{H^+}}$ is the activity of $\mathrm{H^+}$ ions[viii]. The potential difference of this PDE under standard conditions[ix] ($E^{\ominus}$) is *declared* equal to 0 V. This provides a basis for comparison with all other PDEs.[6] Although reproducible, the SHE is experimentally cumbersome owing to the need for hydrogen gas. For routine laboratory use, it is common to use the following alternatives:

The saturated calomel electrode (+0.244 V *vs* SHE):

$$\frac{1}{2}\mathrm{Hg_2Cl_2(s)} + \mathrm{e^-(metal)} \rightleftharpoons \mathrm{Hg(l)} + \mathrm{Cl^-(aq)\ (saturated\ KCl)}$$

The silver-silver chloride electrode (+0.204 V *vs* SHE):

$$\mathrm{AgCl(s)} + \mathrm{e^-(metal)} \rightleftharpoons \mathrm{Ag(s)} + \mathrm{Cl^-(aq)\ (0.1\ mol\ dm^{-3}\ HCl)}$$

It should be noted that in neither case above are all chemicals present in unit activity. Therefore, the quoted potential difference of each half cell is *not* equal to its standard electrode potential.

[viii] In water, $a_{\mathrm{H^+}} = 1$ is equivalent to $c_{\mathrm{H^+}} = 1.2$ mol dm^{-3}.

[ix] Standard conditions are as follows:

temperature	=	273.15 K
pressure	=	1 bar
activity	=	1

1.1.5 The electrical double layer

[7–9] When a potential difference exists across an interface, the ions on the solution

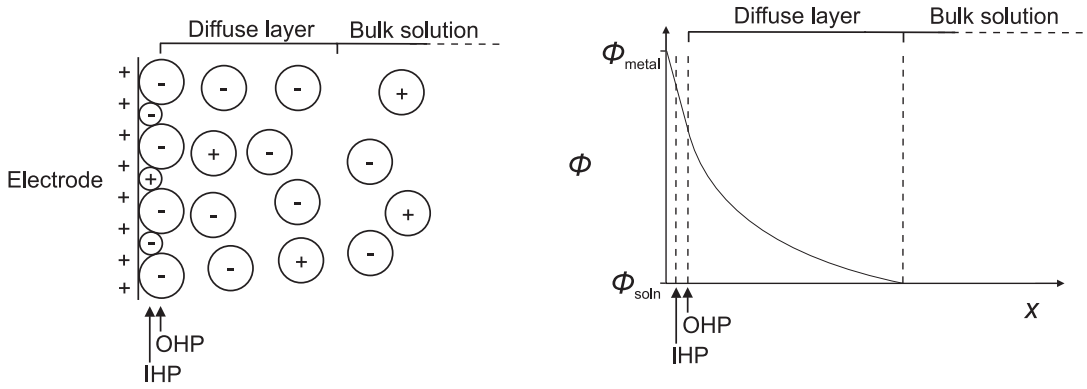

Figure 1.1.2:
Schematic illustration of the electrical double layer for a case in which the electrode is positively charged (left). The corresponding change in potential as a function of distance form the electrode is also shown (right).

side spontaneously adopt an arrangement called the *electrical double layer*. This is shown in figure 1.1.2. The electrical double layer is composed of four parts. In order of increasing distance from the electrode these are: the Inner Helmholtz Plane (IHP); the Outer Helmholtz Plane (OHP); the diffuse layer and bulk solution. The Inner Helmholtz Plane (IHP) is composed of ions, with no solvation shell, adsorbed on the electrode surface. These ions are in direct contact with the electrode (specific adsorption). Therefore, this adsorption interaction is likely to be chemical rather than electrostatic. This layer can contain both positively and negatively charged ions. The Outer Helmholtz Plane (OHP) is composed of ions, with solvation shells, adsorbed on the electrode surface. These ions are *not* in direct contact with the electrode (non-specific adsorption). Therefore, this adsorption interaction is likely to be electrostatic rather than chemical. In this case, the Outer Helmholtz

Plane contains only negatively charged ions. The diffuse layer is composed of both positively and negatively charged ions and represents a compromise between the ordering effect of the electric field, which attracts negatively charged ions towards the electrode, and the disorder brought about by natural thermal motion, which tends to distribute positively and negatively charged ions evenly. Ions can *screen* one another from the effect of the electric field. Therefore, the ordering effect becomes less important with distance from the electrode surface. The surplus of negatively charged ions decreases with distance until, in bulk solution, it is equal to zero.

1.2 Electrode dynamics[1,7,10,12]

1.2.1 Faradaic and non-faradaic currents

$$\mathrm{A}^{z_\mathrm{A}}(\mathrm{soln}) + \mathrm{e}^-(\mathrm{metal}) \rightleftharpoons \mathrm{B}^{z_\mathrm{A}-1}(\mathrm{soln}) \tag{1.2.1}$$

If the equilibrium position of equation 1.2.1 is perturbed, re-equilibration will occur. However, this is not instantaneous. Rather, it is a finite process during which current flows and the potential difference changes. There are two types of current: *faradaic* and *non-faradaic*. The evolution of these currents during equilibration are inextricably linked to the physical and chemical processes underpinning the PDE of interest.

A faradaic current is caused by movement of electrons *through* the interface. One of the electroactive species from equation 1.2.1 approaches the electrode surface and an electron travels, via quantum mechanical tunneling, through the interface. This

process obeys Faraday's law:

$$i_{\text{faradaic}} = A\text{F}j_{\text{A}} = -A\text{F}j_{\text{B}} \tag{1.2.2}$$

where A is the area of the electrode; j_{A} is the flux of species A at the electrode surface and j_{B} is the flux of species B at the electrode surface.

A non-faradaic current[x] is caused by the rearrangement of charge in the electrical double layer. This process is quantitatively identical to capacitative charging:

$$i_{\text{non-faradaic}} = C_{\text{d}}Av \tag{1.2.3}$$

where C_{d} the capacitance and v is the rate at which the potential difference across the interface changes.

Unlike the faradaic current, the non-faradaic current is influenced by factors apart from the PDE of interest. These include the polarity of the solvent and the concentration of inert ions dissolved in the solution. Therefore, when studying a PDE it is preferable to maximise the ratio $i_{\text{faradaic}}/i_{\text{non-faradaic}}$. It is shown in section 1.2.5 that the faradaic current is often proportional to $\sqrt{v}$. Combining this with equation 1.2.3 leads to:

$$\frac{i_{\text{faradaic}}}{i_{\text{non-faradaic}}} \propto \frac{1}{\sqrt{v}} \tag{1.2.4}$$

Therefore, the non-faradaic contribution to the total current is smallest when the potential difference across the interface is changed slowly.

[x]The "non-faradaic current" is also commonly called the "capacitative current".

1.2.2 Quantifying electrode dynamics

$$\mathrm{A}^{z_\mathrm{A}}(\mathrm{soln}) + \mathrm{e}^-(\mathrm{metal}) \rightleftharpoons \mathrm{B}^{z_\mathrm{A}-1}(\mathrm{soln}) \tag{1.2.5}$$

In this section, the relationship between current and potential is quantified and its implications are explored. The current is related to the flux of species A by:

$$i = A\mathrm{F}j_\mathrm{A} \tag{1.2.6}$$

where A is the area of the electrode and j_A is the flux of species A "through" the electrode. The later is equivalent to the overall *rate* of the forward reaction in equation 1.2.5. Equation 1.2.6 can therefore be expanded as a rate equation to give:

$$i = A\mathrm{F}\left(k_\mathrm{red}c_{\mathrm{A},0} - k_\mathrm{ox}c_{\mathrm{B},0}\right) \tag{1.2.7}$$

where $c_{\mathrm{A},\,0}$ is the concentration of species A at the electrode surface; $c_{\mathrm{B},\,0}$ is the concentration of species B at the electrode surface; k_red is the rate constant for reduction, and k_ox is the rate constants for oxidation. It is assumed that these rate constants exhibit Arrhenius type behavior. Therefore:

$$k_\mathrm{red} = Z\exp\left(-\frac{\Delta G^\ddagger_\mathrm{red}}{\mathrm{R}T}\right) \tag{1.2.8}$$

$$k_\mathrm{ox} = Z\exp\left(-\frac{\Delta G^\ddagger_\mathrm{ox}}{\mathrm{R}T}\right) \tag{1.2.9}$$

where $\Delta G^{\ddagger}_{\text{ox}}$ is the activation energy of oxidation; $\Delta G^{\ddagger}_{\text{red}}$ is the activation energy of reduction and Z is the pre-exponential factor. According to the principle of microscopic reversibility, the pre-exponential factor for reduction is equal to the pre-exponential factor for oxidation. The Gibb's energy profile for equation 1.2.5 is

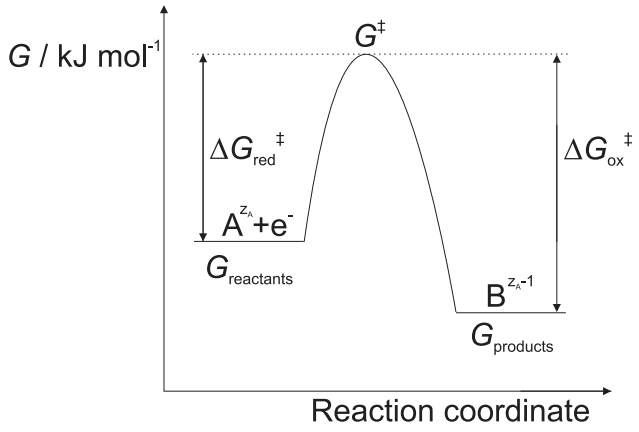

Figure 1.2.1:
The Gibb's energy profile for equation 1.2.5. $G_{\text{reactants}}$ *is the Gibbs energy of the reactants;* G_{products} *is the Gibbs energy of the products and* $G^{\ddagger}$ *is the Gibb's energy of the transition state.*

shown in figure 1.2.1. From this it can be shown that:

$$\Delta G^{\ddagger}_{\text{red}} = G^{\ddagger} - G_{\text{reactants}} \tag{1.2.10}$$

$$\Delta G^{\ddagger}_{\text{ox}} = G^{\ddagger} - G_{\text{products}} \tag{1.2.11}$$

The total Gibb's energy (G_{total}) of a chemical species consists of two components: a chemical term (G_{chem}) and an electrochemical term (G_{elec}):

$$G_{\text{total}} = G_{\text{chem}} + G_{\text{elec}} \tag{1.2.12}$$

The electrochemical component is given by:

$$G_{\text{elec}} = z\text{F}\phi \tag{1.2.13}$$

where z is the charge of the chemical species of interest and ϕ is the potential at the point occupied by the chemical species of interest. Combining equations 1.2.12 and 1.2.13 for reactants and products leads to:

$$G_{\text{reactants}} = G_{\text{reactants chem}} + (z_{\text{A}} - 1)\text{F}\phi_{\text{soln}} - \text{F}\left(\phi_{\text{metal}} - \phi_{\text{soln}}\right) \quad (1.2.14)$$

$$G_{\text{products}} = G_{\text{products chem}} + (z_{\text{A}} - 1)\text{F}\phi_{\text{soln}} \quad (1.2.15)$$

It is assumed that the potential dependence of the transition state lies midway between those of the reactants and products. Therefore:

$$G^{\ddagger} = G^{\ddagger}_{\text{chem}} + (z_{\text{A}} - 1)\text{F}\phi_{\text{soln}} - (1 - \alpha)\text{F}\left(\phi_{\text{metal}} - \phi_{\text{soln}}\right) \quad (1.2.16)$$

where α is an empirical parameter called the transfer coefficient ($0 \leq \alpha \leq 1$). When $\alpha = 0$, the potential dependence of the transition state is identical to that of the reactants. When $\alpha = 1$, the potential dependence of the transition state is identical to that of the products. In general, $\alpha \approx 0.5$. Combining equations 1.2.14 and 1.2.16 leads to:

$$\Delta G^{\ddagger}_{\text{red}} = G^{\ddagger}_{\text{chem}} - G_{\text{reactants chem}} + \alpha\text{F}\left(\phi_{\text{metal}} - \phi_{\text{soln}}\right) \quad (1.2.17)$$

Combining equations 1.2.8 and 1.2.17 leads to:

$$k_{\text{red}} = Z \exp\left(-\frac{G^{\ddagger}_{\text{chem}} - G_{\text{reactants chem}}}{\text{R}T}\right) \exp\left(-\frac{\alpha\text{F}\left(\phi_{\text{metal}} - \phi_{\text{soln}}\right)}{\text{R}T}\right) \quad (1.2.18)$$

Equation 1.2.21 below can trivially be derived from equations 1.2.19 and 1.2.20:

$$E = (\phi_{\text{metal}} - \phi_{\text{soln}})_{\text{working}} - (\phi_{\text{metal}} - \phi_{\text{soln}})_{\text{reference}} \tag{1.2.19}$$

$$E_{\text{f}}^{\ominus} = (\phi_{\text{metal}} - \phi_{\text{soln}})_{\text{working f}}^{\ominus} - (\phi_{\text{metal}} - \phi_{\text{soln}})_{\text{reference}} \tag{1.2.20}$$

$$E - E_{\text{f}}^{\ominus} = (\phi_{\text{metal}} - \phi_{\text{soln}})_{\text{working}} - (\phi_{\text{metal}} - \phi_{\text{soln}})_{\text{working f}}^{\ominus} \tag{1.2.21}$$

Combining equations 1.2.18 and 1.2.21 leads to:

$$k_{\text{red}} = Z \exp\left(-\frac{G_{\text{chem}}^{\ddagger} - G_{\text{reactants chem}} + \alpha\,(\phi_{\text{metal}} - \phi_{\text{soln}})_{\text{working f}}^{\ominus}}{\text{R}T}\right) \exp\left(-\frac{\alpha\,(E - E_{\text{f}}^{\ominus})}{\text{R}T}\right) \tag{1.2.22}$$

The right hand terms of this equation that do not depend on the applied potential (E) can be amalgamated into a constant called k^0:

$$k^0 = Z \exp\left(-\frac{G_{\text{chem}}^{\ddagger} - G_{\text{reactants chem}} + \alpha\,(\phi_{\text{metal}} - \phi_{\text{soln}})_{\text{working f}}^{\ominus}}{\text{R}T}\right) \tag{1.2.23}$$

Combining equations 1.2.22 and 1.2.23 leads to

$$k_{\text{red}} = k^0 \exp\left(\frac{-\alpha\text{F}\,(E - E_{\text{f}}^{\ominus})}{\text{R}T}\right) \tag{1.2.24}$$

where k^0 is called the electrochemical rate constant. In most experiments it's value lies in the range $10^{-9} - 10$ cm s^{-1}. An analogous expression for k_{ox} can be derived

using the same procedure. This leads to:

$$k_{\text{ox}} = k^0 \exp\left(\frac{(1-\alpha)\text{F}\,(E - E_{\text{f}}^{\ominus})}{\text{R}T}\right) \tag{1.2.25}$$

Combining these expressions for k_{red} and k_{ox} with equation 1.2.7 leads to the Butler-Volmer equation[13,14xi]:

$$i = AF\left(k^0 c_{\text{A},0} \exp\left(-\frac{\alpha\text{F}(E - E_{\text{f}}^{\ominus})}{\text{R}T}\right) - k^0 c_{\text{B},0} \exp\left(\frac{(1-\alpha)\text{F}(E - E_{\text{f}}^{\ominus})}{\text{R}T}\right)\right) \tag{1.2.26}$$

The Butler-Volmer equation quantifies the relationship between potential difference and current as a PDE tends towards equilibrium. When equilibrium has been established, the current is equal to zero and the Butler-Volmer equation collapses to the Nernst equation, as expected. It can be seen from equation 1.2.26 that the relationship between current and potential is dependent on two factors: electrode kinetics (k^0 and α) and mass transport of electroactive species to the electrode ($c_{\text{A},0}$ and $c_{\text{B},0}$).

1.2.3 Mass transport

The concentration of an arbitrary chemical species (A) in solution as a function of time depends on four concurrent processes: diffusion, migration, convection and homogeneous kinetics. The quantitative effect of these processes are additive and lead to the following mass transport equation:

[xi] The Butler-Volmer equation was proposed by German chemist Max Volmer (1885-1965) in 1930, based on work published in 1924 by British Chemist John Butler (1899-1977).

$$
\begin{aligned}
\frac{\partial c_{\mathrm{A}}}{\partial t} = \quad & D_{\mathrm{A}}\nabla^2 c_{\mathrm{A}} && \text{Diffusion} \\
& +\nabla c_{\mathrm{A}}\mathbf{v} && \text{Convection} \\
& z_{\mathrm{A}}D_{\mathrm{A}}\nabla c_{\mathrm{A}}\tfrac{F\nabla\phi}{RT} + z_{\mathrm{A}}D_{\mathrm{A}}c_{\mathrm{A}}\tfrac{F\nabla^2\phi}{RT} && \text{Migration} \\
& \textstyle\sum k \prod \mathrm{c_X}^{y} && \text{Homogeneous kinetics}
\end{aligned}
$$

where ∇ and ∇^2 are operators corresponding to the first and second derivatives respectively. The form of these operators is dependent on the geometry of the experiment of interest. Some common examples are given in table 1.1.

Electrode geometry	First derivative	Second derivative
Planar	$\frac{\partial}{\partial x}$	$\frac{\partial^2}{\partial x^2}$
Hemispherical	$\frac{\partial}{\partial r}$	$\frac{\partial^2}{\partial r^2} + \frac{2}{r}\frac{\partial}{\partial r}$
Discal	$\frac{\partial}{\partial z}$ and $\frac{\partial}{\partial r}$	$\frac{\partial^2}{\partial r^2} + \frac{2}{r}\frac{\partial}{\partial r} + \frac{\partial^2}{\partial z^2}$

Table 1.1:
Operators for geometries commonly encountered in electrochemical problems.

Diffusion

Diffusion is the natural movement of material down a concentration gradient. It is quantified by Fick's laws. Fick's first and second laws are respectively:

$$j_{\mathrm{A}} = -D_{\mathrm{A}}\nabla c_{\mathrm{A}} \tag{1.2.27}$$

$$\frac{\partial c_{\mathrm{A}}}{\partial t} = D_{\mathrm{A}}\nabla^2 c_{\mathrm{A}} \tag{1.2.28}$$

where D_{A} the diffusion coefficient and quantifies the rate at which a molecule moves through solution. It depends on a range of factors including the size of the molecule,

the temperature, and the viscosity of the solvent.[15] Diffusion coefficients are of the order 10^{-5} cm^2 s^{-1} in most common solvents. Ionic liquids are notable exception[16] for which diffusion coefficients can be as low as 10^{-7} cm^2 s^{-1}. Diffusion is a natural process, and cannot be eliminated by the design of the experiment (above 0 K).

Migration

Migration is the movement of charged material down a potential gradient. It is quantified by the following equations:

$$j_{\mathrm{A}} = -\frac{z_{\mathrm{A}}\mathrm{F}}{\mathrm{R}T} D_{\mathrm{A}} c_{\mathrm{A}} \nabla\phi \tag{1.2.29}$$

$$\frac{\partial c_{\mathrm{A}}}{\partial t} = \frac{z_{\mathrm{A}}\mathrm{F}}{\mathrm{R}T} D_{\mathrm{A}} (\nabla c_{\mathrm{A}} \nabla\phi + c_{\mathrm{A}} \nabla^2\phi) \tag{1.2.30}$$

The potential difference across an electrode leads to a potential gradient in solution, as discussed in section 1.1.5. The effect of this gradient can be suppressed by adding large quantities of inert, or 'supporting', electrolyte to the solution[xii]. As the concentration of supporting electrolyte increases, the potential gradient becomes compressed closer to the surface of the electrode. Once thinner than *ca.* 1-2 nm, the effect of migration vanishes because over this distance the electrons can bypass the potential gradient by means of quantum mechanical tunneling.[1] Consequently, no electroactive material enters the region occupied by the potential gradient. As a general rule, this effect is achieved if the supporting electrolyte is present in a concentration greater than 30 times that of the electroactive species. In addition

[xii] For example, potassium chloride (KCl) is used for aqueous systems while tert-butylammonium perchlorate (TBAP) is used for non-polar solvent

to reducing the contribution from migration, supporting electrolyte also reduces the ohmic drop, by increasing the conductivity of the solution, and maintains constant activity coefficients, by dominating the effect of variable amounts of naturally occurring electrolyte.[12]

Convection

Convection is the movement of material caused by a mechanical force. There are two types: natural convection and forced convection. Natural convection occurs due density gradients in solution caused by natural variations in background temperature. This is impossible to eliminate but it's effects are minimal over short timescales (typically ~ 20 s). These timescales are suitable for most voltammetric work. Forced convection is brought about by mechanical means such as stirring. Forced convection is quantified by the following equations:

$$j_{\text{convection}} = \mathbf{v}c \tag{1.2.31}$$

$$\frac{\partial c}{\partial t} = \mathbf{v}\nabla c \tag{1.2.32}$$

where v is the velocity of the solution.

Homogeneous kinetics

The chemical species involved in the PDE of interest may also be involved in one or more homogeneous reactions in solution. The most common reaction mechanisms are classified using a form of nomenclature proposed in 1961 by Testa and Reinmuth.[17] The rules are as follows: heterogeneous reactions are indicated by the letter

E; homogeneous reactions are indicated by the letter C; second order reactions are indicated by a subscript 2, and catalytic reactions are indicated by a prime symbol. The Testa-Reinmuth notation for some common reaction mechanisms are shown in table 1.2.

Testa-Reinmuth notation	Reaction mechanism
E	$A + e^- \rightleftharpoons B$
EC	$A + e^- \rightleftharpoons B \rightarrow C$
EC_2	$A + e^- \rightleftharpoons B + C \rightarrow D$
ECE	$A + 2e^- \rightleftharpoons B + e^- \rightarrow C + e^- \rightarrow D$
EC'	$A + B + e^- \rightleftharpoons C + B \rightarrow D + A$

Table 1.2:
Testa-Reinmuth notation for some common reaction mechanisms.

1.2.4 Three electrode systems[7,12]

In a voltammetric experiment, a potential difference is applied across the working electrode in order to perturb the position of the corresponding PDE. The current through the this electrode is measured as equilibrium is re-established. Dynamic information can be derived by analysing the current as a function of the applied potential difference. Naively, such an experiment could be performed using the two electrode system shown in figure 1.2.2(a). The potential difference between the working and reference electrodes (E) is given by Eqn 1.2.33. Since a current flows, an ohmic drop term (iR) must be included in order to account for the inherent

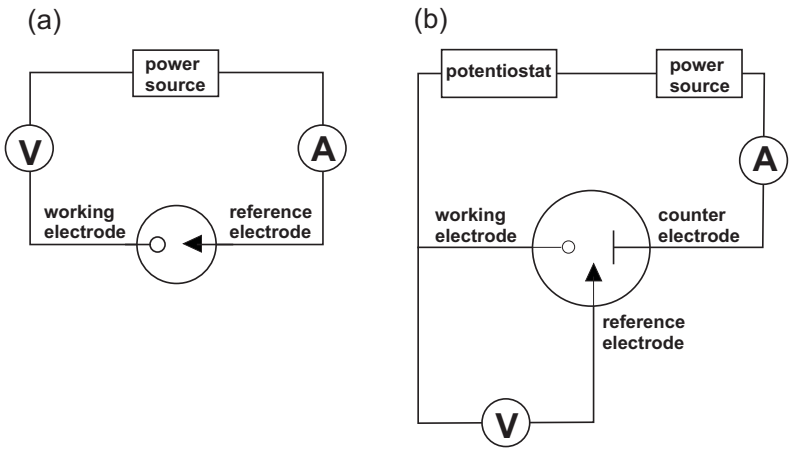

Figure 1.2.2:
(a) Two electrode system (b) Three electrode system

electrical resistance of the cell.

$$E = (\phi_{\text{metal}} - \phi_{\text{soln}})_{\text{working}} - (\phi_{\text{metal}} - \phi_{\text{soln}})_{\text{reference}} + iR \tag{1.2.33}$$

In order to obtain meaningful data, the potential difference applied across the cell must directly control the potential difference across the working electrode. Therefore, the terms $(\phi_{\text{metal}} - \phi_{\text{soln}})_{\text{reference}}$ and iR in equation 1.2.2 must be constant with respect to E. The first condition is satisfied when no current passes through the reference electrode. This is not possible in a two electrode system: a third electrode (called the *counter electrode*[xiii]) must be included as shown in figure 1.2.2(b).

A device called a *potentiostat* drives a current through the counter electrode in order to form a complete circuit with the working electrode. This eliminates the need for a current to flow through the reference electrode. Consequently, the reference electrode possesses a constant composition and, therefore, a stable potential. The counter electrode must possess a high surface area and be positioned very close to the working electrode in order to minimise to ohmic drop term in equation 1.2.33.

[xiii]The "counter electrode" is also commonly called the "auxiliary electrode".

The counter electrode is often separated from the working electrode by a porous frit in order to prevent interference between the chemical species involved in each PDE.

1.2.5 Voltammetric experiments

There are two main types of voltammetric experiment: chronoamperometry and cyclic voltammetry. These techniques are explained in the following sections.

Chronoamperometry

In chronoamperometry, the applied potential difference across the working electrode is stepped from an initial value E_1, at which no electrolysis occurs, to a second value E_2, at which the rate of electrolysis is mass transport limited. This is shown schematically in figure 1.2.3(a). The corresponding transient is shown in figure 1.2.3(b).

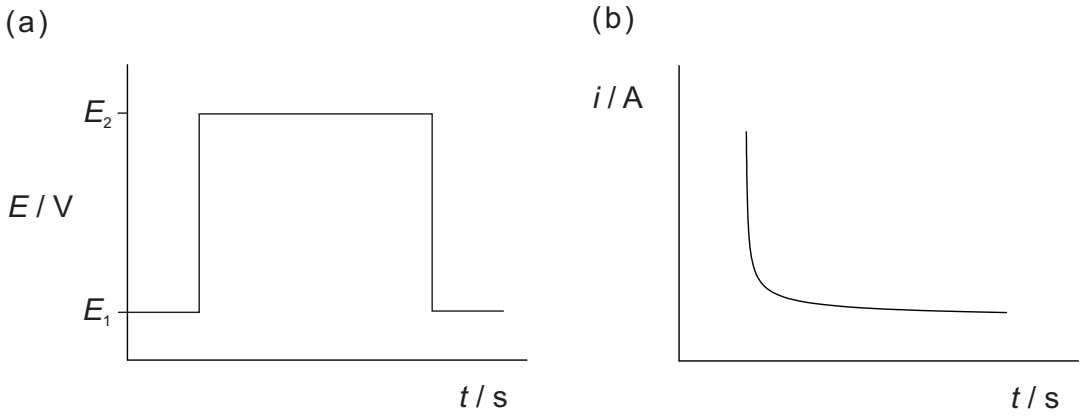

Figure 1.2.3:
(a) Potential difference across the cell as a function of time.
(b) Current through the working electrode as a function of time.

This experiment can be solved analytically for diffusion to a planar electrode (equa-

tion 1.2.35) or to a hemispherical electrode (equation 1.2.35).

$$i = \frac{\mathrm{F}A\sqrt{D_\mathrm{A}}c^*_\mathrm{A}}{\sqrt{\pi t}} \tag{1.2.34}$$

$$i = \mathrm{F}AD_\mathrm{A}c^*_\mathrm{A}\left(\frac{1}{\sqrt{\pi D_\mathrm{A}t}} + \frac{1}{r_\mathrm{e}}\right) \tag{1.2.35}$$

Cyclic Voltammetry[18,19]

In cyclic voltammetry, the applied potential difference across the working electrode varies linearly from an initial value, E_1, at which no electrolysis occurs, to a second value E_2, at which the rate of electrolysis is mass transport limited. The potential is then linearly swept back to E_1. The rate of change of potential with respect to time during the linear sweeps is called the *scan rate* and can vary from a few milivolts per second to several million volts per second depending on the experiment. This is shown schematically in figure 1.2.4(a). A typical transient is shown in figure 1.2.4(b).

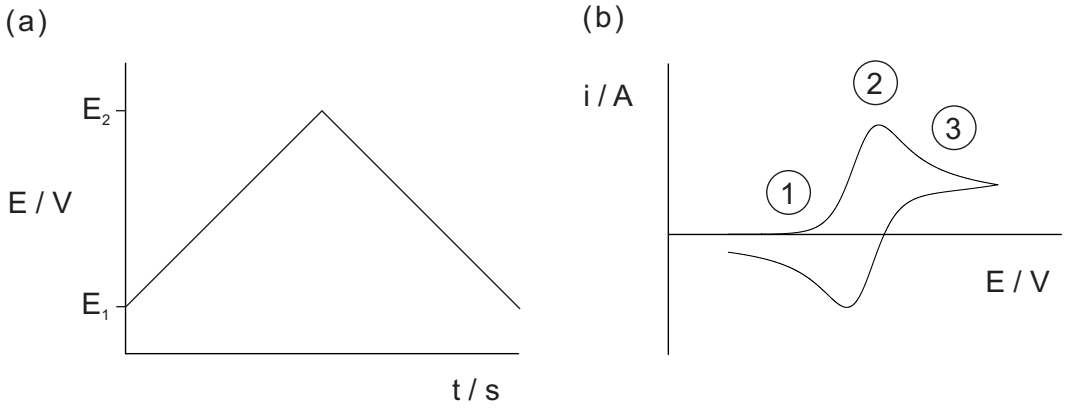

Figure 1.2.4:
(a)Potential difference across the cell as a function of time.
(b)Current through the working electrode as a function of potential difference across the cell.

At point 1 in figure 1.2.4(b), the flux increases with applied potential as quantified by the exponential terms in the Butler-Volmer equation. The current is said to be limited by the electrode kinetics. At point 2, mass transport becomes rate limiting. At point 3, the flux is controlled by mass transport alone. There are three main voltammetric wave shapes: reversible, quasi-reversible and irreversible. When

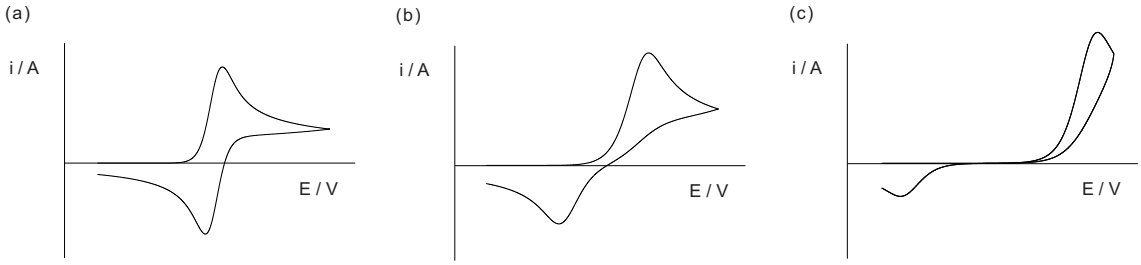

Figure 1.2.5: *(a)Reversible (b)Quasi-reversible (c)Irreversible*

the electrode kinetics are rapid relative to mass transport, species A and B are in equilibrium at the electrode surface. The system is said to be *reversible* and is characterised by a cyclic voltammogram of the form shown in figure 1.2.5(a). The peak to peak separation is 59 mV and the peak current of the forward peak is quantified by the reversible Randles-Ševčík equation:

$$i_{\text{peak}} = (2.69\times10^5)AD_{\text{A}}^{\frac{1}{2}}c_A^*v^{\frac{1}{2}} \tag{1.2.36}$$

When the electrode kinetics are slower, equilibration cannot occur on the experimental timescale. The system is said to be *irreversible* and is characterised by a cyclic voltammogram of the form shown in figure 1.2.5(c). The potential of the forward peak is scan rate dependent and the peak current is governed by the irreversible

Randles-Ševčík equation:

$$i_{\text{peak}} = (2.99\times10^5)\alpha^{\frac{1}{2}} A D_{\text{A}}^{\frac{1}{2}} c_A^* v^{\frac{1}{2}} \tag{1.2.37}$$

Voltammetry between the reversible and irreversible limits is described as being *quasi-reversible* and leads to cyclic voltammetry of the form shown in Figure 1.2.5(b). Matsuda and Ayabe[19] have quantitatively defined electrochemical reversibility based on scan rate v and electrochemical rate constant k^0. This is shown in table 1.3.

Classification	Matsuda-Ayabe condition
Reversible	$k^0 \geq 0.3v^{\frac{1}{2}}$ cm s^{-1}
Quasi-reversible	$0.3v^{\frac{1}{2}}$ cm s^{-1} $> k^0 >$ $2\times10^{-5}v^{\frac{1}{2}}$ cm s^{-1}
Irreversible	$k^0 \leq 2\times10^{-5}v^{\frac{1}{2}}$ cm s^{-1}

Table 1.3:
The Matsuda-Ayabe classification.

Bibliography

[1] Compton, R. G.; Banks, C. E. *Understanding Voltammetry*, 2nd ed.; Imperial College Press, 2010.

[2] Compton, R. G.; Sanders, G. H. W. In *Electrode Potentials*; Compton, R. G., Ed.; OUP, 1996.

[3] Smith, E. B. *Basic Chemical Thermodynamics*; Imperial College Press, 2004.

[4] Reiger, P. H. *Electrochemistry*, 2nd ed.; Chapman & Hall, 1994.

[5] Atkins, P.; De Paula, J. *Atkin's Physical Chemistry*; OUP, 2006.

[6] Bard, A. J., Parsons, R., Jordan, J., Eds. *Standard Potentials in Aqueous Solution*; CRC Press, 1985.

[7] Fisher, A. C. In *Electrode Dynamics*; Compton, R. G., Ed.; Oxford University Press: New York, 1996.

[8] von Helmholtz, H. L. F. *Ann. Physik* **1853**, *89*, 211.

[9] Grahame, D. C. *Chem. Rev.* **1947**, *41*, 441.

[10] Albery, J. *Electrode Kinetics*; OUP, 1975.

[11] Compton, R. G.; Banks, C. E. *Understanding Voltammetry*; World Scientific: Singapore, 2007.

[12] Wang, J. *Analytical Electrochemistry*; VCH, 1994.

[13] Butler, J. A. V. *Trans. Faraday Soc.* **1924**, *19*, 729.

[14] Erdey-Grúz, T.; Volmer, M. *Z. Physik. Chem.* **1930**, *150*, 203–213.

[15] Wilke, C. R.; Chang, P. *Am. Inst. Chem. Eng. J.* **1955**, *1*, 264–270.

[16] Silvester, D. S.; Compton, R. G. *Z. Phys. Chem.* **2006**, *220*, 1247–1274.

[17] Testa, A. C.; Reinmuth, W. H. *Anal. Chem.* **1961**, *33*, 1320–1324.

[18] Nicholson, R. S.; Shain, I. *Anal. Chem.* **1964**, *36*, 706–723.

[19] Matsuda, H.; Ayabe, Y. *Z. Elecktrochem* **1955**, *59*, 494.

Chapter 2

Introduction to numerical modeling

Electrochemistry is almost unique. It lends itself to a wide range of important, everyday applications yet is often amenable to accurate numerical modeling. This chapter provides an overview of numerical modeling in electrochemistry.

2.1 Why model electrochemistry?

Any electrochemical experiment can be expressed as a mathematical problem. Almost all of these problems can be solved. When the reaction mechanism is not known, the correct formulation of the problem can be deduced using an iterative process in which experimental and theoretical results are compared. A flow chart for this process is shown in figure 2.1.1. The correct mathematical model for an experiment is useful for two reasons. First, it can be solved to yield the same result as the experiment, often with considerably less time and expense. Secondly, it provides

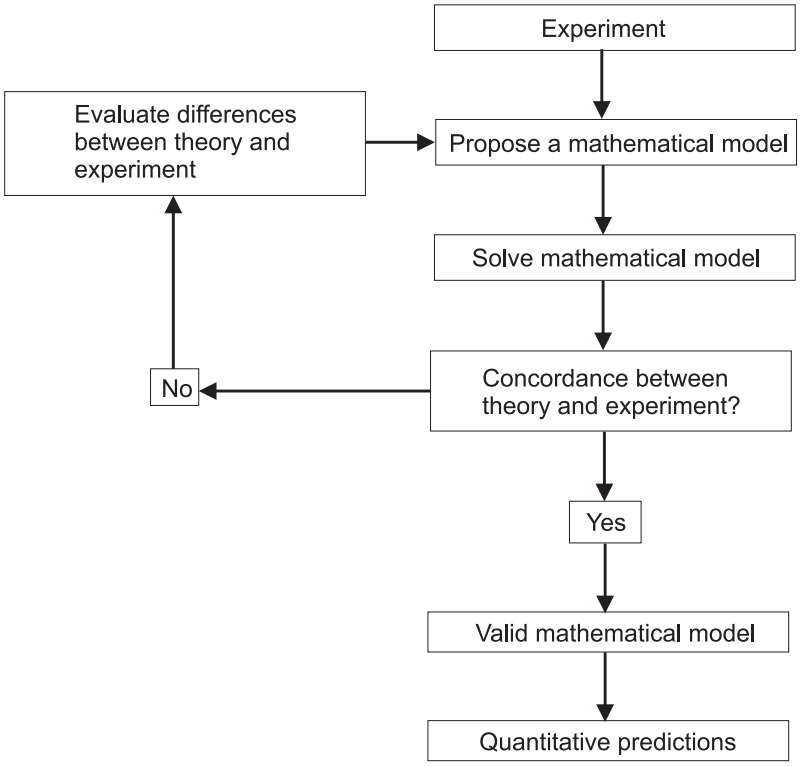

Figure 2.1.1: *Flow diagram showing the process of modeling an electrochemical experiment.*

an insight into the physical and chemical processes underpinning the experiment. Concordance between theoretical and experimental results can be used to provide evidence for a reaction mechanism. Such evidence becomes stronger if concordance can be obtained over a wider range of experimental conditions.

2.2 Mathematical methods

Any electrochemical experiment is mathematically described by one or more mass transport equations, subject to a collection of initial and boundary conditions. The solution of this initial and boundary value problem (abbreviated as IBVP) is normally a concentration profile as a function of space and time. Two types of mathematical method can be used to solve IBVPs: analytical methods and numerical methods.

2.2.1 Analytical methods

Analytical methods produce a solution to an IBVP either in closed form or as a functional series. The functional series is either truncated, yielding an approximate closed solution, or is evaluated to the desired level of accuracy using a computer. Commonly used analytical methods include *integral transforms* and *separation of variables*. The majority of IBVPs encountered in electrochemistry are sufficiently complicated to preclude the straightforward derivation of an analytical solution. Consequently, analytical methods are not used for the majority of the work presented in this thesis.

2.2.2 Numerical methods

Numerical techniques produce an *approximate* solution to an IBVP. The mathematics involved are finite, not continuous, and are therefore amenable to computational manipulations[i]. Commonly used numerical methods include the *finite difference method* and the *finite element method*. The finite element method is difficult to implement but can be applied to solve a wider range of problems, especially those involving irregular experimental geometries. In contrast, the finite difference method is easier to implement, but lends itself only to relatively simple experimental geometries. Since the most useful electrochemical experiments are geometrically simple, the finite difference method is used for the work presented in this thesis.

[i]The first published use of a numerical technique to solve an electrochemical problem was done in 1948 by John Randles.[1] In in lieu of a computer, the calculations were done entirely by hand. According to Britz,[2] the first published use of a numerical method to solve an electrochemical problem with a computer was written by Stephen Feldberg in 1964.[3]

2.3 The finite difference method

2.3.1 Discretisation

A computer cannot store an infinite number of degrees of freedom. Consequently, it is incapable of manipulating a continuous function. *Discretisation* is the process by which a function is made computationally tractable by dividing its coordinates into a *mesh* of discrete points called *nodes*. In this section, we shall consider the arbitrary function $f(x)$ in which the dependent variable is discretised to form an even mesh with internode separation Δx. The discretisation of an arbitrary function, $f(x)$, leads to:

$$f(x) \approx f(x_0), f(x_1), f(x_2), \ldots \tag{2.3.1}$$

There are three ways in which the first derivative can be discretised: the backward,

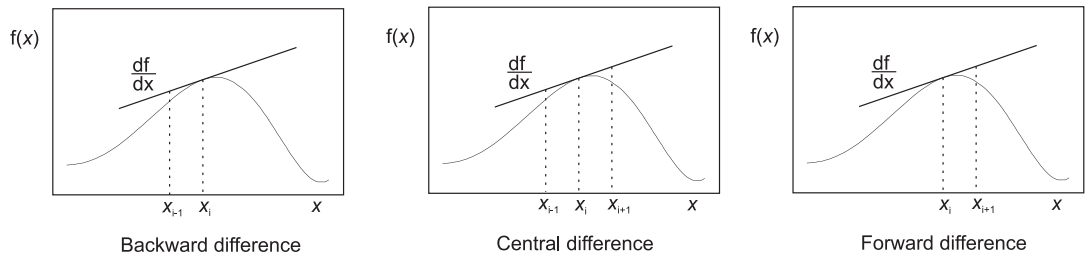

Figure 2.3.1:
The backward, central and forward difference approximations of the first derivative. These are shown for an arbitrary function, $f(x)$, at point x, indicated by the tangent to the curve in each case.

central, and forward difference approximations. These are are shown schematically in figure 2.3.1 and defined mathematically in table 2.1. The backward and forward difference approximations are combined to yield the discrete form of the second derivative, defined mathematically in table 2.1. The accuracy of these discretised

Finite difference approximation	**Mathematical form**
first derivative (backward difference)	$\frac{\mathrm{d}f}{\mathrm{d}x} \approx \frac{f(x)-f(x-\Delta x)}{\Delta x}$
first derivative (central difference)	$\frac{\mathrm{d}f}{\mathrm{d}x} \approx \frac{f(x+\Delta x)-f(x-\Delta x)}{2\Delta x}$
first derivative (forward difference)	$\frac{\mathrm{d}f}{\mathrm{d}x} \approx \frac{f(x+\Delta x)-f(x)}{\Delta x}$
second derivative	$\frac{\mathrm{d}^2f}{\mathrm{d}x^2} \approx \frac{\frac{f(x+\Delta x)-f(x)}{\Delta x} - \frac{f(x)-f(x-\Delta x)}{\Delta x}}{\Delta x}$

Table 2.1:
Mathematical form of various finite difference approximations.

first and second derivatives can be estimated by expanding the function $f(x)$ around an arbitrary point, x_i, in a Taylor expansion:

$$f(x_\mathrm{i} + \Delta x) \approx f(x_\mathrm{i}) + \Delta x \frac{\mathrm{d}f(x_\mathrm{i})}{\mathrm{d}x} + \frac{(\Delta x)^2}{2} \frac{\mathrm{d}^2 f(x_\mathrm{i})}{\mathrm{d}x^2} + \ldots \tag{2.3.2}$$

Combining equation 2.3.2 with the expression for the backward difference approximation for the first derivative from table 2.1 leads to:

$$\frac{\mathrm{d}f(x_\mathrm{i})}{\mathrm{d}x} \approx \frac{f(x_\mathrm{i} + \Delta x) - f(x_\mathrm{i})}{\Delta x} - \frac{\Delta x}{2} \frac{\mathrm{d}^2 f(x_\mathrm{i})}{\mathrm{d}x^2} + \ldots \tag{2.3.3}$$

By comparing equation 2.3.3 with the expression for the backward difference approximation for the first derivative from table 2.1, it can be seen that the leading error term of the latter is directly proportional to the internode spacing, Δx. The backward difference approximation is said to have an error of the order Δx (abbreviated as $O(\Delta x)$). A similar analysis can be applied to the other finite difference approximations. The results of these error analyses are summarised in table 2.2. In

all cases, the error becomes smaller with decreasing internode spacing, Δx. Of the three first derivative approximations, the error decreases at the greatest rate for the central difference approximation. Consequently, this approximation is used where possible.

Finite difference approximation	**Error**
first derivative (backward difference)	$O(\Delta x)$
first derivative (central difference)	$O((\Delta x)^2)$
first derivative (forward difference)	$O(\Delta x)$
second derivative	$O((\Delta x)^2)$

Table 2.2:
Errors for various finite differences.

2.3.2 Diffusion in one dimension

As stated in section 2.2, any electrochemical experiment can be mathematically described by one or more mass transport equations, subject to a collection of initial and boundary conditions. For the example is this section, the mass transport equation is Fick's second law of diffusion:

$$\frac{\partial c}{\partial t} = D\frac{\partial^2 c}{\partial x^2} \tag{2.3.4}$$

where c is an arbitrary concentration; t is the time; D is the diffusion coefficient and x is the spatial coordinate. This mass transport equation is appropriate for a one dimensional problem such as a macrodisc in which edge effects are negligible

(i.e. the diffusion layer is much thinner than the radius of the electrode). The first step is to define the discretised mesh over which equation 2.3.4 is to be solved. In this example, the spatial mesh consists of uniformly spaced nodes (node separation = Δx) in the range $0 \geq x \geq x_{\max}$. The temporal mesh consists of uniformly spaced nodes (node separation = Δt) in the range $0 \leq t \leq t_{\max}$. These discretised meshes are

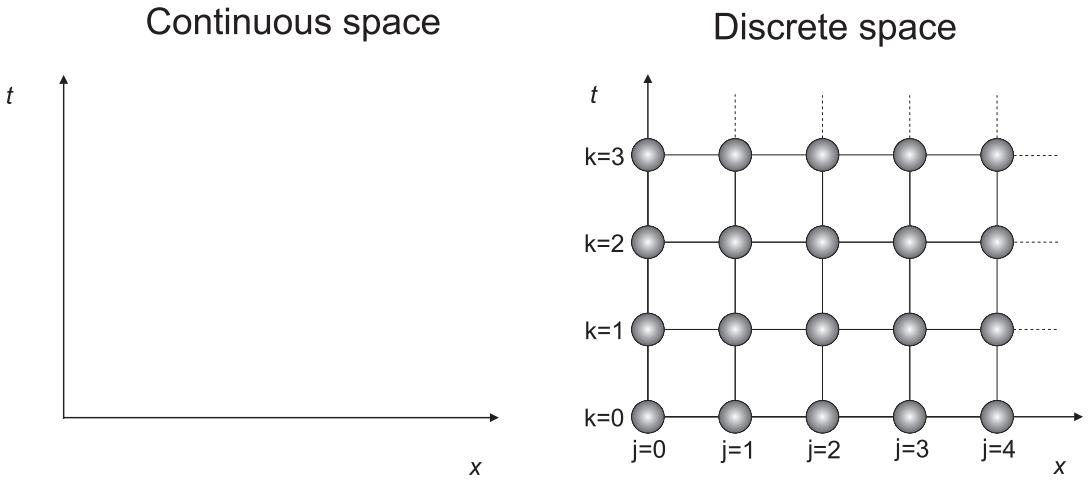

Figure 2.3.2:
Schematic representations of continuous space and discrete space.

shown schematically in figure 2.3.2 and are mathematically described by:

$$x_{\mathrm{j}} = \mathrm{j}\Delta x \text{ for j=0, 1, ..., } N_x \tag{2.3.5}$$

$$t_{\mathrm{k}} = \mathrm{k}\Delta t \text{ for k=0, 1, ..., } N_t \tag{2.3.6}$$

where $x_{\max} = N_x \Delta x$ and $t_{\max} = N_t \Delta t$. Equation 2.3.4 is discretised:

$$\frac{c_{\mathrm{j}}^{\mathrm{k}+1} - c_{\mathrm{j}}^{\mathrm{k}}}{\Delta t} = D \frac{c_{\mathrm{j}+1} - 2c_{\mathrm{j}} + c_{\mathrm{j}-1}}{(\Delta x)^2} \tag{2.3.7}$$

The right hand side of this equation is not yet discretised with respect to time. It is possible to use either t_k or t_{k+1} for this purpose. These are called the *explicit* and *implicit* finite difference methods respectively and are described in the following sections.

Explicit finite difference method in one dimension

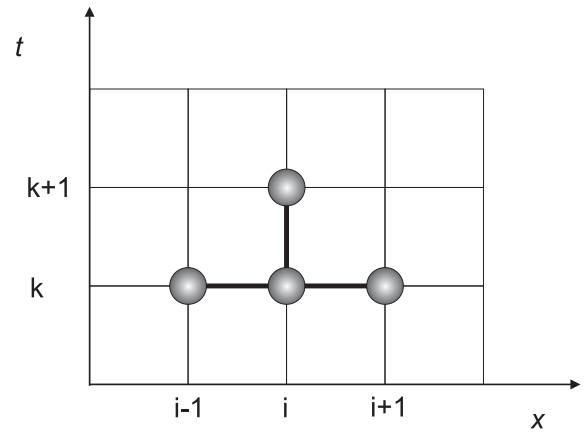

Figure 2.3.3:
Schematic representation of the one dimensional explicit finite difference method.

Explicit discretisation is as follows:

$$\frac{\partial c}{\partial t} = D\frac{\partial^2 c}{\partial x^2} \tag{2.3.8}$$

$$\frac{c_j^{k+1} - c_j^k}{\Delta t} = D\frac{c_{j+1}^k - 2c_j^k + c_{j-1}^k}{(\Delta x)^2} \tag{2.3.9}$$

The computational stencil for this scheme showing how the new point is calculated is shown in figure 2.3.3. The concentration at the new time step (c_j^{k+1}) is calculated from a knowledge of three concentrations at the previous time step (c_{j+1}^k, c_j^k and c_{j-1}^k) and is independent of other concentrations in the new time step.

A numerical method is said to be stable when the error incurred at a given temporal iteration fails to propagate during successive iterations. The stability of a finite

difference scheme is studied using a Fourier stability analysis[4–6ii] and is presented here. Rearrangement of equation 2.3.9 leads to:

$$c_{\mathrm{j}}^{\mathrm{k+1}} = c_{\mathrm{j}}^{\mathrm{k}} + \frac{D\Delta t}{(\Delta x)^2}\left(c_{\mathrm{j+1}}^{\mathrm{k}} - 2c_{\mathrm{j}}^{\mathrm{k}} + c_{\mathrm{j-1}}^{\mathrm{k}}\right) \tag{2.3.10}$$

The round-off error, $\epsilon_{\mathrm{j}}^{\mathrm{k}}$, associated with the discrete concentration $c_{\mathrm{j}}^{\mathrm{k}}$ is given by:

$$\epsilon_{\mathrm{j}}^{\mathrm{k}} = c_{\mathrm{j}}^{\mathrm{k}} - s_{\mathrm{j}}^{\mathrm{k}} \tag{2.3.11}$$

where $s_{\mathrm{j}}^{\mathrm{k}}$ is the exact concentration and $c_{\mathrm{j}}^{\mathrm{k}}$ is the approximate concentration. Combining equations 2.3.10 and 2.3.11:

$$\epsilon_{\mathrm{j}}^{\mathrm{k+1}} = \epsilon_{\mathrm{j}}^{\mathrm{k}} + \frac{D\Delta t}{(\Delta x)^2}\left(\epsilon_{\mathrm{j+1}}^{\mathrm{k}} - 2\epsilon_{\mathrm{j}}^{\mathrm{k}} + \epsilon_{\mathrm{j-1}}^{\mathrm{k}}\right) \tag{2.3.12}$$

The error is composed of two parts: a spatial and temporal. It is known that, for mathematical problems of the type encountered in electrochemistry, the spatial component can be expressed as a Fourier series and the temporal component as an exponential.

$$\epsilon_{\mathrm{j}}^{\mathrm{k}} = \sum_{\mathrm{m}=1}^{\infty} \exp\left(\alpha \mathrm{k}\Delta t\right) \exp\left(\mathrm{i}\beta \mathrm{mj}\Delta x\right) \tag{2.3.13}$$

where α and β are constants. It can be seen from equation 2.3.13 that the growth of error in a single term is identical to that for the whole series. Therefore, only a

[ii] A Fourier stability analysis is also called a von Neumann stability analysis.

single term need be considered. For m = 1:

$$\epsilon_{\mathrm{j}}^{\mathrm{k}} = \exp\left(\alpha \mathrm{k} \Delta t\right) \exp\left(\mathrm{i}\beta \mathrm{j} \Delta x\right) \tag{2.3.14}$$

Combining equations 2.3.12 and 2.3.14 leads to:

$$\frac{\epsilon_{\mathrm{j}}^{\mathrm{k}+1}}{\epsilon_{\mathrm{j}}^{\mathrm{k}}} = \left| 1 - \frac{4D\Delta t}{(\Delta x)^2} \sin^2\left(\frac{\Delta x}{2}\right) \right| \tag{2.3.15}$$

In order that errors do not propagate it is necessary that:

$$\frac{\epsilon_{\mathrm{j}}^{\mathrm{k}+1}}{\epsilon_{\mathrm{j}}^{\mathrm{k}}} \leq 1 \tag{2.3.16}$$

Comparing equations 2.3.15 and 2.3.16 leads to:

$$\frac{D\Delta t}{\Delta x^2} \leq \frac{1}{2} \tag{2.3.17}$$

Consequently, the result of this Fourier stability analysis shows that the one dimensional explicit finite difference method is only stable when $\frac{D\Delta t}{\Delta x^2} \leq \frac{1}{2}$. Although simple to program, the conditional stability of the explicit method makes it unsuitable for solving many problems.

It can be shown that the error associated with the one dimensional explicit method is as follows:

$$\text{error} = O(\Delta t) + O((\Delta x)^2) \tag{2.3.18}$$

Implicit finite difference method in one dimensional

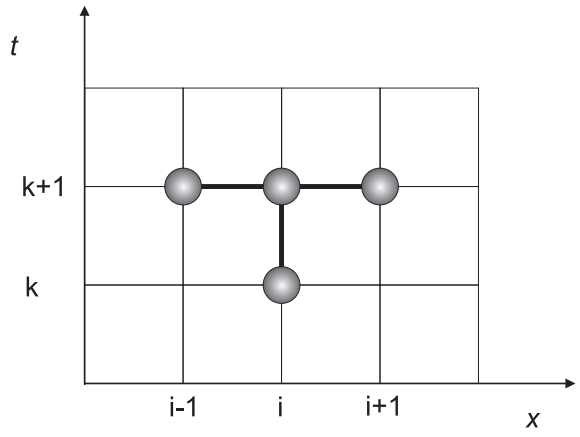

Figure 2.3.4:
Schematic representation of the one dimensional implicit method.

Implicit discretisation is as follows:

$$\frac{\partial c}{\partial t} = D\frac{\partial^2 c}{\partial x^2} \tag{2.3.19}$$

$$\frac{c_{\mathrm{j}}^{\mathrm{k+1}} - c_{\mathrm{j}}^{\mathrm{k}}}{\Delta t} = D\frac{c_{\mathrm{j+1}}^{\mathrm{k+1}} - 2c_{\mathrm{j}}^{\mathrm{k+1}} + c_{\mathrm{j-1}}^{\mathrm{k+1}}}{(\Delta x)^2} \tag{2.3.20}$$

The computational stencil for this scheme showing how the new point is calculated is shown in figure 2.3.4. The concentration at the new time step ($c_{\mathrm{i}}^{\mathrm{k+1}}$) is calculated from a knowledge of one concentrations at the previous time step ($c_{\mathrm{i}}^{\mathrm{k}}$) and from two concentrations in the new time step ($c_{\mathrm{i+1}}^{\mathrm{k+1}}$ and $c_{\mathrm{i-1}}^{\mathrm{k+1}}$). It can be shown, by means of a Fourier stability analysis, that the fully implicit finite difference scheme is *unconditionally stable* (i.e. there is no restriction on the relationship between Δt and Δx).

The error associated with with the one dimensional implicit method is identical to

that for the one dimensional explicit method:

$$\text{error} = O(\Delta t) + O((\Delta x)^2) \tag{2.3.21}$$

2.3.3 Diffusion in two dimensions

If the geometry of the experiment is two dimensional, it is necessary to invoke a two dimensional version of Fick's second law. For the example is this section, the following mass transport will be used:

$$\frac{\partial c}{\partial t} = D\left(\frac{\partial^2 c}{\partial r^2} + \frac{1}{r}\frac{\partial c}{\partial r} + \frac{\partial^2 c}{\partial z^2}\right) \tag{2.3.22}$$

where c is an arbitrary concentration; t is the time; D is the diffusion coefficient; r is the radial spatial coordinate and z is the axial spatial coordinate. This mass transport equation would be appropriate for a situation in which the diffusion layer is large compared to the radius of a disc shaped electrode. The first step is to define the discretised mesh over which equation 2.3.22 will be solved. The spatial grid will consist of uniformly spaced nodes (node separation = Δr and Δz) from $r = 0$ to $r = r_{\max}$ and from $z = 0$ to $z = z_{\max}$. Similarly, the temporal mesh will consist of uniformly spaced nodes (node separation = Δt) from $t = 0$ to $t = t_{\max}$. These

discretised meshes are mathematically described as follows:

$$r_{\mathrm{j}} = \mathrm{j}\Delta r \text{ for } \mathrm{j} = 0,\ 1,\ \ldots,\ N_{\mathrm{r}} \tag{2.3.23}$$

$$z_{\mathrm{i}} = \mathrm{i}\Delta z \text{ for } \mathrm{i} = 0,\ 1,\ \ldots,\ N_{\mathrm{z}} \tag{2.3.24}$$

$$t_{\mathrm{k}} = \mathrm{k}\Delta t \text{ for } \mathrm{k} = 0,\ 1,\ \ldots,\ N_{\mathrm{t}} \tag{2.3.25}$$

Equation 2.3.22 is then discretised leading to:

$$\frac{c_{\mathrm{i,j}}^{\mathrm{k+1}} - c_{\mathrm{i,j}}^{\mathrm{k}}}{\Delta t} = D\left(\frac{c_{\mathrm{i,j-1}} - 2c_{\mathrm{i,j}} + c_{\mathrm{i,j+1}}}{(\Delta r)^2} + \frac{1}{r}\frac{c_{\mathrm{i,j+1}} - c_{\mathrm{i,j-1}}}{\Delta r} + \frac{c_{\mathrm{i-1,j}} - 2c_{\mathrm{i,j}} + c_{\mathrm{i+1,j}}}{(\Delta z)^2}\right) \tag{2.3.26}$$

The right hand side of this equation is not yet discretised with respect to time. It is possible to use either t_{k} or $t_{\mathrm{k+1}}$ for this purpose. These lead to the explicit and implicit finite difference methods respectively. These are described in the following sections.

Explicit finite difference method in two dimensions

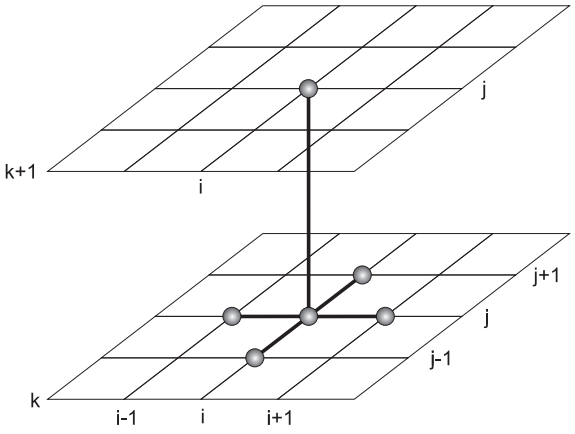

Figure 2.3.5:
Schematic representation of the two dimensional explicit method.

Explicit discretisation is as follows:

$$\frac{c_{i,j}^{k+1} - c_{i,j}^{k}}{\Delta t} = D\left(\frac{c_{i,j-1}^{k} - 2c_{i,j}^{k} + c_{i,j+1}^{k}}{(\Delta r)^2} + \frac{1}{r}\frac{c_{i,j+1}^{k} - c_{i,j-1}^{k}}{\Delta r} + \frac{c_{i-1,j}^{k} - 2c_{i,j}^{k} + c_{i+1,j}^{k}}{(\Delta z)^2}\right) \tag{2.3.27}$$

The computational stencil for this scheme showing how the new point is calculated is shown in figure 2.3.5. The concentration at the new time step ($c_{i,j}^{k+1}$) is calculated from a knowledge of five concentrations at the previous time step ($c_{i,j}^{k}$, $c_{i-1,j}^{k}$, $c_{i+1,j}^{k}$, $c_{i,j-1}^{k}$, and $c_{i,j+1}^{k}$). This processes has stability restrictions and is rarely used.[7]

Implicit finite difference method in two dimensional

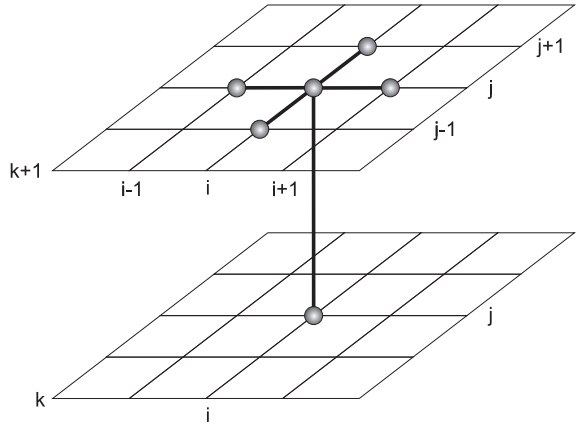

Figure 2.3.6:
Schematic representation of the two dimensional implicit method.

Implicit discretisation is as follows:

$$\frac{c_{i,j}^{k+1} - c_{i,j}^{k}}{\Delta t} = D\left(\frac{c_{i,j-1}^{k+1} - 2c_{i,j}^{k+1} + c_{i,j+1}^{k+1}}{(\Delta r)^2} + \frac{1}{r}\frac{c_{i,j+1}^{k+1} - c_{i,j-1}^{k+1}}{\Delta r} + \frac{c_{i-1,j}^{k+1} - 2c_{i,j}^{k+1} + c_{i+1,j}^{k+1}}{(\Delta z)^2}\right) \tag{2.3.28}$$

The computational stencil for this scheme showing how the new point is calculated is shown in figure 2.3.6. The concentration at the new time step ($c_{i,j}^{k+1}$) is calculated from a knowledge of one concentration at the previous time step ($c_{i,j}^{k}$) and 4 concen-

trations at the new time step ($c^{k+1}_{i-1,j}$, $c^{k+1}_{i+1,j}$, $c^{k+1}_{i,j-1}$, and $c^{k+1}_{i,j+1}$). This processes has no stability restrictions but is computationally expensive.

Alternating direction implicit finite difference method in two dimensions

8,9

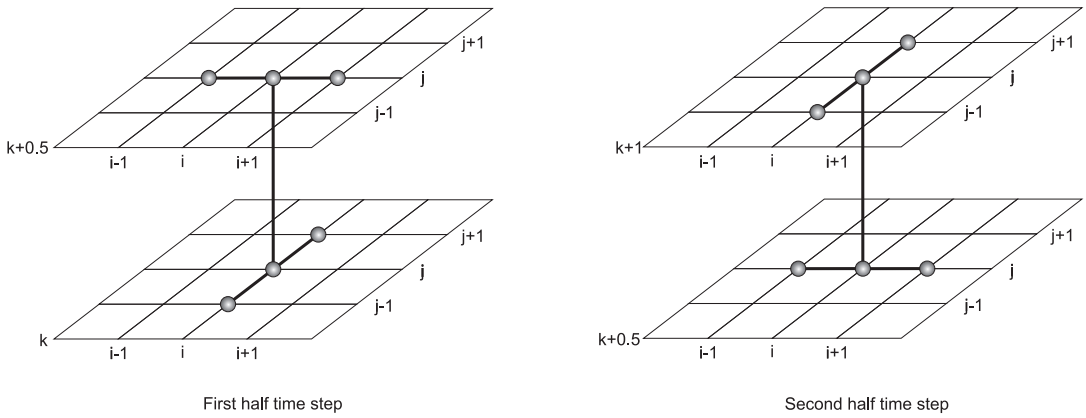

Figure 2.3.7:
Schematic representation of the alternating direction implicit method (ADI).

The alternating direction implicit method (abbreviated as ADI) combines the efficiency of the fully explicit scheme with the unconditional stability of the fully implicit scheme. In this method, each time step (Δt) is split into two half time steps. In the first half time step, the z coordinate is treated implicitly and the r coordinate implicitly. The discretisation is:

$$\frac{c^{k+0.5}_{i,j} - c^{k}_{i,j}}{\Delta t} = D\left(\frac{c^{k+0.5}_{i,j-1} - 2c^{k+0.5}_{i,j} + c^{k+0.5}_{i,j+1}}{(\Delta r)^2} + \frac{1}{r}\frac{c^{k+0.5}_{i,j+1} - c^{k+0.5}_{i,j-1}}{\Delta r} + \frac{c^{k}_{i-1,j} - 2c^{k}_{i,j} + c^{k}_{i+1,j}}{(\Delta z)^2}\right) \tag{2.3.29}$$

In the second half time step, the r coordinate is treated explicitly and the z coordi-

nate implicitly. The discretisation is:

$$\frac{c_{\mathrm{i,j}}^{\mathrm{k+1}} - c_{\mathrm{i,j}}^{\mathrm{k+0.5}}}{\Delta t} = D\left(\frac{c_{\mathrm{i,j-1}}^{\mathrm{k+1}} - 2c_{\mathrm{i,j}}^{\mathrm{k+1}} + c_{\mathrm{i,j+1}}^{\mathrm{k+1}}}{(\Delta r)^2} + \frac{1}{r}\frac{c_{\mathrm{i,j+1}}^{\mathrm{k+1}} - c_{\mathrm{i,j-1}}^{\mathrm{k+1}}}{\Delta r} + \frac{c_{\mathrm{i-1,j}}^{\mathrm{k+0.5}} - 2c_{\mathrm{i,j}}^{\mathrm{k+0.5}} + c_{\mathrm{i+1,j}}^{\mathrm{k+0.5}}}{(\Delta z)^2}\right) \tag{2.3.30}$$

The corresponding finite difference stencils for these steps is shown in figure 2.3.7. The ADI method is computationally efficient and unconditionally stable. Consequently, this method is almost universally employed to solve two dimensional problems of this type.

2.4 Boundary conditions

There are three types of boundary condition: Robin, Dirichlet and Neumann. These are discussed in the following sections.

2.4.1 Robin

A Robin boundary condition relates the value of the derivative normal to a boundary to the value of the variable of interest at the boundary itself. A common example is the application of the Butler-Volmer condition at the electrode surface:

$$\left(\frac{\partial c_{\mathrm{A}}}{\partial z}\right)_{z=0} = \left(k^0 c_{\mathrm{A,\,0}} \exp\left(-\alpha\frac{\mathrm{F}(E - E_{\mathrm{f}}^{\ominus})}{\mathrm{R}T}\right) - k^0 c_{\mathrm{B,\,0}} \exp\left((1-\alpha)\frac{\mathrm{F}(E - E_{\mathrm{f}}^{\ominus})}{\mathrm{R}T}\right)\right) \tag{2.4.1}$$

$$\frac{c_{\mathrm{A,\,1}} - c_{\mathrm{A,\,0}}}{z_1 - z_0} = \left(k^0 c_{\mathrm{A,\,0}} \exp\left(-\alpha\frac{\mathrm{F}(E - E_{\mathrm{f}}^{\ominus})}{\mathrm{R}T}\right) - k^0 c_{\mathrm{B,\,0}} \exp\left((1-\alpha)\frac{\mathrm{F}(E - E_{\mathrm{f}}^{\ominus})}{\mathrm{R}T}\right)\right) \tag{2.4.2}$$

2.4.2 Dirichlet

A Dirichlet boundary condition relates the variable at a boundary to a specific value. An example is a potential step experiment where the response is transport-controlled, we often have $c = 0$ at the electrode surface at time $t > 0$.

2.4.3 Neumann

A Neumann boundary condition relates the derivative of the variable at a boundary to a specific value. An example occurs at the electrode surface where the boundary where the derivative of the concentration in the direction normal to the boundary is zero:

$$\left(\frac{\partial c}{\partial z}\right)_{\mathrm{z=0}} = 0 \tag{2.4.3}$$

$$\frac{c_{\mathrm{A,\,1}} - c_{\mathrm{A,\,0}}}{z_1 - z_0} = 0 \tag{2.4.4}$$

2.5 Solution methods

2.5.1 The Thomas algorithm

[10]The linear system of equations shown above can be solved for matrix x using Gaussian elimination. This algorithm is trivial and will not be discussed further.[11] The matrix equations encountered when solving electrochemical problems have elements close to the leading diagonal. The Thomas algorithm is a simplified form of Gaussian elimination for solving tridiagonal matrix systems. The matrix equation

to be solved is written as:

$$d = [T]u \tag{2.5.1}$$

The tridiagonal matrix $[T]$ is factored into two bidiagonal matrices $[T_{\mathrm{L}}]$ and $[T_{\mathrm{U}}]$ such that

$$[T] = [T_{\mathrm{L}}][T_{\mathrm{U}}] \tag{2.5.2}$$

A solution is then found in the vector f in

$$d = [T_{\mathrm{L}}]f \tag{2.5.3}$$

and f is used to give a final solution for vector u

$$[T_{\mathrm{U}}]u = f \tag{2.5.4}$$

The matrix [T] of n elements can be written as

$$[T] = \begin{pmatrix} b_1 & c_1 & & & 0 \\ a_2 & b_2 & c_2 & & \\ & \ddots & \ddots & \ddots & \\ & & a_{N-1} & b_{N-1} & c_{N-1} \\ 0 & & & a_N & b_N \end{pmatrix}$$

On factorization [T] takes the form

$$[T] = [T_L][T_U] = \begin{pmatrix} \alpha_1 & & & & 0 \\ a_2 & \alpha_2 & & & \\ & \ddots & \ddots & & \\ & & a_{N-1} & \alpha_{N-1} & \\ 0 & & & a_N & \alpha_N \end{pmatrix} \begin{pmatrix} 1 & \beta_1 & & & 0 \\ & 1 & \beta_2 & & \\ & & \ddots & \ddots & \\ & & & 1 & \beta_{N-1} \\ 0 & & & & 1 \end{pmatrix}$$

where α_j and β_j are to be determined. By equating the left- and right- hand sides of the equation $[T] = [T_\mathrm{L}][T_\mathrm{U}]$, the following relations are obtained:

$$\alpha_1 = b_1 \tag{2.5.5}$$

$$\beta_1 = \frac{c_1}{\alpha_1} \tag{2.5.6}$$

$$\alpha_\mathrm{j} = b_\mathrm{j} - a_\mathrm{j}\beta_{\mathrm{j}-1} \quad \mathrm{j} = 2, 3 \ldots N \tag{2.5.7}$$

$$\beta_\mathrm{j} = \frac{c_\mathrm{j}}{\alpha_\mathrm{j}} \quad \mathrm{j} = 2, 3 \ldots N-1 (\alpha_\mathrm{j} \neq 0) \tag{2.5.8}$$

After ontaining α_j and β_j, the equation for f is solved:

$$[T_L]f = d \tag{2.5.9}$$

where elements f_i and f are given by

$$f_1 = \frac{d_1}{\alpha_1} \tag{2.5.10}$$

$$f_\mathrm{i} = \frac{(d_\mathrm{j} - a_\mathrm{j} f_{\mathrm{j}-1})}{\alpha_\mathrm{j}} \quad (\mathrm{j} = 2, 3 \ldots \mathrm{N}) \tag{2.5.11}$$

f is then used to determine the elements of u_{j} of u

$$u_{\mathrm{N}} = f_{\mathrm{N}} \tag{2.5.12}$$

$$u_{\mathrm{j}} = f_{\mathrm{j}} - \beta_{\mathrm{j}} u_{\mathrm{j+1}} \quad (\mathrm{j} = 1, 2 \ldots \mathrm{N} - 1) \tag{2.5.13}$$

By this procedure the matrix equation $[T]u = d$ is solved for u. For such systems, the solution can be obtained in $O(n)(d)^2$ operations instead of $O(n^3)$ required by Gaussian elimination. For electrochemical problems, $n \gg d$ therefore the Thomas algorithm is more efficient than Gaussian elimination by a factor of n^2. Also the Thomas algorithm only requires that the two vectors, and the diagonal matrix elements be stored.

2.5.2 Newton's method

Sometimes the equations to be solved are non-linear and therefore must be solved simultaneously using an iterative method. This is often the case if we have some homogeneous reactions with rate equations that must be combined with the mass transport equations for each species involved. Again, the specific equations for the problems encountered in this thesis will be detailed in the subsequent chapters. Newton's method is the method of choice in this work, used to solve a system of equations in the form $F(y) = 0$. The matrix form is $y^{z+1} = y^z - [J(y^z)]^{-1} F(y^z)$ where J is the Jacobian matrix found by differentiating each equation in the vector

F with respect to each term in y that appears in the equation

$$J(y) = \begin{pmatrix} \frac{\partial f_1}{\partial y_1} & \frac{\partial f_1}{\partial y_2} & \cdots & \frac{\partial f_1}{\partial y_n} \\ \frac{\partial f_2}{\partial y_1} & \frac{\partial f_2}{\partial y_2} & \cdots & \frac{\partial f_2}{\partial y_n} \\ \vdots & \vdots & \ddots & \vdots \\ \frac{\partial f_n}{\partial y_1} & \frac{\partial f_n}{\partial y_2} & \cdots & \frac{\partial f_n}{\partial y_n} \end{pmatrix}$$

introduction of the vector u where $u = y^{z+1} - y^z$ yields the system of equations

$$Ju = -F \tag{2.5.14}$$

which may be solved by a standard linear method. The process is iterated until the termination citeration is met:

$$\sqrt{(y^z + 1 - y^z)^2} < \epsilon \tag{2.5.15}$$

2.6 Unequal node distribution

The results from finite difference equations over a uniform mesh are not accurate at all points. The results are normally less accurate at points where the concentrations change more rapidly. These points are called *singularities*. This can be overcome simply by using a denser grid. However, this strategy leads to a greater number of nodes and, consequently, to longer simulation times. Alternatively, the existing nodes can be redistributed such that the nodes are denser close the singularity and sparser away from the singularity. Since the same number of nodes have been

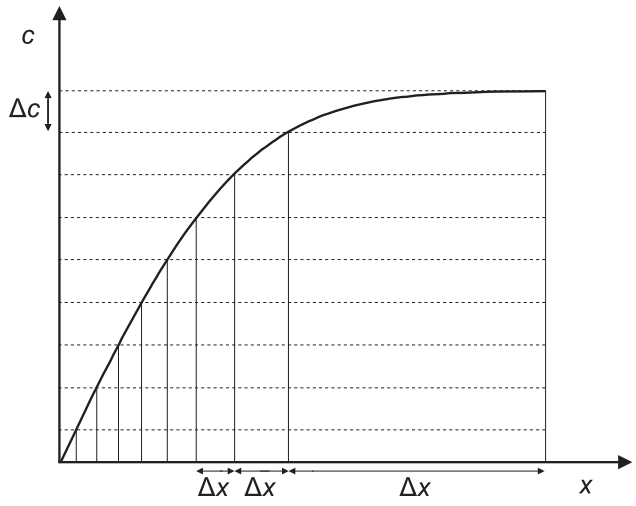

Figure 2.6.1:
A concentration profile divided into equal Δc values but unequal Δx values.

used, this strategy does not lead to longer simulation times. Concentrations most commonly vary most rapidly close to the electrode surface it is common to use a mesh that expands from the electrode surface as shown in figure 2.6.1.

2.7 Normalised parameters

When an electrochemical problem is expressed mathematically, the resulting formulation contains many variables. Consequently, the final result (typically the current) varies as a function of many variables. This, often overwhelming, number of variables makes many electrochemical problems appear, at first sight, to be too difficult to comprehend fully. However, in most cases, the IBVP, and its solution, can be simplified considerably by noting that some of the variables are simple scaling factors that affect the final result in a trivial way. These scaling factors are often linked to the concentrations of the chemicals or to the geometry of the equipment. The problem can be easily generalised by *absorbing* these scaling factors into the other variables. This leads to a simpler form of the problem expressed in terms of *normalised* variables. Common normalised variables are defined in the glossary.

2.8 Finite simulation space

Consider Fick's second law:

$$\frac{\partial c}{\partial t} = D\frac{\partial^2 c}{\partial x^2} \tag{2.8.1}$$

subjected to the following boundary conditions:

$$\begin{aligned} &t = 0, \text{ all } x && c_{\mathrm{A}} = c_{\mathrm{A}}^{*} \\ &t > 0, \; x = x_{\max} && c_{\mathrm{A}} = c_{\mathrm{A}}^{*} \\ &t > 0, \; x \to \infty && c_{\mathrm{A}} = 0 \end{aligned}$$

In many cases it is not possible to simulation space to infinity. In addition, beyond a certain point, far enough away from the electrode, the concentration is unchanged from its starting value and simulation is not required. The position of this point can be estimated by solving the system of equations above. This is a rare situation in which the equation can be solved analytically. The result is:[12,13]

$$c = c^{*}\mathrm{erf}\left(\frac{x}{2\sqrt{Dt}}\right) \tag{2.8.2}$$

where erf is the error function.The layer of depletion is larger than the majority of other situations for two reasons: the electrode is planar so the depletion layer is not limited by a steady-state and the concentration of the electroactive species (A) is zero at the electrode surface so is depleted at a very high rate. The position of x_{max} is taken to be $6\sqrt{Dt}$. When substituted into equation 2.8.2, the value of c at x_max is 0.99997791. This point corresponds to bulk solution enough to be applicable to slightly different experimental setups so long at the highest diffusion

coefficient is used when calculating x_max.[14] it is good practice to confirm this limit is not exceeded by the concentration of any particular simulation.

$$\frac{\partial c}{\partial t} = D\frac{\partial^2 c}{\partial x^2} \tag{2.8.3}$$

2.9 Computational details

The numerical methods were coded by the author in the C++ programming language. The development environment was visual C++ 2010 express edition (www.microsoft.com/visualstudio/en-us/products/2010-editions/visual-cpp-express). This is open source software that incorporates the mingw windows compiler. All source code possesses an object orientated structure in order to facilitate debugging and reuse.[15] All simulations were run on a Dell Precision T3400 desktop computer with an Intel Core2 Quad Q9550 2.83 GHz processor and 3.2 GB of RAM. The operating system was windows XP Professional SP3. Where possible, the simulations were parallelised using the OpenMP API.

2.10 Summary

In this chapter, the principle of mathematical modeling and numerical simulation have been discussed. In this thesis, the finite difference method is used. Non-linear terms are linearised using Newton's method and solved iteratively using the generalised Thomas algorithm. Boundary conditions and sources of error have also been discussed.

Bibliography

[1] Randles, J. E. B. *Trans. Faraday Soc.* **1948**, *44*, 327–338.

[2] Britz, D. *Digital Simulation in Electrochemistry*; Springer-Verlag: New York, 2005.

[3] Feldberg, S. W.; Auerbach, C. *Anal. Chem.* **1964**, *36*, 505–509.

[4] Crank, J.; Nicolson, E. *Proc. Camb. Phil. Soc.* **1947**, *43*, 50–67.

[5] Isaacson, E.; Keller, H. B. *Analysis of Numerical Methods*; Courier Dover Publications, 1994.

[6] Charney, J. G.; Fjrtoft, R.; von Neumann, J. *Tellus* **1950**, *2*, 237254.

[7] Myland, J. C.; Oldham, K. B. *J. Electroanal. Chem.* **2005**, *576*, 353 – 362.

[8] Peaceman, J. W.; Rachford, H. H. *J. Soc. Indust. Appl. Math.* **1955**, *3*, 28–41.

[9] Heinze, J. *J. Electroanal. Chem.* **1981**, *124*, 73–86.

[10] Compton, R. G.; Pilkington, M. B. G.; Stearn, G. M. *J. Chem. Soc., Faraday Trans. 1* **1988**, *84*, 2155–2171.

[11] Press, W. H., Teukolsky, S. A., Vetterling, W. T., Flannery, B. P., Eds. *Numerical Recipes: The Art of Scientific Computing*; Cambridge University Press, 2007.

[12] Cottrell, F. G. *Z. Physik. Chem.* **1902**, *44*, 385.

[13] Compton, R. G.; Banks, C. E. *Understanding Voltammetry*, 2nd ed.; Imperial College Press, 2010.

[14] Svir, I. B.; Oleinick, A. I.; Compton, R. G. *Radiotekhnika* **2001**, *116*, 114.

[15] Solter, N. A.; Kleper, S. J. *Professional C++*; Wiley Publishing: New Jersey, 2005.

Chapter 3

Nanoparticles in electrochemistry: a review

A nanoparticle is a material with at least one dimension of order one nanometre. This chapter provides an introductory account into the uses of nanoparticles in electrochemistry and gives an overview of recent research. This has been publised as a review in *Physical Chemistry Chemical Physics*.[1] Some of the material described in this chapter is extended in chapter 4.

3.1 Introduction

Metals in the form of nanoparticles can show qualitatively different behaviour from that of the bulk material.[2] Perhaps the most clear example of this is that of gold. Bulk gold is a relatively non-reactive metal. However, as nanocrystals of a few hundred atoms it becomes highly active catalytically, for example in respect of selective oxidation reactions such as alkene epoxidation or alcohol oxidation, and

the synthesis of hydrogen peroxide from hydrogenation of di-oxygen.[3,4]

Bulk metals are, of course, widely deployed as electrode materials to facilitate a variety of electrolytic processes. The latter range from the synthetic (aluminium, chlorine, and nylon synthesis) through the analytical (sensors for smoke detection via carbon monoxide in air, or for glucose in blood to facilitate the regulation of diabetes) to the energy storage/production areas of fuels cells, batteries, solar cells, etc. The range of metallic materials used in electrochemistry is wide and diverse; that said, the properties of electrodes for selected tasks have been improved and optimised by means of their 'chemical modification'.[5,6] That is, by immobilising molecules, polymers, films, etc. on the surface of conventional electrode materials, their properties can be changed notably, for example in respect to the electron transfer kinetics for various selected target species. Recently,[8] electrode surfaces have been modified by growing or casting 'arrays' of nanoparticles onto the electrode. Providing then that the nanoparticles are in electrical contact with the substrate electrode, each nanoparticle can act as a tiny electrode, so that the electrode surface has the electrochemical properties of the nanoparticle material rather than (or strictly as well as) that of the supporting electrode. Typically, the latter might be carbon based for reasons of cost effectiveness, but a wide range of other supports have been used.[8] Figure 3.1.1 (page 55) shows the growth of cobalt nanoparticles onto the surface of a boron-doped diamond electrode[7] as imaged by electrochemical atomic force microscopy; in these experiments the cobalt nanoparticles are grown via electro-deposition. The purpose of this chapter is to consider the behaviour of nanoparticle modified electrodes and to ask in what ways this can differ from that

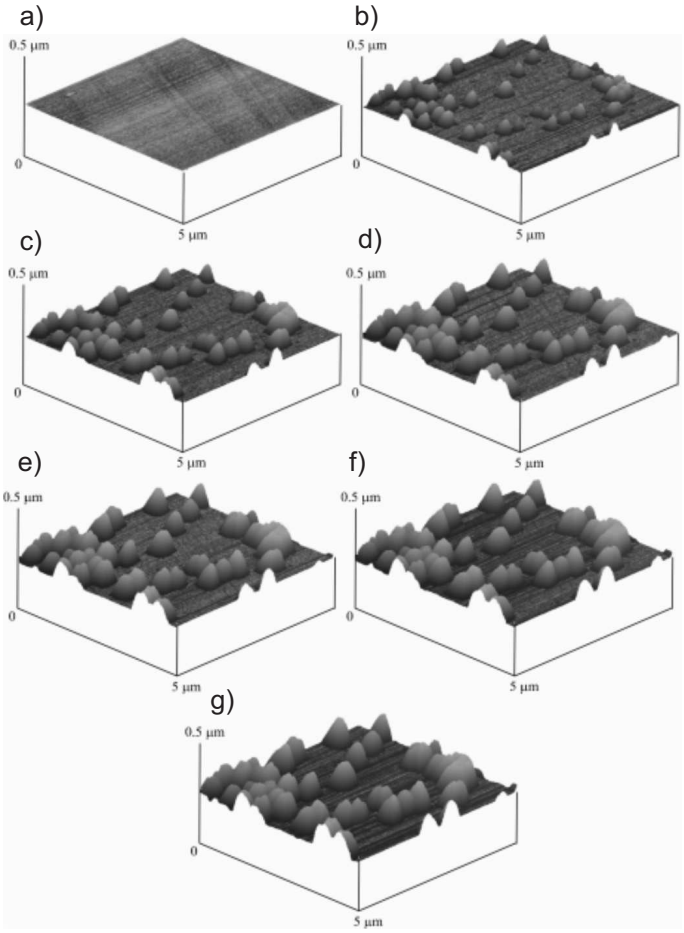

Figure 3.1.1:
In-situ electrochemical atomic force microscopy of cobalt nuclei growth, deposited onto boron doped diamond from 10 mM Co(ii) solution at -1.15 V vs *SCE for a)-g) 0, 10, 20, 30, 40, 50, and 60 s respectively.*[7]

of conventional unmodified macroscale electrodes. In contrast figure 3.1.2 (page 55) shows scanning electron microscopy (SEM) images of silver nanoparticles which, for analytical purposes, can be cast onto an electrode made of basal plane pyrolytic graphite.[9]

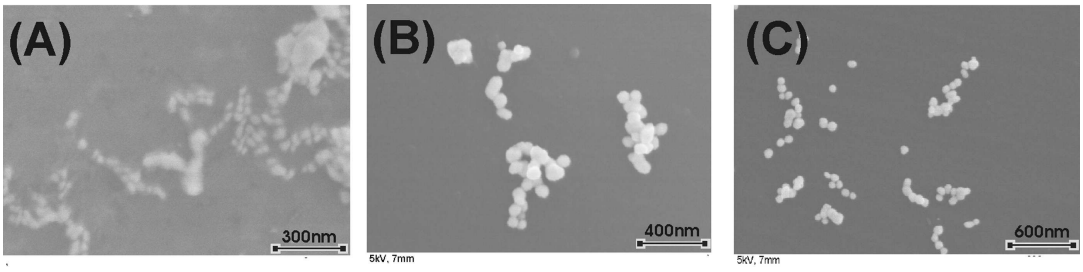

Figure 3.1.2:
SEM images of colloidal citrate-capped AgNPs: (A) 20-40 nm, (B) 50-70 nm, and (C) 80-120 nm. SEM carried out on a carbon film/copper grid substrate.[9]

3.2 Types of electrode reaction

The general reader will be familiar with the concepts of outer sphere and inner sphere electron transfer as pertaining to electron transfer between two molecules in homogeneous solution.[10] In heterogeneous electron transfer, analogous kinetic cases are also seen, with the outer sphere case corresponding to the reactant being located at the Outer Helmholtz Plane, corresponding to the distance of closest approach to the electrode such that the layer of solvent molecules adsorbed on the electrode surface is not penetrated by the reactant or its coordination sphere.[11] In contrast, the inner sphere limit corresponds to specific adsorption of the reactant on the electrode surface.

It is evident that the latter type of electrode process is likely to show differences between the macro- and nanoscales. Since adsorption will be sensitive to the surface structure: both electronic and topological. The next section considers examples of such differences before we make the same comparison for outer sphere type electrode processes.

3.3 Electrode reactions involving adsorption

A first example of changed electrochemical behaviour between the nano and macroscales concerns the phenomenon of underpotential deposition (upd). This is the electrodeposition of a monolayer, or sub-monolayer, of one metal onto a different (substrate) metal at potentials more positive (less negative) than those required for the bulk

deposition:

$$M^{n+}(aq) + ne^- \rightleftharpoons M(ads) \quad E_1^\circ \tag{3.3.1}$$

$$M^{n+}(aq) + ne^- \rightleftharpoons M(bulk) \quad E_2^\circ \tag{3.3.2}$$

where $E_1^\circ > E_2^\circ$. The upd of thallium on silver macro-electrodes has been studied using both polycrystalline and single crystal electrodes:

$$Tl^+(aq) + e^- \rightleftharpoons Tl(ads) \tag{3.3.3}$$

The structure of the surface sensitively influenced the ease with which the metal could be deposited: Ag(111)>Ag(100)>Ag(110)>polycrystalline Ag.[12,13] These observations encouraged a study of the corresponding phenomenon on silver nanoparticles (AgNPs) of varying sizes[14] which were synthesised by a seed mediated citrate reduction process with the formation of AgNPs with the following diameters: 20-40 nm, 50-70 nm and 80-120 nm. The resulting colloidal AgNPs suspensions were cast on the surface of a basal plane pyrolytic graphite electrode (BPPG). Thallium upd was first carried out on a macrodisc electrode (diameter 0.7 cm) using a solution of 10mM $TlNO_3$ in 1.5 M KNO_3.

Figure 3.3.1 (page 58) shows the resulting voltammetry with underpotential deposition with a peak potential of -0.545 V *vs* the saturated calomel electrode (SCE) and corresponding stripping at -0.440 V. The bulk deposition of thallium is apparent at more negative potentials, together with a bulk stripping peak on the positive going

sweep of the voltammogram. Comparison of this behaviour with differently sized

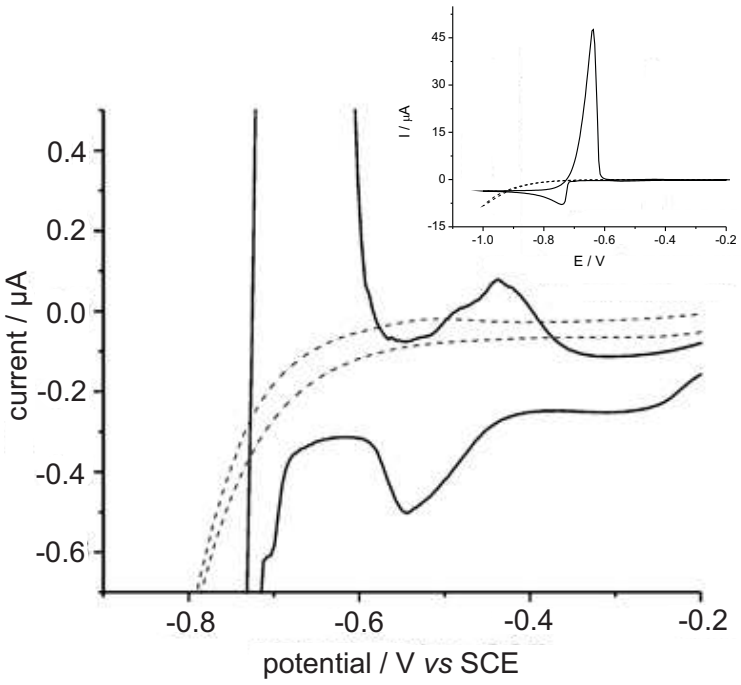

Figure 3.3.1: *Thallium deposition on a silver macrodisk electrode.*[14] *Experimental conditions:* KNO_3 *(1.5 M) +* $TlNO_3$ vs *SCE. Scan rate:* 50 mV s^{-1}. *Solid line: 10 mM* $TlNO_3$ *Dashed line: 0 mM* $TlNO_3$

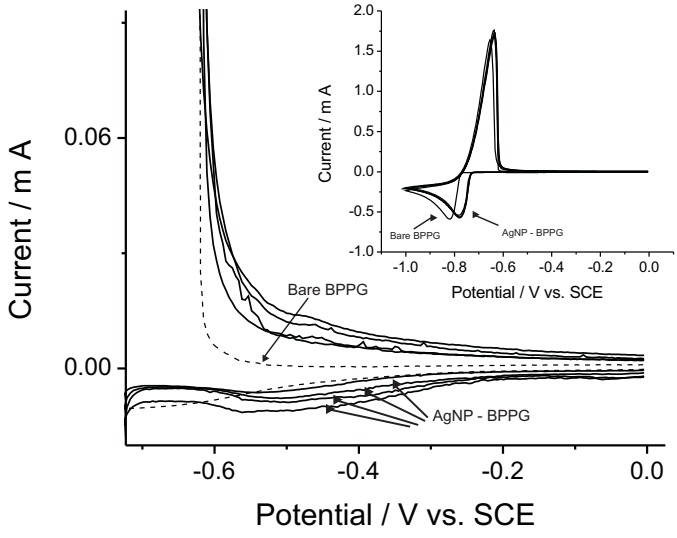

Figure 3.3.2: *Thallium deposition on AgNP−BPPG (2040 nm) electrode.*[14] *Experimental conditions:* KNO_3 *(1.5 M) +* $TlNO_3$ vs. *SCE. Scan rate:* 50 mV s^{-1}. *(Solid line: AgNPBPPG (2040 nm) electrode; dashed line: bare BPPG.)*

AgNPs on BPPG showed the responses shown in figures 3.3.2 (page 58) and 3.3.3 (page 59). In all cases bulk deposition is seen but the thallium upd is only apparent for the nanoparticles of 80-120 nm diameter and is not observed for the 20-40 nm

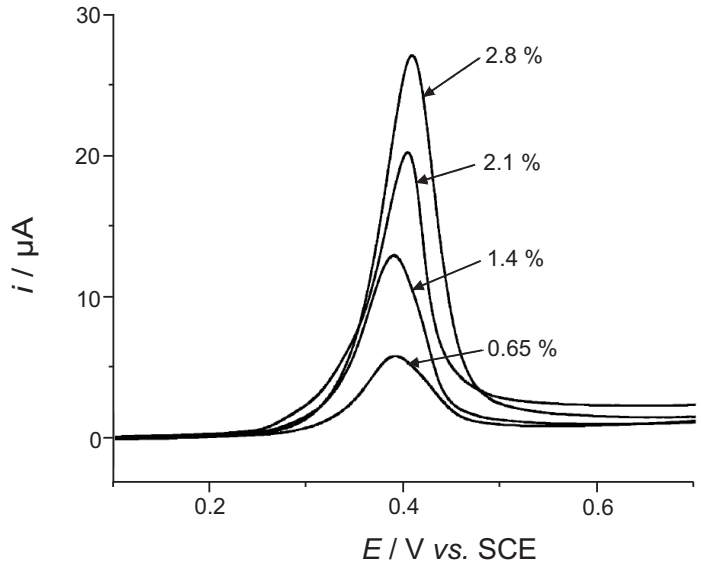

Figure 3.3.3: *Stripping voltammetry recorded for increasing surface coverage of AgNPs (2040 nm, 0.5 and 3.0 %).*[14] *Experimental conditions:* $NaClO_4$ *(0.1 M)* vs *SCE. Scan rate:* 20 mV s^{-1}.

sized particles. The results show that qualitatively different adsorption behaviour is seen with a size threshold of *ca* 50 nm with thallium adsorption absent below. Such behaviour in other systems can, of course, explain differences in electrode reaction mechanisms between the macro- or micro- and the nanoscales. Analogous observations have been made for the upd of lead and cadmium on AgNPs.[15] Similarly the upd of thallium has been studied in respect of gold nanoparticles (AuNPs) supported on multiwalled carbon nanotubes (MWCNT), as shown in figure 3.3.4[16] (page 60). The upd deposition and study of thallium was observed on macro-gold and on large nanoparticles (30-60 nm diameter) but was completely absent on the 10 nm diameter sized gold nanoparticles despite the fact that the nano-particles were shown to be in electrical contact with the nanotubes and supporting electrode. As a second illustration of changed adsorption between the macro- and nano-scale we consider the reduction of hydrogen peroxide at silver electrodes under acidic conditions. For polycrystalline macro-electrodes the work of Ertl[17] has shown that

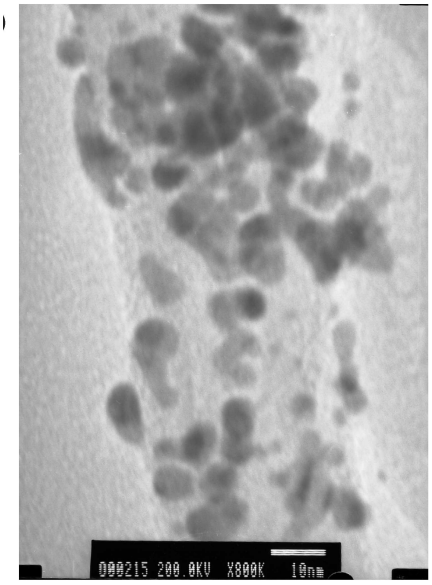

Figure 3.3.4:
A transmission electron microscopy (TEM) image showing the gold nanoparticles encrusting a carbon nanotube.[16]

two parallel mechanisms operate: first the 'normal' reduction (at potentials < -0.4 V *vs* Hg/Hg_2SO_4) with a transfer coefficient, $\alpha \approx 0.23$ and an 'activated' mechanism seen at a less negative potential (-0.1 V vs Hg/Hg_2SO_4, $\alpha \approx 0.40$). The mechanism of the normal reduction is thought to be:

$$H_2O_2 + H^+ + e^- \xrightarrow{\text{slow}} OH(ads) + H_2O \tag{3.3.4}$$

$$H^+ + OH(ads) + e^- \xrightarrow{\text{fast}} H_2O \tag{3.3.5}$$

The normal reduction provides an initial source of OH(ads) which allows the activated process to occur at a faster rate via the following mechanism:

$$H_2O_2 + e^- \rightarrow OH^- + OH(ads) \tag{3.3.6}$$

$$H_2O_2 + H^+ + OH(ads) + e^- \rightarrow 2OH(ads) + H_2O \tag{3.3.7}$$

The mechanism is 'autocatalytic' as the presence of adsorbed OH increases the

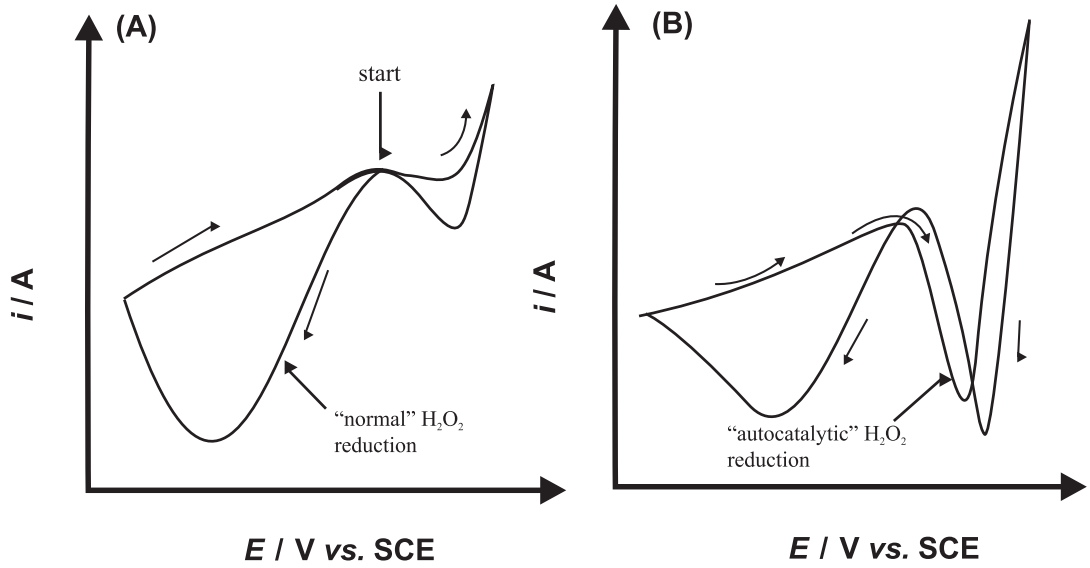

Figure 3.3.5:
Schematic representation of voltammetry at a stationary Ag electrode in an electrolyte of 0.1 M $HClO_4$ + 20 mM H_2O_2, with a scan rate of 100 mV s^{-1}. *[18] (A) First scan, beginning at the start point and sweeping the potential first in a positive direction. Only normal H_2O_2 reduction can be observed in the reverse sweep. (B) Subsequent scans displaying an autocatalytic reduction peak at more positive potential as well as the normal reduction at a higher overpotential.*

rate of the above process and results in further OH adsorption on the silver surface. Figure 3.3.5 (page 61) shows the voltammetry associated with the two processes. Figure 3.3.6 (page 62) shows the voltammetry at a AgNP modified electrode. In contrast to the macroelectrode behaviour, the autocatalytic process was entirely absent under all conditions studied, testifying to the changed adsorption behaviour at the nanoscale.

Figures 3.3.7 (page 62) and 3.3.8 (page 63) show further data for the H_2O_2/AgNP system. First, when the AgNP coverage is such that the nanoparticles are diffusionally isolated then the peak potential for the reduction wave varies with the particle size (r_{np}) as shown in figure 3.3.7 (page 62), with the reduction moving to more

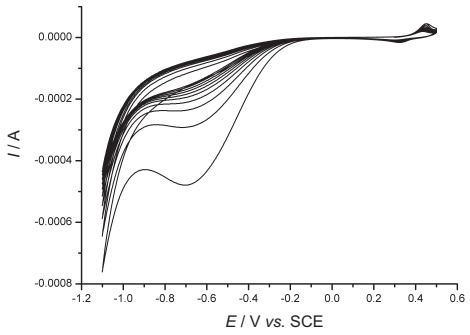

Figure 3.3.6:
Reduction of H_2O_2 at a AgNP-modified electrode: autocatalytic reduction absent in the voltammetry. Data is shown for a high nanoparticle surface coverage.[18]

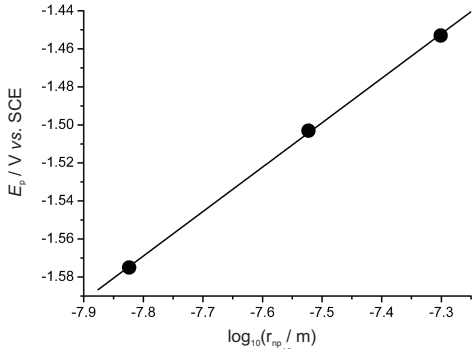

Figure 3.3.7:
Reduction of H_2O_2 at AgNP-modified electrode: E_p vs $\log_{10}(r_\mathrm{np})$ for isolated nanoparticles; $\alpha = 0.253$.[18]

negative values as the radius shrinks. Second, as shown in figure 3.3.8 (page 63), the peak potential is sensitive to the coverage of nanoparticles on the electrode; as the coverage increases, the peak potential for the reduction moves to more positive (less negative) potentials.

The dependence of the peak potential on both the radius and the coverage reflects both the rate of the electrolytic process and that of the mass transport to and from the nanoparticles. In the case of the data shown in figures 3.3.6 (page 62) and 3.3.7 (page 62), the size of the nanoparticles is sufficiently large and the concentration of supporting electrolyte sufficiently high that a diffusion-only approach to transport can be usefully adopted, as discussed in the next section.

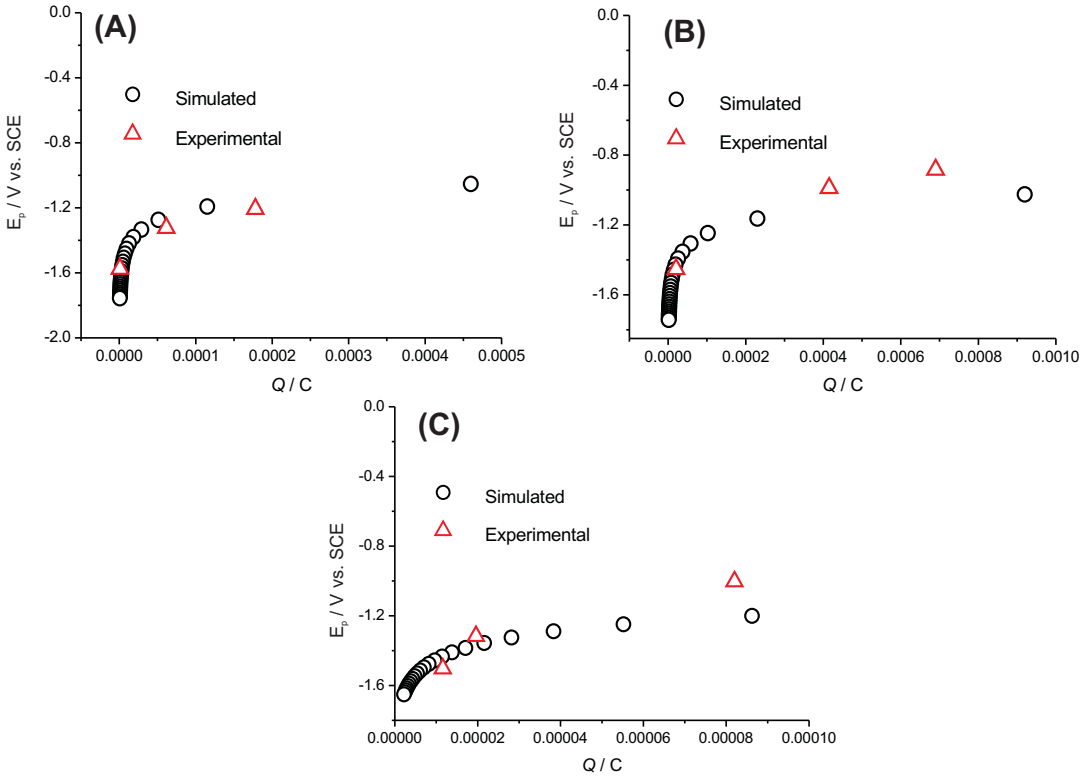

Figure 3.3.8:
Plot of peak potential, E_{p}, calculated for an array of AgNPs and those obtained experimentally against charge (Q/C), representing the coverage of NPs on the electrode surface.[18] *Data plotted for three sizes of NPs with varying degrees of NP coverage: (A) $r_{\mathrm{np}} = 15$ nm, (B) $r_{\mathrm{np}} = 30$ nm, and (C) $r_{\mathrm{np}} = 50$ nm.*

3.4 Electrolysis at large nanoparticles and their arrays

3.4.1 Isolated nanoparticles

For sufficiently large and diffusionally isolated nanoparticles supported on a planar electrode, a diffusion only model can provide a useful insight into the expected current-voltage behaviour, assuming the electrolysis is confined to the surface of the nanoparticle with none occurring on the electrode support. The approach is likely to

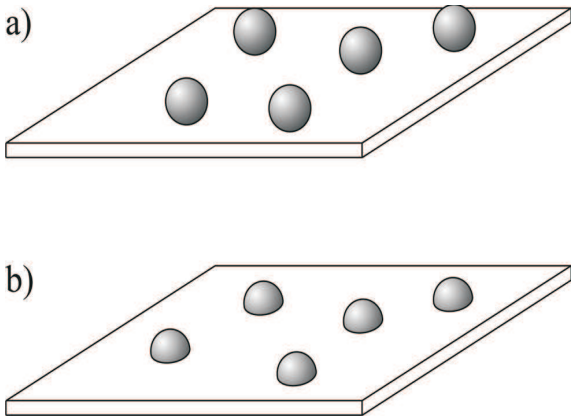

Figure 3.4.1:
Well-separated nanoparticles on an electrode:[19]
(a) spherical
(b) hemispherical

be quantitative for nanoparticles larger than *ca* 10 nm in size, provided the electrolysis is conducted in the presence of a sufficiently large concentration of supporting electrolyte. Figure 3.4.1 (page 64) schematically shows (well separated) nanoparticles on an electrode with identical spherical and hemispherical shapes; figure 3.4.2 (page 64) shows coordinate systems used to describe these isolated nanoparticles. The current-voltage response at the isolated nanoparticles will depend on the volt-

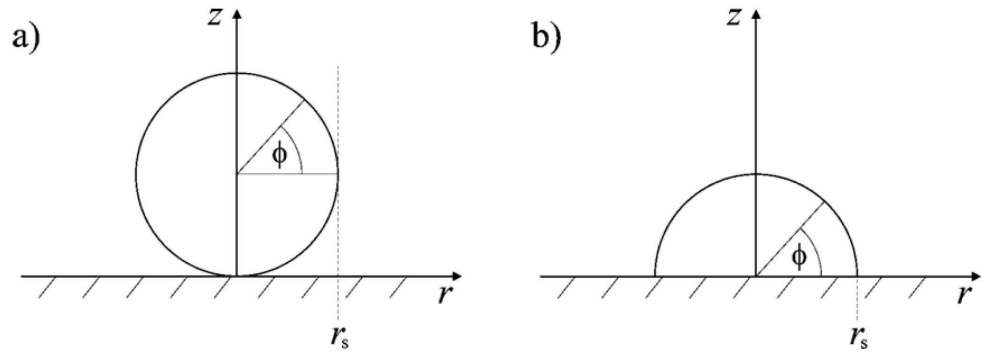

Figure 3.4.2:
Schematic diagram of:[19]
(a) a spherical particle
(b) a hemispherical particle sitting upon a supporting planar surface

age scan rates (V s^{-1}). However, for suitably slow scan rates a diffusion limited

current, i_{lim}, will be established. For a hemispherical electrode:

$$i_{\text{lim}} = 2\pi n F D_{\text{A}} r_{\text{np}} [\text{A}]_{\text{bulk}} \tag{3.4.1}$$

where r is the radius for the nanoparticle and D_{A} is the diffusion coefficient of the electroactive species A, which undergoes the following electrocatalytic process at the surface of the hemispherical nanoparticles:

$$\text{A} \pm n\text{e}^- \rightarrow \text{products} \tag{3.4.2}$$

F is the Faraday constant and $[\text{A}]_{\text{bulk}}$ is the bulk concentration of A. For the case of a sphere,

$$i_{\text{lim}} = 8.71 n F D_{\text{A}} r_{\text{np}} [\text{A}]_{\text{bulk}} \tag{3.4.3}$$

Figure 3.4.3 (page 65) shows the concentration profile of A surrounding the nanopar-

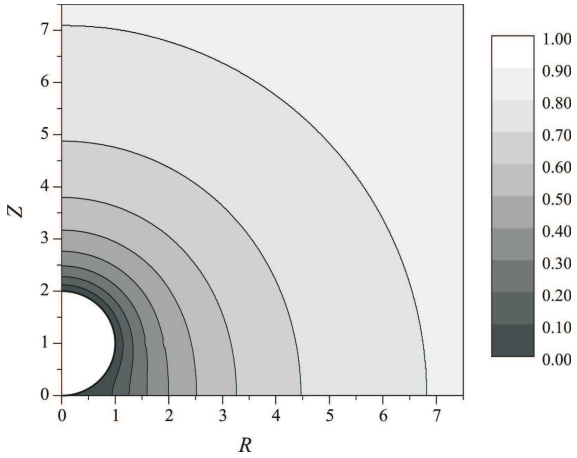

Figure 3.4.3:
Simulated concentration profile at a spherical particle supported on an electrically insulating surface under diffusion-limiting conditions.[19]

ticle under these conditions ($R = \frac{r}{r_{\text{np}}}$ and $Z = \frac{z}{r_{\text{np}}}$). For an isolated sphere in free

solution, i_{lim} is given by equation:

$$i_{\text{lim}} = 4\pi n F D_{\text{A}} r_{\text{np}} [\text{A}]_{\text{bulk}} \tag{3.4.4}$$

Analogous expression for spheroids and hemispheroids[20] have been reported. Note that the limiting current for a free sphere (eqn 3.4.4) and a sphere attached to a surface (eqn 3.4.3) are not equal. This discrepancy is derived from the 'shielding effect' caused by the substrate that reduces the limiting current in the latter situation. For fast voltage scan rates, peak shaped responses are seen. It is helpful to define a dimensionless scan rate:

$$\sigma = \left(\frac{F}{RT}\right)\left(\frac{r_{\text{np}}^2}{D_{\text{A}}}\right) v \tag{3.4.5}$$

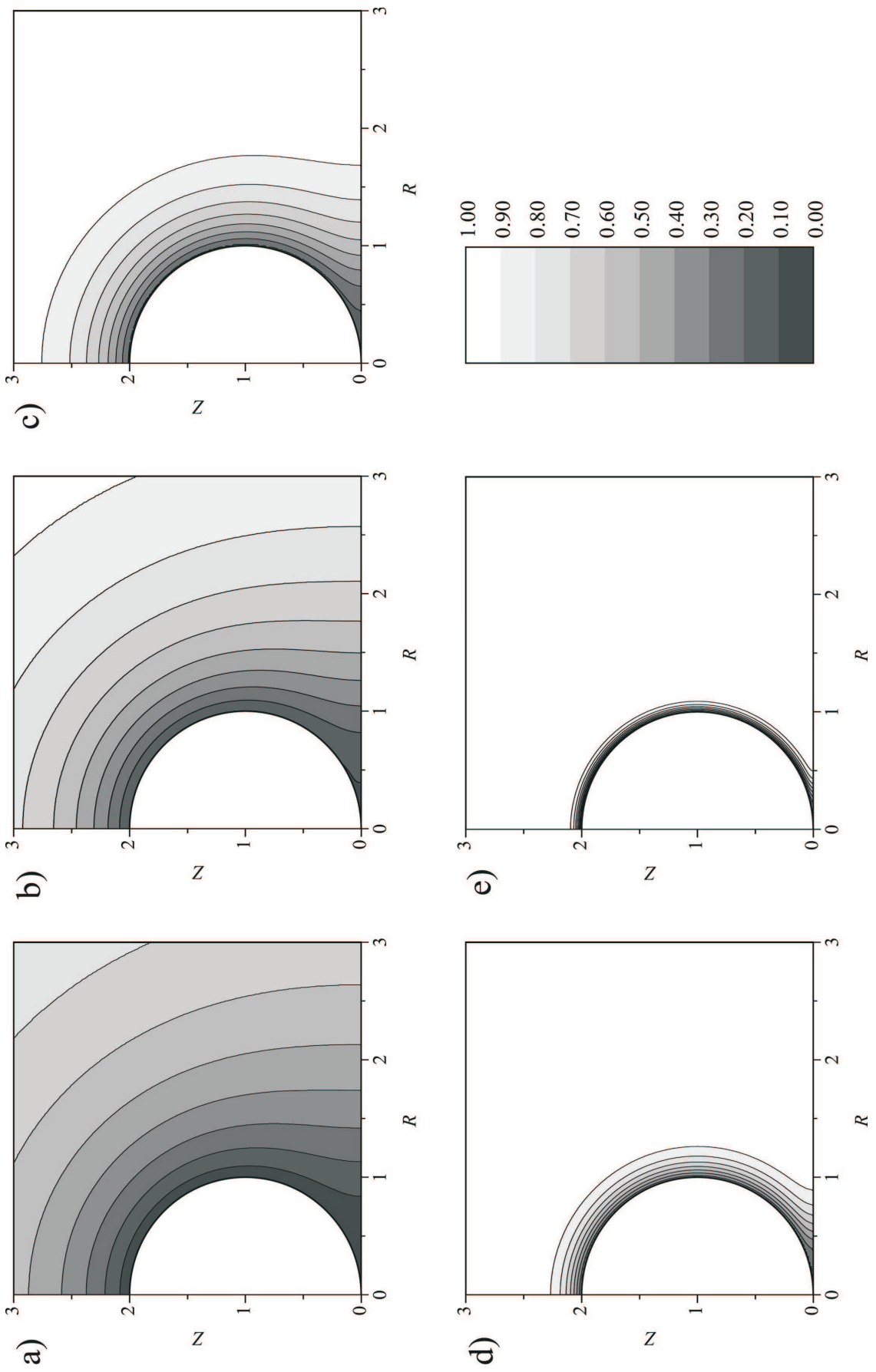

Figure 3.4.4:
Simulated concentration profiles at a spherical particle supported on an electrically insulating surface: (a) $\sigma = 0.1$, (b) $\sigma = 1$, (c) $\sigma = 10$, (d) $\sigma = 100$, (e) $\sigma = 1000$.[19]

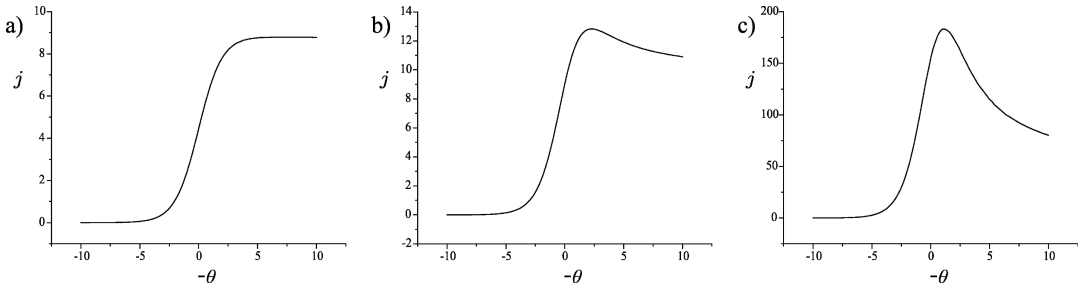

Figure 3.4.5:
Simulated voltammetry for a reversible electrode transfer at the spherical particle. The following scan rates are used: (a) $\sigma = 10^{-3}$, (b) $\sigma = 1$, (c) $\sigma = 1000$.[19]

where v is the true scan rate (V s^{-1}), R is the universal gas constant and T is the absolute temperature. Figure 3.4.5 (page 68) shows the simulated voltammetry at a spherical nanoparticle for scan rates of $\sigma = 10^{-3}$, $\sigma = 1$ and $\sigma = 10^3$. The emergence of peak-shaped behaviour at faster scan rates is evident. Figure 3.4.4 (page 67) shows the concentration profiles of A at the potential corresponding to the peak current. It can be seen that the layer of depletion of A (the 'diffusion layer') shrinks as σ increases to the point that, for $\sigma = 10^3$, it is confined to a very thin layer adjacent to the nanoparticle surface. The peak current changes from a scan rate independent value at low scan rates to one which apparently scales with $\sqrt{\sigma}$ at very fast scan rates. This reflects the change, implicit in figure 3.4.4 (page 67), from convergent to linear diffusion. The voltammograms shown in figure 3.4.5 (page 68) were calculated for fast ('reversible') electrode kinetics.

The reasons for the nanoparticle size dependence of the peak potential is that this quantity reflects a switchover between rate-determining electrode kinetics, which controls the current before the peak potential, to rate determining mass transport (diffusion) after the peak potential. Thus, for a fixed rate of transport, the faster

the electrode kinetics, the lower the peak potential, and this is the key observation required to identify 'electrocatalysis'. Note therefore that it is not the magnitude of the current but rather the value of E_p which is the key diagnostic for changes in electrode kinetics.

If the same processes are considered at electrodes of decreasing size, for example, figure 3.3.7 (page 62) showing the variation of E_p with radius for the reduction of H_2O_2 at isolated AgNPs, then the rate of mass transport increases as the size shrinks, and so for the same electrode kinetics the peak potential will occur at increasingly high potentials (more positive for an oxidation, more negative for a reduction).

It follows from the above that for an electrochemically reversible process, the peak potential will appear on nanoparticles with an *apparently* larger overpotential than at the corresponding macroelectrode and that the smaller the nanoparticle size then the greater the apparent overpotential. Both of these features are apparent in the H_2O_2 reduction at silver described above. Comparison of figure 3.3.5 (page 61) and figure 3.3.8 (page 63) shows that large overpotentials are seen on the nanoscale as opposed to the macroscale and figure 3.3.7 (62) shows that E_p becomes increasingly negative as the radius of the nanoparticle shrinks.

3.4.2 Nanoparticle arrays

A nanoparticle array is an assembly of nanoparticles supported on a conductive substrate. As with the isolated case, electrolysis is assumed to occur solely on the surface of the nanoparticles and not the underlying substrate. Nanoparticle arrays can be synthesised in a wide variety of ways and were reviewed by Campbell *et al.*[8]

The surface coverage of the nanoparticles is defined in terms of the area obscured in a top down view of the substrate. The relationship between the nanoparticle radius (r_{np}), the nanoparticle separation (r_{sep}) and the fractional surface coverage (Θ) is given by:

$$\Theta = \left(\frac{r_{\mathrm{np}}}{r_{\mathrm{sep}}}\right)^2 \tag{3.4.6}$$

The electrode kinetics observed at a given nanoparticle are independent of the others in the array and therefore conform with the discussion in Section 3.6 below. In contrast, mass transport towards an array is substantially different than that to an isolated nanoparticle. Mass transport to a random array can be understood in terms analogous, but complementary, to those for partially blocked electrodes[21,22] and microdisc electrodes[23–26] and is based on the interaction between diffusional layers as a function of the experimental timescale and of the surface coverage. This is discussed with respect to a reversible 1 electron oxidation:

$$\mathrm{A} - \mathrm{e}^- \rightleftharpoons \mathrm{B} \tag{3.4.7}$$

As the experimental timescale increases and the nanoparticle surface coverage decreases, the diffusional interaction changes from category 1 through to category 4 as shown in figure 3.4.6 (page 71). In category 1, the diffusion layers are small and each nanoparticle is diffusionally isolated: mass transport is 1 dimensional and linear. As explained in chapter 1, cyclic voltammograms in this category are peak shaped and obey the Randles-Ševčík equation ($i_{\mathrm{peak}} \propto \sqrt{\sigma}$); the chronoamperometry obeys the Cottrell equation ($i \propto \frac{1}{\sqrt{t}}$). In category 2, the diffusion layers are large and approxi-

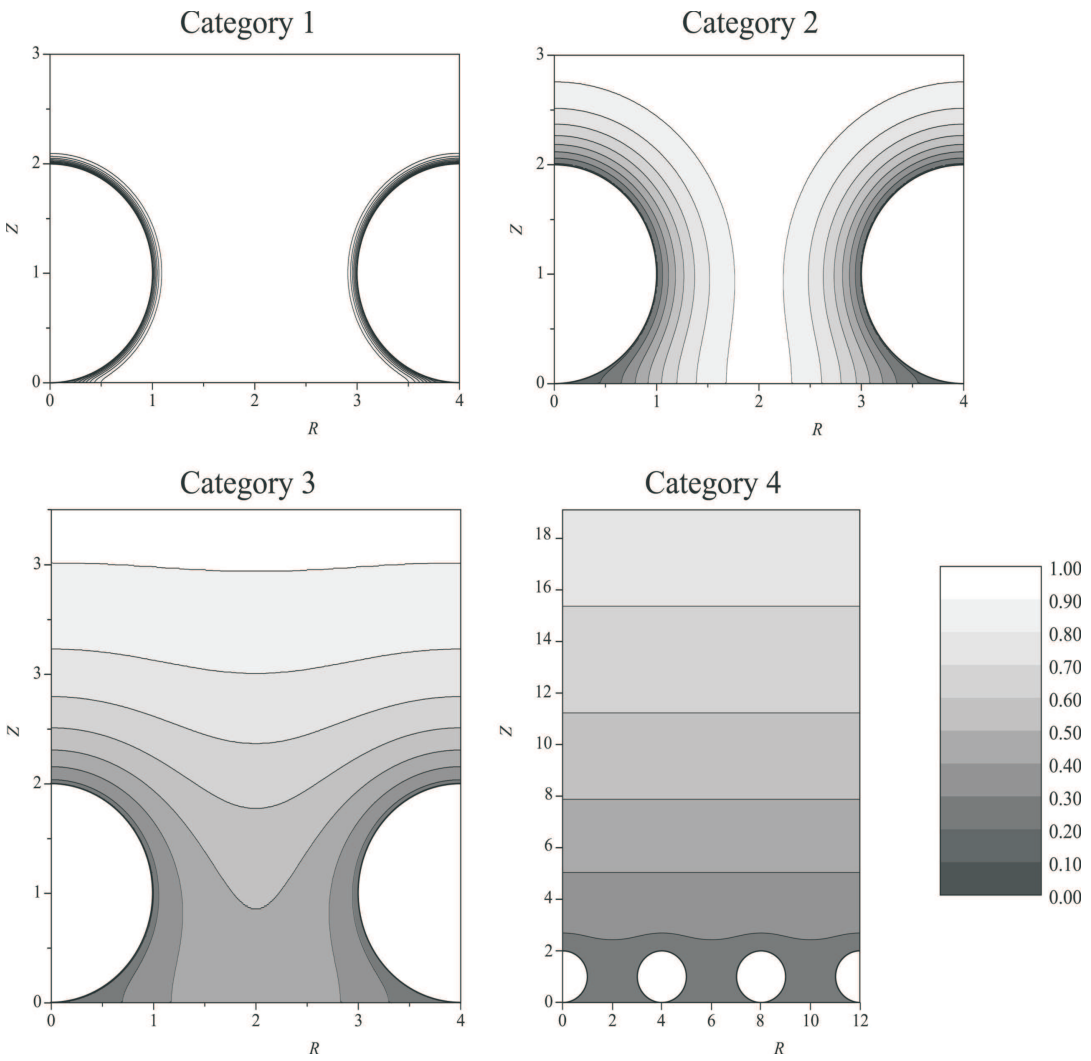

Figure 3.4.6:
Simulated concentration profiles at a diffusion domain containing a spherical particle on an electrically insulating surface. Category 1: $\sigma = 1000$. *Category 2:* $\sigma = 10$. *Category 3:* $\sigma = 1$. *Category 4:* $\sigma = 0.01$. *For all categories* $R_{\text{sep}} = \frac{r_{\text{sep}}}{r_{\text{np}}} = 2$. *Concentration profiles were taken at the linear sweep peak potential.*[20]

mately hemispherical but diffusional isolation between nanoparticles is maintained. The corresponding cyclic voltammograms are in steady-state with a limiting current given by equation 3.4.3. In category 3, the depletion layers overlap and are relatively small compared to the nanoparticle separation. The cyclic voltammetry is peak shaped and the absolute current is smaller than that given by equation 3.4.3. In category 4, the diffusion layers overlap and are relatively large compared to the

nanoparticle separation. Mass transport is effectively 1 dimensional and linear over the entire array. As with category 1, cyclic voltammograms in this category are peak shaped and obey the Randles-Ševčík equation while the chronoamperometry obeys the Cottrell equation. The current response is similar to that obtained had the entire substrate been electroactive. This latter property is useful in catalysis as, in the category 4 region, a nanoparticle array yields a similar amount of electrolytic depletion to a macroelectrode of the same total area. This property is of practical importance as minimal amounts of expensive catalyst, such as platinum or gold, can be used to offer a maximal electrochemical response. Figure 3.4.6 (page 71) shows concentration profiles corresponding to each category for which $R_{\mathrm{sep}} = \frac{r_{\mathrm{sep}}}{r_{\mathrm{np}}} = 2$. Note the change in scale required to resolve the increase in diffusion layer size from category 1 to category 4. Figure 3.4.7 (page 72) shows linear sweep voltammetry

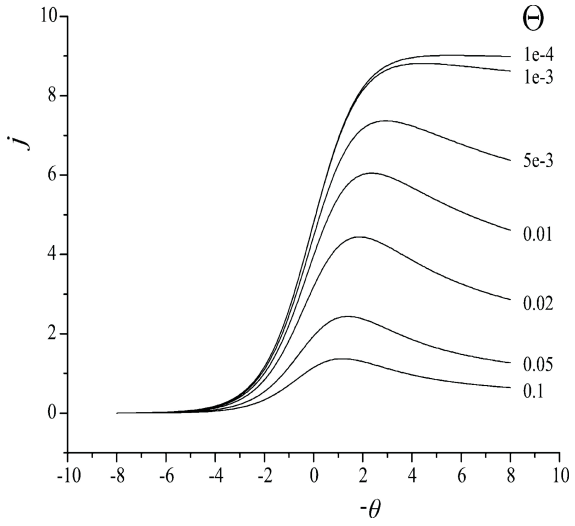

Figure 3.4.7:
Simulated linear sweep voltammetry of a reversible electron transfer at a spherical particle modified electrode. Scan rate $\sigma = 0.01$*,* Θ *varies from* 10^{-4} *to 0.1.*[20]

for a fixed dimensionless scan rate ($\sigma = 0.01$) and variable fractional surface coverage (Θ). The axes are given in terms of the dimensionless current *per nanoparticle* ($j = \frac{i}{ND_{\mathrm{A}}r_{\mathrm{np}}Fc_{\mathrm{A}}}$). When the fractional surface coverage is very small ($\Theta = 10^{-4}$), the

nanoparticles are diffusionally isolated and the voltammetry is necessarily in category 1 or 2. In this situation, the experimental timescale is long enough for category 2 (steady-state) behaviour to be observed. As the fractional surface coverage is increased, the nanoparticle separation decreases and the voltammetric response passes through category 3 until eventually reaching category 4. Note that, as the surface coverage increases, the absolute size of the dimensionless current per nanoparticle decreases since the region of solution available to each nanoparticle is less. Figure

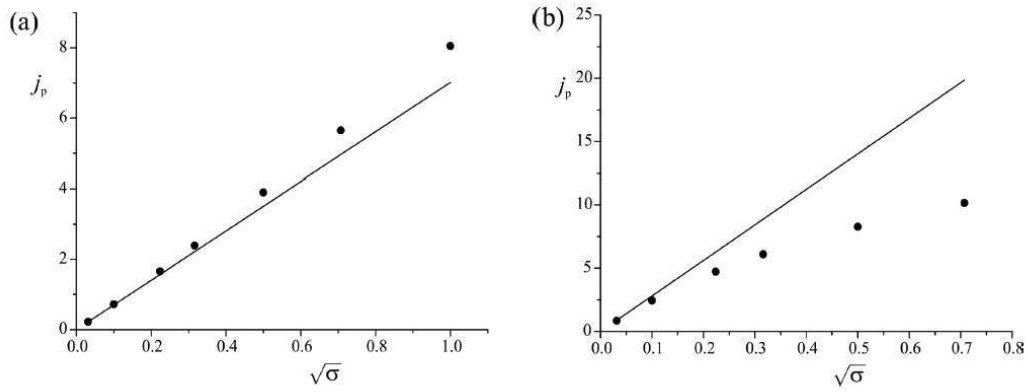

Figure 3.4.8:
Peak current, j_p, versus square root of the scan rate, $\sqrt{\sigma}$. Simulated data is shown by circles, the solid line the shows Randles-Ševčík values for planar diffusion. (a) $\Theta = 0.2$ and (b) $\Theta = 0.05$.[20]

3.4.8 (page 73) shows the dimensionless peak current (j_p) as a function of $\sqrt{\sigma}$ for two fractional surface coverages. In each diagram the solid line plots the Randles-Ševčík equation ($j_p \propto \sqrt{\sigma}$). Category 4 behaviour can be observed at the low scan rates where overlapping of the diffusion layers is greatest. With a surface coverage of $\Theta = 0.05$, the peak current is smaller than the planar diffusion peak current at higher scan rates. This indicates incomplete overlapping of diffusion layers and a transition into category 3 diffusional behaviour. With a surface coverage of $\sigma = 0.2$,

the peak current is larger than the simulated peak current from the planar diffusion value at higher scan rates. The spherical particles considered here are able to draw a higher current because their height above the electrode surface makes them diffusionally accessible to a greater region of the solution on a short experimental time scale.

It is useful to compare experimental data with the theory discussed above. Consider the electrocatalytic reduction of protons at a palladium particle modified electrode:

$$H^+(aq) + e^- \rightleftharpoons H_2(g) \tag{3.4.8}$$

Figure 3.4.9 (page 74) shows SEM images of glassy carbon microspheres before

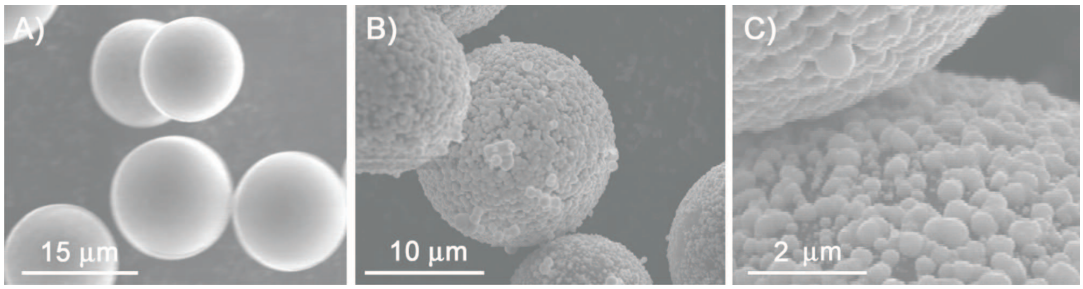

Figure 3.4.9:
SEM images of glassy carbon microspheres:[27] (A) shows the non-modified microspheres, and (B) and (C) show the microspheres with a Pd shell.

and after modification with Pd nanoparticles. The Pd nanoparticles are shown to be approximately spherical in shape. Figure 3.4.10 (page 75) shows a range of experimentally recorded voltammograms using this system. When $\Theta = 0.445$ the diffusion layers overlap extensively and category 4 behaviour is observed for all scan rates studied. Accordingly, the voltammograms are peak shaped and the Randles-Ševčík equation is obeyed. When $\Theta = 0.118$ category 4 behaviour is observed in the

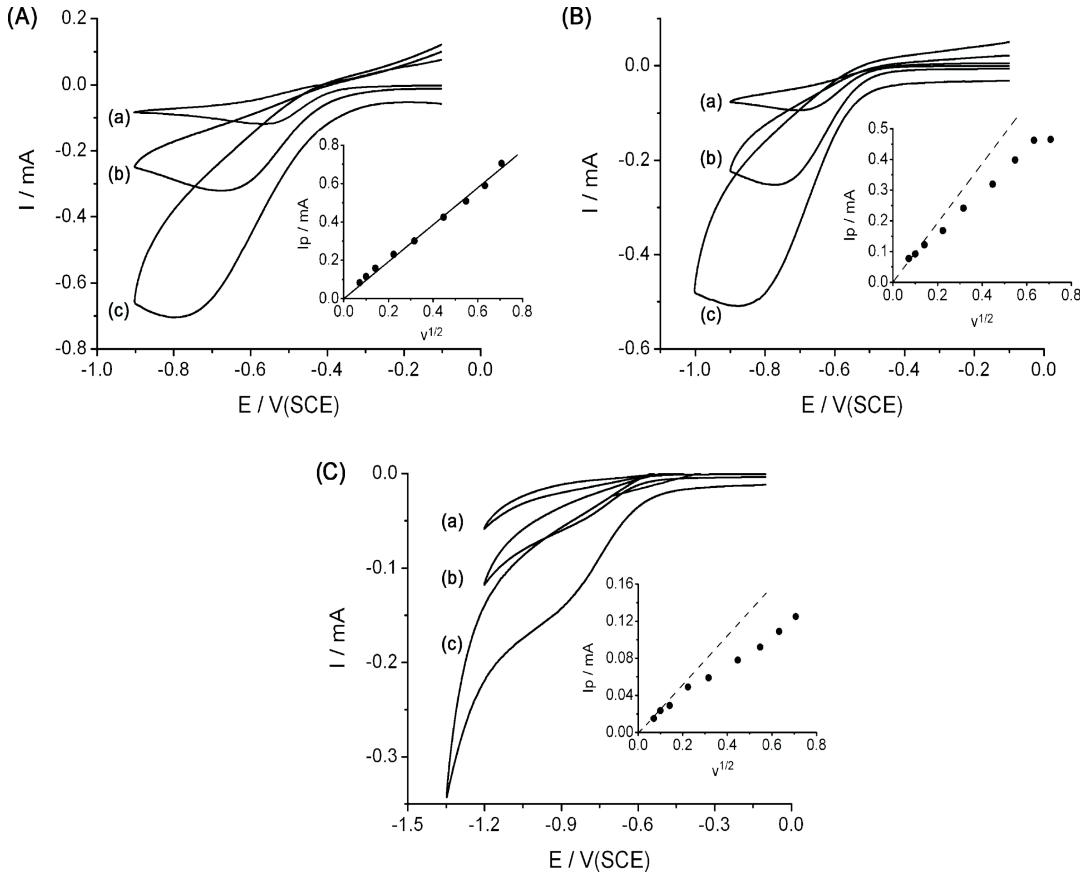

Figure 3.4.10:
Cyclic voltammetry in 3 mM HCl, 0.1 M KCl at a 5 mm diameter BPPG electrode modified by the abrasive attachment of different amounts of Pd-CMs.[27] *The fractional surface coverage of particles is (A) 0.445, (B) 0.118, and (C)* 7.6×10^{-3}. *For each graph curves (a), (b), and (c) correspond respectively to voltammograms recorded at 10, 100, and 500* mV s^{-1}.

limit of low scan rates while category 2 behaviour is observed in the limit of high scan rates. The Randles-Ševčík equation is obeyed in the limit of low scan rates while at high scan rates, the peak current is invariant with scan-rate corresponding to steady-state voltammetry in the category 2 region. When $\Theta = 7.6 \times 10^{-3}$, category 4 behaviour is observed in the limit of low scan rates while category 2 behaviour is observed at intermediate scan rates and category 1 behaviour is observed at high scan rates. The Randles-Ševčík equation is obeyed in the limit of low scan rates while at intermediate scan rates, the peak current is invariant with scan-rate corresponding to

steady-state voltammetry in the category 2 region. At very high scan rates, category 1 behaviour occurs and the Randles-Ševčík equation is obeyed: albeit multiplied by the factor 4Θ in order to account for the fact that diffusion occurs to each nanoparticle individually rather than towards the entire array.[28] Figure 3.4.11 (page

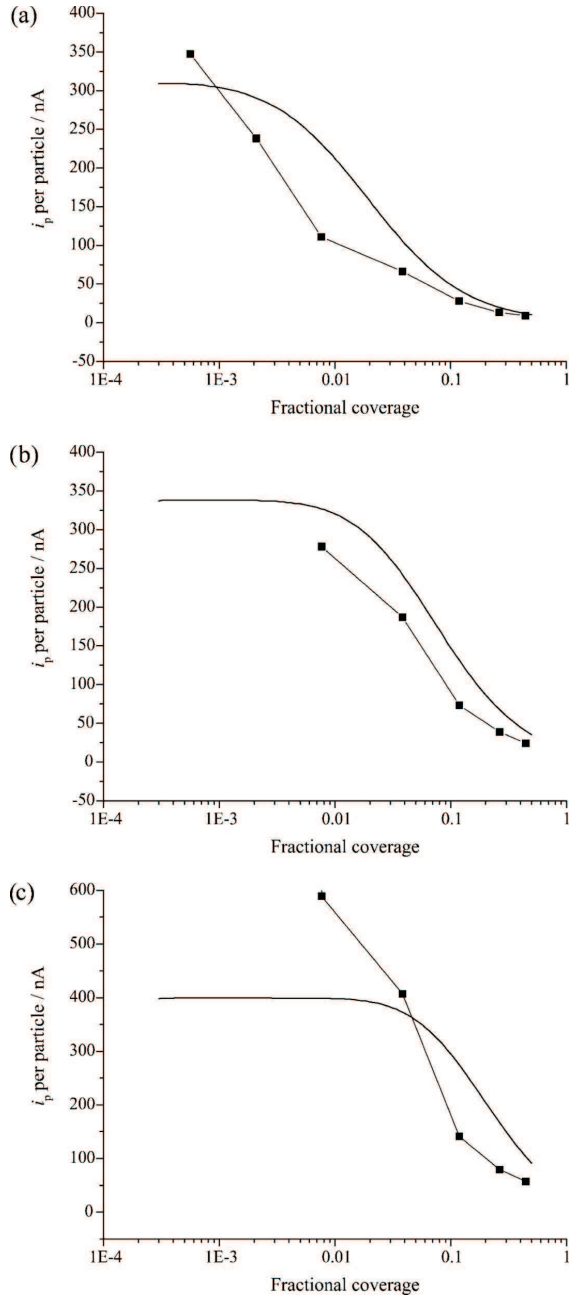

Figure 3.4.11:
Variation of linear sweep peak height per particle with surface coverage of particles.[27] *Scan rates: (a) 0.01, (b) 0.1, (c) 0.5 V* s^{-1}. *Simulated data is shown by a solid line; experimental data is shown by connected squares.*

76) shows a comparison between the peak current (normalised by the number of

nanoparticles in the array) for experiment and simulation for a range of fractional surface coverages. As the fractional surface coverage decreases, the region of solution available to each nanoparticle increases leading to a larger relative current. In the limit of very low surface coverages, a steady-state response is attained, corresponding to the category 2 region.

A similar model to that considered above can be applied to stripping voltammetry. Ward-Jones *et al*[29] have studied the reversible stripping reaction shown in Equation 3.4.9 at a random array of AgNPs:

$$Ag^{+}(aq) + e^{-} \rightleftharpoons Ag(aq) \tag{3.4.9}$$

The stripping voltammetry for different surface coverages is shown in figure 3.4.12

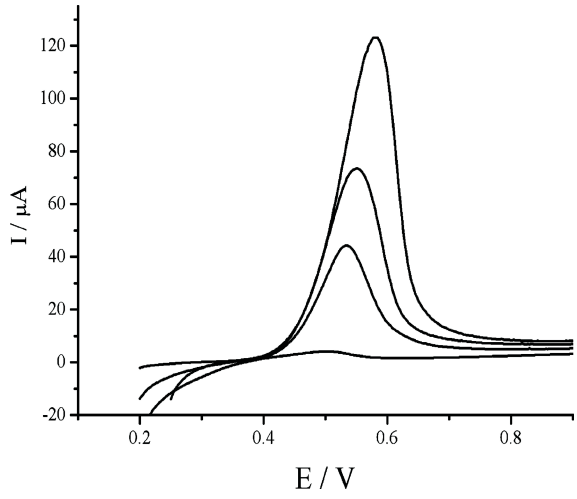

Figure 3.4.12:
Stripping voltammetry for four different loadings of 80-120 nm diameter nanoparticles stripped into a 0.1 M $NaClO_4$ *solution at a scan rate of* $\sigma = 20$ mV s^{-1}.[29]

(page 77). When the nanoparticles are of equal size, the stripping charge, Q, (measured by integrating the area under the voltammogram) is directly proportional to the nanoparticle surface coverage. Figure 3.4.13 (page 78) shows plots of E_p as a function of stripping charge. It can be seen that the peak potential becomes more

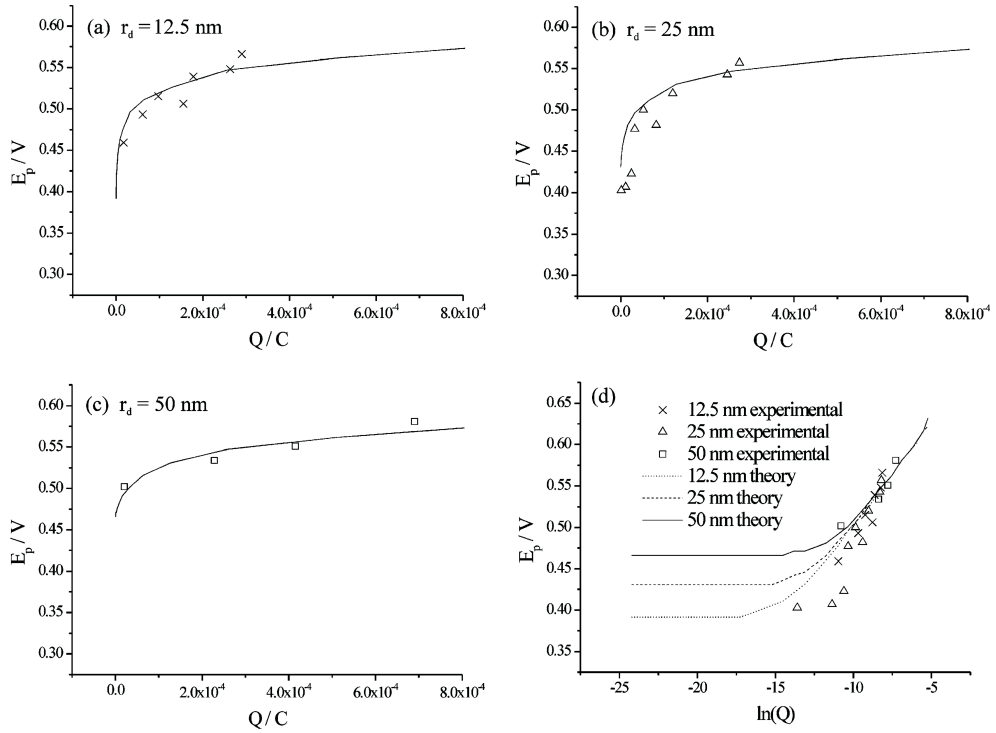

Figure 3.4.13:
Plots of peak potential, E_{p}, measured experimentally (symbols) and predicted by a computational model (solid line) against the stripping charge, Q.[29] *Nanoparticle radius (r_{np}): (a) 12.5 nm (sample 1), (b) 25 nm (sample 2), and (c) 50 nm (sample 3). (d) Same data plotted against* $\ln(Q)$. *In all cases, the scan rate, σ, is 0.02 V s^{-1}.*

positive as the stripping charge (hence surface coverage) becomes higher. The diffusion layers are derived from Ag^+ moving away from the surface during stripping. The diffusion layers overlap leading to category 1-4 behaviour as explained above. As the surface coverage increases, the diffusion layers overlap to a greater extent and hinder the diffusion of Ag^+ from the surface. This leads to the effect of rate determining mass transport (and hence the voltammetric peak) being offset to more positive potentials.

3.5 Porosity effects: a caveat

The above discussion has assumed that the nanoparticles on the electrode surface are present at monolayer coverage or less. In some applications, especially electroanalysis,[2,8] thicker layers of nanoparticles may be used, so forming a porous layer on the electrode surface. This quantitatively changes the mass transport characteristics at the interface. For a thick (> monolayer) modifying layer, the electrode surface

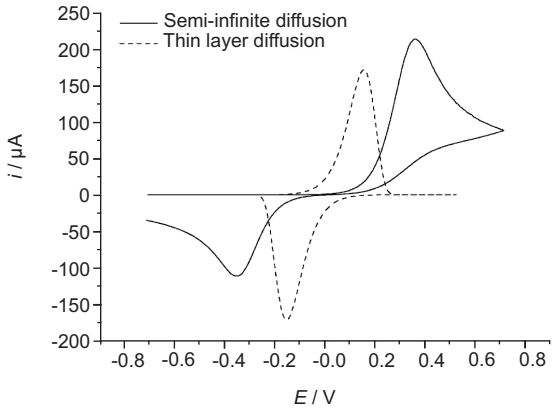

Figure 3.5.1:
Comparison of linear sweep voltammetry using a semi-infinite and thin layer planar diffusion models.[30] *For both models,* $k_0 = 10^{-4}$ cm s^{-1}; $D = 10^{-5}$ cm^2 s^{-1}; $\sigma = 0.1$ V s^{-1}; $c = 10^{-6}$ *mol* cm^{-3}. *Semi-infinite diffusion electrode area,* $A =$ *1* cm^2; *thin layer area,* $A = 30$ cm^2; *thickness,* $l = 1$ μm.

can be thought of as a porous layer in which products in solution[30] are transported in between multiple layers of nanoparticles. The electrolysis of species within the porous layer can be approximately described using a model of a thin-layer cell of high electrode area (much higher than the area of the modifying supporting electrode) reflecting the large surface area of the nanoparticles within the porous layer. This contrasts with electrolysis at the corresponding 'naked' (unmodified) electrode where semi-infinite planar diffusion is the appropriate transport model. Figure 3.5.1 (page 79) shows comparative voltammograms simulated using the two models using a standard electrochemical rate constant of $k_0 = 10^{-4}$ cm s^{-1}, a diffusion coefficient of 10^{-5} cm^{-1} s^{-1} and scan rate of 100 mV s^{-}1 and assuming that the surface area

of the nanoparticles is 30 times that of the naked electrode. Butler-Volmer kinetics is also assumed. Note that the thin layer model predicts a smaller peak to peak separation than the semi-infinite diffusion model and that the peaks appear with a larger overpotential in the latter model. It is evident that if the current measured at a nanoparticle modified electrode has a significant contribution from a porous layer then the impression of an erroneously large electrochemical rate constant may be inferred. That is, a porous layer can give the false impression of speeding up an electrode process whereas in fact it is simply reducing the diffusional overpotential. Porosity effects have been shown to operate in electrodes modified with thick layers of carbon nanotubes[30–33] and of C_{60}.[34,35] They are also likely to exist in some or even many electrodes modified with thick layers of metallic nanoparticles.

3.6 Changed electrode kinetics and mechanisms at the nanoscale

Earlier in this chapter, it was suggested that the changed electronic structure and adsorption behaviour at the nanoscale might induce changes of electrolytic reaction mechanism and kinetics. Thus, for example, gold atomic clusters (Au_n; $5 \leq n \leq 13$) stabilised by surfactants can reduce oxygen to water:[36,37]

$$O_2 + 4H^+ + 4e^- \rightleftharpoons 2H_2O \tag{3.6.1}$$

	α	k_0
macro silver	0.36	6×10^{-12} cm s^{-1}
silver nanoparticles	0.16	1×10^{-6} cm s^{-1}

Table 3.1: *Kinetic data for hydrogen evolution at silver.*[38]

whereas at bulk gold a two electron process is seen:

$$O_2 + 2H^+ + 2e^- \rightleftharpoons H_2O_2 \tag{3.6.2}$$

In the above example a double electrode (ring-disc) was used to identify the presence or absence of H_2O_2 generated on a disc electrode covered with electro-deposited layers of the nano-material.

In other work sub-monolayers of larger nanoparticles have been employed.[38] Thus the hydrogen evolution reaction:

$$H^+(aq) + e^- \rightleftharpoons 0.5H_2(g) \tag{3.6.3}$$

carried out using either a silver macroelectrode or an array of silver nanoparticles showed very different Butler-Volmer kinetics as reported in Table 3.1: where α is the transfer coefficient and k_0 is the standard electrochemical rate constant. Important in this work was the correction for mass transport effects as described elsewhere in this article. Similarly the reaction of 4-nitrophenol[39] in aqueous solution was shown to have a quite different mechanism between a silver macro-electrode and arrays of 15-50 nm order nanoparticles. In the former case an α close to unity supported the possibility of the fast formation of the radical anion followed by a rate determining

chemical step, whereas for the nanoparticles a low α value suggested slow, rate determining electrode kinetics.

3.7 Modelling the behaviour of small (< 10 nm) nanoparticles

The Debye length, the distance over which electric fields are effectively screened in an electrolytic solution, ranges between 1 and 10 nm in aqueous solution for typical concentrations of electrolyte from 1 to 100 mM. The longer part of the range ($r_{\mathrm{D}} \approx 10$ nm) corresponds to weakly or self-supported solutions, as may be of interest in, for instance, biological applications.[40] For electrodes with dimensions which approach this size, electric fields and migration effects strongly influence behaviour close to the electroactive surface, especially when the concentration of supporting electrolyte is small. Therefore, the study of electrolysis at small nanoparticles no longer admits some common assumptions such as electroneutrality, but rather requires a more thorough theoretical treatment. A range of 'non-classical' effects have been identified. These effects are discussed in this section.

In consideration of the diffuse double layer, which at steady state compensates the excess charge on a nanoelectrode, recent work has shown that the effect of curvature on the double layer at a nanoparticle with radius less than or close to the solution Debye length causes deviation from the classical Gouy-Chapman theory,[41,42] for both hemispherical and cylindrical geometries. In particular, elevated and increasingly potential independent diffuse double layer capacitance is predicted, together with

increased electric field at the nanoparticle surface and hence reduced ohmic drop at the plane of electron transfer. Since the Debye length is inversely dependent on the square root of the ionic strength, these effects ought to occur at larger nanoparticles under conditions of low electrolytic support.

Size effects are equally important under conditions of dynamic electrolysis, such as in a voltammetric experiment with a potential step or potential sweep. Since the dimensions of the electrode, and hence the plane of electron transfer, are of the same order as the Debye length, the double layer and diffusion layer are entangled in a complex manner close to the electrode surface. The overall behaviour is not yet well understood, but it is safe to say that any attempt to model electrolysis at small nanoparticles must explicitly consider double layer structure. For instance, in a study of weakly supported chronoamperometry, Streeter et al. demonstrated that the decoupling of ohmic drop and double layer capacitance by a zero-field approximation is invalid at nanoelectrodes;[43] by contrast, this approximation has been successfully applied to fit experimental data for weakly supported voltammetry at larger electrodes.[44,45] Yang et al. have considered some features of the influence of the double layer on voltammetry at nanoelectrodes.[46]

Furthermore, the magnitudes of charge and distance associated with small nanoparticles render continuum theories altogether inappropriate under many circumstances. For example, a 5 nm particle with a mean surface capacitance of 10 μF cm^{-2} will have an excess charge of fewer than 50 electrons at a 200 mV overpotential away from the potential of zero charge. For such small excess charges, components of the electron conduction bands may be observably discrete, and the charging process is

therefore quantised. The tunnelling of single electrons to and from discrete wavefunctions within the nanoparticle may be measured, with charging occurring one electron at a time in a so-called 'Coulomb staircase'[47–49] - alkanethiol-modified Au nanoparticles have been the most popular systems for experimental investigation to date. Classical interpretations of capacitance clearly do not apply here; any theoretical treatment which ignores quantisation will exclude experimentally significant effects.

Finite molecule or ion volume effects may equally become significant at a small nanoparticle scale. Traditional mean field (continuum) theories cease to be reliable at very short length scales, and a fuller consideration of finite volume effects leads to a revised understanding of double layer structure. López-García et al. have considered this topic most completely using a simulation method based on the modified Poisson-Boltzmann equation;[50] the references therein represent an adequate review of the prior literature.

Similarly, the assumption of a continuous solvent is weaker, since the surface structure of the nanoparticle controls the local orientation of solvent molecules, and the number of solvent molecules making up the compact double layer is not sufficiently large to treat solution as continuous approaching the surface. Especially in consideration of the close coupling of the double layer to the diffusion layer, such effects may influence experimental observations for voltammetry or impedance spectroscopy experiments. The magnitude of such effects has not yet been thoroughly investigated in an electrochemical context, although some studies have used molecular dynamics to investigate the limitations of mean field theories[51–53] for describing the electrical

double layer. The fuller analysis of charge dynamics and electrolysis at the nanoscale remains in its infancy, however.

3.8 Conclusion

It has been shows that, in almost all cases, the voltammetric response from a nanoparticle modified electrode is substantially different from that expected from a macroelectrode. Discrepancies occur due to a combination of electrode kinetics and mass transport. Using computer simulations, it is possible to deconvolute these factors and obtain useful experimental information regarding the nanoparticle specific effects. In the following chapter, the simulation of these arrays is investigated.

Bibliography

[1] Belding, S. R.; Campbell, F. W.; Compton, R. G. *Phys. Chem. Chem. Phys.* **2010**, *12*, 11208–11221.

[2] Welch, C. M.; Compton, R. G. *Anal. Bioanal. Chem.* **2006**, *384*, 601–619.

[3] Hutchings, G. J. *Chem. Commun.* **2008**, 1148–1164.

[4] Hughes, M. D.; Xu, Y.-J.; Jenkins, P.; McMorn, P.; Landon, P.; Enache, D. I.; Carley, A. F.; Attard, G. A.; Hutchings, G. J.; King, F.; Stitt, H. E.; Johnston, P.; Griffin, K.; Kiely, C. J. *Nature* **2005**, *437*, 1132–1135.

[5] Templeton, A. C.; Wuelfing, W. P.; Murray, R. W. *Acc. Chem. Res.* **2000**, *33*, 27–36.

[6] Murray, R. W. *Electroanal. Chem.* **1984**, *13*, 191–368.

[7] Simm, A. O.; Ji, X.; Banks, C. E.; Hyde, M. E.; Compton, R. G. *ChemPhysChem* **2006**, *7*, 704–709.

[8] Campbell, F. W.; Compton, R. G. *Anal. Bioanal. Chem.* **2010**, *396*, 241–259.

[9] Campbell, F. W.; Belding, S. R.; Baron, R.; Xiao, L.; Compton, R. G. *J. Phys. Chem. C* **2009**, *113*, 9053–9062.

[10] Taube, H. *Angewandte Chemie International Edition in English* **1984**, *23*, 329–339.

[11] Weaver, M. J.; Anson, F. C. *Inorg. Chem.* **1976**, *15*, 1871–81.

[12] Mao, B. W.; Tian, Z. Q.; Fleischmann, M. *Electrochim. Acta* **1992**, *37*, 1767–1770.

[13] Wang, J. X.; Adzic, R. R.; Magnussen, O. M.; Ocko, B. M. *Surf. Sci.* **1995**, *344*, 111–121.

[14] Campbell, F. W.; Zhou, Y.-G.; Compton, R. G. *New J. Chem.* **2010**, *34*, 187–189.

[15] Campbell, F. W.; Compton, R. G. *Int. J. Electrochem. Sci.* **2010**, *5*, 407 – 413.

[16] Batchelor-McAuley, C.; Wildgoose, G. G.; Compton, R. G. *New J. Chem.* **2008**, *32*, 941–946.

[17] Flatgen, G.; Wasle, S.; Lubke, M.; Eickes, C.; Radhakrishnan, G.; Doblhofer, K.; Ertl, G. *Electrochim. Acta* **1999**, *44*, 4499–4506.

[18] Campbell, F. W.; Belding, S. R.; Baron, R.; Xiao, L.; Compton, R. G. *J. Phys. Chem.* In Press.

[19] Streeter, I.; Compton, R. G. *The Journal of Physical Chemistry C* **2007**, *111*, 18049–18054.

[20] Streeter, I.; Compton, R. G. *J. Phys. Chem. C* **2007**, *111*, 18049–18054.

[21] Davies, T. J.; Brookes, B. A.; Fisher, A. C.; Yunus, K.; Wilkins, S. J.; Greene, P. R.; Wadhawan, J. D.; Compton, R. G. *J. Phys. Chem. B* **2003**, *107*, 6431–6444.

[22] Brookes, B. A.; Davies, T. J.; Fisher, A. C.; Evans, R. G.; Wilkins, S. J.; Yunus, K.; Wadhawan, J. D.; Compton, R. G. *J. Phys. Chem. B* **2003**, *107*, 1616–1627.

[23] Davies, T. J.; Ward-Jones, S.; Banks, C. E.; Del Campo, J.; Mas, R.; Munoz, F. X.; Compton, R. G. *J. Electroanal. Chem.* **2005**, *585*, 51–62.

[24] Davies, T. J.; Compton, R. G. *J. Electroanal. Chem.* **2005**, *585*, 63–82.

[25] Davies, T. J.; Banks, C. E.; Compton, R. G. *J. Solid State Electrochem.* **2005**, *9*, 797–808.

[26] Belding, S. R.; Dickinson, E. J. F.; Compton, R. G. *J. Phys. Chem. C* **2009**, *113*, 11149–11156.

[27] Campbell, F. W.; Belding, S. R.; Baron, R.; Xiao, L.; Compton, R. G. *J. Phys. Chem. C* Submitted.

[28] Belding, S. R.; Compton, R. G. *J. Phys. Chem. C* **2010**, in press.

[29] Ward Jones, S. E.; Campbell, F. W.; Baron, R.; Xiao, L.; Compton, R. G. *J. Phys. Chem. C* **2008**, *112*, 17820–17827.

[30] Streeter, I.; Wildgoose, G. G.; Shao, L.; Compton, R. G. *Sens. Actuators, B* **2008**, *B133*, 462–466.

[31] Menshykau, D.; Compton, R. G. *Electroanalysis* **2008**, *20*, 2387–2394.

[32] Sims, M. J.; Rees, N. V.; Dickinson, E. J. F.; Compton, R. G. *Sens. Actuators B* **2010**, *B144*, 153–158.

[33] Keeley, G. P.; Lyons, M. E. G. *Int. J. Electrochem. Sci.* **2009**, *4*, 794–809.

[34] Xiao, L.; Wildgoose, G. G.; Compton, R. G. *Sens. Actuators B* **2009**, *B138*, 524–531.

[35] Xiao, L.; Wildgoose, G. G.; Crossley, A.; Compton, R. G. *Sens. Actuators. B* **2009**, *B138*, 397–401.

[36] Rodriguez-Vazquez, M. J.; Blanco, M. C.; Lourido, R.; Vazquez-Vazquez, C.; Pastor, E.; Planes, G. A.; Rivas, J.; Lopez-Quintela, M. A. *Langmuir* **2008**, *24*, 12690–12694.

[37] Jeyabharathi, C.; Kumar, S. S.; Kiruthika, G. V. M.; Phani, K. L. N. *Angew. Chem., Int. Ed.* **2010**, *49*, 2925–2928, S2925/1–S2925/9.

[38] Campbell, F. W.; Belding, S. R.; Baron, R.; Xiao, L.; Compton, R. G. *J. Phys. Chem. C* **2009**, *113*, 14852–14857.

[39] Campbell, F. W.; Belding, S.; Compton, R. *ChemPhysChem* **2010**, in press.

[40] Compton, R. G.; Banks, C. E. *Understanding Voltammetry*; World Scientific: Singapore, 2007.

[41] Dickinson, E. J. F.; Limon-Petersen, J. G.; Rees, N. V.; Compton, R. G. *J. Phys. Chem. C* **2009**, *113*, 11157–11171.

[42] Henstridge, M. C.; Dickinson, E. J. F.; Compton, R. G. *Chem. Phys. Lett.* **2010**, *485*, 167–170.

[43] Streeter, I.; Compton, R. G. *J. Phys. Chem. C* **2008**, *112*, 13716–13728.

[44] Dickinson, E. J. F.; Compton, R. G. *J. Phys. Chem. C* **2009**, *113*, 17585–17589.

[45] Limon-Petersen, J. G.; Han, J. T.; Rees, N. V.; Dickinson, E. J. F.; Streeter, I.; Compton, R. G. *J. Phys. Chem. C* **2010**, *114*, 2227–2236.

[46] Yang, X.; Zhang, G. *Nanotechnology* **2007**, *18*, 335201/1–335201/9.

[47] Chen, S.; Ingrma, R. S.; Hostetler, M. J.; Pietron, J. J.; Murray, R. W.; Schaaff, T. G.; Khoury, J. T.; Alvarez, M. M.; Whetten, R. L. *Science* **1998**, *280*, 2098–2101.

[48] Graf, H.; Vancea, J.; Hoffmann, H. *Appl. Phys. Lett.* **2002**, *80*, 1264–1266.

[49] Negishi, R.; Hasegawa, T.; Tanaka, H.; Terabe, K.; Ozawa, H.; Ogawa, T.; Aono, M. *Surf. Sci.* **2007**, *601*, 3907–3911.

[50] López-García, J. J.; Aranda-Rascón, M. J.; Horno, J. *J. Colloid Interface Sci.* **2007**, *316*, 196–201.

[51] Spohr, E. *Solid State Ionics* **2002**, *150*, 1–12.

[52] Grün, F.; Jardat, M.; Turq, P.; Amatore, C. *J. Chem. Phys.* **2004**, *120*, 9648–9655.

[53] White, R. J.; White, H. S. *Langmuir* **2008**, *24*, 2850–2855.

Chapter 4

Numerical simulation of nanoparticle arrays

As seen in chapter 3, nanoparticle arrays are increasingly used in electrochemical research and important applications are being found. This chapter presents work into voltammetry at nanoparticle arrays. The work presented in this chapter has been published partly in *The Journal of Physical Chemistry*[1] and partly in *Chemical Physics Letters*.[2] The experimental work was performed by Dr. Fallyn W. Campbell and Ms. Yige Zhou.

4.1 Introduction

The search for improved amperometric sensors and for electrodes capable of resolving fast kinetics for processes of importance in fuel cells, batteries and other energy conversion devices has led to the increasingly wide study of electrodes modified with small quantities of electrocatalytically active nanoparticles.[3,4] The nanoparticles are

supported on a conductive substrate with the added expectation that electrolysis occurs solely on the surface of the nanoparticles and not the underlying substrate. It is established[5] that, for appropriate surface coverages, such an array can show a current response corresponding to transport controlled electrolysis at the geometric area of the substrate electrode; despite the latter being partially covered by nanoparticles. In this way, minimal amounts of expensive catalyst, such as platinum or gold, can be used to offer a maximal electrochemical response.

In addition, the use of nanoparticles can produce electrochemical behaviour at the nanoscale which is different to that seen on either the micro- or macro-scales. Recent literature has shown that underpotential deposition adsorption of thallium onto gold nanoparticles switches off for gold particles of diameter smaller than *ca* 50 nm[6] whilst the kinetics of the hydrogen evolution reaction at silver are significantly altered between the macro- and nano-scales.[7] The reduction of hydrogen peroxide at silver nanoparticles shows a mechanism distinct to that on the macro-scale.[8] Such differences in behaviour can occur either through a change in the electronic properties of the particles from the macro to the nano-range, influencing, for example, the work function of the metal, and also through the altered surface crystallography at the nano-scale, where high index planes are more likely to occur and where the sheer size limits the extent to which large terraces of a low index plane can exist.

In order to explore the electrochemistry of nanoparticles and to discover the kinetics and mechanism of electrocatalytic processes, it is necessary to develop a theory of voltammetry at substrates partially covered with nanoparticles. In previous research, the steady-state voltammetry has been calculated for isolated nanoparticles

of various shapes[9] supported on an inert planar conducting electrode. The predictions were confirmed experimentally.[10] More recently this was extended to voltammetry at an electrode covered with an array of nanoparticles, assumed to be flat disks.[11] This chapter examines the more realistic case in which the nanoparticles are spherical. The approximation of spheres by discs is shown to be justified in most, but not all, experimental situations. Theoretical results are verified experimentally using the well-defined one electron reduction[12] of Cr^{3+} in aqueous solution (4.1.1) using an array of silver nanoparticles.

$$Cr^{3+}(aq) + e^- \rightleftharpoons Cr^{2+}(aq) \tag{4.1.1}$$

4.2 Theory

We consider a one electron electron reduction of the form:

$$A + e^- \rightleftharpoons B \tag{4.2.1}$$

in which the diffusion coefficients of species A and B are equal ($D_A = D_B$). The reaction occurs on an infinitely large, random array of nanoparticles supported on a planar electrode. The nanoparticles are perfect spheres of equal size that catalyse the reaction shown in Eqn 4.2.1. This reaction is assumed to occur exclusively on the surface of the nanoparticles, with negligible adsorption effects so that the voltammetry is exclusively diffusional in character.

4.2.1 Categorisation of the diffusional behaviour

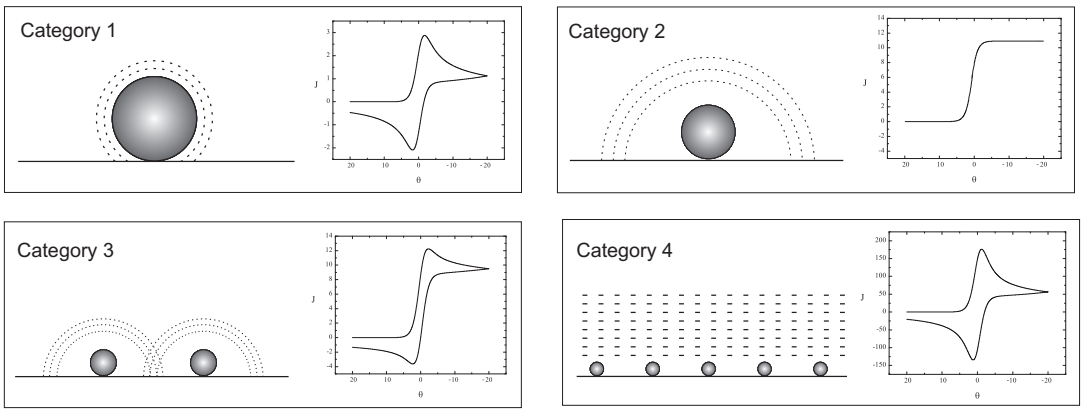

Figure 4.2.1:
Categorisation of the diffusional behaviour.

Mass transport to a random array of spherical nanoparticles can be understood in terms analogous, but complementary, to those for partially blocked electrodes[13,14] and microdisk electrodes.[15,16] The interaction between the diffusional zone of each nanoparticle varies as a function of the experimental timescale and of the nanoparticle surface coverage. As the experimental timescale increases and the nanoparticle surface coverage decreases, the diffusional interaction changes from category 1 through to category 4 as shown in Figure 4.2.1. In category 1, the diffusion layers are small and each nanoparticle is diffusionally isolated: mass transport is 1 dimensional and linear. This behaviour leads to peak shaped cyclic voltammograms. In category 2, the diffusion layers are large and approximately hemispherical but diffusional isolation between nanoparticles is maintained. This behaviour leads to steady-state cyclic voltammograms. In category 3, the depletion layers overlap and are relatively small compared to the nanoparticle separation. The cyclic voltammetry is intermediate between categories 2 and 4. In category 4, the diffusion layers overlap but are

relatively large compared to the nanoparticle separation. Mass transport is effectively 1 dimensional and linear over the entire array. The current response is equal to that obtained had the substrate been electroactive. This behaviour leads to peak shaped cyclic voltammograms.

4.2.2 Voltammetry for a random array of nanoparticles

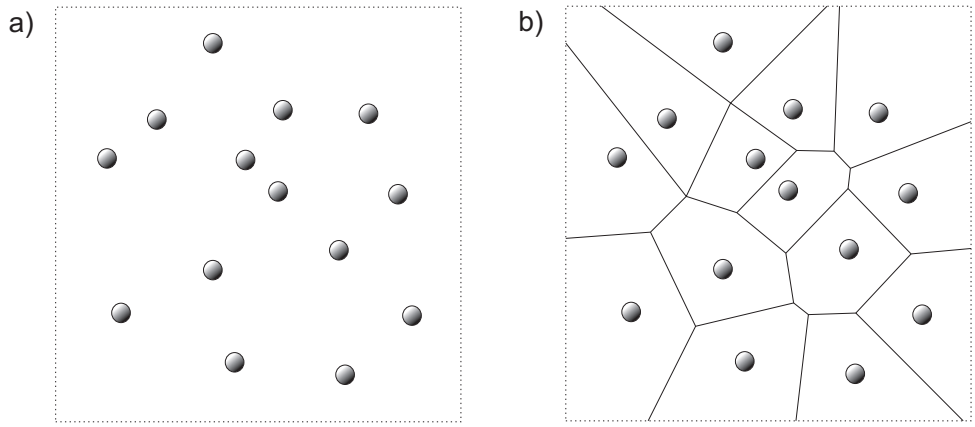

Figure 4.2.2:
(a) Top-down view of a section of a random array of nanoparticles.
(b) Top-down view shown in "(a)" divided into Voronoi cells.

Nanoparticles of equal size and are randomly distributed over the surface of an infinitely large supporting electrode; a section of which is shown in Figure 4.2.2(a). This assembly is divided into hypothetical units called Voronoi cells as shown in Figure 4.2.2(b). Each 'wall' is situated midway between adjacent nanoparticles. Consequently, to good approximation, the walls can be considered no flux boundaries. The Voronoi cells are therefore diffusionally independent and can be simulated separately. The final voltammogram is constructed by summing the voltammogram derived from each Voronoi cell, weighted by the size distribution of the Voronoi cells. An arbitrary Voronoi cell is shown in Figure 4.2.3(a); the simulation of which is a

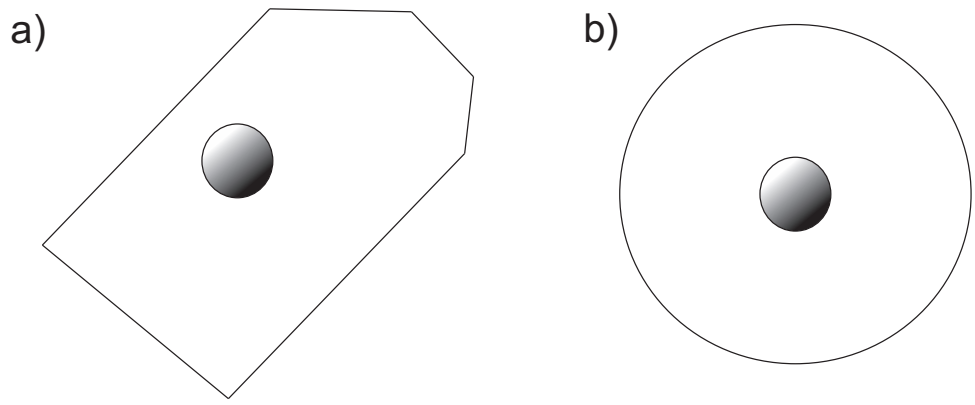

Figure 4.2.3:
(a)Arbitrary Voronoi cell.
(b)Circular cell derived from "(a)" using the diffusion domain approximation.

computationally intractable 3 dimensional problem. The problem is computationally simplified by applying the diffusion domain approximation proposed by Gileadi and Amatore.[17,18] The irregular Voronoi cell shown in Figure 4.2.3(a) is transformed into the circular diffusion domain shown in Figure 4.2.3(b). The diffusion domain is of equal area to the original cell and is concentric with respect to the nanoparticle. Since the diffusion domain corresponds to a cylindrical simulation space, the problem is rendered two dimensional and can be solved numerically using a desktop computer. This technique is well established and has been used to simulate a range of experiments.[7,8] The validity of the diffusion domain approximation has been studied in detail by Godino *et al.*[19] In general, a high degree of concordance was shown to occur between the experimental and simulated data. Significant discrepancies occurred for small arrays. In these cases a large proportion of the nanoparticles were situated at peripheral points in the array. Over long timescales, diffusion towards these peripheral points become important and mass transport was convergent towards the entire array. This contrasts with the case of an infinitely large array

in which, over long timescales, mass transport is linear towards the entire array (category 4). The diffusion domain approach is best suited for large arrays with significantly more microelectrodes in inner than in perimetric positions. The size

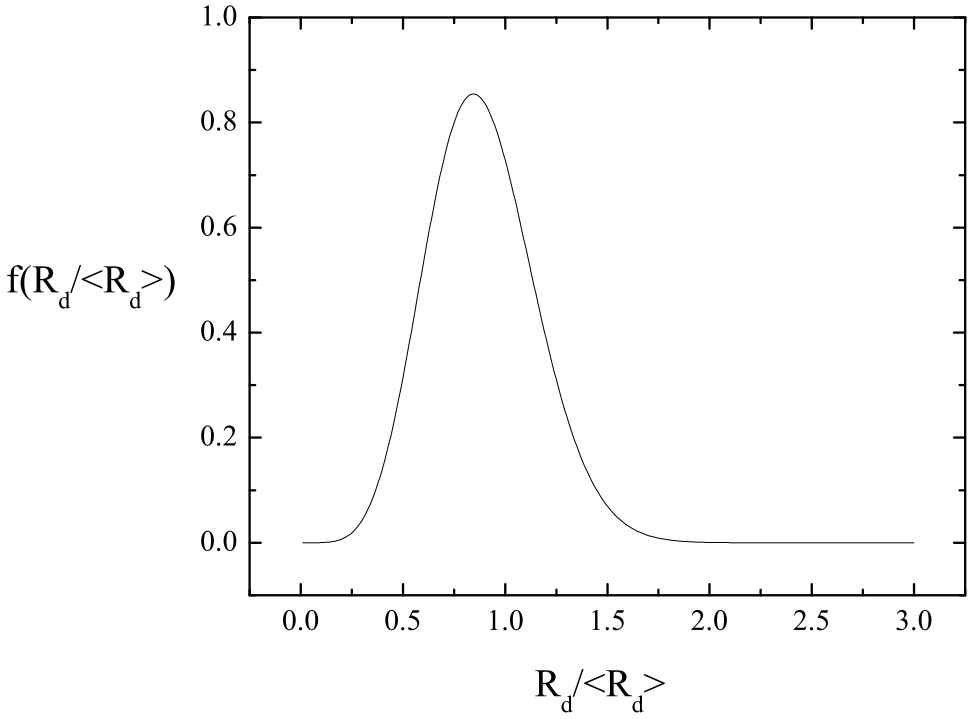

Figure 4.2.4:
Size distribution function for a random array.

distribution of the Voronoi cells is given by the function f $\left(\frac{r_\mathrm{d}}{\langle r_\mathrm{d}\rangle}\right)$ where r_d is radius of a given diffusion domain and $\langle r_\mathrm{d}\rangle$ is the mean radius of the Voroni cells in the array (related to surface coverage, as considered in Section 4.2.3). Although an exact analytical expression for this function does not exist, Ferenc *et al*[?] have numerically derived a result using Monte Carlo-type simulation methods. The distribution is given by equation 4.2.2:

$$\mathrm{f}\left(\frac{r_\mathrm{d}}{\langle r_\mathrm{d}\rangle}\right) = \frac{343}{15}\sqrt{\frac{7}{2\pi}}\left(\frac{r_\mathrm{d}}{\langle r_\mathrm{d}\rangle}\right)^5 \exp\left(-\frac{7}{2}\left(\frac{r_\mathrm{d}}{\langle r_\mathrm{d}\rangle}\right)^2\right) \qquad (4.2.2)$$

The voltammetric response for the random array ($\mathrm{V_{random}}$) is constructed by summing the voltammogram derived from each Voronoi cell ($\mathrm{V_{cell}}$). Each voltammogram in this sum is weighted by the function $\mathrm{f}\left(\frac{r_\mathrm{d}}{\langle r_\mathrm{d}\rangle}\right)$ in order to account for the mean diffusion domain radius, $\langle r_\mathrm{d}\rangle$:

$$\mathrm{V_{random}}(\langle r_\mathrm{d}\rangle) = \int_0^\infty \mathrm{f}\left(\frac{r_\mathrm{d}}{\langle r_\mathrm{d}\rangle}\right) \mathrm{V_{cell}}(r_\mathrm{d})\,\mathrm{d}r_\mathrm{d} \tag{4.2.3}$$

The diffusion domain radius, r_d, is discretised as follows:

$$r_\mathrm{d}^p \leq r_\mathrm{np} \qquad r_\mathrm{d}^p = 0.01(p+1)r_\mathrm{np} \qquad p = 0, 1, 2, ..., 97, 98, 99$$

$$r_\mathrm{d}^p > r_\mathrm{np} \qquad r_\mathrm{d}^p = (1 + 10^{-3+0.01p})r_\mathrm{np} \qquad p = 100, 101, 102, ..., 598, 599, 600$$

The logarithmic form of this discretization allows it to be used over a range of $\langle r_\mathrm{d}\rangle$ values and is converged for those considered in this chapter ($1 \leq \langle r_\mathrm{d}\rangle \leq 50$). When $r_\mathrm{d}^p < r_\mathrm{np}$, corresponding to nanoparticle overlap, diffusion is approximately linear and the voltammetry can be approximated as:[20]

$$\mathrm{V_{cell}}(r_\mathrm{d}) = \left(\frac{r_\mathrm{d}}{r_\mathrm{np}}\right)^2 \mathrm{V_{cell}}(r_\mathrm{d}^{p=99}) \tag{4.2.4}$$

The geometry of the nanoparticle with respect to the diffusion domain can be equivalently defined with respect any 2 dimensional coordinate system. The spatial boundary condition at the surface of the nanoparticle is most easily given in terms of spherical coordinates (r_sph and ϕ_sph) while the remaining spatial boundary conditions are most easily given in terms of cylindrical coordinates (r_cyl and z_cyl). These coordinate systems are shown in Figure 4.2.5. As explained in Section 8.1.3, the

$\langle R_\mathrm{d} \rangle$	**Surface Coverage / %**
1.75	31.93
3.25	9.47
5.75	3.02
10.00	1.00

Table 4.1:
Comparison between the mean diffusion domain radius ($\langle R_\mathrm{d} \rangle$) and percentage coverage for a random array.

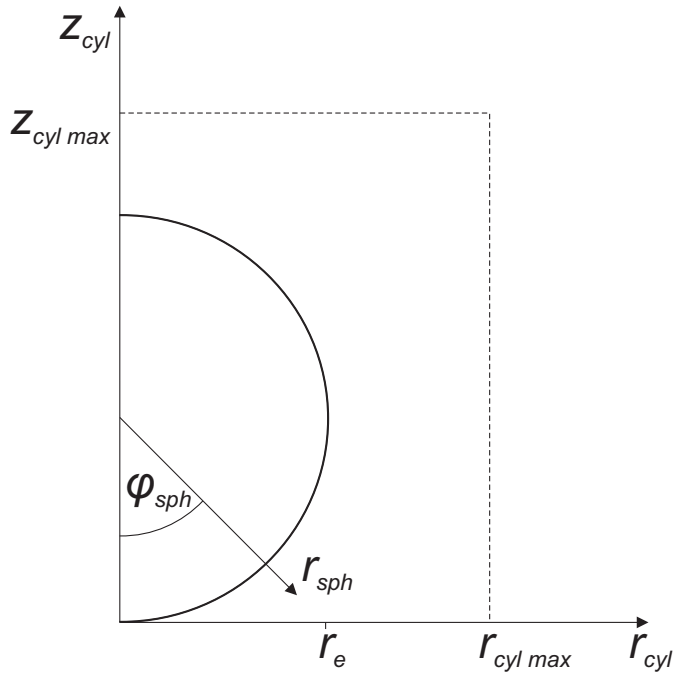

Figure 4.2.5:
Spherical nanoparticle defined with respect to a system of spherical coordinates (r_sph and ϕ_sph) and to a system of cylindrical coordinates (r_cyl and z_cyl).

problem is solved more efficiently if spherical coordinates are used.

A chronoamperogram or voltammogram is a solution to Fick's 2$^\mathrm{nd}$ law of diffusion:

$$\frac{\partial c_\mathrm{A}}{\partial t} = \frac{2}{r_\mathrm{sph}} \frac{\partial c_\mathrm{A}}{\partial r_\mathrm{sph}} + \frac{\partial^2 c_\mathrm{A}}{r_\mathrm{sph}^2} + \frac{1}{r_\mathrm{sph}^2 \tan\phi} \frac{\partial c_\mathrm{A}}{\partial \phi} + \frac{1}{r_\mathrm{sph}^2} \frac{\partial^2 c_\mathrm{A}}{\partial \phi^2} \tag{4.2.5}$$

with respect to the following boundary conditions:

$$
\begin{array}{llll}
t = 0 & 0 \le \phi \le \pi & r_{\mathrm{sph}} \ge r_{\mathrm{np}} & c_{\mathrm{A}} = \; c_{\mathrm{A}}^{*} \\
t > 0 & 0 \le \phi \le \pi & r_{\mathrm{sph}} \ge r_{\mathrm{np}} & \frac{\partial c_{\mathrm{A}}}{\partial r_{\mathrm{sph}}} = \; k^{0} c_{\mathrm{A}} \exp[-\alpha \frac{F(E-E^{0'})}{RT}] \\
 & & & \quad -k^{0}(1-c_{\mathrm{A}}) \exp[(1-\alpha)\frac{F(E-E^{0'})}{RT}] \\
t > 0 & 0 \le \phi < \tan^{-1} r_{\mathrm{cyl\,max}} & r_{\mathrm{sph}} = \frac{1}{\cos\phi} & \frac{\partial c_{\mathrm{A}}}{\partial r_{\mathrm{sph}}} = \; 0 \\
t > 0 & \tan^{-1} r_{\mathrm{cyl\,max}} \le \phi < \frac{\pi}{2} & r_{\mathrm{sph}} = \frac{r_{\mathrm{cyl\,max}}}{\cos\left(\frac{\pi}{2}-\phi\right)} & \frac{\partial c_{\mathrm{A}}}{\partial r_{\mathrm{sph}}} = \; 0 \\
t > 0 & \frac{\pi}{2} \le \phi < \tan^{-1}\left(\frac{z_{\mathrm{cyl\,max}}}{r_{\mathrm{cyl\,max}}}\right) + \frac{\pi}{2} & r_{\mathrm{sph}} = \frac{r_{\mathrm{cyl\,max}}}{\cos\left(\phi-\frac{\pi}{2}\right)} & \frac{\partial c_{\mathrm{A}}}{\partial r_{\mathrm{sph}}} = \; 0 \\
t > 0 & \tan^{-1}\left(\frac{z_{\mathrm{cyl\,max}}}{r_{\mathrm{cyl\,max}}}\right) + \frac{\pi}{2} \le \phi < \pi & r_{\mathrm{sph}} = \frac{z_{\mathrm{cyl\,max}}}{\cos(\phi-\pi)} & \frac{\partial c_{\mathrm{A}}}{\partial r_{\mathrm{sph}}} = \; 0
\end{array}
$$

For chronoamperometry the applied potential is stepped from a value at which no reaction occurs (E_{initial}) to one in with mass transport is effectively diffusion controlled (E_{final}):

$t < t_{\mathrm{start}} \quad E = E_{\mathrm{initial}}$

$t \ge t_{\mathrm{start}} \quad E = E_{\mathrm{final}}$

For cyclic voltammetry, the applied potential, E, varies as a function of time, t, according to:

$$E = |-vt + E_{\mathrm{start}} - E_{\mathrm{vertex}}| + E_{\mathrm{vertex}} \tag{4.2.6}$$

where E_{start} and E_{vertex} are the starting and vertex potentials respectively.

4.2.3 Surface coverage

The nanoparticle surface coverage, Θ, is defined as the fraction of the substrate electrode obscured in a top-down view of the array. That is:

$$\Theta = \frac{N\pi r_{\mathrm{np}}^{2}}{A} \tag{4.2.7}$$

where N is the number of nanoparticles in the array and A is the area of the substrate electrode. The nanoparticle surface coverage, Θ, varies as a function of the mean diffusion domain radius, $\langle r_{\mathrm{d}} \rangle$:[11]

$$\Theta = \frac{\int_0^{r_{\mathrm{np}}} \mathrm{f}\left(\frac{r_{\mathrm{d}}}{\langle r_{\mathrm{d}} \rangle}\right) r_{\mathrm{d}}^2 \mathrm{d}r_{\mathrm{d}} + \int_{r_{\mathrm{np}}}^{\infty} \mathrm{f}\left(\frac{r_{\mathrm{d}}}{\langle r_{\mathrm{d}} \rangle}\right) \mathrm{d}r_{\mathrm{d}}}{\int_0^{\infty} \mathrm{f}\left(\frac{r_{\mathrm{d}}}{\langle r_{\mathrm{d}} \rangle}\right) r_{\mathrm{d}}^2 \mathrm{d}r_{\mathrm{d}}} \tag{4.2.8}$$

Data for this function are included on the attached CD
(file entitled "chapter_4_supplementry_info.xls"). When Θ is small, the mean nanoparticle separation is large and the equation for the nanoparticle surface coverage is considerably simplified:

$$\Theta = \frac{r_{\mathrm{np}}^2}{r_{\mathrm{d}}^2} \tag{4.2.9}$$

In order for this equation to exhibit < 0.1 % accuracy, the nanoparticle surface coverage must be less than 0.12.

4.2.4 Numerical simulation

The problem is generalised by means of a transformation into a conventional set of normalised parameters (defined in the glossary). The problem is solved numerically using the Alternating Direction Implicit (ADI) variant of the finite difference method.[21] The differential equations are discretised using a standard 3 point finite difference scheme. As discussed in Section 4.2.2, the problem is most easily formulated in either spherical or cylindrical coordinates. Spatial mesh density must be higher in regions where the concentration changes rapidly. In the problem considered, mesh density must be highest at the surface of the nanoparticle.[22] In addition,

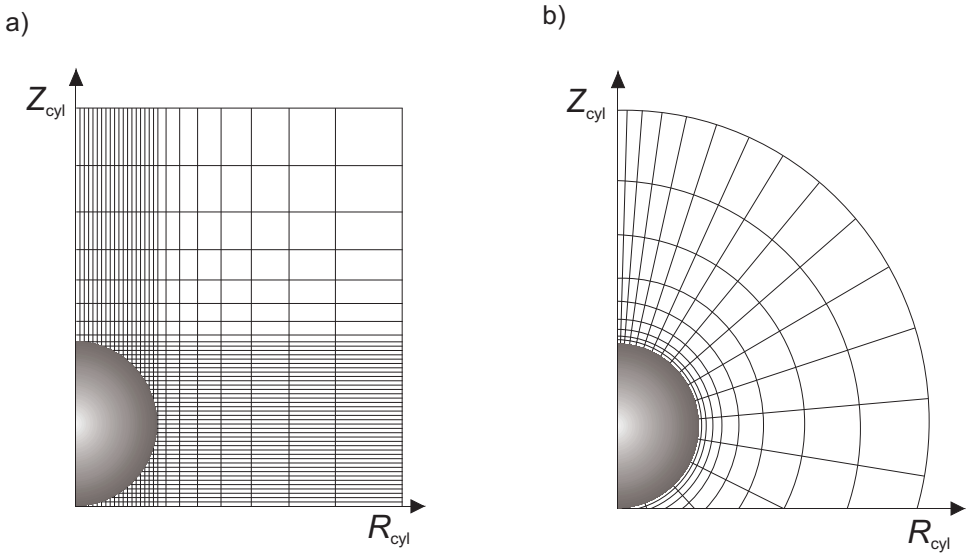

Figure 4.2.6:
Discretised spatial grid used in the numerical simulations.

there should be high mesh density adjacent to the $Z_{\rm cyl}$ axis in order to prevent the no-flux boundary condition extending too far into the solution when the equations are discretised. The requisite spatial mesh for cylindrical and spherical coordinates are shown in Figure 4.2.6(a) and Figure 4.2.6(b) respectively. Given that simulation times increase with the number of node on the spatial mesh, a system of spherical coordinates will yield the most efficient simulations. The problem considered here is solved in terms of spherical coordinates. The spatial mesh was discretised as follows:

$$R_{\rm sph,j=0} = 1 \tag{4.2.10}$$

$$R_{\rm sph,j=1} = 1 + (5 \times 10^{-5}) \tag{4.2.11}$$

$$R_{\rm sph,j+1} = R_{\rm sph,j} + 1.15(R_{\rm sph,j} - 1) \tag{4.2.12}$$

$$\phi_{\mathrm{sph,i=0}} = 0 \tag{4.2.13}$$

$$\phi_{\mathrm{sph,i=max}} = \pi \tag{4.2.14}$$

$$\phi_{\mathrm{sph,i+1}} = 0.025\left(\frac{\phi_i}{\pi}\right) + 1 \times 10^{-4}\left(\frac{\pi - \phi_i}{\pi}\right) \tag{4.2.15}$$

For chronoamperometry, the temporal mesh was discretised as follows:

$\tau_{\mathrm{k}} = k(10^{-12})$ $\qquad k = 1, 2, 3..., 98, 99, 100$

$\tau_{\mathrm{k+1}} = \tau_{\mathrm{k}}(1.01)$ $\qquad k = 100, 101, 102, ...,$

For cyclic voltammetry, the temporal mesh was discretised as follows:

$\tau_{\mathrm{k=0}} = 0$

$\tau_{\mathrm{k+1}} = \tau_{\mathrm{k}} + \frac{1}{200\sigma}$

The programs were written in C++ and compiled using a Borland compiler. Simulations were run on a quad core desktop PC with 3.25 GB of RAM and processor speeds of 2.83 GHz. The simulations were converged to an accuracy of 0.5 % relative to the analytical expression for the steady state current:[23]

$$i_{\mathrm{ss}} = 4\pi \ln(2) n c_{\mathrm{A}} D_{\mathrm{A}} r_{\mathrm{np}} F \tag{4.2.16}$$

4.3 Theoretical results and discussion

4.3.1 Chronoamperometry

Figure 4.3.1 shows chronoamperograms ($\tau = 10^{-6}$—10^{6}) as a function of the mean diffusion domain radius, $\langle R_{\mathrm{d}} \rangle$. At short times, the diffuse layer is small and diffusion

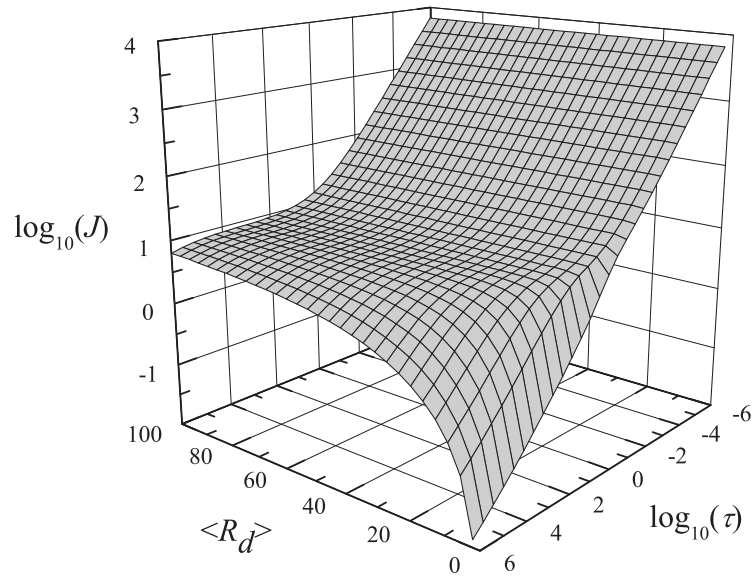

Figure 4.3.1: *Chronoamperograms as a function of mean diffusion domain radius* $\langle R_\mathrm{d} \rangle$

is 1 dimensional and linear (category 1). The gradient between $\log_{10}(J)$ and $\log_{10}(\tau)$ in this region is equal to the Cottrellian value of -0.5. At longer times, the diffusion layer is more hemispherical and a steady-state current is attained (category 2). The steady-state current is equal to the theoretical value:[23]

$$J_\mathrm{ss} = 4\pi \ln(2) \tag{4.3.1}$$

Over longer timescales, the current decreases from the steady-state value (category 3) due to diffusion layer overlap and the gradient between $\log_{10}(J)$ and $\log_{10}(\tau)$ tends towards -0.5 (category 4). The timescale over which each of the categories occur changes as a function of the mean diffusion domain radius, $\langle R_\mathrm{d} \rangle$. The diffusion layer for Category 1 is confined to the region close to each nanoparticle and is therefore approximately invariant to $\langle R_\mathrm{d} \rangle$. As $\langle R_\mathrm{d} \rangle$ increases, the timescale over which category 3 behaviour occurs becomes larger. It takes correspondingly longer to attain the limit of category 4 behaviour. At very small values of $\langle R_\mathrm{d} \rangle$, the

timescale over which cases 2 and 3 occur is vanishingly small and a Cottrellian response is observed at all times. This behaviour corresponds to a macroelectrode in which the entire area is electroactive.

In some applications or especially in fundamental studies, it is desirable for the array to exhibit only category 1 and 2 behaviour. Since the nanoparticles are diffusionally isolated, the current drawn at each nanoparticle is maximised. It is therefore of interest to devise a semi-empirical expression, $g(\tau)$, which is accurate over all times simulated. Following Shoup *et al*[24] we consider a function of the form:

$$g(\tau) = 8.67\left(A + \frac{B}{\sqrt{\tau}} + (1-A)\exp\left(\frac{-C}{\sqrt{\tau}}\right)\right) \tag{4.3.2}$$

This function possess the correct limiting behaviour since:

$\tau \to 0$ $\qquad g(\tau) = 8.67\left(\frac{B}{\sqrt{\tau}}\right)$

$\tau \to \infty$ $\qquad g(\tau) = 8.67$

Over very short times (category 1) the exact analytical solution is:

$$g(\tau) = \sqrt{\frac{2\pi}{\tau}} \tag{4.3.3}$$

Therefore, $B = 0.29$. We now choose A and C such that the equation is valid over the remainder of the transient. The transient was fitted using the a non-linear curve fitting function in the software package Origin 7.0 (Microcal Software Inc.). In this way it was found that:

$A = 0.958$

$B = 0.29$

$C = 0.9$

therefore:

$$g(\tau) = 8.67\left(0.958 + \frac{0.29}{\sqrt{\tau}} + 0.042\exp\left(\frac{-0.9}{\sqrt{\tau}}\right)\right) \tag{4.3.4}$$

This expression exhibits maximum error of 0.09 % relative to the simulations over the range $10^{-6} < \tau < 10^{6}$. Since the simulations themselves are accurate to 0.5 %, the expression exhibits maximum error of 0.6 % over the range $10^{-6} < \tau < 10^{6}$ relative to the true transient: well within typical experimental accuracy. In this sense, it may be regarded as a *de facto* solution of the problem. In dimensional form, Eqn 4.3.4 is:

$$i = 8.67nc_{\mathrm{A}}^{*}D_{\mathrm{A}}r_{\mathrm{np}}F\left(0.958 + \frac{0.29}{\sqrt{\frac{tD_{\mathrm{A}}}{r_{\mathrm{np}}^{2}}}} + 0.042\exp\left(\frac{-0.9}{\sqrt{\frac{tD_{\mathrm{A}}}{r_{\mathrm{np}}^{2}}}}\right)\right) \tag{4.3.5}$$

4.3.2 Cyclic voltammetry

Cyclic voltammograms were characterised by the dimensionless peak-to-peak separation (θ_{pp}) and the dimensionless peak current obtained during the forward sweep (J_{peak}). Figure 4.3.2 shows $\log_{10}(J_{\mathrm{peak}})$ as a function of $\langle R_{\mathrm{d}}\rangle$ and $\log_{10}(\sigma)$ in the reversible ($K^{0} = 10^{3}$) and irreversible ($K^{0} = 10^{-2}$) limits. In each case, in the Category 1 region, the gradient between $\log_{10}(J_{\mathrm{peak}})$ and $\log_{10}(\sigma)$ is equal to $\frac{1}{2}$ and is consistent with the respective Randles-Ševčík equations. At high values of $\langle R_{\mathrm{d}}\rangle$

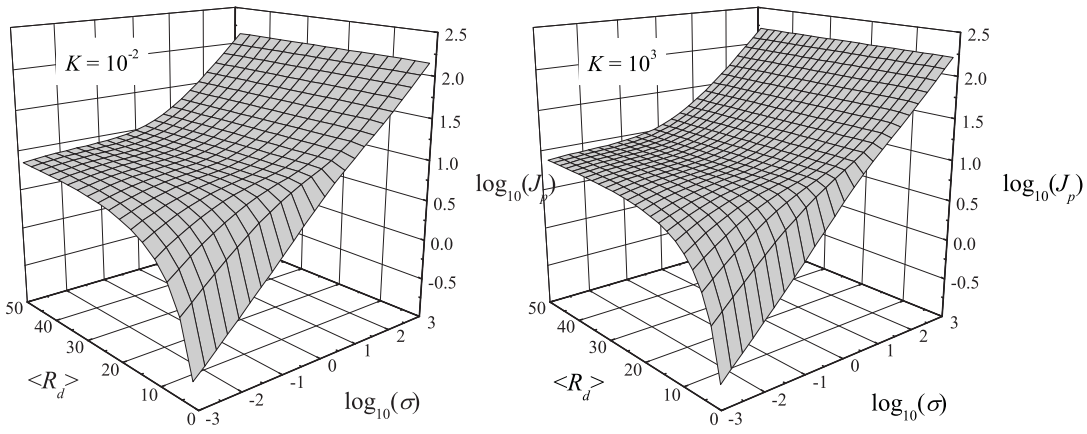

Figure 4.3.2:
$\log_{10}(J_{\text{peak}})$ *as a function of* $\langle R_{\text{d}} \rangle$ *and* $\log_{10}(\sigma)$ *in the reversible* ($K = 10^3$) *and irreversible* ($K = 10^{-2}$) *limits.*

and low scan-rates (Category 2), a near constant flux occurs. This is consistent with mass transport under steady-state conditions. As $\langle R_{\text{d}} \rangle$ is decreased from 50 to less than 10, J_{peak} drops steeply at low scan-rates; corresponding to depletion of electroactive material caused by overlapping depletion layers (categories 3 and 4). Figure 4.3.3 shows the analogous plot to Figure 4.3.2 in terms of the dimensionless

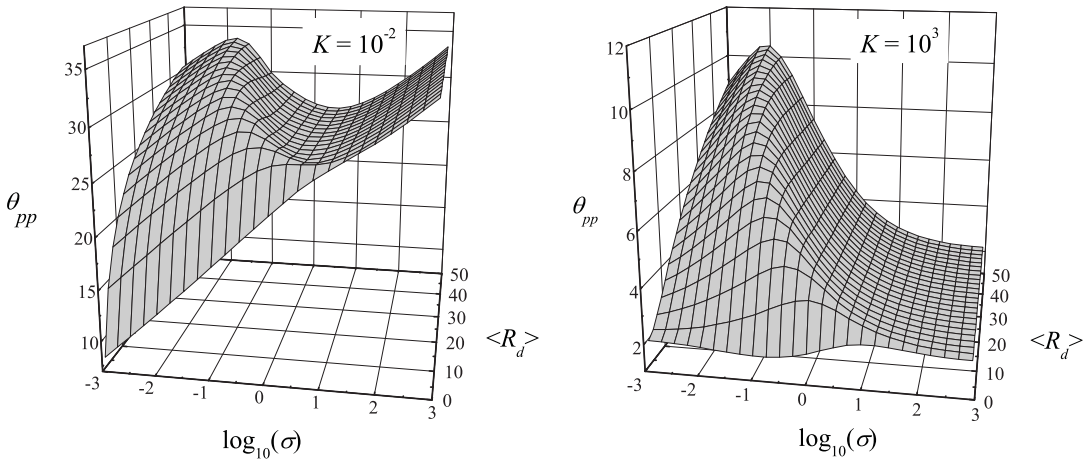

Figure 4.3.3:
θ_{pp} *as a function of* $\langle R_{\text{d}} \rangle$ *and* $\log_{10}(\sigma)$ *in the reversible* ($K = 10^3$) *and irreversible* ($K = 10^{-2}$) *limits.*

peak-to-peak separation (θ_{pp}). For the reversible limit, in the Category 1 region, the

peak to peak separation is characteristic of the electrochemically reversible limit at a planar surface[25] ($\approx$ 59 mV at 298 K). This limit is also approached at low $\langle R_{\rm d} \rangle$) values over all scan-rates, corresponding to linear diffusion in the Category 4 region. At intermediate scan-rates and $R_{\rm d}$ values, the operation of Category 2 and 3 are revealed by much larger peak to peak separations consistent with voltammograms close to steady-state. For the irreversible limit, analogous trends are observed except that in categories 1 and 4, when diffusion is linear, $\theta_{\rm pp}$ increases with scan rate. Figure

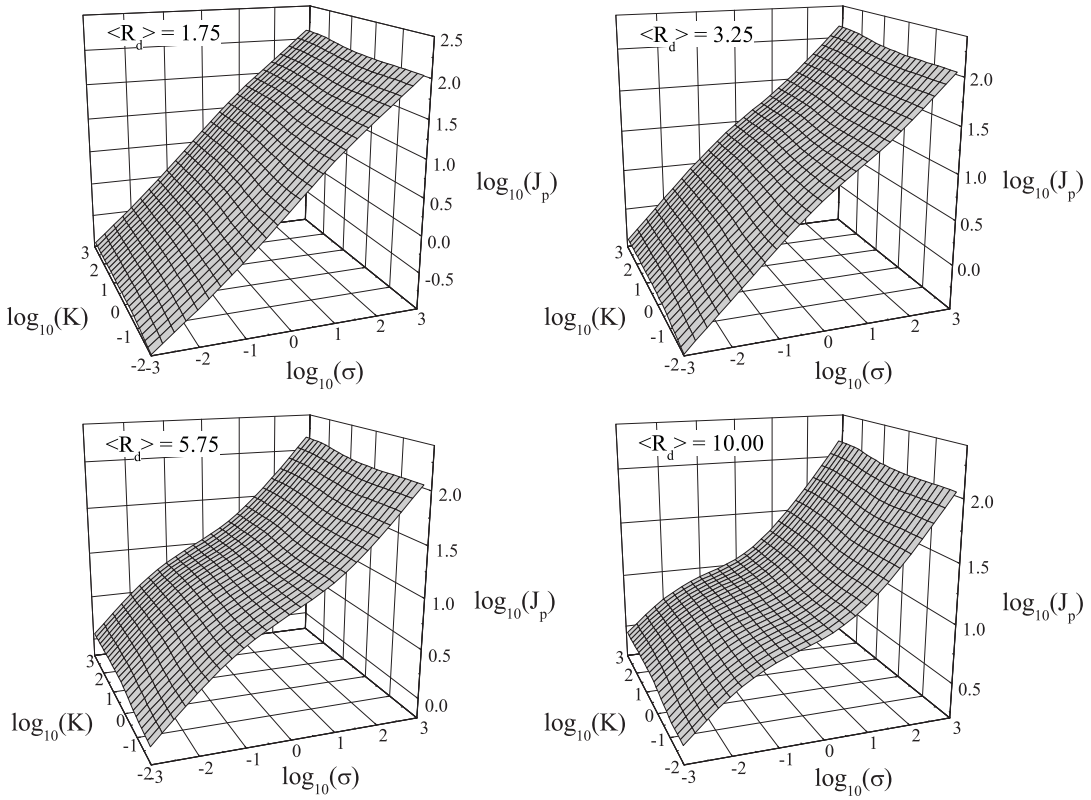

Figure 4.3.4:
$\log_{10}(J_{\rm peak})$ *as a function of* $\log_{10}(K)$ *and* $\log_{10}(\sigma)$ *for various values of* $\langle R_{\rm d} \rangle$.

4.3.4 shows $\log_{10}(J_{\rm peak})$ as a function of $\log_{10}(K)$ and $\log_{10}(\sigma)$ for various diffusion domain radii ($\langle R_{\rm d} \rangle$). In each case, $\log_{10}(J_{\rm peak})$ increases marginally with $\log_{10}(K)$ at constant $\log_{10}(\sigma)$. This corresponds to the transition from irreversible to reversible

electrode kinetics. At very high scan-rates (Category 1) and very low scan-rates (Category 4) diffusion is linear and the gradient between $\log_{10}(J_{\text{peak}})$ and $\log_{10}(\sigma)$ is equal to $\frac{1}{2}$. This is consistent with the semi-empirical Randles-Ševčík equations for linear diffusion in the reversible and irreversible limits. At intermediate scan-rates, $\log_{10}(J_{\text{p}})$ is less sensitive to $\log_{10}(\sigma)$ and corresponds to voltammetry close to steady-state. The lowest scan-rate at which this approximate 'plateau' region occurs decreases with decreasing $\langle R_{\text{d}} \rangle$) owing to diffusion zone overlap (Category 3). Figure 4.3.5 shows the analogous plot to Figure 4.3.4 in terms of the normalised

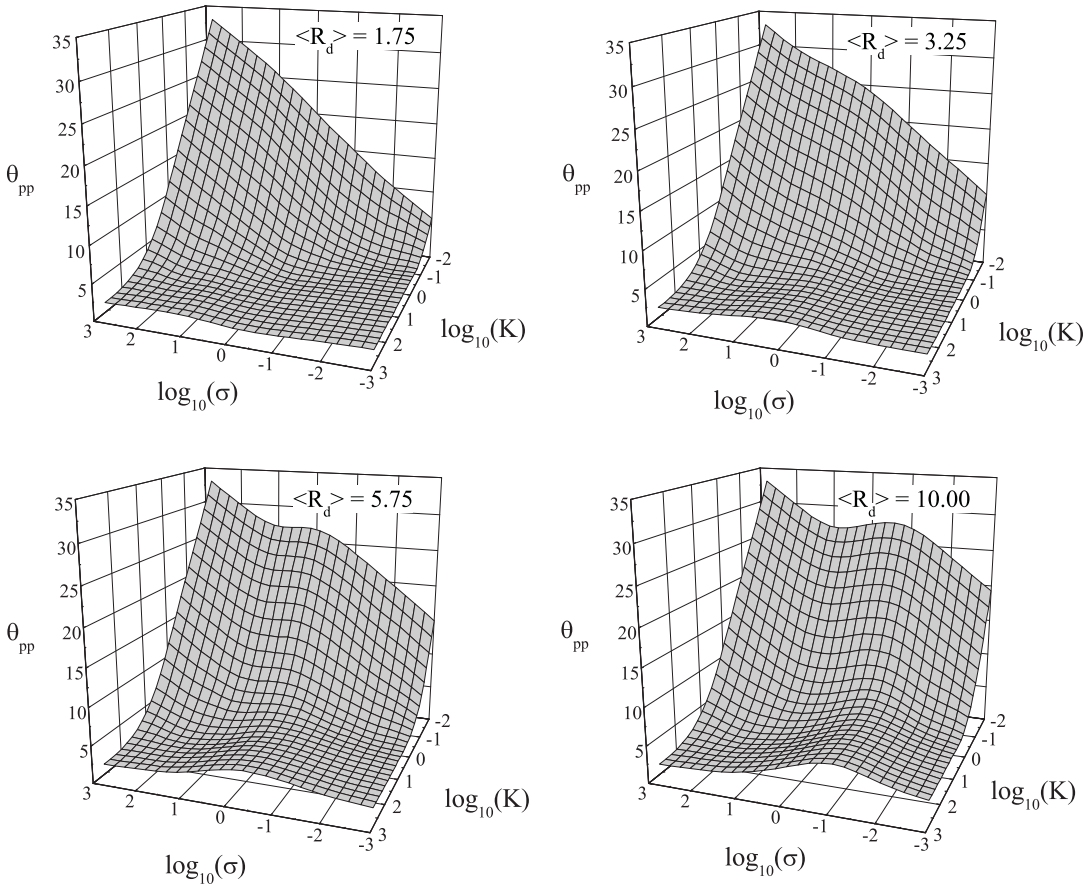

Figure 4.3.5:
θ_{pp} as a function of $\log_{10}(K)$ *and* $\log_{10}(\sigma)$ *for various values of* $\langle R_{\text{d}} \rangle$.

peak to peak separation (θ_{pp}). For very high scan rates (Category 1) and very

low scan rates (Category 4), in the irreversible limit (low K), $\theta_{\rm pp}$ scales linearly with $\log_{10}(K)$: consistent with cyclic voltammetric theory.[25] In the reversible limit, $\theta_{\rm pp} \approx 2.4$; consistent with cyclic voltammetric theory[25] and corresponds to ≈ 59 mV at 298 K. At intermediate scan-rates, $\theta_{\rm pp}$ is larger and corresponds to voltammograms close to steady-state. The timescale over which this region occurs decreases with increasing surface coverage owing to diffusion zone overlap (Case 3). Figures

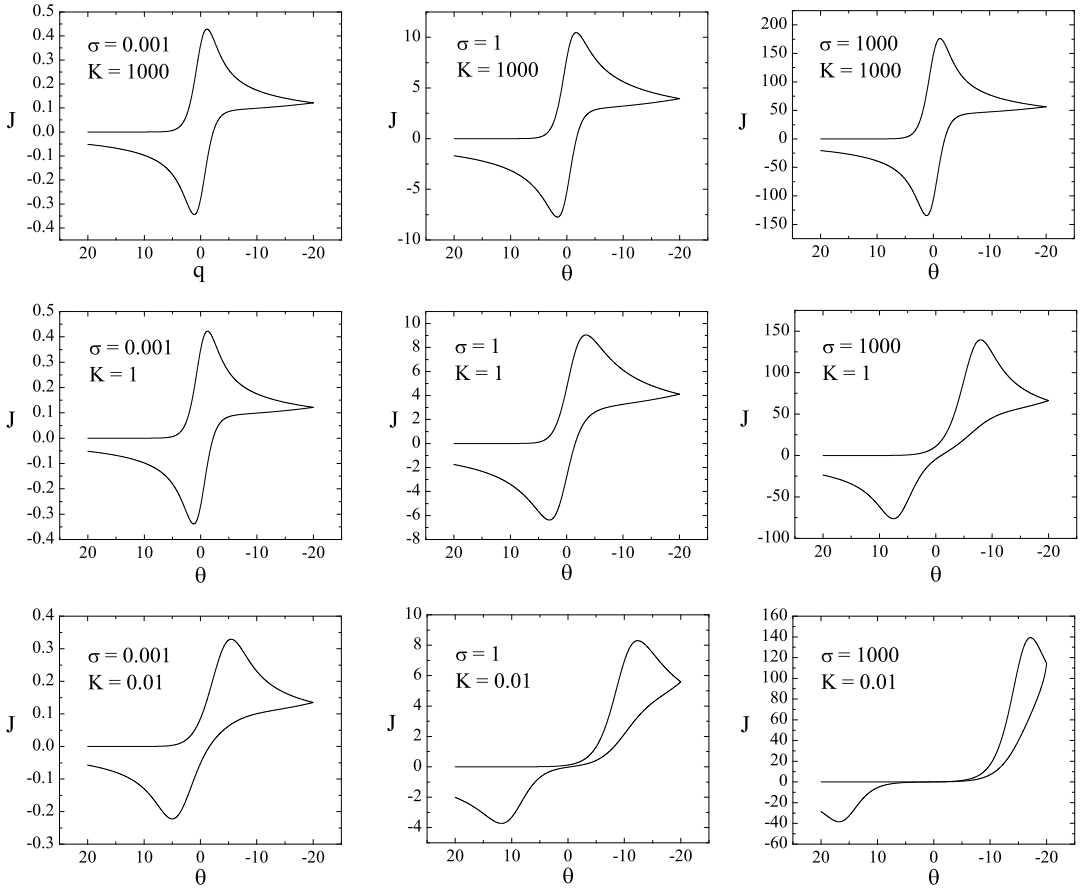

Figure 4.3.6:
Cyclic Voltammograms for various parameters for which $R_{\rm d} = 3.25$ *and* $\Theta = 0.0947$.

4.3.6 and 4.3.7 show cyclic voltammograms for various parameters when $\langle R_{\rm d} \rangle = 3.25$ and $\langle R_{\rm d} \rangle = 10.00$. These diffusion domain sizes correspond approximately to fractional surface coverages of 0.1 and 0.01 respectively. In each case, when $\sigma = 1000$,

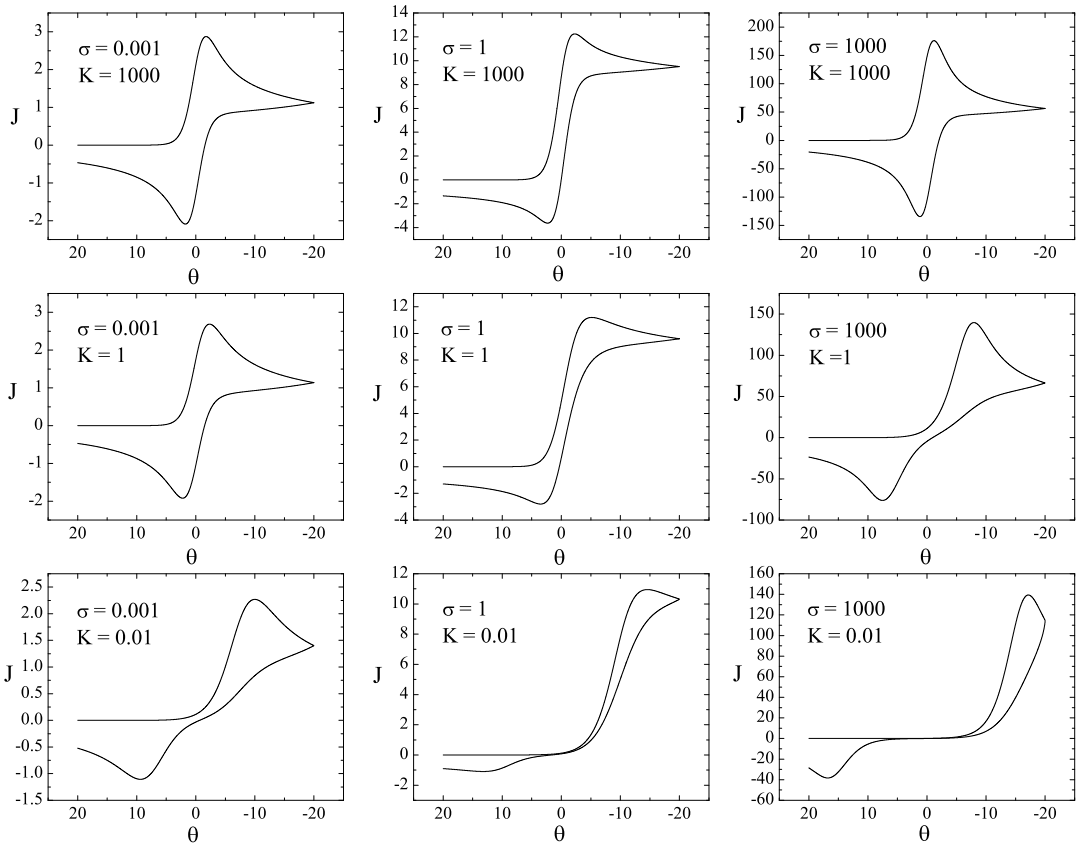

Figure 4.3.7:
Cyclic Voltammograms for various parameters for which $R_{\mathrm{d}} = 10.00$ *and* $\Theta = 0.01$.

diffusion lies within the Category 1 region. Consequently, the voltammetric shape is unchanged between the two $\langle R_{\mathrm{d}} \rangle$ values. When $\sigma = 1$ and $\langle R_{\mathrm{d}} \rangle = 10.00$, diffusion is close to the case 2 region and the voltammetry is approximately steady-state. In contrast, when $\langle R_{\mathrm{d}} \rangle = 3.25$ diffusion layers overlap and Category 3/4 four behaviour is observed. When $\sigma = 0.001$, diffusion lies within the Category 4 region for both $\langle R_{\mathrm{d}} \rangle$ values. Mass transport is slower when $\langle R_{\mathrm{d}} \rangle = 3.25$ due to each nanoparticle being replenished by a smaller area of bulk solution leading to two consequences. First the current for $\langle R_{\mathrm{d}} \rangle = 3.25$ is smaller than for $\langle R_{\mathrm{d}} \rangle = 10.00$; second, when $K = 0.01$, the waveshape for $\langle R_{\mathrm{d}} \rangle = 10.00$ is more electrochemically reversible than for $\langle R_{\mathrm{d}} \rangle = 3.25$.

4.3.3 Comparison between spheres and discs

A paper by Belding *et al*[26] considered diffusional cyclic voltammetry at a random array of nanoparticles in which the latter were assumed to be inlaid discs. Here we compare the voltammetry for a random array of spheres with one of inlaid discs of the same radius and surface coverage. We consider two different diffusion domain radii, $\langle R_{\mathrm{d}} \rangle = 3.25$ and $\langle R_{\mathrm{d}} \rangle = 10.00$. These diffusion domain radii correspond to surface coverages, Θ, of 0.0947 and 0.01 respectively. These are considered to be experimentally realistic nanoparticle coverages. Figure 4.3.8 shows a comparison

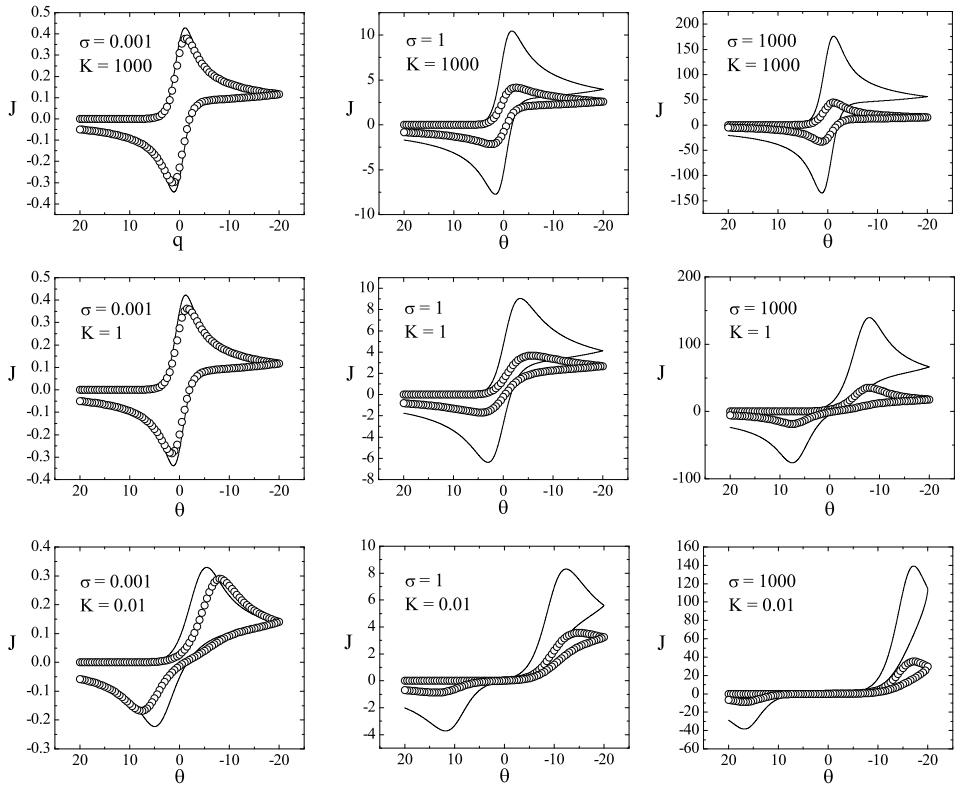

Figure 4.3.8:
Cyclic voltammograms for a random array of discs (◯) and spheres (—). $\langle R_{\mathrm{d}} \rangle = 3.25$ *and* $\Theta = 0.0947$.

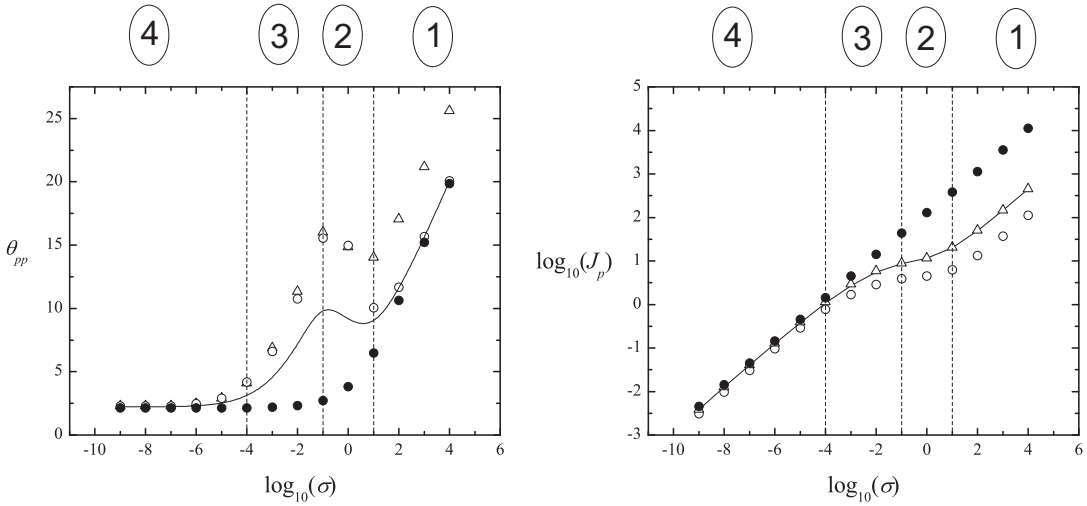

Figure 4.3.9:
Peak to peak separations ($\theta_{\rm pp}$) and peak currents ($J_{\rm p}$) as a function of $\log_{10}(\sigma)$ *for spheres (—) and disks (◯) for which* $K = 1$ *and* $\langle R_{\rm d}\rangle = 10.00$. *In addition, data is shown for spheres for which* $K = 0.25$ *and* $\langle R_{\rm d}\rangle = 10.00$ *(△) and for disks for which* $K = 1$ *and the surface is fully active (•). The diffusional categories are assigned as shown.*

between the cyclic voltammograms for spheres and discs for which $\langle R_{\rm d}\rangle = 3.25$ ($\Theta = 0.0947$). The cyclic voltammograms are shown over a range of σ and K. Figure 4.3.9 plots $\theta_{\rm pp}$ and $\log(J_{\rm p})$ as a function of $\log(\sigma)$ for which $K = 1$ and $\langle R_{\rm d}\rangle = 10$ ($\Theta = 0.01$). A large range of σ values are considered in the latter figure in order to attain experimental timescales appropriate to observe categories 1–4 (as shown). In addition, the limits of electrochemical reversibility and irreversibility are accessible. When σ is large, Category 1 behaviour occurs. The diffusion layer is confined to each diffusion domain and, since diffusion is linear, the current is directly proportional to the surface area of the nanoparticle. The surface area of a sphere ($= 4\pi r^2$) is 4 times that of a disk ($= \pi r^2$). Therefore, at all applied potentials, the current for an array of spheres is 4 times that for an array discs of the same surface coverage. Since the mass transport and electrode kinetics for these processes are identical, the peak to peak separations are equal. In addition, the voltammetric features for the disks are

identical to those for a fully active planar electrode. In the Category 2 region, J_{p} is approximately invariant with σ owing to convergent diffusion. The θ_{pp} values are very large and correspond to voltammograms close to steady-state. In this region, the peak currents are equal to the appropriate (dimensionless) equations for mass transport limited steady-state diffusion towards spheres and disks (Eqns 4.3.6 and 4.3.7 respectively).

$$J_{\mathrm{ss}} = 4\pi \ln(2) \tag{4.3.6}$$

$$J_{\mathrm{ss}} = 4 \tag{4.3.7}$$

It follows that the ratio of peak currents, $J_{\mathrm{p(sphere)}}/J_{\mathrm{p(disk)}}$, is equal to $\pi \ln(2)$ in this region. In addition, it is clear from Figure 4.3.9 that the timescale over which spheres exhibit Category 2 behaviour is shorter than for disks. This is because, at short times, the spheres draw a much larger current compared to the disks. Spheres attain Category 3 behaviour over a shorter timescale than do disks. For irreversible electrode kinetics in the Category 4 region, $\log(J_{\mathrm{p}})$ and θ_{pp} each vary directly with $\log(\sigma)$ in accordance with voltammetric theory. It is clear, from Figures 4.3.8 and 4.3.9, that, in the Category 3/4 region, spherical nanoparticles appear to give rise to more reversible electrochemical responses compared to disks. In the limit of electrochemical irreversibility, the flux through the electrode is much slower than the rate of diffusion of material over the electrode surface: the flux over the surface of each nanoparticle is uniform. It follows that, for a given surface coverage, in the

Category 3/4 region:

$$J_{\text{array}} = \frac{(\text{np surface area})}{(\text{disk area})} J_{\text{array disks}} \tag{4.3.8}$$

Since diffusion is linear, the array behaves like an array of disks with an apparent rate constant, K_{apparent}, which is affected by the surface area, and hence morphology, of the nanoparticles:

$$K_{\text{apparent}} = \frac{(\text{np surface area})}{(\text{disk area})} K \tag{4.3.9}$$

Amatore *et al*[27] have shown that, for flat disks, the apparent rate constant varies with surface coverage. The theory proposed here is based on morphological effects at a constant surface coverage. In Figure 4.3.9, the comparison between spheres and discs is performed for equal surface coverages. However, the surface area of a sphere is four times that for a disc. This behavior corresponds to a situation in which K for a sphere appears 4 times larger than for a disk (leading to a larger peak-to-peak separation but approximately the same peak current). This is confirmed in Figure 4.3.9 where there is concordance between disks ($K = 1$) and spheres ($K = 0.25$) of the same surface coverage. The trends discussed above in terms of Figure 4.3.9 are equally applicable to Figure 4.3.10 which shows data plotted for $K = 0.01$ at two different surface coverages. Figure 4.3.11 shows shows $J_{p(sphere)}/J_{p(disc)}$ as a function of $\log_{10}(K)$ and $\log_{10}(\sigma)$. At very high scan-rates (Category 1), diffusion is linear in each case and $J_{p(sphere)}/J_{p(disc)} = 4$ (owing to their respective surface areas). At very low scan-rates (Category 4) diffusion is linear over the entire array and the peak currents are equal. At between these limits, the value of $J_{p(sphere)}/J_{p(disc)}$ is

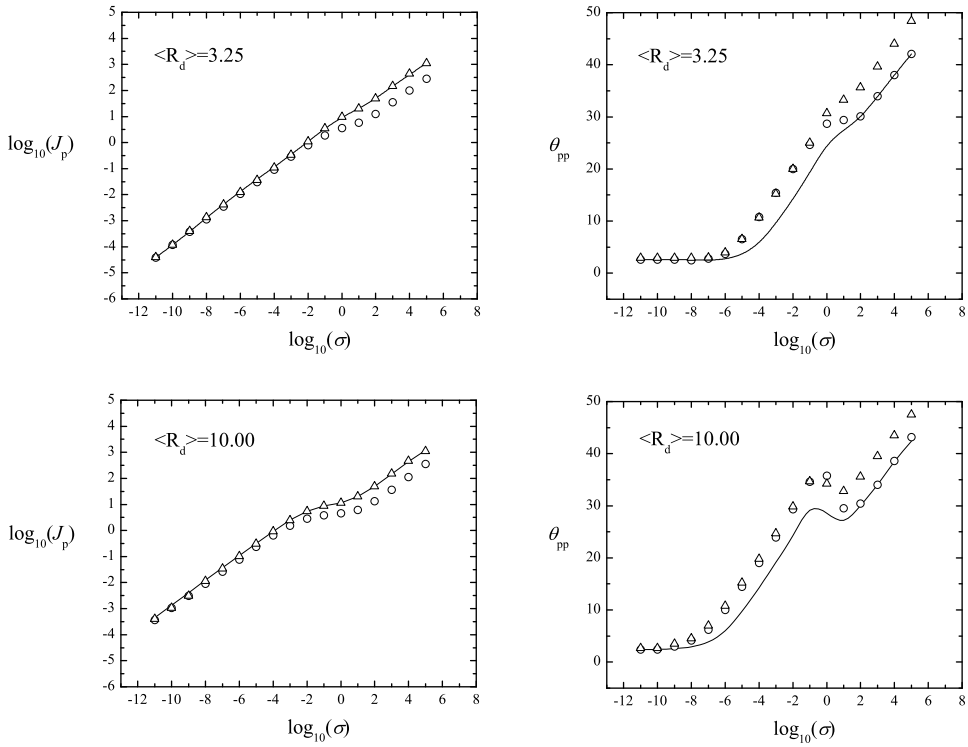

Figure 4.3.10:
Peak to peak separations ($\theta_{\rm pp}$) and peak currents ($J_{\rm p}$) as a function of $\log_{10}(\sigma)$ *for spheres (—) and disks (◯) for which* $K = 0.01$. *In addition, data is shown for spheres for which* $K = 0.0025$ *(⋀). Data is shown for* $\langle R_{\rm d}\rangle = 3.25$ *and* $\langle R_{\rm d}\rangle = 10.00$.

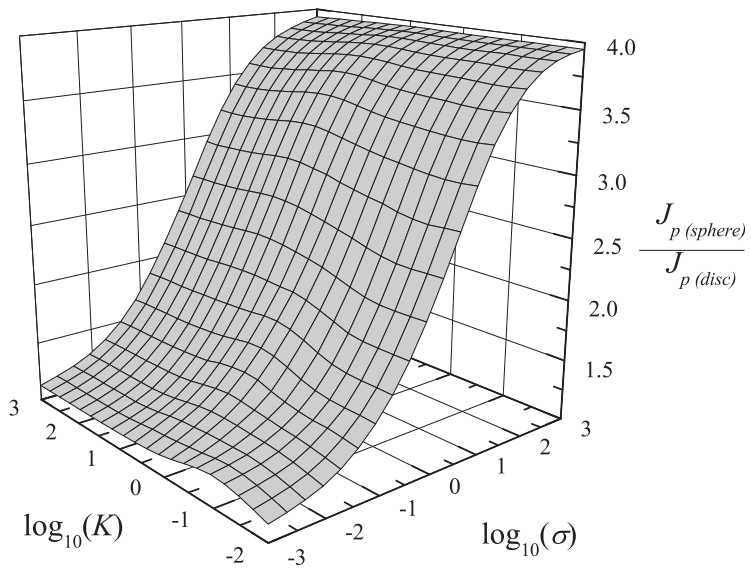

Figure 4.3.11:
The ratio of peak currents $J_{p(sphere)}/J_{p(disc)}$ *as a function of* $\log_{10} K$ *and* $\log_{10}\sigma$. *Data is shown for* $\langle R_{\rm d}\rangle = 3.25$.

intermediate. Figure 4.3.12(a) shows $\frac{\theta_{pp(sphere)}-\theta_{pp(disc)}}{\theta_{pp(sphere)}}$ as a function of $\log_{10}(K)$ and

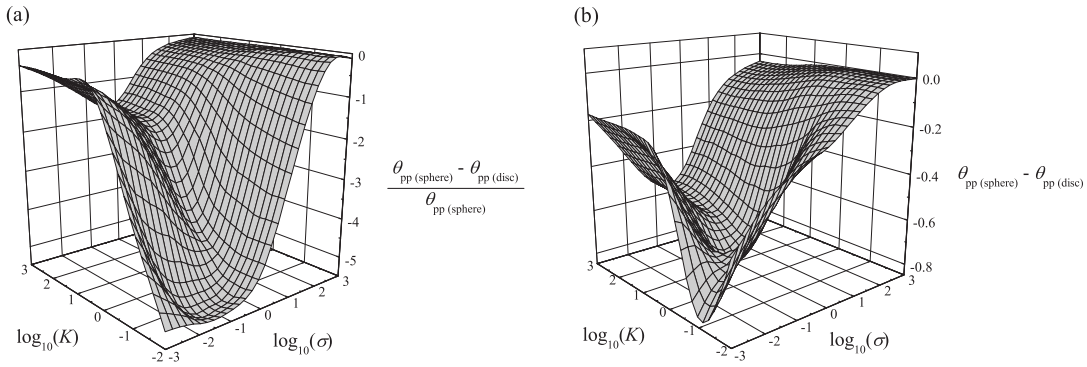

Figure 4.3.12:
(a) The relative difference in the peak potentials $\frac{\theta_{pp(sphere)}-\theta_{pp(disc)}}{\theta_{pp(sphere)}}$ *as a function of* $\log_{10} K$ *and* $\log_{10}\sigma$*. Data is shown for* $\langle R_{\rm d}\rangle = 3.25$*.(b) The difference in the peak potentials* $\theta_{pp(sphere)} - \theta_{pp(disc)}$ *as a function of* $\log_{10} K$ *and* $\log_{10}\sigma$*.*

$\log_{10}(\sigma)$. At very high scan-rates (Category 1), diffusion is linear in each case and the peak-to-peak separation for spheres and discs equal to 2.4 (corresponding to 59 mV at 298 K)). Owing to their larger surface area, spheres possess a larger diffusion layer at a given time. Therefore, during Category 3, the extent of diffusion layer overlap is greater for spheres than for discs. Hence, in Category 3, spheres appear more reversible compared to discs and have a smaller peak-to-peak separation. At very low scan-rates (Category 4) diffusion is linear over the entire array. As discussed above, disks appear more irreversible compared to spheres. For low K and low σ the difference $\theta_{pp(sphere)} - \theta_{pp(disc)}$ is constant and therefore the value of $\frac{\theta_{pp(sphere)}-\theta_{pp(disc)}}{\theta_{pp(sphere)}}$ decreases with decreasing K due to increasing $\theta_{pp(sphere)}$. Figure 4.3.12(b) shows a similar plot with $\theta_{pp(sphere)} - \theta_{pp(disc)}$ as a function of $\log_{10}(K)$ and $\log_{10}(\sigma)$.

4.4 Experimental results and discussion

The experiments in this section were conducted by Dr. Fallyn W. Campbell and Ms. Yige Zhou. The detailed experimental method is described in Appendix A. Silver

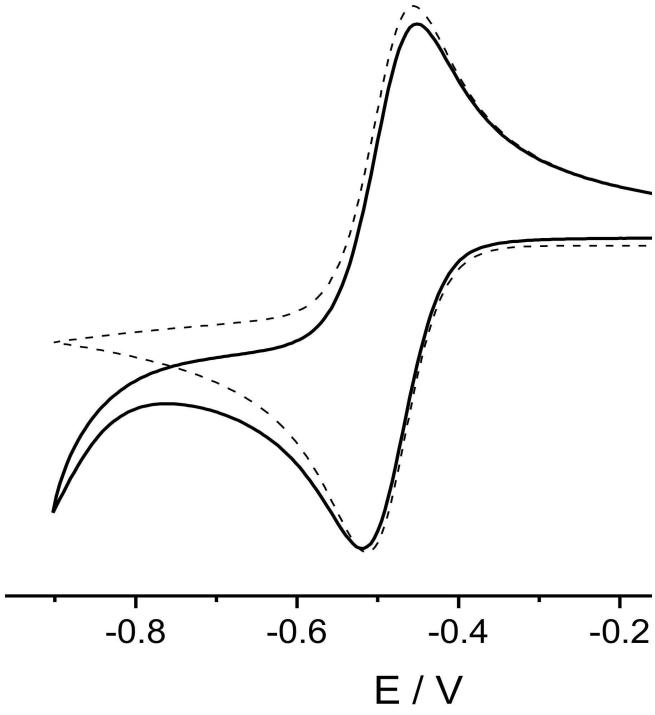

Figure 4.4.1: *Silver macro-disk voltammetry in 1 M $NaClO_4$ + 10 mM Cr^3+. Scan rate:* 50 mV s^{-1}. *Solid line: experiment; dashed line:* DIGISIM *simulation.*

electrodes are known to display electrocatalytic activity towards the reduction of chromium species in solution, displaying a distinct reversible redox wave.[12] When we compare the macro-disk behaviour to a AgNP-modified BPPG electrode, we see some distinct differences in the nature of the voltammetry. We first consider figure 4.4.1, which shows the voltammetry of 10 mM Cr^{3+} in a 1 M $NaClO_4$ electrolyte solution at a 5 mm diameter silver macro-disk electrode ($E_{p,c} = -0.581$ V and

Parameter	Value
E_f^0 (V) vs. SCE	-0.485
D ($m^2\ s^{-1}$)	1.6×10^{-10}
k^0 ($m\ s^{-1}$)	1.0×10^{-3}
α	0.5

Table 4.2: *Silver macro-disk fitting parameters.*

$E_{p,a} = -0.451$ V (*vs.* SCE)).

Variable scan rate experiments showed a linear plot of current *vs.* square root of the scan rate ($\sqrt{v}$), implying a diffusion-controlled process. By applying the Randles-Sevčik equation,[28] an experimentally measured diffusion coefficient of 1.5×10^{-10} $m^2\ s^{-1}$ was extracted. Using DIGISIM we were able to model the redox behaviour at the silver macro-disk as shown in figure 4.4.1. This allowed us to determine the kinetic parameters for this process based on the on electron reduction of Cr^{3+} to Cr^{2+} ($Cr^{3+} + e^- \leftrightharpoons Cr^{2+}$). In a solution of 1 M $NaClO_4$, the kinetic parameters were optimized as shown in table 4.2.

The next step was to examine the behaviour of a AgNP-modified BPPG electrode towards the reduction of Cr^{3+} in $NaClO_4$ electrolyte solution. Figure 4.4.2 shows the experimentally obtained voltammetry for several AgNP-modified BPPG electrodes, with varying NP densities, towards the reduction of Cr^{3+}. The voltammetry displays a clear relationship between degree of surface coverage and the voltammetric wave shape. The recorded current increases as we increase the active surface area of silver on the electrode. we also observe an increase in the apparent reversibility of the system with increasing NP coverage as the oxidation peak becomes more well-

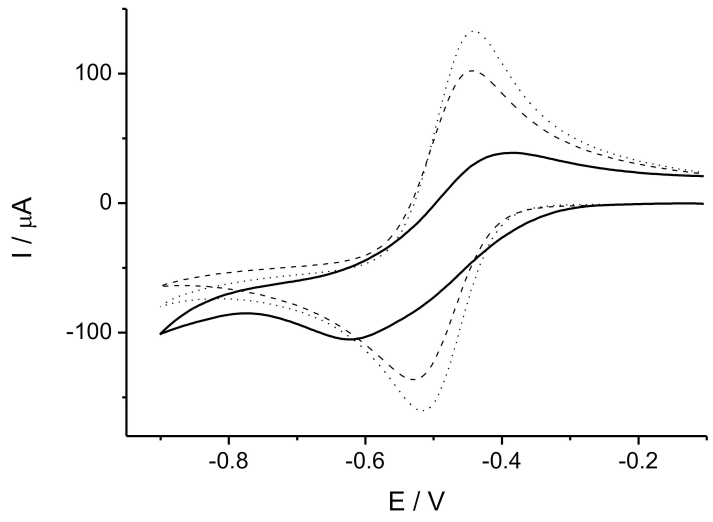

Figure 4.4.2: *the experimentally obtained voltammetry for several AgNP-modified BPPG electrodes, with varying NP densities, towards the reduction of* Cr^{3+}.

defined and peak-to-peak separation decreases. Furthermore, we also report a small positive shift in reduction potential (∼0.15 V from 0.3% to 10.2%) as previously reported in the literature, for the reduction of hydrogen peroxide,[19] protons[12] and 4-nitrophenol[29] at AgNP arrays. This occurs at least in part due to the change in diffusion regime experienced at the NP-array as we increase the surface coverage from 0.3% to 10.2%.

This experimental data in the range of 0.3-10.2% nanoparticle coverage, was then first approximately fitted using DIGISIM™ . This fitting approximates the mass-transport to the array as linear. The data was fitted by varying the values of Butler-Volmer parameters, k_{apparent} and α where k_{apparent} is the apparent rate constant describing the fit between theory and experiment. The result was a linear relation between apparent rate constant (k_{apparent}) ascertained from the approximate DIGISIM™ fitting s and the degree of surface coverage as shown in Figure 4.4.3. We refer to this value of rate constant as k_{apparent} due to the fact that it has been claimed

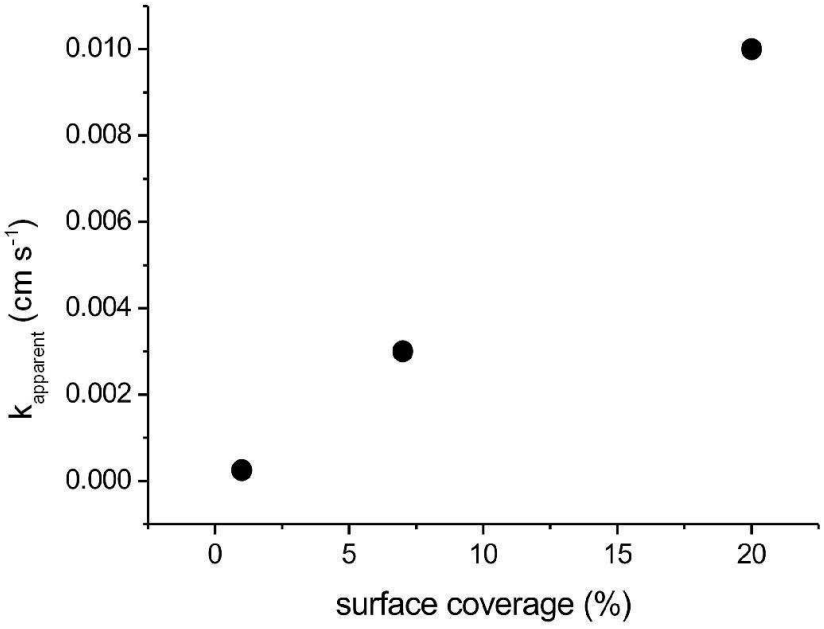

Figure 4.4.3: *Linear plot of ($k_{apparent}$) vs. surface coverage as obtained from the approximate fitting of AgNP voltammetry using* DIGISIM™

assuming the diffusion to the surface is considered to be linear rather than a mixture of convergent and linear diffusion as actually occurs at arrays of nanoparticles and also that the entire electrode surface is uniformly electro-active. Extrapolation of this linear plot estimated k_{apparent} for full coverage ($\theta = 1$) as $\sim 0.9 \times 10^{-3}$ ms^{-1}, based on the relation shown in (4.4.1):

$$k_{\text{apparent}}(\text{ms}^{-1}) = k^0(\text{ms}^{-1})\theta \tag{4.4.1}$$

k^0 is the intrinsic rate constant for the silver macroelectrode. Note that the extrapolation gives a value close to that recorded experimentally for the silver macroelectrode, which was 1.0×10^{-3} ms^{-1}. In order to account more precisely for the different diffusional behaviour at an array of nanoparticles, the AgNP voltammetry was then fitted using a diffusional model based on a regular array of discs, as developed above.[30] The values of D, E_f^0 and k^0 were taken to be equal to the macro-disk

Silver nanoparticle surface coverage (θ)	0.003	0.035	0.102
E_f^0 V	-0.485	-0.485	-0.485
D m^2s^{-1}	1.6×10^{-10}	1.6×10^{-10}	1.6×10^{-10}
k^0 ms^{-1}	1.0×10^{-3}	1.0×10^{-3}	1.0×10^{-3}
α	0.5 ± 0.1	0.4 ± 0.1	0.4 ± 0.1
$[Cr^{3+}](mM)$	10 ± 1	10 ± 1	10 ± 1

Table 4.3:
Fitting parameters for AgNP-BPPG with varying surface coverage

values. The surface coverage (θ) is also input into the model in order to define the diffusion domain. It was therefore possible to fit the experimental data as shown in figure 4.4.4. The optimized parameters for AgNP fitting obtained from this model

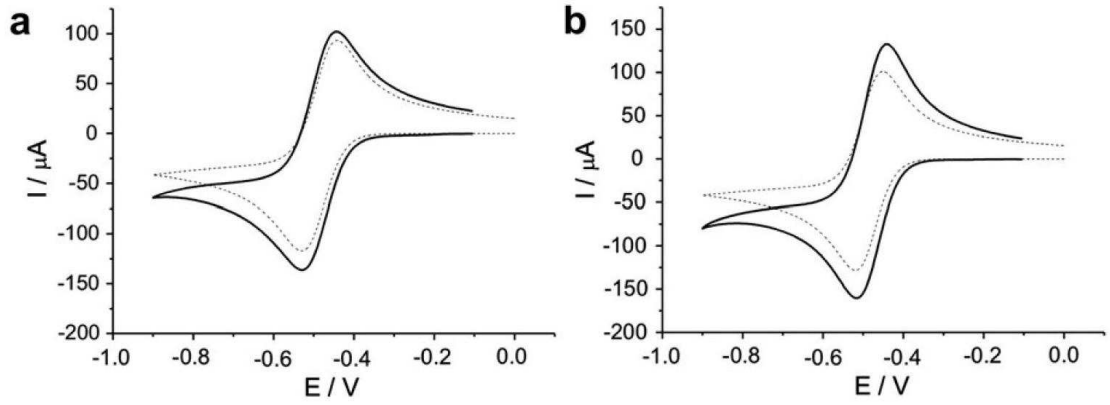

Figure 4.4.4:
Disc simulation fitting for AgNP-BPPG electrode coverage. (a) 3.5%, and (b) 10.2%. Solid line: experimental voltammetry; dashed line: disc simulation.

are shown in table 4.3.

In summary, an increase in the extent of surface coverage alters the mass-transport regime, resulting in a transition from convergent to linear diffusional behaviour. At 10.2% surface coverage the electrode exhibits near-macro-disk behaviour due to greatest degree of diffusional overlap.

4.5 Conclusion

Diffusional chronoamperometry and cyclic voltammetry at a random array of nanoparticles can be simulated efficiently and rationalised in terms of four categories which define different extents of diffusion layer overlap. The cyclic voltammetry in the Category 3/4 region has been shown to be morphology dependent for voltammetry that is not electrochemically reversible.

The reduction Cr^{3+} to Cr^{2+} was carried out experimentally on an array of silver nanoparticles (80-120 nm diameter). A clear relationship was shown to exist between the degree of surface coverage (θ) and the nature of the voltammetry. Increasing the coverage resulted in an increase in the apparent reversibility of the process as well as an increased current due to the greater surface area available for the reaction to take place. This is due to the transition from convergent diffusion to linear diffusion with increasing surface coverage. By increasing the nanoparticle density the electrode kinetics tend towards those of a macro-disk electrode.

Bibliography

[1] Belding, S. R.; Compton, R. G. *J. Phys. Chem. C* **2010**, *114*, 8309–8319.

[2] Zhou, Y.-G.; Campbell, F. W.; Belding, S. R.; Compton, R. G. *Chemical Physics Letters* **2010**, *497*, 200–204.

[3] Welch, C. M.; Compton, R. G. *Anal. Bioanal. Chem.* **2006**, *384*, 601–619.

[4] Campbell, F. W.; Compton, R. G. *Anal. Bioanal. Chem.* **2010**, *396*, 241–259.

[5] Davies, T. J.; Banks, C. E.; Compton, R. G. *J. Solid State Electrochem.* **2005**, *9*, 797–808.

[6] Campbell, F. W.; Zhou, Y.-G.; Compton, R. G. *New J. Chem.* **2010**, *34*, 187–189.

[7] Campbell, F. W.; Belding, S. R.; Baron, R.; Xiao, L.; Compton, R. G. *J. Phys. Chem. C* **2009**, *113*, 14852–14857.

[8] Campbell, F. W.; Belding, S. R.; Baron, R.; Xiao, L.; Compton, R. G. *J. Phys. Chem. C* **2009**, *113*, 9053–9062.

[9] Streeter, I.; Baron, R.; Compton, R. G. *J. Phys. Chem. C* **2007**, *111*, 17008–17014.

[10] Streeter, I.; Compton, R. G. *J. Phys. Chem. C* **2007**, *111*, 18049–18054.

[11] Belding, S. R.; Dickinson, E. J. F.; Compton, R. G. *J. Phys. Chem. C* **2009**, *113*, 11149–11156.

[12] Yudi, L. M.; Baruzzi, A. M.; Solos, V. M. *J. Appl. Electrochem.* **1988**, *18*, 417.

[13] Davies, T. J.; Brookes, B. A.; Fisher, A. C.; Yunus, K.; Wilkins, S. J.; Greene, P. R.; Wadhawan, J. D.; Compton, R. G. *J. Phys. Chem. B* **2003**, *107*, 6431–6444.

[14] Brookes, B. A.; Davies, T. J.; Fisher, A. C.; Evans, R. G.; Wilkins, S. J.; Yunus, K.; Wadhawan, J. D.; Compton, R. G. *J. Phys. Chem. B* **2003**, *107*, 1616–1627.

[15] Davies, T. J.; Ward-Jones, S.; Banks, C. E.; Del Campo, J.; Mas, R.; Munoz, F. X.; Compton, R. G. *J. Electroanal. Chem.* **2005**, *585*, 51–62.

[16] Davies, T. J.; Compton, R. G. *J. Electroanal. Chem.* **2005**, *585*, 63–82.

[17] Reller, H.; Kirowa-Eisner, E.; Gileadi, E. *J. Electroanal. Chem.* **1982**, *138*, 65–77.

[18] Amatore, C.; Savéant, J. M.; Tessier, D. *J. Electroanal. Chem.* **1983**, *147*, 39–51.

[19] Godino, N.; Borissé, X.; Munoz, F. X.; del Campo, F. J. *J. Phys. Chem. C* **2009**, *113*, 11119.

[20] Dickinson, E. J. F.; Streeter, I.; Compton, R. G. *J. Phys. Chem. C* **2008**, *112*, 11637–11644.

[21] Heinze, J. *J. Electroanal. Chem.* **1981**, *124*, 73–86.

[22] Britz, D. *Digital Simulation in Electrochemistry*; Springer-Verlag: New York, 2005.

[23] Bobbert, P. A.; Wind, M. M.; Vlieger, J. *Physica A: Statistical and Theoretical Physics* **1987**, *141*, 58 – 72.

[24] Shoup, D.; Szabo, A. *J. Electroanal. Chem.* **1982**, *140*, 237–245.

[25] Compton, R. G.; Banks, C. E. *Understanding Voltammetry*; World Scientific: Singapore, 2007.

[26] Belding, S. R.; Dickinson, E. J. F.; Compton, R. G. *J. Phys. Chem. C* **2009**, *113*, 11149–11156.

[27] Amatore, C.; Savéant, J. M.; Tessier, D. *Journal of Electroanalytical Chemistry* **1983**, *147*, 39 – 51.

[28] Bard, A. J.; Faulkner, L. R. *Electrochemical Methods Fundamentals and Applications*; John Wiley and Sons, 2001.

[29] Svir, I. B.; Oleinick, A. I.; G, C. R. *Radiotekhnika* **2001**, *116*, 114.

[30] Belding, S. R.; Dickinson, E. J. F.; Compton, R. G. *J. Phys. Chem. C* **2009**, *113*, 11149.

Chapter 5

Cyclic voltammetry: the effect of analyte charge

This chapter presents research showing how cyclic voltammetry is affected by the electric charge on the analyte ions when mass transport is a composite of diffusion and migration. The contents of this chapter have been published in the *Journal of Electroanalytical Chemistry*.[1] The work described here is extended in chapters 6 and 7.

5.1 Introduction

Since the publication of Nicholson and Shain's landmark paper of 1964,[2] cyclic voltammetry has evolved into one of the most widely used and useful techniques in analytical chemistry. The experiments are relatively simple yet can provide fundamental information for a spectrum of chemical systems. Diverse applications have been found and range from chemical sensors[3–6] to the use as an experimental probe

with which to investigate the electrocatalytic properties of nanoparticles[7] or the various theories of electron transfer.[8]

Two modes of mass transport operate in a quiescent solution: diffusion and migration.[9,10] Although it is possible, and in some cases necessary,[11,12] to conduct voltammetry in the presence of both, so-called 'diffusion-only' conditions are generally preferred because the experiments are easily reproducible and can be quantified by fast, accurate numerical modeling.[13]

When the potential applied at the working electrode is changed, electrolysis occurs and a net charge is formed in solution. The charge is dissipated by migration between the working and counter electrodes. Resistance to this flow of current leads to the establishment of a potential gradient across the solution. The potential available to drive electrolysis at the working electrode is correspondingly diminished: the difference is called 'ohmic drop'. Electrolysis therefore establishes concentration and potential gradients along which chemical species diffuse and migrate respectively. The potential gradient leads to two main qualitative differences in the voltammetry compared to diffusion-only conditions: first, the peak to peak separation is greater because the applied potential at which the electrode kinetics outrun mass transport is offset by ohmic drop; secondly, the peak heights are distorted because mass transport is augmented (either positively or negatively) by the migration of ions along the potential gradient.

Diffusion-only conditions must be attained by adding a large quantity of inert salt, so-called 'supporting electrolyte', to the solution.[14–19] As the resistivity of the solution decreases, the potential gradient decreases and becomes increasingly confined to

the surface of the working electrode. In practice, experimentalists need only add sufficient supporting electrolyte to compress the potential gradient to within *ca* 10 Å of the working electrode.[10,20] In this situation, voltammetry is purely diffusional because the electrons "bypass" the potential gradient by quantum mechanical tunneling.[10]

In cases where diffusion-only conditions are assumed, it is imperative that sufficient supporting electrolyte be present. For example, if the potential gradient was naively ignored, a large peak to peak separation, derived from an appreciable ohmic drop, might erroneously be ascribed to a low electrochemical rate constant. As a general rule, voltammetric experiments can be considered purely diffusional when the concentration of supporting electrolyte exceeds 30 times that of the electroactive species.[21] However, this value, often called the 'support ratio', is known to vary according to the experimental conditions. For example, the support ratio required to achieve purely diffusional steady-state voltammetry is known to be more forgiving than in the corresponding transient cases.[22]

In this chapter, the cyclic voltammetry of the reduction, $A^{Z_A} + ne^- \rightleftharpoons B^{Z_B}$ ($1 \leq n \leq 2$), assumed to be electrochemically reversible, is studied using numerical simulations. The effect of adding different concentrations of supporting electrolyte is studied as a function of the scan rate, the diffusion coefficient of species B and the diffusion coefficients of the ions in the supporting electrolyte. These studies cover the following Z_A/Z_B redox couples: 2/1, -1/-2, 8/7, and -7/-8. This chapter extends Dickinson *et al*[21] work on unsupported systems of relatively low ion charge ($A^{3+} + e^- \rightleftharpoons B^{2+}$ and $A^+ + e^- \rightleftharpoons B^0$) in three ways. First, a fuller range of

charges of the electroactive species are considered (see Section 5.2.1 for a definition of the charge range used). Secondly, both one and two electron transfers are studied. Thirdly, a comprehensive supporting information is included which tabulates the minimum concentration of supporting electrolyte required to achieve fully supported voltammetry. This data can be found on the attached CD in the file entitled "Chapter_5_supplementry_info.xls". The data is pertaining to a range of scan rates ($10^{-1} \leq \frac{F\nu r_e^2}{D_A RT} \leq 10^5$) and a range of charges of the electroactive species (see Section 5.2.1 for a definition of the charge range used) and for both one electron and concurrent two electron transfer ($n = 1$ or 2 respectively). This allows experimental conditions to be defined so that any particular Nernstian electrochemical system may be studied under diffusion-only conditions without the need for additional experiments or simulations.

5.2 Theory

In this section, the type of experiment studied is explained and cast in mathematical form. The method of numerical simulation is also described. All symbols are defined in the glossary.

5.2.1 Reaction mechanism

We consider a solution containing an electroactive species, A, of charge Z_A, which is capable of undergoing a n electron reduction to form species B, of charge Z_B. The

process is entirely heterogeneous and takes place at an inert hemispherical electrode.

$$\mathrm{A}^{z_\mathrm{A}} + n\mathrm{e}^- \rightleftharpoons \mathrm{B}^{z_\mathrm{A}-n} \tag{5.2.1}$$

Species A is accompanied by an inert, monovalent, counterion, X^-, and the solution is supported by a monovalent 1:1 inert salt, $\mathrm{M}^+\mathrm{X}^-$. Three further assumptions are made: first, the magnitude of the highest charge, Z_A, is 8; secondly, the maximum number of electrons transfered in the electrochemical process is 2; finally, ion pairing is completely absent. This leads to 16 permissible combinations of Z_A, Z_B and n. Note that ions of high charge, such as dendrimers, can exist without substantial ion pairing.[20]

5.2.2 Experiment

The reaction described in Section 5.2.1 is studied using cyclic voltammetry. The applied potential, E, varies as a function of time, t, according to:

$$E = |-vt + E_\mathrm{start} - E_\mathrm{vertex}| + E_\mathrm{vertex} \tag{5.2.2}$$

where E_start and E_vertex are the starting and vertex potentials respectively.

5.2.3 Mathematical formulation

The concentration of each species varies in space and time according to the Nernst-Planck (NP) equation for mass transport in a hemispherical coordinate system:

$$
\begin{aligned}
\frac{\partial c_{\mathrm{A}}}{\partial t} &= D_{\mathrm{A}}\left(\frac{\partial^2 c_{\mathrm{A}}}{\partial r^2}+\frac{2}{r}\frac{\partial c_{\mathrm{A}}}{\partial r}\right)+D_{\mathrm{A}}z_{\mathrm{A}}\left(\frac{\partial c_{\mathrm{A}}}{\partial r}\frac{\partial \phi}{\partial r}+c_{\mathrm{A}}\frac{\partial^2 \phi}{\partial r^2}+c_{\mathrm{A}}\frac{2}{r}\frac{\partial \phi}{\partial r}\right)\\
\frac{\partial c_{\mathrm{B}}}{\partial t} &= D_{\mathrm{B}}\left(\frac{\partial^2 c_{\mathrm{B}}}{\partial r^2}+\frac{2}{r}\frac{\partial c_{\mathrm{B}}}{\partial r}\right)+D_{\mathrm{B}}(z_{\mathrm{A}}-n)\left(\frac{\partial c_{\mathrm{B}}}{\partial r}\frac{\partial \phi}{\partial r}+c_{\mathrm{B}}\frac{\partial^2 \phi}{\partial r^2}+c_{\mathrm{B}}\frac{2}{r}\frac{\partial \phi}{\partial r}\right)\\
\frac{\partial c_{\mathrm{M}}}{\partial t} &= D_{\mathrm{M}}\left(\frac{\partial^2 c_{\mathrm{M}}}{\partial r^2}+\frac{2}{r}\frac{\partial c_{\mathrm{M}}}{\partial r}\right)+D_{\mathrm{M}}z_{\mathrm{M}}\left(\frac{\partial c_{\mathrm{M}}}{\partial r}\frac{\partial \phi}{\partial r}+c_{\mathrm{M}}\frac{\partial^2 \phi}{\partial r^2}+c_{\mathrm{M}}\frac{2}{r}\frac{\partial \phi}{\partial r}\right)\\
\frac{\partial c_{\mathrm{X}}}{\partial t} &= D_{\mathrm{X}}\left(\frac{\partial^2 c_{\mathrm{X}}}{\partial r^2}+\frac{2}{r}\frac{\partial c_{\mathrm{X}}}{\partial r}\right)+D_{\mathrm{X}}z_{\mathrm{X}}\left(\frac{\partial c_{\mathrm{X}}}{\partial r}\frac{\partial \phi}{\partial r}+c_{\mathrm{X}}\frac{\partial^2 \phi}{\partial r^2}+c_{\mathrm{X}}\frac{2}{r}\frac{\partial \phi}{\partial r}\right)
\end{aligned}
$$

Each equation consists of two terms: the first quantifies diffusion while the second quantifies migration. This system of 4 independent equations contains 5 unknowns: the concentration for the each of the 4 species (c_{A}, c_{B}, c_{M} and c_{X}) and an additional term for the potential (ϕ). Consequently, the description of the problem is incomplete and a further relationship must be introduced. For this purpose, the Poisson equation is invoked:

$$\frac{\partial^2 \phi}{\partial r^2}+\frac{2}{r}\frac{\partial \phi}{\partial r}=-\frac{F}{\epsilon_{\mathrm{r}}\epsilon_0}\sum_{\mathrm{s}} z_{\mathrm{s}}c_{\mathrm{s}} \tag{5.2.3}$$

This relationship follows from Maxwell's equations; however, many workers have attempted to simplify the problem by invoking, instead, the electroneutrality approximation

$$0=-\frac{F}{\epsilon_{\mathrm{r}}\epsilon_0}\sum_{\mathrm{s}} z_{\mathrm{s}}c_{\mathrm{s}} \tag{5.2.4}$$

The electroneutrality equation is well obeyed because the Gibb's energy of the heterogeneous process is insufficient to overcome the strong coulombic forces between the ions of the solution. Although useful when deriving analytical solutions, the

electroneutrality approximation does not, in general, make numerical solutions more straightforward or more stable.[23,24] Consequently, in this chapter, the Poisson equation is used.

The mass transport equations and the Poisson equation are solved in the region $r_e \leq r \leq \infty$ subject to an appropriate collection of boundary conditions. However, the problem is considerably simplified, without affecting the result, by defining a finite upper limit, $r = r_{max}$. In this chapter

$$r_{max} = r_e + 6\sqrt{D_{max}t} \tag{5.2.5}$$

where D_{max} is the diffusion coefficient of the most itinerant species in the solution.[25] Beyond the point $r = r_{max}$, all concentrations are temporally invariant and the flux of each species at can be set equal to zero at all times. In addition, since the concentrations of species in the solution are equal to the initial values, the solution must be electroneutral. It follows, from the Poisson equation combined with electroneutrality, that at $r = r_{max}$

$$\left.\frac{\partial^2\phi}{\partial r^2}\right|_{r=r_{max}} = 0 \tag{5.2.6}$$

Integrating this equation subject to the condition $\phi \to 0$ as $r \to \infty$ leads to a boundary condition for the potential at $r = r_{max}$

$$\left.\frac{\partial\phi}{\partial r}\right|_{r=r_{max}} = -\frac{\phi}{r} \tag{5.2.7}$$

The complete set of boundary conditions for the problem are:

$$
\begin{aligned}
&t = 0, \text{ all } r && c_{\mathrm{A}} = c_{\mathrm{A}}^{*} && c_{\mathrm{B}} = 0 \\
&c_{\mathrm{M}} = c_{\mathrm{M}}^{*} && c_{\mathrm{X}} = c_{\mathrm{M}}^{*} && \phi = 0 \\
&t > 0,\ r = r_{\max} && \left.\frac{\partial c_{\mathrm{A}}}{\partial r}\right|_{r=r_{\max}} = 0 && \left.\frac{\partial c_{\mathrm{B}}}{\partial r}\right|_{r=r_{\max}} = 0 \\
&\left.\frac{\partial c_{\mathrm{M}}}{\partial r}\right|_{r=r_{\max}} = 0 && \left.\frac{\partial c_{\mathrm{X}}}{\partial r}\right|_{r=r_{\max}} = 0 && \left.\frac{\partial \phi}{\partial r}\right|_{r=r_{\max}} = -\frac{\phi}{r} \\
&t > 0,\ r = r_{\mathrm{e}} && c_{\mathrm{A}} = && c_{\mathrm{B}} \exp\left(\frac{F(E - E^{\ominus}_{\mathrm{f,A/B}} - \Delta\phi)}{RT}\right) \\
& && D_{\mathrm{B}} \left.\frac{\partial c_{\mathrm{B}}}{\partial r}\right|_{r=r_{\mathrm{e}}} = && -D_{\mathrm{A}} \left.\frac{\partial c_{\mathrm{A}}}{\partial r}\right|_{r=r_{\mathrm{e}}} \\
& && D_{\mathrm{M}} \left.\frac{\partial c_{\mathrm{M}}}{\partial r}\right|_{r=r_{\mathrm{e}}} = && 0 \\
& && D_{\mathrm{X}} \left.\frac{\partial c_{\mathrm{X}}}{\partial r}\right|_{r=r_{\mathrm{e}}} = && 0
\end{aligned}
$$

where E is the potential applied at the electrode; $E^{\ominus}_{\mathrm{f,A/B}}$ is the formal potential of the A/B redox couple. $\Delta\phi$ is the difference in potential between bulk solution and the edge of the double layer at which location we assumed species A and B to be Nernstian equilibrated. The parameter $\Delta\phi$ is therefore the loss in 'driving force' for the reaction. In particular, the modified Nernstian boundary condition was implemented by using Butler-Volmer kinetics of the form

$$
\begin{aligned}
t > 0,\ r = r_{\mathrm{e}} \qquad D_{\mathrm{A}} \left.\frac{\partial c_{\mathrm{A}}}{\partial r}\right|_{r=r_{\mathrm{e}}} = \quad & k^{0}_{\mathrm{A/B}} c_{\mathrm{A},0} \exp\left(-\alpha_{\mathrm{A/B}} \frac{F(E_{\mathrm{app}} - E^{\ominus}_{\mathrm{f,A/B}} - \Delta\phi)}{RT}\right) \\
& - k^{0}_{\mathrm{A/B}} c_{\mathrm{B},0} \exp\left((1 - \alpha_{\mathrm{A/B}}) \frac{F(E_{\mathrm{app}} - E^{\ominus}_{\mathrm{f,A/B}} - \Delta\phi)}{RT}\right)
\end{aligned}
$$

and taking the electrochemical rate constant, k^{0} to infinity in order to obtain equilibration. This was done for ease of computation.

The current was calculated as follows:

$$
i = 2\pi F c_{\mathrm{A}}^{*} D_{\mathrm{A}} r_{\mathrm{e}} n \left.\frac{\partial c_{\mathrm{A}}}{\partial r}\right|_{r=r_{\mathrm{e}}} \tag{5.2.8}
$$

5.2.4 Numerical methods

The problem is readily formulated in terms of a conventional set of normalised parameters, defined in the glossary. This procedure reduces the number of solutions by amalgamating parameters that act as scaling factors into parameters that do not. The NPP equations are discretised in this simulation space according to the Crank-Nicholson method,[26] which is characterised as stable and accurate for 1D simulations.[27] The resulting set of coupled non-linear simultaneous equations is solved using the iterative Newton-Raphson method.[28]

The spatial simulation mesh is composed of an irregular grid of points, expanding in R away from the electrode. This grid corresponds to that used in previous work,[11,29–31] with a region of extremely dense regular grid spacing close to the electrode that expands proportionally to R beyond some characteristic switching point R_{s}. Mathematically, the R position of a point R_{j} is defined as:

$$R < R_{\mathrm{s}} \qquad R_{\mathrm{j}} = R_{\mathrm{j}-1} + \gamma_{\mathrm{R}}(R_{\mathrm{s}} - 1) \tag{5.2.9}$$

$$R \geq R_{\mathrm{s}} \qquad R_{j} = R_{\mathrm{j}-1} + \gamma_{\mathrm{R}}(R_{\mathrm{j}-1} - 1) \tag{5.2.10}$$

where the point at the electrode surface, R_0, is equal to 1. A regular time grid was employed, where the number of time-steps per unit θ_{app} is given by a parameter τ_{PT} . Convergence studies were used to find optimal grid parameters which for the majority of systems were: $\gamma_{\mathrm{R}} = 1 \times 10^{-2}$; $R_{\mathrm{s}} = R_0 + (2 \times 10^{-3})$; $\tau_{\mathrm{PT}} = 50$. The simulations were converged to 0.5%.

5.3 Results and discussion

5.3.1 Preliminaries

The supporting information contains data for the *range* of 16 different combinations of Z_A, Z_B and n (see section 5.2.1). In order to explain the *trends* in the voltammetry, only 4 cases are studied in detail in this section:

$$A^{2+} + e^- \rightleftharpoons B^+ \tag{5.3.1}$$

$$A^{8+} + e^- \rightleftharpoons B^{7+} \tag{5.3.2}$$

$$A^- + e^- \rightleftharpoons B^{2-} \tag{5.3.3}$$

$$A^{7-} + e^- \rightleftharpoons B^{8-} \tag{5.3.4}$$

In each case, the effect of varying the support ratio is studied as a function of four parameters: the scan rate, σ; the diffusion coefficient of species B, D'_B and the diffusion coefficients of the ions in the supporting electrolyte, D'_M and D'_X. The dimensionless scan rate, σ, is given by $\frac{F\nu r_e^2}{D_A RT}$ and the dimensionless diffusion coefficient for species i is given by $D'_i = D_i/D_A$. Unless otherwise stated, the effect of each parameter is studied with respect to an electrochemically reversible system in which all diffusion coefficients are equal ($D'_B = D'_M = D'_X = 1$).

In what follows, all systems are assumed to be electrochemically reversible. The effect of changing the electrochemical rate constant from this limit to the limit of

electrochemical irreversibility has been studied. The electrochemical rate constant does not significantly affect the required support ratio.

5.3.2 Effect of scan rate (σ)

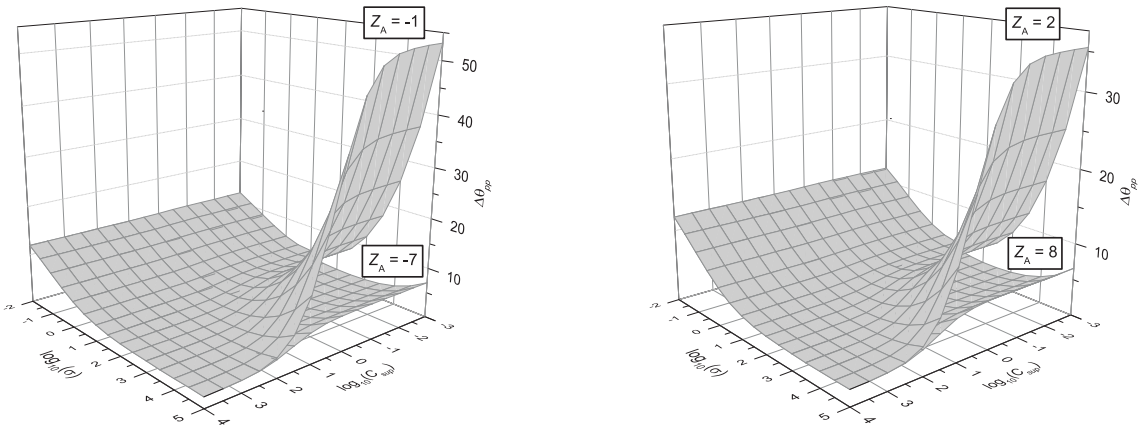

Figure 5.3.1:
Peak to peak separation, $\Delta\theta_{\mathrm{pp}}$, as a function of scan rate, σ, and support ratio, C_{sup}. The redox reaction is $A^{Z_{\mathrm{A}}} + e^- \rightleftharpoons B^{Z_{\mathrm{B}}}$. $D'_{\mathrm{A}} = D'_{\mathrm{B}} = D'_{\mathrm{M}} = D'_{\mathrm{X}}$.

Figure 5.3.1 shows the peak to peak separation, $\Delta\theta_{\mathrm{pp}}$, as a function of the scan rate, σ, and the support ratio, C_{sup} ($= \frac{c_{\mathrm{A}}}{c_{\mathrm{supporting}}}$). At full support, the ohmic drop is zero and the effective overpotential experienced by the solution is simply given by difference between the dimensionless applied potential and the dimensionless formal potential ($\theta - \theta_{\mathrm{f}}$). The rate of mass transport increases with scan rate: a higher scan rate leads to a thinner layer of depletion and a steeper concentration gradient close to the electrode. As the scan rate decreases, the voltammetry becomes more sigmoidal and the peak to peak separation tends towards infinity. As the scan rate increases, the peak to peak separation tends towards a limiting value of approximately $2.22\frac{F}{RT}$, which corresponds to $\Delta E_{\mathrm{pp}} \approx 57$ mV at 298 K.[20]

At low support, the ohmic drop is non zero and the effective overpotential experi-

enced by the solution is given by '$\theta - \theta_f - \Delta\theta$' where θ is the dimensionless applied potential; θ_f is the dimensionless formal potential and $\Delta\theta$ is the loss in potential driving force at the electrode surface as explained in section 5.2.2. The ohmic drop is proportional to two variables: the current through the electrode and the resistance of the solution. Over low scan rates ($\sigma \approx 10^{-2} - 10^{0}$), the current is very small and the ohmic drop is effectively zero. In this scan rate range, the peak to peak separation is therefore almost independent of support ratio. Over higher scan rates ($\sigma \approx 10^{0} - 10^{5}$), the current is significant and increases with increasing scan rate (as explained in the previous paragraph). Therefore, ohmic drop increases with increasing scan rate. The potential applied at the working electrode required to bring about rate limiting mass transport is correspondingly higher. Therefore, increasing the scan rate at low support leads to an increase in the peak to peak separation.

Over high scan rates, ($\sigma \approx 10^{2} - 10^{5}$), the peak to peak separation increases with decreasing support ratio. This occurs due to an increase in the ohmic drop. As explained in the previous paragraph, ohmic drop increases with the resistance of the solution. Solution resistance is inversely related to ionic strength and contains two components: one from the supporting electrolyte and one from the electroactive ions themselves. As the support ratio decreases, the contribution to the solution resistance derived from the supporting electrolyte decreases while that derived from the electroactive ions themselves stays constant. In the limit of very low support ratios, the ohmic drop is almost independent of support ratio. This is called the limit of self support.[21]

Increasing the charge of the electroactive ions increases the contribution to the

solution's ionic strength and consequently decreases the contribution to the ohmic drop. Therefore, the self support limit corresponds to a much smaller peak to peak separation as the magnitude of the analyte charge increases. Since the ohmic drop has little effect on the peak to peak separation over low scan rates ($10^{-2} - 10^{0}$), the effect of analyte charge is effectively zero in that region. The potential window required to observe both peaks in a cyclic voltammogram, over a range of support ratios and scan rates, becomes smaller as the charge of the analyte ions increases. For example, a dimensionless potential window required to observe a voltammogram is approximately 70 (E = 1.80 V at 298 K) when $Z_{\mathrm{A}} = -1$ but is approximately $\theta = 15$ ($E = 0.39$ V at 298 K) when $Z_{\mathrm{A}} = -7$. Therefore complications associated with the use of a wide potential window, for example solvent breakdown, are much less important for analyte ions of high charge. Figure 5.3.2 shows the forward peak flux, J_{pf}, as a function of the support ratio, C_{sup}, and the scan rate, σ. At low scan rates, the peak currents corresponds to the steady state signal arising from a very large potential step ($\theta - \theta_{\mathrm{f}} \gg 0$). In the limit of self support, these values can be derived analytically.[32] In this limit, the steady state current increases as the charge of the reduced species becomes more positive. The heterogeneous process increases the net negative charge close to the electrode surface and positive ions must migrate towards that region to neutralise the charge. This also increases the concentration gradient of positive analyte ions in the vicinity of the electrode. As the support ratio decreases, a greater proportion of the ions that must migrate increases. Therefore, the number of positive analyte ions required to neutralise the excess charge at the electrode surface increases as the support ratio decreases. Consequently, the steady

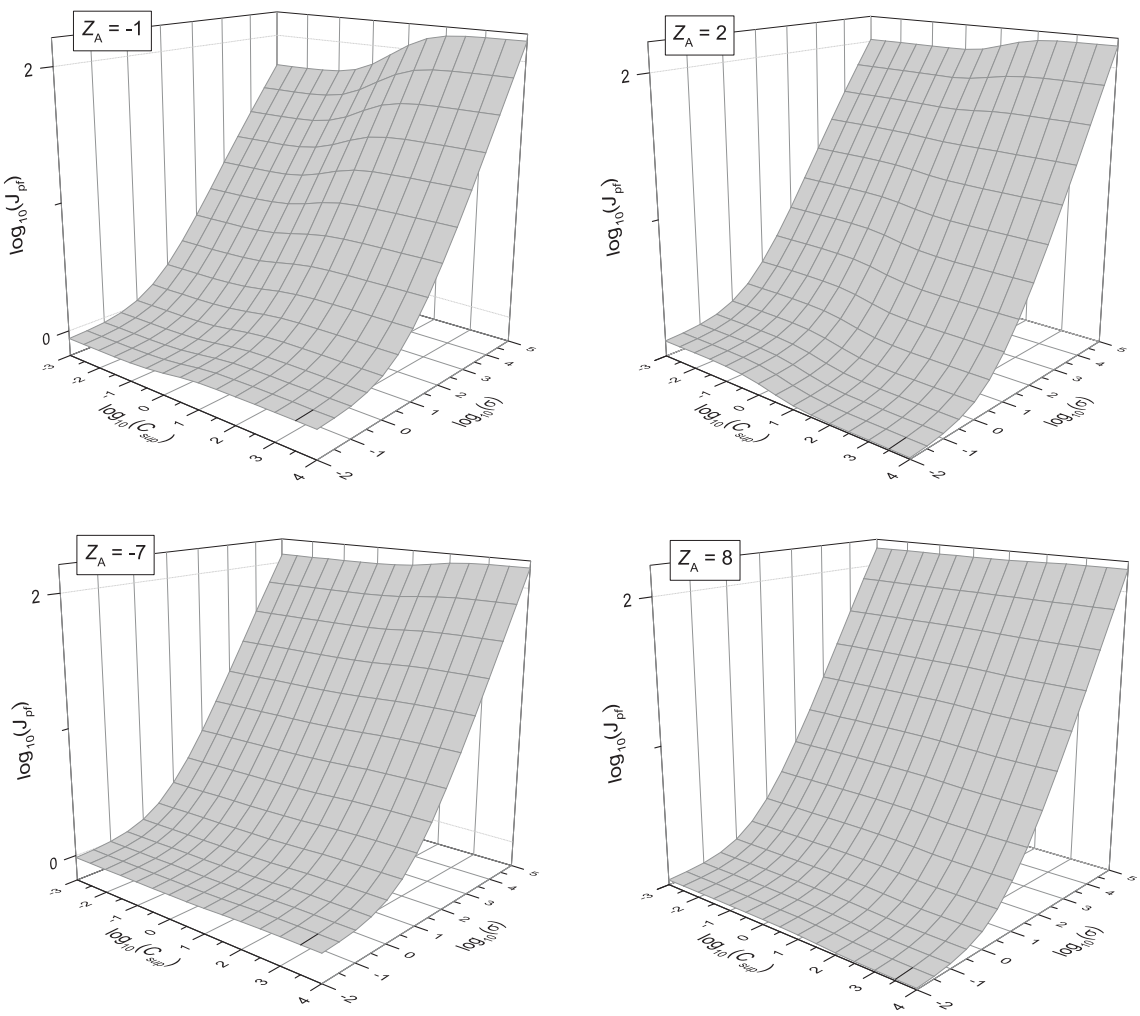

Figure 5.3.2:
Forward peak flux, J_{pf}, as a function of scan rate, σ, and support ratio, C_{sup}. The redox reaction is $A^{Z_{\mathrm{A}}} + e^- \rightleftharpoons B^{Z_{\mathrm{B}}}$. $D'_{\mathrm{A}} = D'_{\mathrm{B}} = D'_{\mathrm{M}} = D'_{\mathrm{X}}$.

state current increases as the analyte ion becomes more positive. The opposite effect occurs for analyte negative ions. As the charge of the analyte ions increase, the number of analyte ions required to migrate to neutralise the excess charge at the electrode is reduced. Consequently, the steady state current is much less sensitive to changes in support ratio.

At high scan rates ($10^0 - 10^5$), the peak current increases with the effective scan rate ($\frac{\partial(\theta - \Delta\theta)}{\partial\tau}$). As the support ratio decreases, the ohmic drop term increases and the

scan rate ($\frac{\partial\theta}{\partial\tau}$) required to achieve the the same effective scan rate ($\frac{\partial(\theta-\Delta\theta)}{\partial\tau}$) increases. This decrease in J_{peak} with decreasing support ratio becomes less important as the analyte charge increases owing to a decrease in the ohmic drop. A self support limit is also observed in each case.

When Z_{A} is positive, the steady-state current increases as the support ratio decreases. However, the trend is reversed at higher scan rates. There is therefore an intermediate scan rate at which the peak currents at full and zero support are equal. This corresponds to the point at which the effect of ohmic drop is exactly canceled out by changes in concentration profiles brought about by migration.

At very high scan rates ($10^2 - 10^5$) and at full support, the logarithm of peak current varies linearly the logarithm of scan rate according to the Randles-Ševčík equation.[33,34] Under self support, this plot is still linear but the gradient is attenuated by the ohmic drop effect discussed above. It was found to be possible to empirically fit peak current as a function of scan rate in the limit of self support. This was done in the range $10^2 - 10^5$; with a maximum error of 1.38% over the entire range of redox couples defined in Section 5.3.1. The fitting was done numerically using the least squares minimisation method.[28] The dimensionless form of the equation is:

$$J_{\text{pf}} = 10^{a_1}\sigma^{a_2} \tag{5.3.5}$$

In dimensional form this is:

$$i_{\text{pf}} = (2\pi F c^*_{\text{A}} D_{\text{A}} r_{\text{e}})^{a_1} \left(\frac{F\nu}{RT}\right)^{a_2} \tag{5.3.6}$$

where the coefficients, a_1 and a_2, for each redox couple are given in Table 5.1 on

Z_A	Z_B	a_2	a_1	Max % error
-1	-2	0.382535	-0.159753	0.936277
-1	-3	0.363767	0.116757	0.400534
-2	-3	0.415161	-0.186128	0.797462
-2	-4	0.396223	0.102953	0.705241
-3	-4	0.43426	-0.208738	0.618542
-3	-5	0.416578	0.0881252	0.609666
-4	-5	0.446477	-0.225329	0.490326
-4	-6	0.43063	0.0749998	0.562463
-5	-6	0.454676	-0.23704	0.834472
-5	-7	0.44076	0.0643412	0.479898
-6	-7	0.460377	-0.245265	1.19008
-6	-8	0.448275	0.0559744	0.386897
-7	-8	0.464459	-0.251076	1.45837
2	1	0.404108	0.00994755	0.799481
3	1	0.397646	0.414916	0.555227
3	2	0.426654	-0.0627735	0.643874
4	2	0.416939	0.323657	0.568358
4	3	0.441312	-0.110246	0.538515
5	3	0.430665	0.265628	0.541013
5	4	0.45113	-0.142733	0.463856
6	4	0.440724	0.224703	0.474374
6	5	0.457911	-0.165726	0.846649
7	5	0.448248	0.194438	0.39208
7	6	0.46272	-0.182453	1.14794
8	6	0.45398	0.171338	0.417912
8	7	0.466215	-0.194941	1.38497

Table 5.1:
Empirical parameters for calculating peak currents using Eqn 5.3.6. Error is measured with respect to the peak current obtained from numerical simulations (converged to 0.5%).

page 139. This empirical equation is valid in the region $10^2 < \frac{r_e^2 F v}{D_A R T} < 10^5$ when $D_A = D_B$.

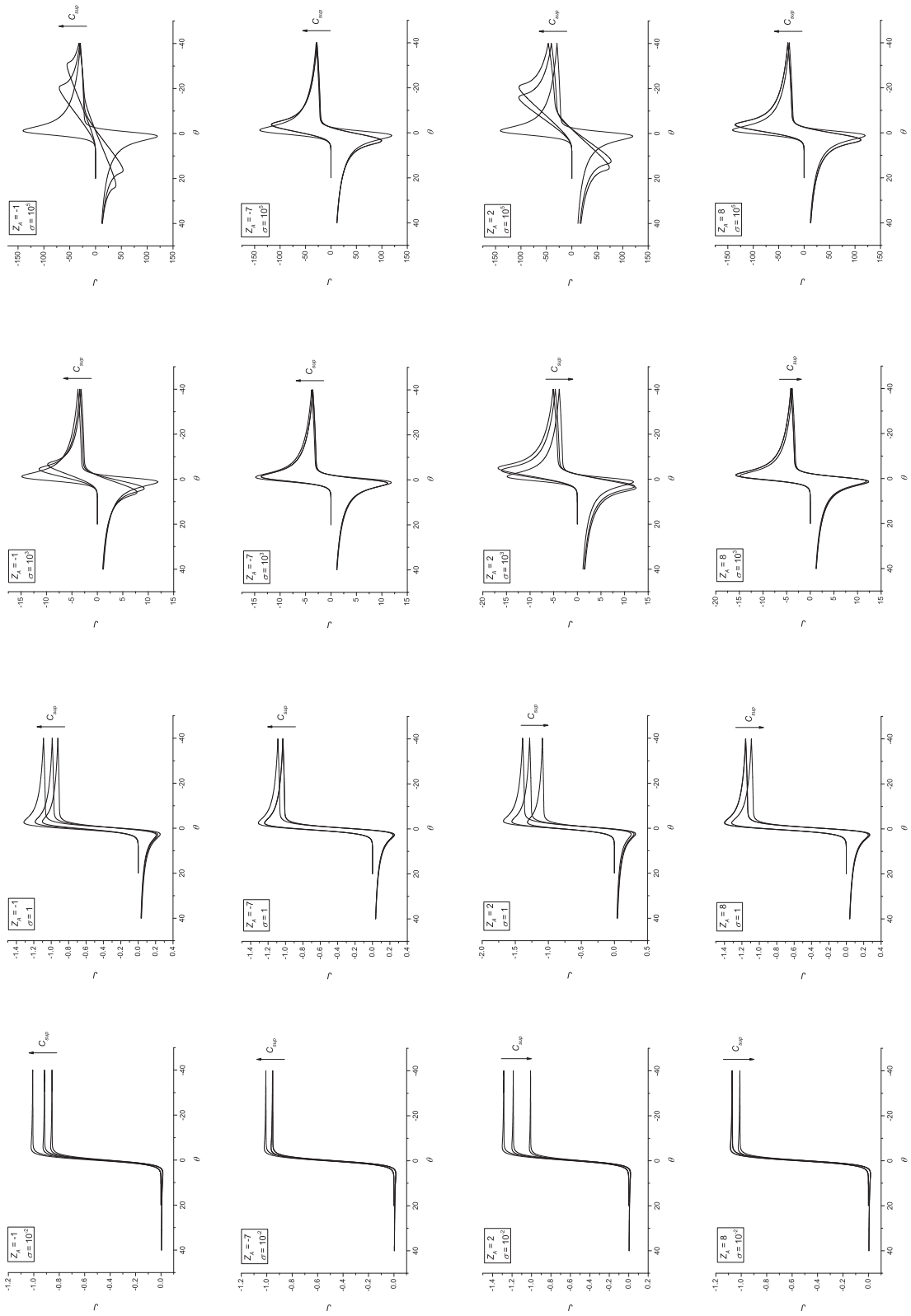

Figure 5.3.3:
Cyclic voltammetry for 16 different points in figures 5.3.1 and 5.3.2. The redox reaction is $A^{Z_A} + e^- \rightleftharpoons B^{Z_B}$. $D'_A = D'_B = D'_M = D'_X$.

Figure 5.3.3 shows the cyclic voltammograms at 16 points across figures 5.3.1 and 5.3.2. At low scan rates, the effect of changing C_{sup} is to change the value of the peak current. As the scan rate increases, there are two effects: the ohmic drop increases and the depletion layer at electrode surface becomes thinner. The first effect leads to an increase in peak to peak separation while the second leads to an increase in the peak current *and* an increase in peak to peak separation (due to an increase in ohmic drop according to Ohm's law). As the scan rate increases from zero, the peak height increases but the peak to peak separation remains approximately constant: the voltammograms become more concordant and the *percentage* difference in peak heights becomes smaller. At higher scan rates, both the peak height *and* peak to peak separation increase: the voltammograms become less concordant. Therefore, at intermediate scan rates, concordance between full and self supported regimes is maximized (as observed in Figure 5.3.3). This effect is investigated further in figure 5.3.4. This shows the variation in error relative to the diffusion-only (i.e. fully supported) regime as a function of σ and C_{sup}. The error is defined as follows:

$$\text{Error} = \frac{1}{N}\sum\left|\frac{J - J_{\text{diffusion-only}}}{|\left(J_{\text{pf}} - J_{\text{pr}}\right)_{\text{diffusion-only}}|}\right| \tag{5.3.7}$$

In this equation, the discrepancy between the currents between the considered voltammogram and the diffusion-only (i.e. fully supported) voltammogram ($J - J_{\text{diffusion-only}}$) is compared with the difference in the peak currents ($J_{\text{pf}} - J_{\text{pr}}$). This is necessary because, when experimental voltammograms are compared with simulations, the entire range of recorded currents are viewed together. The error minimum

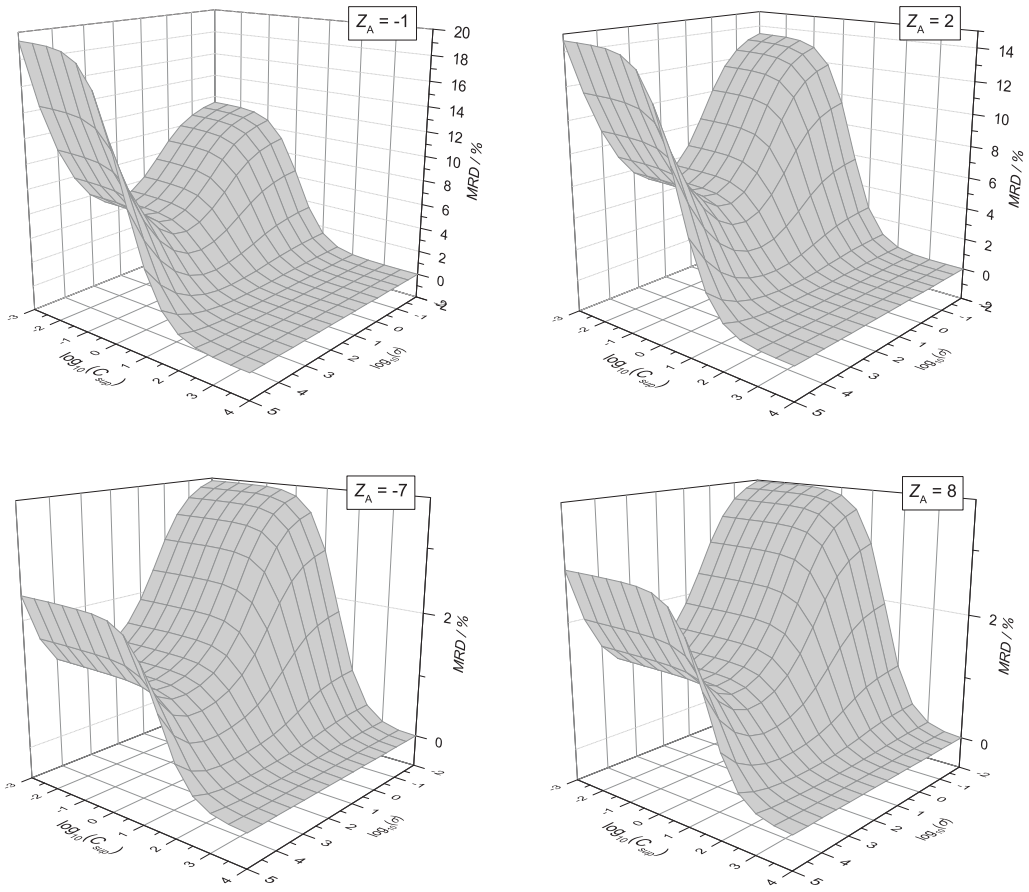

Figure 5.3.4:
Mean deviation relative to $C_{\mathrm{sup}} = 10^4$ *(full support) as a function of scan rate,* σ*, and support ratio,* C_{sup}*.*

at intermediate scan rates is clearly visible for all redox couples shown. The minimum errors for $Z_{\mathrm{A}} = -7/Z_{\mathrm{B}} = -8$ system and $Z_{\mathrm{A}} = 8/Z_{\mathrm{B}} = 7$ system are very small because the effect of increasing ohmic drop with scan rate is offset by the large contribution to the ionic strength from the highly charged electroactive ions. In fact, figure 5.3.3 shows that, for these redox couples, the voltammograms at $\sigma = 10^3$ are practically identical, regardless of the concentration of supporting electrolyte. Figure 5.3.4 implies that this might be the case over a range of scan rates. This is confirmed in figure 5.3.5 where qualitative concordance is achieved over scan rates spanning two orders of magnitude- a range sufficient to obtain semi-quantitative

voltammetric information from the system.

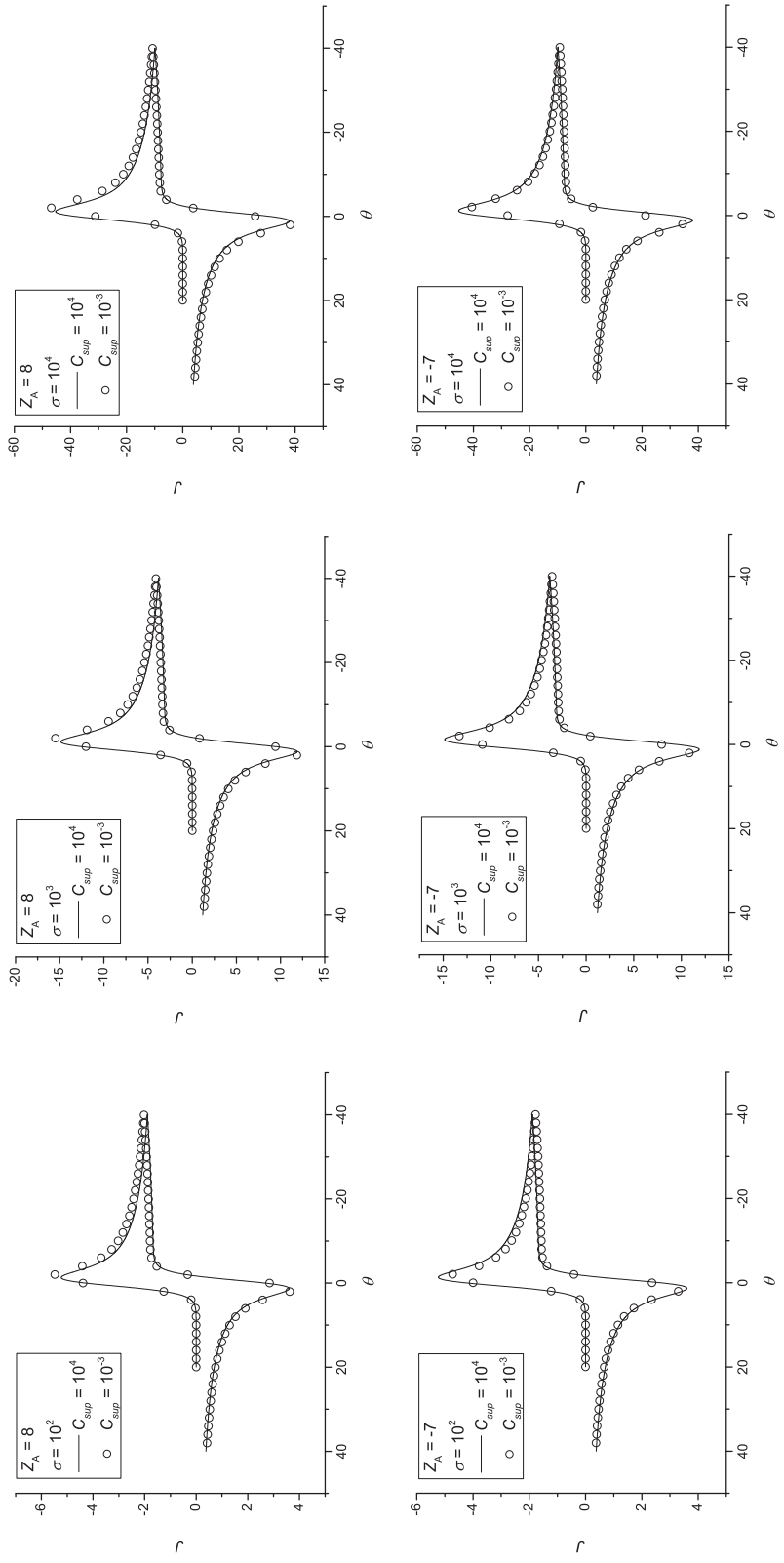

Figure 5.3.5:
Cyclic voltammograms showing the concordance between $C_{\text{sup}} = 10^4$ *(full support) and* $C_{\text{sup}} = 10^{-3}$ *(self support) for high analylate charges* ($Z_{\text{A}} = -7$ *and* $Z_{\text{A}} = 8$*) over a wide range of scan rates* ($\sigma = 10^2 - 10^4$*). The redox reaction is* $A^{Z_{\text{A}}} + e^- \rightleftharpoons B^{Z_{\text{B}}}$*.* $D'_{\text{A}} = D'_{\text{B}} = D'_{\text{M}} = D'_{\text{X}}$*.*

5.3.3 Effect of diffusion coefficients of supporting electrolyte (D'_{M} and D'_{X})

In the steady-state limit ($\frac{\partial c}{\partial t} = 0$), the diffusion coefficients of the supporting electrolyte, D'_{M} ($= \frac{D_{\mathrm{M}}}{D_{\mathrm{A}}}$) and D'_{X} ($= \frac{D_{\mathrm{X}}}{D_{\mathrm{A}}}$), can be factored out of the mathematical formulation of the experiment given in Section 5.2.3.

The mass transport equation:

$$\begin{aligned}
0 &= \left(\frac{\partial^2 c_{\mathrm{A}}}{\partial r^2} + \frac{2}{r}\frac{\partial c_{\mathrm{A}}}{\partial r}\right) + z_{\mathrm{A}}\left(\frac{\partial c_{\mathrm{A}}}{\partial r}\frac{\partial \phi}{\partial r} + c_{\mathrm{A}}\frac{\partial^2 \phi}{\partial r^2} + c_{\mathrm{A}}\frac{2}{r}\frac{\partial \phi}{\partial r}\right) \\
0 &= \left(\frac{\partial^2 c_{\mathrm{B}}}{\partial r^2} + \frac{2}{r}\frac{\partial c_{\mathrm{B}}}{\partial r}\right) + (z_{\mathrm{A}} - n)\left(\frac{\partial c_{\mathrm{B}}}{\partial r}\frac{\partial \phi}{\partial r} + c_{\mathrm{B}}\frac{\partial^2 \phi}{\partial r^2} + c_{\mathrm{B}}\frac{2}{r}\frac{\partial \phi}{\partial r}\right) \\
0 &= \left(\frac{\partial^2 c_{\mathrm{M}}}{\partial r^2} + \frac{2}{r}\frac{\partial c_{\mathrm{M}}}{\partial r}\right) + z_{\mathrm{M}}\left(\frac{\partial c_{\mathrm{M}}}{\partial r}\frac{\partial \phi}{\partial r} + c_{\mathrm{M}}\frac{\partial^2 \phi}{\partial r^2} + c_{\mathrm{M}}\frac{2}{r}\frac{\partial \phi}{\partial r}\right) \\
0 &= \left(\frac{\partial^2 c_{\mathrm{X}}}{\partial r^2} + \frac{2}{r}\frac{\partial c_{\mathrm{X}}}{\partial r}\right) + z_{\mathrm{X}}\left(\frac{\partial c_{\mathrm{X}}}{\partial r}\frac{\partial \phi}{\partial r} + c_{\mathrm{X}}\frac{\partial^2 \phi}{\partial r^2} + c_{\mathrm{X}}\frac{2}{r}\frac{\partial \phi}{\partial r}\right)
\end{aligned}$$

The Poisson equation is:

$$\frac{\partial^2 \phi}{\partial r^2} + \frac{2}{r}\frac{\partial \phi}{\partial r} = -\frac{F}{\epsilon_{\mathrm{r}}\epsilon_0}\sum_{\mathrm{s}} z_{\mathrm{s}} c_{\mathrm{s}} \tag{5.3.8}$$

The complete boundary conditions are:

$t = 0$, all r	$c_{\mathrm{A}} = c^*_{\mathrm{A}}$	$c_{\mathrm{B}} = 0$
$c_{\mathrm{M}} = c^*_{\mathrm{M}}$	$c_{\mathrm{X}} = c^*_{\mathrm{M}}$	$\phi = 0$
$t > 0$, $r = r_{\max}$	$\left.\frac{\partial c_{\mathrm{A}}}{\partial r}\right\|_{r=r_{\max}} = 0$	$\left.\frac{\partial c_{\mathrm{B}}}{\partial r}\right\|_{r=r_{\max}} = 0$
$\left.\frac{\partial c_{\mathrm{M}}}{\partial r}\right\|_{r=r_{\max}} = 0$	$\left.\frac{\partial c_{\mathrm{X}}}{\partial r}\right\|_{r=r_{\max}} = 0$	$\left.\frac{\partial \phi}{\partial r}\right\|_{r=r_{\max}} = -\frac{\phi}{r}$

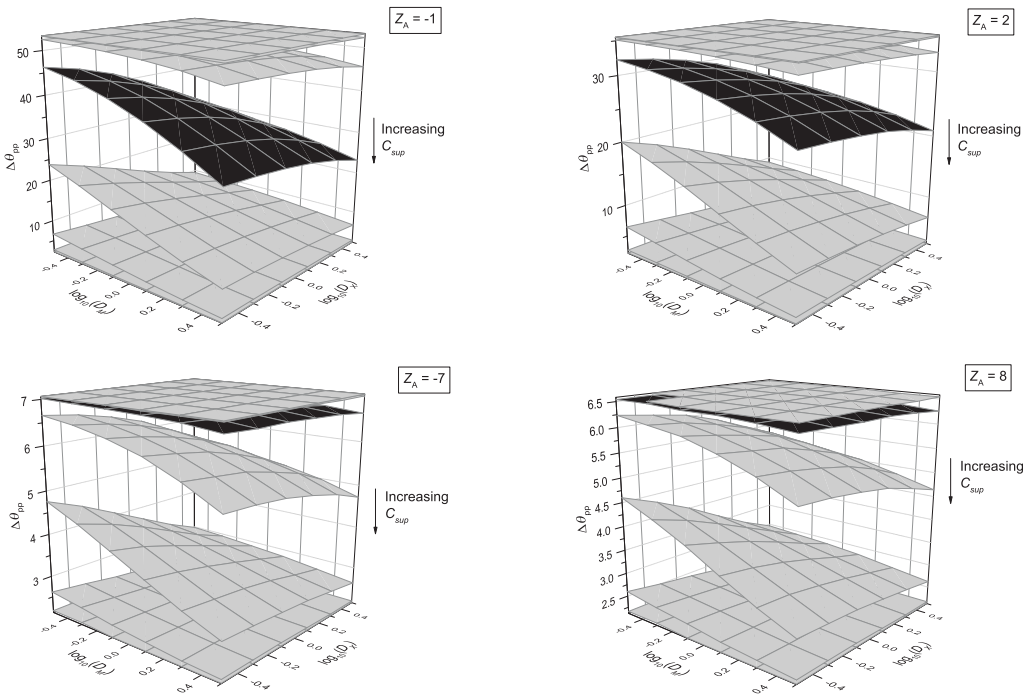

Figure 5.3.6:
Peak to peak separation, $\Delta\theta_{\mathrm{pp}}$, as a function of the diffusion coefficient of species M, D_{M}, and the diffusion coefficient of species X, D_{X}. Data is shown for the following support ratios: $C_{\mathrm{sup}} = 10^{-3}$, 10^{-2}, 10^{-1}, 10^{0}, 10^{1}, 10^{2}, 10^{3} and 10^{4}. In each case, the surface corresponding to $C_{\mathrm{sup}} = 10^{0}$ is shown in black. The redox reaction is $A^{Z_{\mathrm{A}}} + e^{-} \rightleftharpoons B^{Z_{\mathrm{B}}}$. $\sigma = 10^{5}$ and $D'_{\mathrm{A}} = D'_{\mathrm{B}}$.

$$
\begin{aligned}
t > 0,\, r = r_{\mathrm{e}} \qquad c_{\mathrm{A}} &= c_{\mathrm{B}} \exp\left(\frac{F(E - E^{\ominus}_{\mathrm{f,A/B}} - \Delta\phi)}{RT}\right) \\
D_{\mathrm{B}} \frac{\partial c_{\mathrm{B}}}{\partial r}\bigg|_{r=r_{\mathrm{e}}} &= -D_{\mathrm{A}} \frac{\partial c_{\mathrm{A}}}{\partial r}\bigg|_{r=r_{\mathrm{e}}} \\
\frac{\partial c_{\mathrm{M}}}{\partial r}\bigg|_{r=r_{\mathrm{e}}} &= 0 \\
\frac{\partial c_{\mathrm{X}}}{\partial r}\bigg|_{r=r_{\mathrm{e}}} &= 0
\end{aligned}
$$

The current was calculated as follows:

$$
i = 2\pi F c^{*}_{\mathrm{A}} D_{\mathrm{A}} r_{\mathrm{e}} n \frac{\partial c_{\mathrm{A}}}{\partial r}\bigg|_{r=r_{\mathrm{e}}} \tag{5.3.9}
$$

Therefore, voltammograms obtained in this limit are independent of the diffusion coefficients of the supporting electrolyte, D'_{M} ($= \frac{D_{\mathrm{M}}}{D_{\mathrm{A}}}$) and D'_{X} ($= \frac{D_{\mathrm{X}}}{D_{\mathrm{A}}}$). The rate at

which the supporting electrolyte can move through solution becomes less important as the experimental timescale tends towards infinity. However, over short experimental timescales (i.e. under transient conditions), D'_{M} and D'_{X} must be included in the mathematical formulation of the experiment and are therefore expected to affect the resulting voltammetry. Figure 5.3.6 shows the peak to peak separation, $\Delta\theta_{\mathrm{pp}}$ at $\sigma = 10^5$, as a function of the diffusion coefficient of species M, D'_{M}, and the diffusion coefficient of species X, D'_{X}. Data is shown for the range of support ratios : $10^{-3} - 10^4$. In each case, the peak to peak separation is independent of D'_{M} and D'_{X} at very high support ratios: this corresponds to diffusion-only conditions. The peak to peak separation is also independent of D'_{M} and D'_{X} at very low support ratios: this corresponds to the self supported case in which the concentration of supporting electrolyte is equal to zero. Peak to peak separation varies most strongly with D'_{M} and D'_{X} over intermediate support ratios. In this region, the support ratio is low enough to allow mass transport to occur by diffusion *and* migration but is high enough to ensure that a significant part of the solution's ionic strength is derived from the supporting electrolyte. The concentration of supporting electrolyte at which the voltammetry varies most strongly with D'_{M} and D'_{X} increases with the charge on the analyte ion. At this support ratio, the ionic strength derived from the supporting electrolyte is comparable to that derived from the analyte ions. As the charge of the analyte ions increases, a higher support ratio is required to obtain the same contribution to the total ionic strength of the solution. Figure 5.3.6 shows that the peak to peak separation, hence ohmic drop, decreases as the diffusion coefficients, D'_{M} and D'_{X}, increase. The net charge generated at the surface of the

electrode can be neutralised more rapidly as the ions of the supporting electrolyte become more itinerant. Figure 5.3.7 shows cyclic voltammetry from different points in Figure 5.3.6. It is seen that the effect of the itinerary of the supporting electrolyte is less pronounced for analyte ions of high charge. In these cases, the analyte ions make an appreciable contribution to the ionic strength of the solution and therefore, the effect of supporting electrolyte is less important.

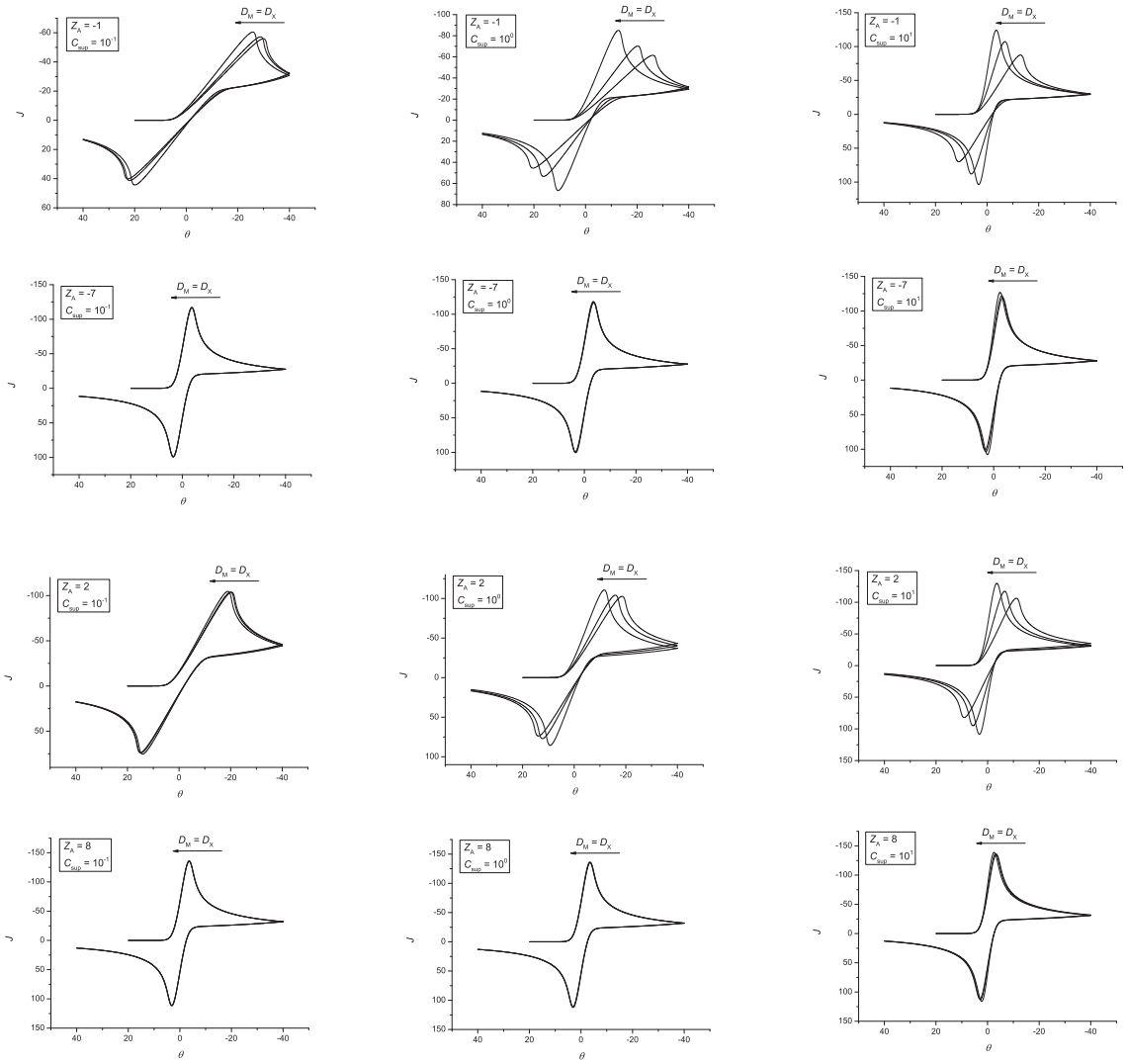

Figure 5.3.7:
Cyclic voltammetry from different points in figure 5.3.6. The values of $D'_{\mathrm{M}} = D'_{\mathrm{X}}$ *are* $10^{-0.5}$, 10^{0} *and* $10^{0.5}$. *The redox reaction is* $A^{Z_{\mathrm{A}}} + e^{-} \rightleftharpoons B^{Z_{\mathrm{B}}}$. $\sigma = 10^{5}$ *and* $D'_{\mathrm{A}} = D'_{\mathrm{B}}$.

5.3.4 Effect of diffusion coefficients of species B (D'_{B})

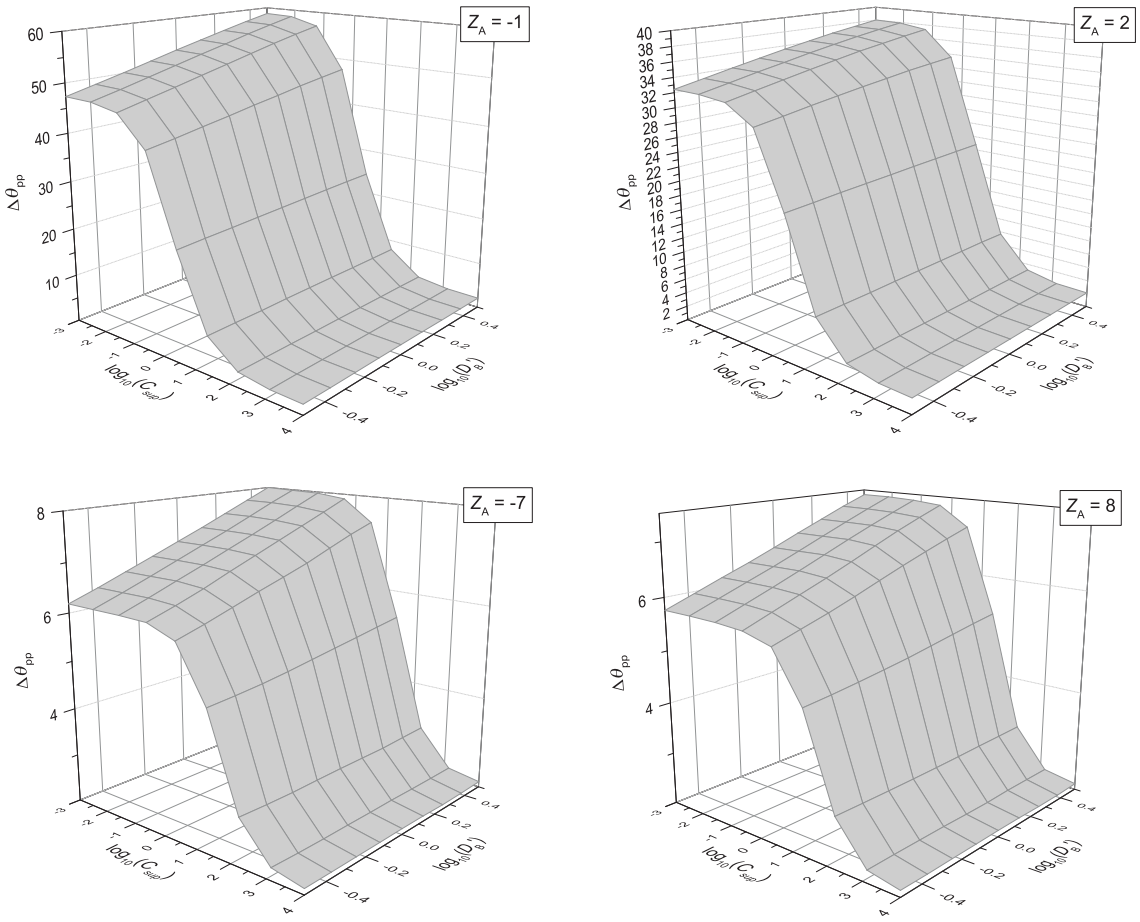

Figure 5.3.8:
Peak to peak separation, $\Delta\theta_{\mathrm{pp}}$, as a function of support ratio, C_{sup}, and diffusion coefficient of species B, D'_{B}. The redox reaction is $A^{Z_{\mathrm{A}}} + e^- \rightleftharpoons B^{Z_{\mathrm{B}}}$. $\sigma = 10^5$ and $D'_{\mathrm{A}} = D'_{\mathrm{M}} = D'_{\mathrm{X}}$.

Figure 5.3.8 shows the peak to peak separation, $\Delta\theta_{\mathrm{pp}}$, as a function of the support ratio, C_{sup}, and the diffusion coefficient of species B, D'_{B}. The scan rate, σ, is 10^5. At low support ratios, $\Delta\theta_{\mathrm{pp}}$ increases with increasing D'_{B}. Species B is formed at the electrode surface. As D'_{B} increases, species B moves into bulk solution more rapidly and the self supported contribution to the ionic strength at the surface of the electrode is less. This effect becomes more pronounced as the charge, hence ionic strength, of species B increases. As the concentration of supporting electrolyte

increases, the contribution from self support becomes relatively less important and the peak to peak separation does not vary with D'_{B}. As expected, the concentration of supporting electrolyte required to achieve this effect increases as the charge of the analyte ion increases. Figure 5.3.9 shows cyclic voltammetry from different points in figure 5.3.8. Figure 5.3.10 shows the forward peak current, J_{pf}, as a function of

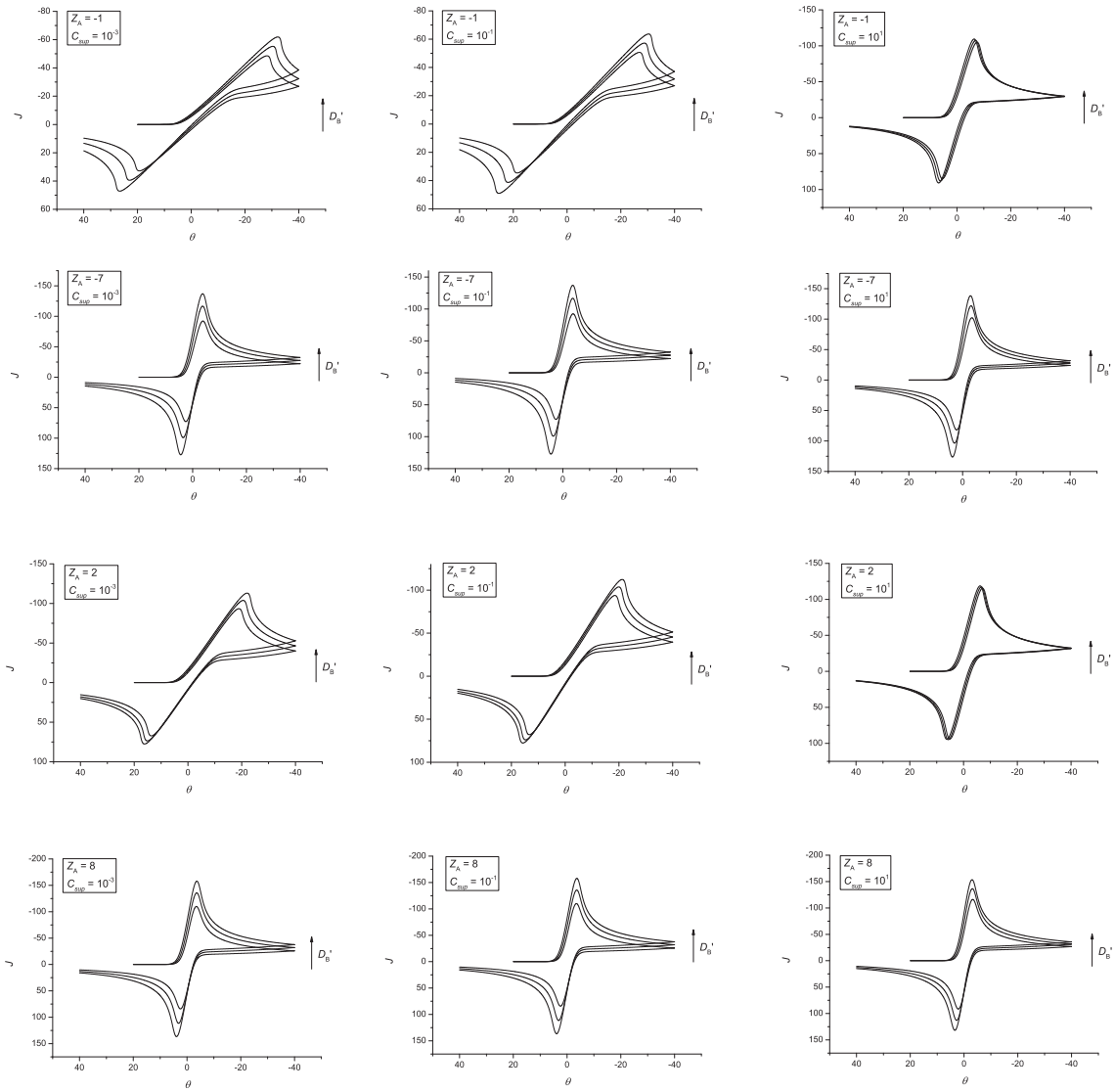

Figure 5.3.9:
Cyclic voltammetry from different points in figure 5.3.8. The values of D'_{B} *are* $10^{-0.5}$, 10^{0} *and* $10^{0.5}$. *The redox reaction is* $A^{Z_{\mathrm{A}}} + e^{-} \rightleftharpoons B^{Z_{\mathrm{B}}}$. $\sigma = 10^{5}$ *and* $D'_{\mathrm{A}} = D'_{\mathrm{M}} = D'_{\mathrm{X}}$.

the support ratio, C_{sup}, and the diffusion coefficient of species B, D'_{B}. The scan rate,

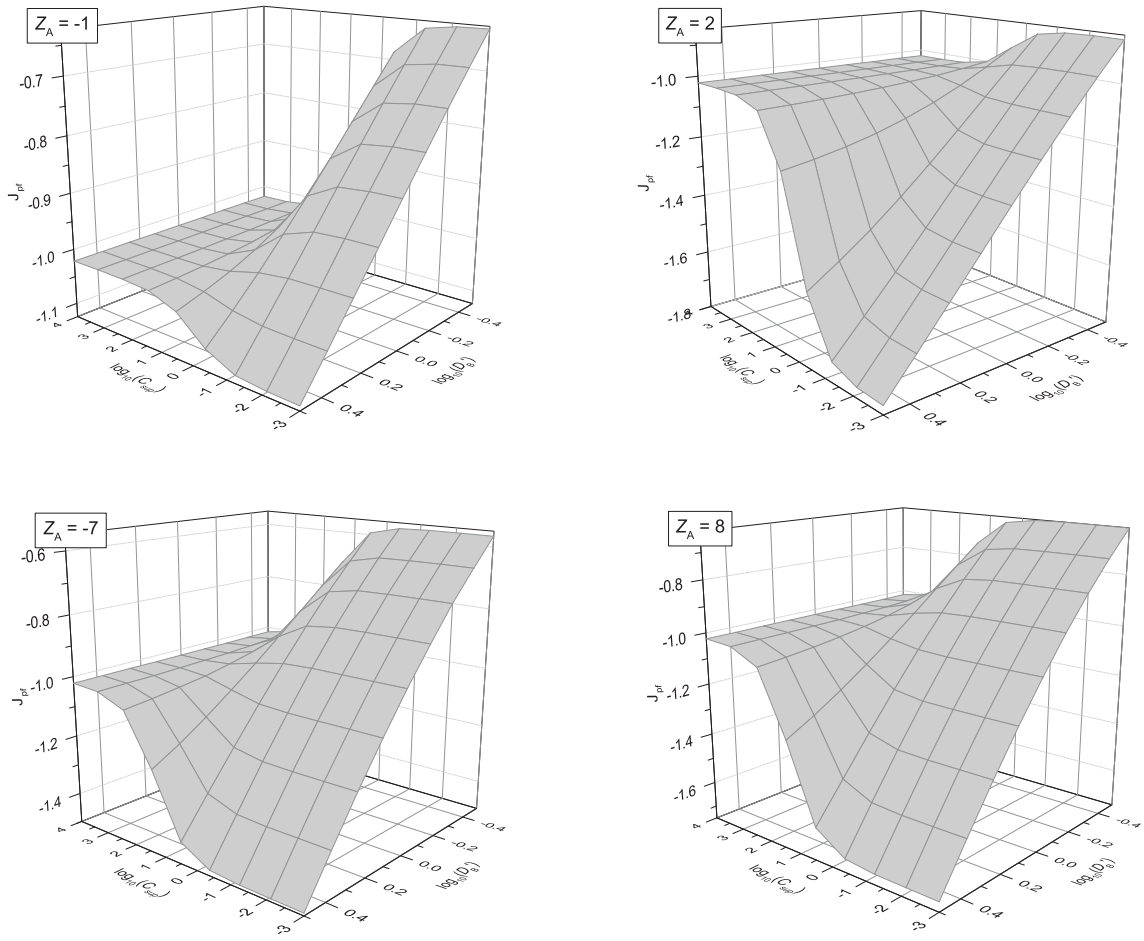

Figure 5.3.10:
Peak current, J_{pf}, as a function of support ratio, C_{sup}, and diffusion coefficient of species B, D'_{B}. The redox reaction is $A^{Z_{\mathrm{A}}} + e^- \rightleftharpoons B^{Z_{\mathrm{B}}}$. $\sigma = 10^{-2}$ and $D'_{\mathrm{A}} = D'_{\mathrm{M}} = D'_{\mathrm{X}}$.

σ, is 10^{-2}. At low support ratios, the magnitude of J_{pf} increases with increasing D'_{B}. As species B becomes more itinerant, the net charge at the electrode surface becomes larger and more species A is required to neutralise that charge. This effect becomes more pronounced as the charge, hence ionic strength, of the analyte ions increases. As the concentration of supporting electrolyte increases, the contribution from self support becomes relatively less important and the forward peak current separation does not vary with D'_{B}. As expected, the concentration of supporting electrolyte required to achieve this effect increases as the charge on the analyte ion

increases. Figure 5.3.11 shows cyclic voltammetry from different points in figure 5.3.10.

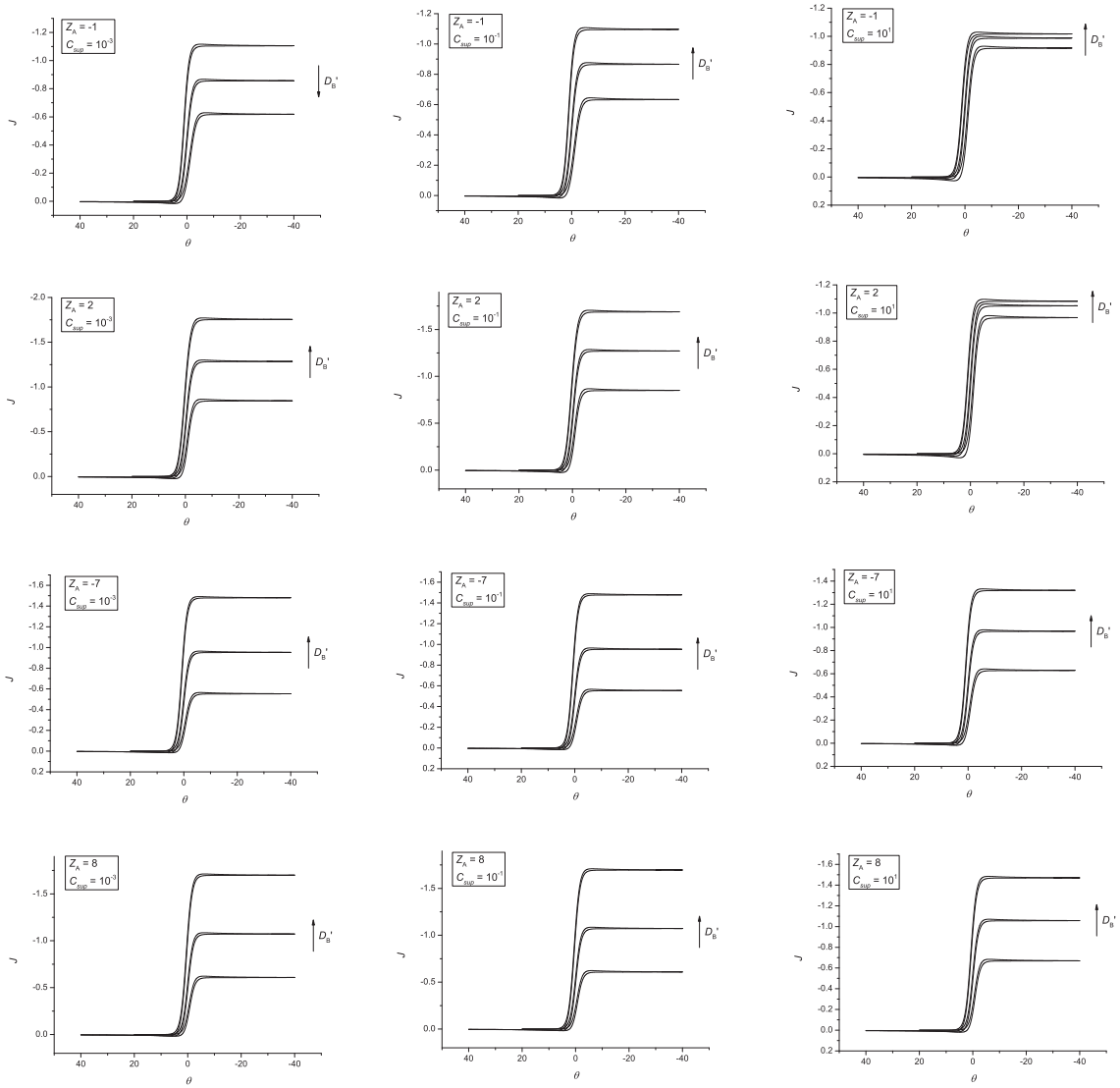

Figure 5.3.11:
Cyclic voltammetry from different points in figure 5.3.10. The values of D'_{B} *are* $10^{-0.5}$, 10^{0} *and* $10^{0.5}$. *The redox reaction is* $A^{Z_{\mathrm{A}}} + e^{-} \rightleftharpoons B^{Z_{\mathrm{A}}-1}$. $\sigma = 10^{-2}$ *and* $D'_{\mathrm{A}} = D'_{\mathrm{M}} = D'_{\mathrm{X}}$.

5.3.5 Effect of the number of electrons transferred (n)

The effect of the number of transferred electrons is studied with respect to the following redox couples:

$$\mathrm{A}^{-3+n} + n\mathrm{e}^- \rightleftharpoons \mathrm{B}^{-3} \tag{5.3.10}$$

$$\mathrm{A}^{-8+n} + n\mathrm{e}^- \rightleftharpoons \mathrm{B}^{-8} \tag{5.3.11}$$

Figure 5.3.12 shows the peak to peak separation ratios as a function of the support

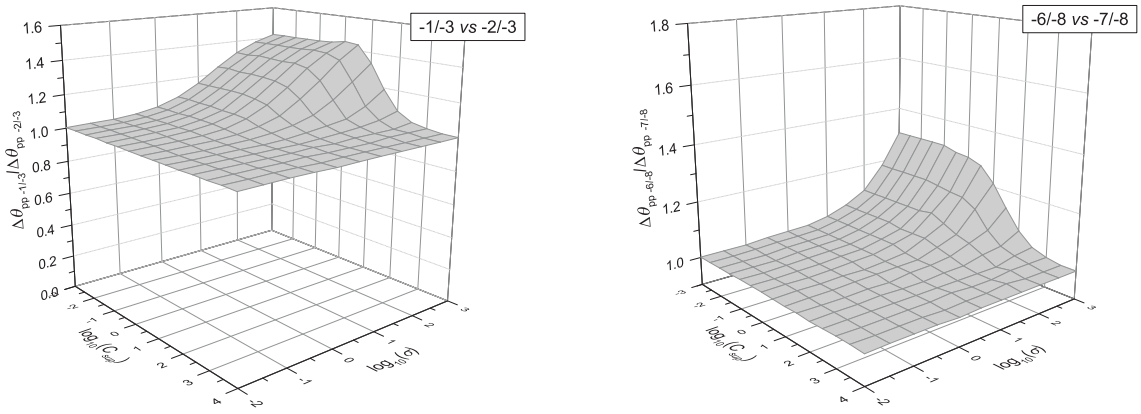

Figure 5.3.12:
Peak to peak separation ratios as a function of the support ratio, C_{sup}, and the scan rate, σ. The redox reaction is $A^{Z_{\mathrm{A}}} + 2e^- \rightleftharpoons B^{Z_{\mathrm{A}}-1}$. $D'_{\mathrm{A}} = D'_{\mathrm{B}} = D'_{\mathrm{M}} = D'_{\mathrm{X}}$.

ratio, C_{sup}, and the scan rate, σ. At high support ratios, peak to peak separations are equal because migration much less important than diffusion. The peak to peak separation does not vary as a function of *either* peak height or peak to peak separation. At low scan rates, peak to peak separations all tend towards infinity (steady state sigmoidal CVs) and therefore the ration of peak to peak separations tends to equality. The discrepancy in $\Delta\theta_{\mathrm{pp}}$ increases with increasing scan rate and decreasing support ratio because more extensive migration is required when two

charges are generated at an electrode as compared to only one. The ohmic drop in the former case is therefore larger, leading a greater $\Delta\theta_{\mathrm{pp}}$ value. This increase is more significant for ions of lower charge because, under conditions of self support, the ionic strength, and hence also the ability to neutralise excess charge, is smaller. Figure 5.3.13 shows the forward peak current ratios as a function of the support

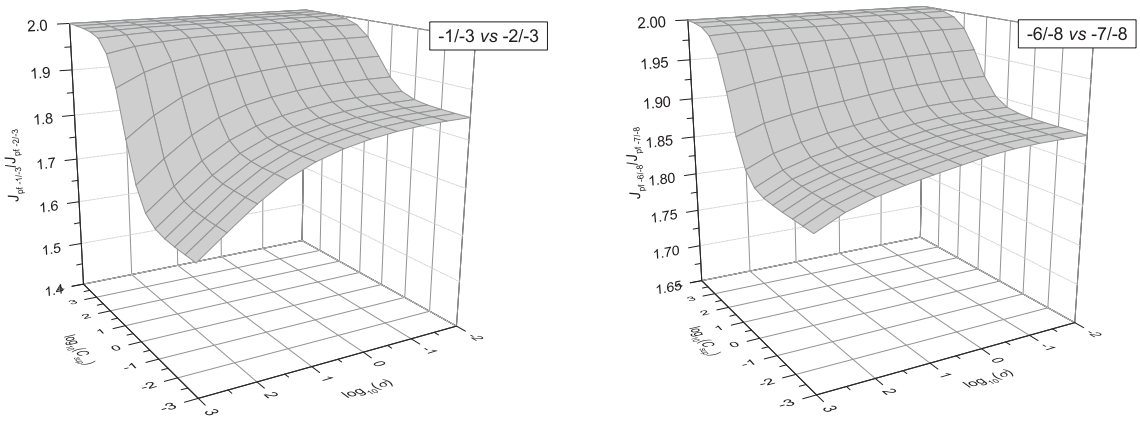

Figure 5.3.13:
Forward peak current ratios as a function of the support ratio, C_{sup}, and the scan rate, σ. The redox reaction is $A^{Z_{\mathrm{A}}} + 2e^- \rightleftharpoons B^{Z_{\mathrm{B}}-1}$. $D'_{\mathrm{A}} = D'_{\mathrm{B}} = D'_{\mathrm{M}} = D'_{\mathrm{X}}$.

ratio, C_{sup}, and the scan rate, σ. At high support ratios, forward peak current ratios are equal because migration much less important than diffusion. The forward peak current ratios is simply equal to the ratio of the transferred electrons (= 2). The discrepancy in J_{pf} increases with increasing scan rate and decreasing support ratio because more extensive migration is required when two charges are generated at an electrode as compared to only one. Since this is a reduction reaction, negative charge is generated at the electrode surface and must therefore be compensated for by the migration of negatively charged analyte ions away from the electrode surface. Fewer analyte ions are required to migrate away from the electrode surface and the charge on the analyte ions increases and as the number of electrons transferred at

the electrode decreases.

5.4 Conclusion

The cyclic voltammetry of the E reduction, $A^{Z_A} + ne^- \rightleftharpoons B^{Z_B}$, has been studied using numerical simulations. The effect of adding different concentrations of supporting electrolyte has been studied as a function of the scan rate, the diffusion coefficient of species B, the diffusion coefficients of the ions in the supporting electrolyte and the charges of the analyte ions.

The minimum support ratio required observe quantitative diffusion-only cyclic voltammetry has been shown to vary as a function of the scan rate, σ, the diffusion coefficients of the supporting electrolyte, D'_M and D'_X, and the charge of the analyte ion, Z_A. The diffusion coefficient of species B has been show to have no effect on the peak to peak separation close to the diffusion-only limit (although it will change the peak position).

Bibliography

[1] Belding, S. R.; Compton, R. G. *J. Electroanal. Chem.* **2012**, *683*, 1–13.

[2] Nicholson, R. S.; Shain, I. *Anal. Chem.* **1964**, *36*, 706–723.

[3] Kachoosangi, R. T.; Wildgoose, G. G.; Compton, R. G. *Analyst* **2008**, *133*, 888–895.

[4] Xiong, L.; Batchelor-McAuley, C.; Gonalves, L. M.; Rodrigues, J. A.; Compton, R. G. *Biosensors and Bioelectronics* **2011**, *26*, 4198 – 4203.

[5] Kozub, B. R.; Rees, N. V.; Compton, R. G. *Sensors and Actuators B: Chemical* **2010**, *143*, 539 – 546.

[6] Huang, X.-J.; Aldous, L.; OMahony, A. M.; del Campo, F. J.; Compton, R. G. *Analytical Chemistry* **2010**, *82*, 5238–5245, PMID: 20469834.

[7] Belding, S. R.; Campbell, F. W.; Dickinson, E. J. F.; Compton, R. G. *Phys. Chem. Chem. Phys.* **2010**, *12*, 11208–11221.

[8] Laborda, E.; Wang, Y.; Henstridge, M. C.; Martnez-Ortiz, F.; Molina, A.; Compton, R. G. *Chemical Physics Letters* **2011**, *512*, 133 – 137.

[9] Albery, J. *Electrode Kinetics*; OUP, 1975.

[10] Bard, A. J.; Faulkner, L. R. *Electrochemical Methods, Fundamentals and Applications*, 2nd ed.; John Wiley & Sons Inc.: Hoboken, NJ, 2001.

[11] Belding, S. R.; Limon-Petersen, J. G.; Dickinson, E. J. F.; Compton, R. G. *Angew. Chem. Int. Ed.* **2010**, *49*, 9242–9245.

[12] Norton, J. D.; White, H. S. *J. Electroanal. Chem.* **1992**, *325*, 341–350.

[13] Alden, J. A.; Bond, A. M.; Colton, R.; Compton, R. G.; Eklund, J. C.; Mah, Y. A.; Mahon, P. J.; Tedesco, V. *J. Electroanal. Chem.* **1998**, *447*, 155 – 171.

[14] Bond, A. M.; Coomber, D. C.; Feldberg, S. W.; Oldham, K. B.; Vu, T. *Anal. Chem.* **2001**, *73*, 352–359.

[15] Bond, A. M.; Feldberg, S. W. *J. Phys. Chem. B* **1998**, *102*, 9966–9974.

[16] Smith, C. P.; White, H. S. *Anal. Chem.* **1993**, *65*, 3343–53.

[17] Norton, J. D.; Benson, W. E.; White, H. S.; Pendley, B. D.; Abruña, H. D. *Anal. Chem.* **1991**, *63*, 1909–1914.

[18] Amatore, C.; Bento, M. F.; Montenegro, M. I. *Anal. Chem.* **1995**, *67*, 2800–2811.

[19] Amatore, C.; Deakin, M. R.; Wightman, R. *J. Electroanal. Chem.* **1987**, *225*, 49 – 63.

[20] Compton, R. G.; Banks, C. E. *Understanding Voltammetry*, 2nd ed.; World Scientific: Singapore, 2010.

[21] Dickinson, E. J. F.; Limon-Petersen, J. G.; Rees, N. V.; Compton, R. G. *J. Phys. Chem. C* **2009**, *113*, 11157–11171.

[22] Oldham, K. B.; Zoski, C. G. In *Mass Transport to Electrodes. In ComprehensiVe Chemical Kinetics*; Bamford, C. H., Compton, R. G., Eds.; Elsevier: Amsterdam, The Netherlands, 1986; Vol. 26.

[23] Dickinson, E. J.; Limon-Petersen, J. G.; Compton, R. G. *J. Solid State Electrochem.* **2011**, *15*, 1335–1345.

[24] Klymenko, O. V.; Amatore, C.; Svir, I. *Anal. Chem.* **2007**, *79*, 6341–6347.

[25] Svir, I. B.; Oleinick, A. I.; Compton, R. G. *Radiotekhnika* **2001**, *116*, 114.

[26] Crank, J.; Nicolson, E. *Proc. Camb. Phil. Soc.* **1947**, *43*, 50–67.

[27] Störzbach, M.; Heinze, J. *J. Electroanal. Chem.* **1993**, *346*, 1 – 27, An International Journal Devoted to all Aspects of Electrode Kinetics, Interfacial Structure, Properties of Electrolytes, Colloid and Biological Electrochemistry.

[28] Press, W. H., Teukolsky, S. A., Vetterling, W. T., Flannery, B. P., Eds. *Numerical Recipes: The Art of Scientific Computing*; Cambridge University Press, 2007.

[29] Limon-Petersen, J. G.; Streeter, I.; Rees, N. V.; Compton, R. G. *J. Phys. Chem. C* **2009**, *113*, 333–337.

[30] Limon-Petersen, J. G.; Dickinson, E. J. F.; Rees, N. V.; Compton, R. G. *J. Phys. Chem. C* **2009**, *113*, 15320–15325.

[31] Limon-Petersen, J. G.; Han, J. T.; Rees, N. V.; Dickinson, E. J. F.; Streeter, I.; Compton, R. G. *J. Phys. Chem. C* **2010**, *114*, 2227–2236.

[32] Cooper, J. B.; Bond, A. M.; Oldham, K. B. *J. Electroanal. Chem.* **1992**, *331*, 877–895.

[33] Randles, J. E. B. *Trans. Faraday Soc.* **1948**, *44*, 327–338.

[34] Sevcik, A. *Collect. Czech. Chem. Commun.* **1948**, *13*, 349–377.

Chapter 6

Diffusion-migration voltammetry: extra kinetic and mechanistic insights

Despite it's relatively low cost, voltammetry is an astonishingly powerful technique with which reaction mechanisms can be determined. There exist, however, some reactions that cannot by conclusively elucidated voltammetrically if, as is common, mass transport occurs by diffusion alone. This chapter extends the usefulness of voltammetry to an important class of such mechanisms by utilising mass transport that occurs by a combination of diffusion and migration. This chapter therefore extends the work presented in chapter 5. The work presented in this thesis has been published as an article in Angewandte Chemie International Edition.[1]

6.1 Introduction

In a quiescent voltammetric experiment, there are two modes of mass transport: diffusion and migration. Diffusion is an entropic process and is undergone by any species in a system above absolute zero. In contrast, migration is exclusive to ions and can be suppressed by the addition of excess inert electrolyte ('supporting electrolyte'). These 'diffusion-only' systems are conventionally used by researchers because the modeling is greatly simplified and the results are relatively easy to rationalise through the use of suitable equations or simulations.[2–4]

When electrolysis occurs in a solution, ions migrate due to the resulting potential gradient in order to minimise charge separation in the solution. The rate at which a solution can respond to an applied potential is therefore limited by the rate at which ions can migrate to disperse the change in potential gradient at the electrode. Because the response of the system is not instantaneous, there is a difference between the potential applied at the electrode and the effective potential experienced by the solution adjacent to the electrode surface. Traditionally, this discrepancy is called the 'ohmic drop' however, since Ohm's law is not obeyed, the term 'potential drop' is preferred.[5] The resulting voltammogram is distorted both by the complicated mass transport, which is a combination of diffusion and migration, and also by the potential drop at the electrode surface. Both effects can be suppressed by adding large quantities of inert, or 'supporting', electrolyte to the solution. As the concentration of supporting electrolyte increases the potential gradient is compressed towards the electrode surface. In other words, charge separation caused by the

heterogeneous process can be dispersed more effectively by a greater number of ions. The solution can therefore respond more rapidly to changes in the applied potential and the potential drop at the electrode surface is suppressed.

When the concentration of supporting electrolyte is high (approximately 1 M), the potential gradient is confined to within a region *ca.* 10 nm from the electrode surface and electrons can tunnel directly between the electrode and bulk solution. Therefore, at no point in the system does mass transport take place in the presence of a significant potential gradient: migration has been eliminated. Dickinson *et al.*[6] have shown that, as a general rule, transient voltammetry can be considered purely diffusional if the supporting electrolyte is present in a concentration greater than 100 times that of the electroactive species.

While voltammetric results obtained using diffusion-only conditions are useful, several situations exist in which kinetic and mechanistic information can be unobtainable or ambiguous. For example and in particular, stepwise two electron reactions are commonly encountered in electrochemistry and have been reviewed by Evans, himself a noted contributer to the field[7,8]

$$\mathrm{A} + \mathrm{e}^- \rightleftharpoons \mathrm{B} \quad E^{\ominus}_{\mathrm{f,A/B}} \tag{6.1.1}$$

$$\mathrm{B} + \mathrm{e}^- \rightleftharpoons \mathrm{C} \quad E^{\ominus}_{\mathrm{f,B/C}} \tag{6.1.2}$$

$$\mathrm{A} + \mathrm{C} \rightleftharpoons 2\mathrm{B} \tag{6.1.3}$$

Comproportionation between species A and C is thermodynamically favourable when the formal potential of the second step is much more negative than the first

($E^{\ominus}_{\mathrm{f,A/B}} > E^{\ominus}_{\mathrm{f,B/C}}$). This situation is commonly encountered because the electron added in the first step repels the electron added in the second. Insightful pioneering work by Savéant and Andrieux[9] has shown that voltammetry is necessarily blind to the presence of comproportionation in situations where both electron transfers are reversible and the diffusion coefficients of species A, B and C are equal. In addition, it has been shown numerically that, when the values of the diffusion coefficients are similar, the presence or absence of comproportionation, as determined by means of voltammetric techniques, is ambiguous;[10] the current-voltage curves are almost identical regardless of whether comproportionation takes place or not. This frequently occurs because the substrate and product in a heterogeneous reaction are often structurally very similar, leading to similar diffusion coefficients for A, B and C. It possible to voltammetrically distinguish the presence of comproportionation in situations where the diffusion coefficients differ significantly: for example in ionic liquid solvents,[11] where ions of higher charge interact more strongly with the solvent, or in solvents of low polarity,[10] where ions of different charge associate to different extents with ions of the supporting electrolyte. In each case, electroactive ions of higher charge move more slowly in solution and therefore possess smaller diffusion coefficients. In addition, Evans has demonstrated that it is possible to resolve mechanistic information when the second electron transfer is irreversible.[12] In other situations, it is necessary to use non-voltammetric techniques to provide evidence for the comproportionation reaction. For example, Savéant and Andrieux have used electron spin resonance.[9] It is useful to develop a voltammetric technique that can resolve reaction mechanisms of this type, and others, unambiguously.

One possible solution is to perform the experiments in the presence of a low concentration of supporting electrolyte. Under such conditions, as will be shown below, voltammetric equivalence is not observed, even when the diffusion coefficients of A, B and C are equal, owing to the inclusion of a migrational term in the mass transport equations.

Electrochemistry in weakly supported media is most useful when a theoretical model can be obtained, either analytically or numerically, to explain the experimental observations. In 1987, Amatore[13] was first to construct such a model, for a simple E reaction. Several more complicated mechanisms have been studied since.[13–17] Most publications to date have only considered systems at steady state, owing to the lack of a reliable model with which to describe transient experiments. Bond, Feldberg and Oldham were first to publish work under the latter conditions.[18–20] The authors relied on simulations based on an explicit, as opposed to an implicit, system of equations. The resulting simulations could only simulate heterogeneous systems and, furthermore, all diffusion coefficients had to be similar. In addition, the authors, perhaps unknowingly, made a serious approximation by assuming the concentration and potential profiles to be linear at disc shaped electrodes over short timescales. In the experience of the present authors, while it is possible to obtain linear concentration profiles under such conditions, potential profiles are necessarily much larger and can be hemispherical. Consequently, the simulated results of Bond *et al.* compared rather poorly with experimental data.[19,20] Recently, Streeter *et al.*[21] published work on transient systems using a more robust simulation technique. The theory was based on the 'zero field' approximation which states that, when the

electrode is sufficiently large (> 1 μm), it is valid to consider the electrical double layer to be infinitely thin compared to the diffusion layer. It follows, from Gauss's law, that the derivative of the potential at the outside edge of the double layer is equal to zero. The theory has been successfully applied to experimental systems involving only heterogeneous processes.[22–24]

The EE mechanism considered here has been studied numerically by Norton *et al.*,[25,26] analytically by Amatore *et al.*[27] and experimentally by Kowski *et al.*[28] All considered exclusively steady-state conditions and the theoretical treatments applied only to extreme cases in which comproportionation was either absent or exclusively diffusionally controlled. In the present chapter, a more general model is used to numerically simulate this process at a range of comproportionation rates, under both steady-state and transient conditions, with an arbitrary set of diffusion coefficients. In Section 6.5, numerical simulations, using the model of Streeter *et al.*[21] described above, are used to explore the behaviour of this system as a function of several variables. The simulations are applied to the electroreduction of anthraquinone (figure 6.1.1) in acetonitrile, for which diffusion controlled comproportionation is shown to occur. When using cyclic voltammetry to elucidate a reaction mechanism, it is good practice to compare theory and experiment over a range of scan rates (covering linear to convergent diffusion regimes). This improves the reliability of the data because the relative sensitivity of the voltammetry to each of the parameters changes with the experimental timescale. In this chapter it is shown that, in addition, the sensitivity of the voltammetry to many of the parameters varies with the concentration of supporting electrolyte. In the experimental study presented here, the validity of

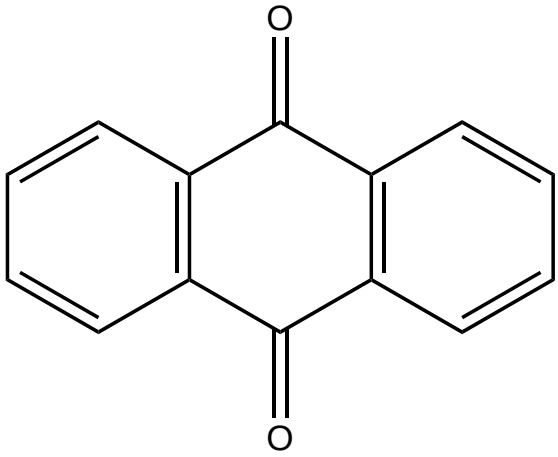

Figure 6.1.1:
Structure of anthraquinone, AQ.

the data is improved considerably by comparing theory and experiment over a range of scan rates and a range of concentrations of the supporting electrolyte.

We anticipate electrochemistry in solutions of variable ionic strength is therefore likely to become widely used and is expected to greatly enhance the scope of voltammetry in detecting kinetic and thermodynamic parameters.

6.2 Theory

All symbols used in this chapter are defined in the glossary.

6.2.1 Reaction mechanism

We consider a solution containing an electroactive species, A, which is capable of undergoing two, reversible, single electron reductions, forming species B and C respectively. These heterogeneous processes occur at a hemispherical electrode and imply an additional homogeneous comproportionation/disproportionation equilib-

rium

$$\mathrm{A}^{z_\mathrm{A}} + \mathrm{e}^- \rightleftharpoons \mathrm{B}^{z_\mathrm{A}-1} \quad E^\ominus_{\mathrm{f,A/B}} \tag{6.2.1}$$

$$\mathrm{B}^{z_\mathrm{A}-1} + \mathrm{e}^- \rightleftharpoons \mathrm{C}^{z_\mathrm{A}-2} \quad E^\ominus_{\mathrm{f,B/C}} \tag{6.2.2}$$

$$\mathrm{A}^{z_\mathrm{A}} + \mathrm{C}^{z_\mathrm{A}-2} \rightleftharpoons 2\mathrm{B}^{z_\mathrm{A}-1} \quad K_\mathrm{eqm} = \frac{k_\mathrm{comp}}{k_\mathrm{disp}} \tag{6.2.3}$$

Species A is accompanied by a counterion, $\mathrm{Y}^{-z_\mathrm{A}}$, and the solution is supported by a monovalent 1:1 inert salt, $\mathrm{M}^+\mathrm{X}^-$. In this chapter, z_A is relatively small and ion pairing is assumed to be completely absent in solution. The equilibrium constant for comproportionation, K_eqm, depends on the formal potentials for both of the heterogeneous steps, $E^\ominus_{\mathrm{f,A/B}}$ and $E^\ominus_{\mathrm{f,B/C}}$

$$K_\mathrm{eqm} = \exp\left(\frac{F}{RT}(E^\ominus_{\mathrm{f,A/B}} - E^\ominus_{\mathrm{f,B/C}})\right) \tag{6.2.4}$$

In this chapter, $E^\ominus_{\mathrm{f,A/B}} \gg E^\ominus_{\mathrm{f,B/C}}$: thermodynamically, the comproportionation reaction is favoured.

6.2.2 Mathematical formulation

The concentration of each species varies in space and time according to the mass transport equations

$$
\begin{aligned}
\frac{\partial c_{\mathrm{A}}}{\partial t} &= D_{\mathrm{A}}\left(\frac{\partial^2 c_{\mathrm{A}}}{\partial r^2}+\frac{2}{r}\frac{\partial c_{\mathrm{A}}}{\partial r}\right)+D_{\mathrm{A}}z_{\mathrm{A}}\left(\frac{\partial c_{\mathrm{A}}}{\partial r}\frac{\partial \phi}{\partial r}+c_{\mathrm{A}}\frac{\partial^2 \phi}{\partial r^2}+c_{\mathrm{A}}\frac{2}{r}\frac{\partial \phi}{\partial r}\right)-k_{\mathrm{comp}}c_{\mathrm{A}}c_{\mathrm{C}}+k_{\mathrm{disp}}c_{\mathrm{B}}^2\\
\frac{\partial c_{\mathrm{B}}}{\partial t} &= D_{\mathrm{B}}\left(\frac{\partial^2 c_{\mathrm{B}}}{\partial r^2}+\frac{2}{r}\frac{\partial c_{\mathrm{B}}}{\partial r}\right)+D_{\mathrm{B}}(z_{\mathrm{A}}-1)\left(\frac{\partial c_{\mathrm{B}}}{\partial r}\frac{\partial \phi}{\partial r}+c_{\mathrm{B}}\frac{\partial^2 \phi}{\partial r^2}+c_{\mathrm{B}}\frac{2}{r}\frac{\partial \phi}{\partial r}\right)+2k_{\mathrm{comp}}c_{\mathrm{A}}c_{\mathrm{C}}-2k_{\mathrm{disp}}c_{\mathrm{B}}^2\\
\frac{\partial c_{\mathrm{C}}}{\partial t} &= D_{\mathrm{C}}\left(\frac{\partial^2 c_{\mathrm{C}}}{\partial r^2}+\frac{2}{r}\frac{\partial c_{\mathrm{C}}}{\partial r}\right)+D_{\mathrm{C}}(z_{\mathrm{A}}-2)\left(\frac{\partial c_{\mathrm{C}}}{\partial r}\frac{\partial \phi}{\partial r}+c_{\mathrm{C}}\frac{\partial^2 \phi}{\partial r^2}+c_{\mathrm{C}}\frac{2}{r}\frac{\partial \phi}{\partial r}\right)-k_{\mathrm{comp}}c_{\mathrm{A}}c_{\mathrm{C}}+k_{\mathrm{disp}}c_{\mathrm{B}}^2\\
\frac{\partial c_{\mathrm{M}}}{\partial t} &= D_{\mathrm{M}}\left(\frac{\partial^2 c_{\mathrm{M}}}{\partial r^2}+\frac{2}{r}\frac{\partial c_{\mathrm{M}}}{\partial r}\right)+D_{\mathrm{M}}(z_{\mathrm{M}})\left(\frac{\partial c_{\mathrm{M}}}{\partial r}\frac{\partial \phi}{\partial r}+c_{\mathrm{M}}\frac{\partial^2 \phi}{\partial r^2}+c_{\mathrm{M}}\frac{2}{r}\frac{\partial \phi}{\partial r}\right)\\
\frac{\partial c_{\mathrm{X}}}{\partial t} &= D_{\mathrm{X}}\left(\frac{\partial^2 c_{\mathrm{X}}}{\partial r^2}+\frac{2}{r}\frac{\partial c_{\mathrm{X}}}{\partial r}\right)+D_{\mathrm{X}}(z_{\mathrm{X}})\left(\frac{\partial c_{\mathrm{X}}}{\partial r}\frac{\partial \phi}{\partial r}+c_{\mathrm{X}}\frac{\partial^2 \phi}{\partial r^2}+c_{\mathrm{X}}\frac{2}{r}\frac{\partial \phi}{\partial r}\right)\\
\frac{\partial c_{\mathrm{Y}}}{\partial t} &= D_{\mathrm{Y}}\left(\frac{\partial^2 c_{\mathrm{Y}}}{\partial r^2}+\frac{2}{r}\frac{\partial c_{\mathrm{Y}}}{\partial r}\right)+D_{\mathrm{Y}}(-z_{\mathrm{A}})\left(\frac{\partial c_{\mathrm{Y}}}{\partial r}\frac{\partial \phi}{\partial r}+c_{\mathrm{Y}}\frac{\partial^2 \phi}{\partial r^2}+c_{\mathrm{Y}}\frac{2}{r}\frac{\partial \phi}{\partial r}\right)
\end{aligned}
$$

Each equation is composed of three terms. The first quantifies diffusion, the second migration, and the third quantifies the homogeneous chemical reaction. Since species M, X and Y are chemically inert, the latter term in the respective mass transport equations is equal to zero. This system of 6 independent equations contains 7 unknowns: the concentration for the each of the 6 species and an additional term for the potential. Consequently, the description of the problem is incomplete and a further relationship must be introduced. For this purpose, we invoke the Poisson equation

$$
\frac{\partial^2 \phi}{\partial r^2}+\frac{2}{r}\frac{\partial \phi}{\partial r}=-\frac{F}{\epsilon_{\mathrm{r}}\epsilon_0}\sum_{\mathrm{s}} z_{\mathrm{s}}c_{\mathrm{s}}=-\frac{F}{\epsilon_{\mathrm{r}}\epsilon_0}[z_{\mathrm{A}}c_{\mathrm{A}}+(z_{\mathrm{A}}-1)c_{\mathrm{B}}+(z_{\mathrm{A}}-2)c_{\mathrm{C}}+z_{\mathrm{M}}c_{\mathrm{M}}+z_{\mathrm{X}}c_{\mathrm{X}}-z_{\mathrm{A}}c_{\mathrm{Y}}] \tag{6.2.5}
$$

This relationship follows from Maxwell's equations; however, many workers have attempted to simplify the problem by invoking, instead, the electroneutrality ap-

proximation

$$0 = -\frac{F}{\epsilon_r \epsilon_0} \sum_s z_s c_s = -\frac{F}{\epsilon_r \epsilon_0} [z_A c_A + (z_A - 1)c_B + (z_A - 2)c_C + z_M c_M + z_X c_X - z_A c_Y] \tag{6.2.6}$$

In the experience of the present authors, this relationship, although well obeyed over the majority of simulation space, does not significantly increase simulation efficiency. It is therefore regarded in the presented work as an unnecessary, additional, approximation.

The mass transport equations and the Poisson equation can be solved in the region $r_e \leq r \leq \infty$ subject to a set of boundary conditions. However, the problem is considerably simplified, without affecting the result, by defining a finite upper limit, $r = r_{max}$. In this chapter

$$r_{max} = r_e + 6\sqrt{D_{max} t} \tag{6.2.7}$$

where D_{max} is the diffusion coefficient of the fastest moving species in solution.[29] Beyond the point $r = r_{max}$, all concentrations are temporally invariant and the flux of each species at can be set equal to zero at all times. In addition, it follows, from the Poisson equation combined with electroneutrality, that at $r = r_{max}$

$$\frac{\partial^2 \phi}{\partial r^2}\Big|_{r=r_{max}} = 0 \tag{6.2.8}$$

Integrating this equation subject to the condition $\theta \to 0$ as $r \to \infty$ leads to a

boundary condition for the potential at $r = r_{\max}$

$$\left.\frac{\partial \phi}{\partial r}\right|_{r=r_{\max}} = -\frac{\phi}{r} \tag{6.2.9}$$

The complete set of boundary conditions for the problem are

$t = 0$, all r	$c_{\mathrm{A}} = c_{\mathrm{A}}^*$	$c_{\mathrm{B}} = 0$	$c_{\mathrm{C}} = 0$	$c_{\mathrm{Y}} = c_{\mathrm{A}}^*$
	$c_{\mathrm{M}} = c_{\mathrm{M}}^*$	$c_{\mathrm{X}} = c_{\mathrm{M}}^*$	$\phi = 0$	
$t > 0$, $r = r_{\max}$	$\left.\frac{\partial c_{\mathrm{A}}}{\partial r}\right\|_{r=r_{\max}} = 0$	$\left.\frac{\partial c_{\mathrm{B}}}{\partial r}\right\|_{r=r_{\max}} = 0$	$\left.\frac{\partial c_{\mathrm{C}}}{\partial r}\right\|_{r=r_{\max}} = 0$	$\left.\frac{\partial c_{\mathrm{Y}}}{\partial r}\right\|_{r=r_{\max}} = 0$
	$\left.\frac{\partial c_{\mathrm{M}}}{\partial r}\right\|_{r=r_{\max}} = 0$	$\left.\frac{\partial c_{\mathrm{X}}}{\partial r}\right\|_{r=r_{\max}} = 0$	$\left.\frac{\partial \phi}{\partial r}\right\|_{r=r_{\max}} = -\frac{\phi}{r}$	

$$\begin{aligned}
t > 0,\ r = r_{\mathrm{e}} \qquad D_{\mathrm{A}} \left.\frac{\partial c_{\mathrm{A}}}{\partial r}\right|_{r=r_{\mathrm{e}}} &= k^0_{\mathrm{A/B}} c_{\mathrm{A},0} \exp\left(-\alpha_{\mathrm{A/B}} \frac{F(E_{\mathrm{app}} - E^{\ominus}_{\mathrm{f,A/B}} - \phi_{\mathrm{PET}})}{RT}\right) \\
&\quad - k^0_{\mathrm{A/B}} c_{\mathrm{B},0} \exp\left((1-\alpha_{\mathrm{A/B}}) \frac{F(E_{\mathrm{app}} - E^{\ominus}_{\mathrm{f,A/B}} - \phi_{\mathrm{PET}})}{RT}\right) \\
D_{\mathrm{B}} \left.\frac{\partial c_{\mathrm{B}}}{\partial r}\right|_{r=r_{\mathrm{e}}} &= -D_{\mathrm{A}} \left.\frac{\partial c_{\mathrm{A}}}{\partial r}\right|_{r=r_{\mathrm{e}}} - D_{\mathrm{C}} \left.\frac{\partial c_{\mathrm{C}}}{\partial r}\right|_{r=r_{\mathrm{e}}} \\
D_{\mathrm{C}} \left.\frac{\partial c_{\mathrm{C}}}{\partial r}\right|_{r=r_{\mathrm{e}}} &= -k^0_{\mathrm{B/C}} c_{\mathrm{B},0} \exp\left(-\alpha_{\mathrm{B/C}} \frac{F(E_{\mathrm{app}} - E^{\ominus}_{\mathrm{f,B/C}} - \phi_{\mathrm{PET}})}{RT}\right) \\
&\quad + k^0_{\mathrm{B/C}} c_{\mathrm{C},0} \exp\left((1-\alpha_{\mathrm{B/C}}) \frac{F(E_{\mathrm{app}} - E^{\ominus}_{\mathrm{f,B/C}} - \phi_{\mathrm{PET}})}{RT}\right) \\
D_{\mathrm{M}} \left.\frac{\partial c_{\mathrm{M}}}{\partial r}\right|_{r=r_{\mathrm{e}}} &= 0 \\
D_{\mathrm{X}} \left.\frac{\partial c_{\mathrm{X}}}{\partial r}\right|_{r=r_{\mathrm{e}}} &= 0 \\
D_{\mathrm{Y}} \left.\frac{\partial c_{\mathrm{Y}}}{\partial r}\right|_{r=r_{\mathrm{e}}} &= 0
\end{aligned}$$

The boundary condition at $r = r_{\mathrm{e}}$ invokes the 'zero field approximation' which states that the double layer at the electrode surface is negligible in extent compared to the diffusion layer, such that the charge on the electrode is fully compensated at $r \approx r_{\mathrm{e}}$. This point is called the 'plane of electron transfer', PET. It follows from Gauss's law that

$$\left.\frac{\partial \phi}{\partial r}\right|_{r=r_{\mathrm{e}}} = 0 \tag{6.2.10}$$

For cyclic voltammetry, the applied potential, E_{app}, varies as a function of time, t, according to

$$E_{\text{app}} = |-vt + E_{\text{start}} - E_{\text{vertex}}| + E_{\text{vertex}} \tag{6.2.11}$$

where E_{start} and E_{vertex} are the starting and vertex potentials respectively.

The flux at surface of the electrode, j, is calculated using

$$j = 2\frac{\partial c_{\text{A}}}{\partial r}\Big|_{r=r_{\text{e}}} + 2\frac{D_{\text{B}}}{D_{\text{A}}}\frac{\partial c_{\text{B}}}{r}\Big|_{r=r_{\text{e}}} \tag{6.2.12}$$

which may be related to the current, i

$$i = 2\pi F c^*_{\text{A}} D_{\text{A}} r_{\text{e}} j \tag{6.2.13}$$

6.3 Novel method for determining the presence of comproportionation

In this section it is shown analytically, for a hemisphere in fully supported media, the steady state $2e^-$ current when comproportionation is absent is equal to that when comproportionation is diffusionally controlled, regardless of the values of D_{A}, D_{B} and D_{C}.

The steady state 2 e^- current in the absence of comproportionation is[2]

$$i = \frac{FAD_{\text{A}}c^*_{\text{A}}j}{r_{\text{e}}} \tag{6.3.1}$$

The mechanism, in the presence of comproportionation, is

$$A + e^- \rightleftharpoons B \tag{6.3.2}$$

$$B + e^- \rightleftharpoons C \tag{6.3.3}$$

$$A + C \rightleftharpoons 2B \tag{6.3.4}$$

The corresponding concentration profile is shown schematically in figure 6.3.1.

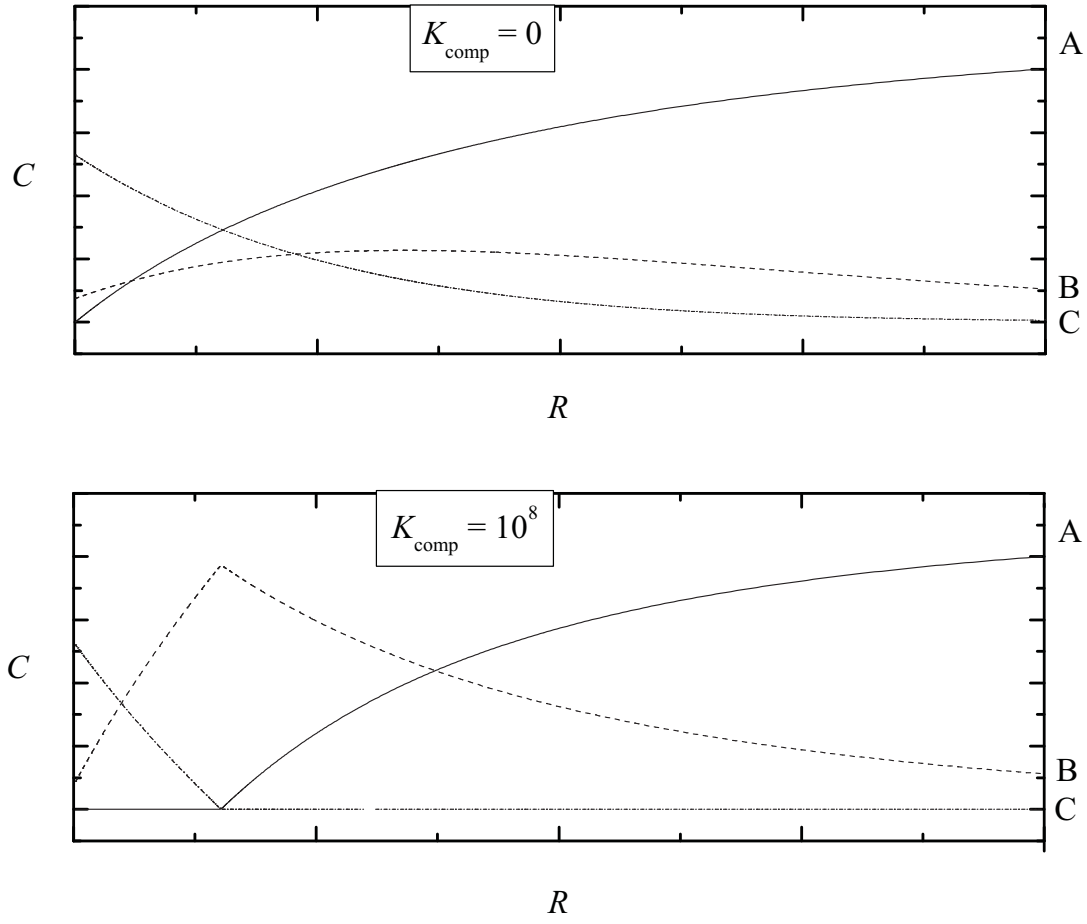

Figure 6.3.1:
Schematic concentration profiles for $K_{comp} = 10^{-8}$ *and* 10^8. *The general shape of each profile is invariant to the kinetic and thermodynamic parameters simulated.*

There is a reaction front, r_{front}, below which species A does not exist and above

which species C does not exist. The problem is solved in two parts: the first for $r \leq r_{\text{front}}$ and the second for $r \geq r_{\text{front}}$. The species names are given the subscripts "l" and "u" in the respective parts of the problem.

6.3.1 Lower part

The mass transport equations are

$$c_{\text{Al}} = 0 \tag{6.3.5}$$

$$D_{\text{B}}\left(\frac{\partial^2 c_{\text{Bl}}}{\partial r^2} + \frac{2}{r}\frac{\partial c_{\text{Bl}}}{\partial r}\right) = 0 \tag{6.3.6}$$

$$D_{\text{C}}\left(\frac{\partial^2 c_{\text{Cl}}}{\partial r^2} + \frac{2}{r}\frac{\partial c_{\text{Cl}}}{\partial r}\right) = 0 \tag{6.3.7}$$

Integration of these equations leads to

$$c_{\text{Al}} = 0 \tag{6.3.8}$$

$$c_{\text{Bl}} = \frac{p_{\text{Bl}}}{r} + q_{\text{Bl}} \tag{6.3.9}$$

$$c_{\text{Cl}} = \frac{p_{\text{Cl}}}{r} + q_{\text{Cl}} \tag{6.3.10}$$

where p_{Bl}, p_{Cl}, q_{Bl}, q_{Cl} are constants of integration. When $r = r_{\text{e}}$, $c_{\text{Bl}} = 0$. Therefore

$$p_{\text{Bl}} + q_{\text{Bl}} = 0 \tag{6.3.11}$$

When $r = r_{\text{e}}$, $\frac{D_{\text{C}}}{D_{\text{A}}}\nabla c_{\text{Cl}} = \frac{D_{\text{B}}}{D_{\text{A}}}\nabla c_{\text{Bl}}$. Therefore

$$-\frac{D_{\text{C}}}{D_{\text{A}}} = \frac{p_{\text{Bl}}}{p_{\text{Bl}}} \tag{6.3.12}$$

When $r = r_{\mathrm{front}}$, $c_{\mathrm{C\,l}} = 0$. Therefore

$$\frac{p_{\mathrm{C\,l}}}{r_{\mathrm{front}}} + q_{\mathrm{C\,l}} = 0 \tag{6.3.13}$$

6.3.2 Upper part

The mass transport equations are

$$D_{\mathrm{A}} \left(\frac{\partial^2 c_{\mathrm{A\,u}}}{\partial r^2} + \frac{2}{r} \frac{\partial c_{\mathrm{A\,u}}}{\partial r} \right) = 0 \tag{6.3.14}$$

$$D_{\mathrm{B}} \left(\frac{\partial^2 c_{\mathrm{B\,u}}}{\partial r^2} + \frac{2}{r} \frac{\partial c_{\mathrm{B\,u}}}{\partial r} \right) = 0 \tag{6.3.15}$$

$$c_{\mathrm{C\,u}} = 0 \tag{6.3.16}$$

Integration of these equations leads to

$$c_{\mathrm{A\,u}} = \frac{p_{\mathrm{A\,u}}}{r} + q_{\mathrm{A\,u}} \tag{6.3.17}$$

$$c_{\mathrm{B\,u}} = \frac{p_{\mathrm{B\,u}}}{r} + q_{\mathrm{B\,u}} \tag{6.3.18}$$

$$c_{\mathrm{C\,u}} = 0 \tag{6.3.19}$$

When $r = r_{\mathrm{front}}$, $c_{\mathrm{A\,u}} = 0$. Therefore

$$\frac{p_{\mathrm{A\,u}}}{r_{\mathrm{front}}} + q_{\mathrm{A\,u}} = 0 \tag{6.3.20}$$

When $r = r_{\text{front}}$, $\nabla c_{\text{A u}} = \frac{D_{\text{C}}}{D_{\text{A}}} \nabla c_{\text{C l}}$. Therefore

$$-\frac{p_{\text{A u}}}{p_{\text{C l}}} = \frac{D_{\text{C}}}{D_{\text{A}}} \tag{6.3.21}$$

When $r = r_{\text{front}}$, $\frac{D_{\text{B}}}{D_{\text{A}}} \nabla c_{\text{B l}} - \frac{D_{\text{B}}}{D_{\text{A}}} \nabla c_{\text{B u}} = 2 \nabla c_{\text{A u}}$. Therefore

$$\frac{D_{\text{B}}}{D_{\text{A}}} c_{\text{B l}} - \frac{D_{\text{B}}}{D_{\text{A}}} c_{\text{B u}} = 2 p_{\text{A u}} \tag{6.3.22}$$

When $r \to \infty$, $c_{\text{A u}} = c_{\text{A}}^*$. Therefore

$$q_{\text{A u}} = c_{\text{A}}^* \tag{6.3.23}$$

When $r \to \infty$, $c_{\text{B u}} = 0$. Therefore

$$q_{\text{B u}} = 0 \tag{6.3.24}$$

From this information it is possible to show that

$$p_{\mathrm{B\,l}} = -\frac{D_{\mathrm{A}}}{D_{\mathrm{B}}} r_{\mathrm{front}} \tag{6.3.25}$$

$$q_{\mathrm{B\,l}} = \frac{D_{\mathrm{A}}}{D_{\mathrm{B}}} r_{\mathrm{front}} \tag{6.3.26}$$

$$p_{\mathrm{C\,l}} = \frac{D_{\mathrm{A}}}{D_{\mathrm{C}}} r_{\mathrm{front}} \tag{6.3.27}$$

$$q_{\mathrm{C\,l}} = -\frac{D_{\mathrm{A}}}{D_{\mathrm{C}}} \tag{6.3.28}$$

$$p_{\mathrm{A\,u}} = -r_{\mathrm{front}} \tag{6.3.29}$$

$$q_{\mathrm{A\,u}} = c^*_{\mathrm{A}} \tag{6.3.30}$$

$$p_{\mathrm{B\,u}} = \frac{D_{\mathrm{A}}}{D_{\mathrm{B}}} r_{\mathrm{front}} \tag{6.3.31}$$

$$q_{\mathrm{B\,u}} = 0 \tag{6.3.32}$$

The current is given by

$$i = FAD_{\mathrm{A}} c^*_{\mathrm{A}} j \tag{6.3.33}$$

$$i = FAD_{\mathrm{A}} c^*_{\mathrm{A}} \left(2\nabla c_{\mathrm{A\,l}} + \frac{D_{\mathrm{B}}}{D_{\mathrm{A}}} \nabla c_{\mathrm{B\,l}} \right) \tag{6.3.34}$$

$$i = FAD_{\mathrm{A}} c^*_{\mathrm{A}} r_{\mathrm{front}} \tag{6.3.35}$$

When $r = r_{\mathrm{front}}$, $c_{\mathrm{B\,u}} = c_{\mathrm{B\,l}}$. It follows, from eqns 6.3.9 and 6.3.18 that

$$r_{\mathrm{front}} = 2r_{\mathrm{e}} \tag{6.3.36}$$

Therefore

$$i = 2FAD_{\mathrm{A}} c^*_{\mathrm{A}} r_{\mathrm{e}} \tag{6.3.37}$$

This is the same result as for the absence of comproportionation.

6.4 Numerical methods

The problem is readily formulated in terms of a conventional set of normalised parameters, defined in the glossary. The problem is discretised using the fully implicit finite difference method. The resulting nonlinear equations are solved using the Newton-Raphson method and the Thomas algorithm.[30] It is known[31] that when K_{comp} is large, a singularity in species B exists at a time dependent point R_{B}. It is therefore necessary to constructed a spatial mesh of high density close to the electrode surface *and* close to R_{B}. This can be achieved either by using a mesh that is uniformally dense[31] or, more efficiently, by using a temporally dynamic mesh that adapts to changes in the concentration profile at each timestep.[32–34] In the latter case, the dynamically adaptive gridding techniques could handle any mechanism. In so doing, the authors sacrificed computational efficiency in favour of mechanistic generality. In this chapter a dynamically adaptive grid is used that is specifically tailored to the EE reaction, with comproportionation. The singularity in species B is only considered when $R_{\mathrm{B}} > 1.1$. When $R_{\mathrm{B}} < 1.1$, the mesh density close to the electrode is sufficient to resolve the singularity caused by species B. Linear interpolations are used to calculate concentration profiles at successive timesteps. The variation in grid density during the voltammogram, when K_{comp} is large, is shown in figure 6.4.1. The discretization quantitatively expressed as

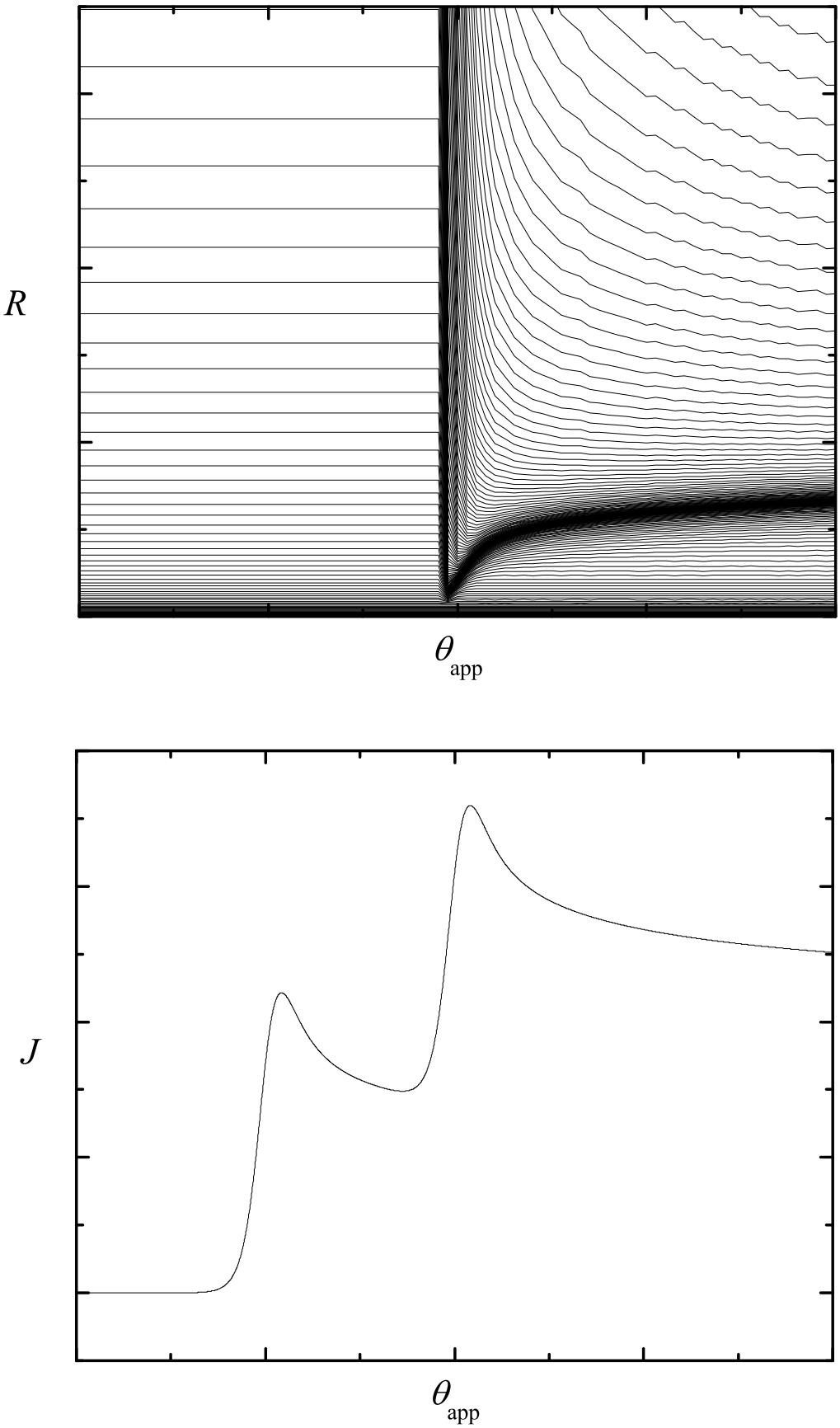

Figure 6.4.1:
Schematic representation of the spatial grid as a function of θ_{app}. *The corresponding voltammogram is shown for comparison. Note the singularity that occurs away from the electrode at large* θ_{app} *values corresponding to approximately* $R = 1$.

$$
\begin{aligned}
&R_0 = 0 \\
&R_\mathrm{j} < \tfrac{R_\mathrm{B}}{2} && R_\mathrm{j} = R_{\mathrm{j}-1} + \gamma_\mathrm{R}\left(H(R_\mathrm{s} - R_\mathrm{j})R_\mathrm{s} + H(R_\mathrm{j} - R_\mathrm{s})R_{\mathrm{j}-1} - 1\right) \\
&\tfrac{R_\mathrm{B}}{2} < R_\mathrm{j} < R_\mathrm{B} && R_\mathrm{j} = R_\mathrm{B} - (R_\mathrm{B} - R_{\mathrm{j}-1}) + \gamma_\mathrm{R}\left(H(R_\mathrm{s} - R_\mathrm{j} + R_\mathrm{B})R_\mathrm{s} + H(R_\mathrm{j} + R_\mathrm{B} - R_\mathrm{s})(R_\mathrm{B} - R_{\mathrm{j}-1}) - 1\right) \\
&R_\mathrm{j} > R_\mathrm{B} && R_\mathrm{j} = R_\mathrm{B} + (R_{\mathrm{j}-1} - R_\mathrm{B}) + \gamma_\mathrm{R}\left(H(R_\mathrm{s} - R_\mathrm{j} - R_\mathrm{B})R_\mathrm{s} + H(R_\mathrm{j} - R_\mathrm{B} - R_\mathrm{s})(R_{\mathrm{j}-1} - R_\mathrm{B}) - 1\right)
\end{aligned}
$$

where H is the Heaviside step function. The parameters are converged to yield $< 1\%$ error ($\gamma_\mathrm{R} = 1 \times 10^{-2}$ and $R_\mathrm{s} = 2 \times 10^{-3}$). The mesh density is considerably higher than that used in simple 'diffusion only' studies[35–37] owing to the extremely tight coupling between the migration electrical fields and concentration profiles of ionic species.[15,38] All simulations were programmed in C++ and run on a desktop computer (Intel Core2 Quad 2.4 GHz, 2 GB RAM), with running times of 30-60 minutes per voltammogram being typical.

6.5 Theoretical results and discussion

6.5.1 Preliminaries

The mechanism considered varies as a function of several parameters. Discussions in this section are based on a system in which $\frac{D_\mathrm{B}}{D_\mathrm{A}} = \frac{D_\mathrm{C}}{D_\mathrm{A}} = 1$, $z_\mathrm{A} = 0$, $z_\mathrm{B} = -1$, $z_\mathrm{C} = -2$, $R_\mathrm{e} = 2660$ and the electrode kinetics are reversible. The value of R_e is derived from $c_\mathrm{A} = 1$ mM, $r_\mathrm{e} = 25$ μm and $\epsilon_\mathrm{r} = 37.5$, which correspond to the experiments in acetonitrile considered in the experimental section.[39]

Figure 6.3.1 shows schematic concentration profiles for which $K_\mathrm{comp} = 0$ and $K_\mathrm{comp} = 10^8$ at the second peak. Trivially, when $K_\mathrm{comp} = 0$, species A travels towards the electrode from bulk solution while species C travels away. Species B, formed in the first wave, has remained very close to the electrode and, consequently, is al-

most depleted at the second peak. The concentration profile when $K_{\text{comp}} = 10^8$ is more complicated. As before, during the second wave, all 3 electroactive species are present in solution. Species A travels towards the electrode from bulk solution while species C travels away. At an intermediate point in solution, a homogeneous comproportionation reaction occurs between species A and C leading to a maximum in the concentration of species B.

The comproportionation can be studied using cyclic voltammetry. During the second wave of the forward sweep, all three electroactive species (A, B and C) are present in appreciable quantities close to the electrode surface. It follows that the peak current for this wave (J_{peak2}) is the most sensitive measure of the rate constant, K_{comp}. As is conventional,[2] this current is quoted relative to a baseline derived from the forward wave of the corresponding one electron process. This procedure is illustrated schematically in figure 6.5.1.

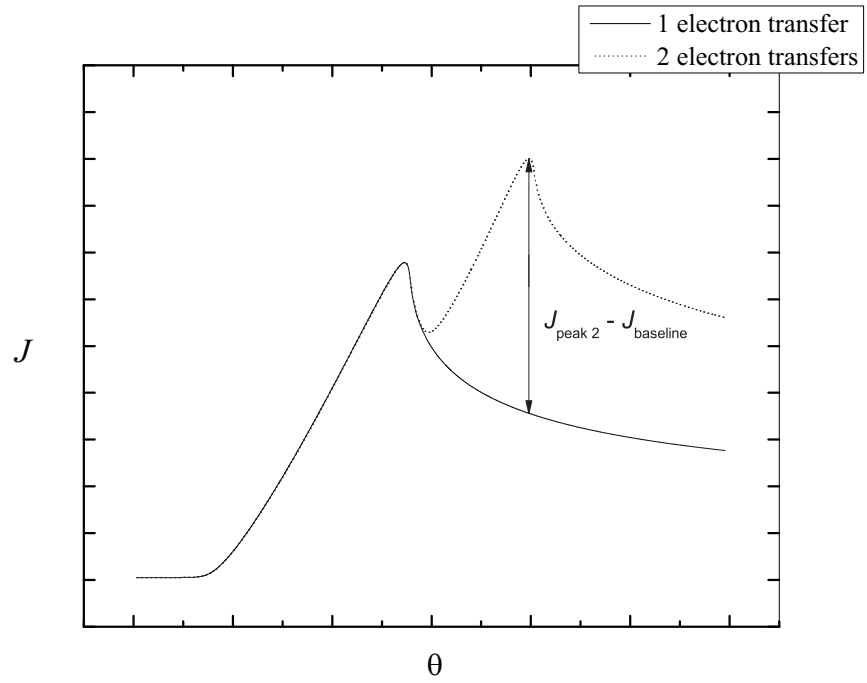

Figure 6.5.1: *Schematic voltammograms for 1 electron,* $A + e^- \rightleftharpoons B$, *and two electron,* $A+2e^- \rightleftharpoons B+e^- \rightleftharpoons C$, *processes. The procedure for calculating baseline corrected currents for the second peak,* $J_{\text{peak 2}} - J_{\text{baseline}}$, *is shown.*

6.5.2 Effect of C_{supp}

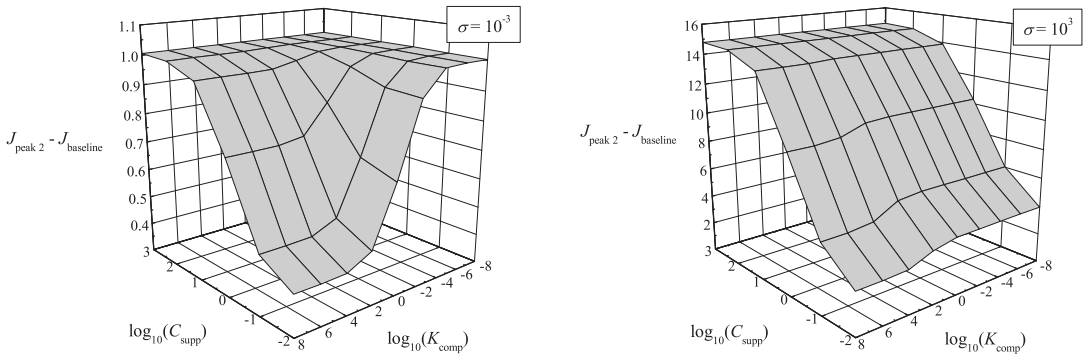

Figure 6.5.2:
$J_{\text{peak}\,2} - J_{\text{baseline}}$ *as a function of* C_{supp} *and* K_{comp} *for* $\sigma = 10^{-3}$ *and* 10^3.

Figure 6.5.2 shows $J_{\text{peak2}} - J_{\text{baseline}}$ as a function of C_{supp} and K_{comp}. When C_{supp} is high, the ionic strength is sufficiently high at every point in solution to suppress potential gradients. In this region, migration does not occur and the voltammetry is purely diffusional. As explained in the introduction to this chapter, the effects of K_{comp} are not voltammetrically distinguishable under diffusion only conditions. This manifests figure 6.5.2, as $J_{\text{peak2}} - J_{\text{baseline}}$ is invariant with K_{comp} when C_{supp} is high. Additionally, it is known that when $\frac{D_{\text{B}}}{D_{\text{A}}}$ and $\frac{D_{\text{C}}}{D_{\text{A}}}$ both close to unity, the value of K_{comp}, though experimentally obtainable using voltammetry, is not unambiguous.[10] As C_{supp} decreases, the ionic strength in solution decreases and the potential gradient close to the electrode increases. Migration makes a progressively more significant contribution to mass transport. In every case, the current is given by:

$$J = \frac{D_{\text{B}}}{D_{\text{A}}} \left(\frac{\partial C_{\text{B}}}{\partial R} \right)_0 + 2 \left(\frac{\partial C_{\text{A}}}{\partial R} \right)_0 \tag{6.5.1}$$

When $\sigma = 1000$, the timescale of the experiment is short and, during the second

wave, B is present in appreciable quantities close to the surface of the electrode when K_{comp} large *and* when K_{comp} is small. Therefore, in both situations, as the value of C_{supp} decreases the current decreases. When C_{supp} is small, the current increases with decreasing K_{comp}. This occurs because the term in species B is more important for the current when K_{comp} is large, due to the higher concentration of species B close to the electrode. Lower values of C_{supp} are required to reach the self support limit as the scan rate increases. The ions of the supporting electrolyte move to nullify to effect of the potential gradient close to the electrode. As the scan rate decreases, the time over which the ions can adapt to a given potential at the electrode increases and the extent of this shielding effect becomes more significant. When $\sigma = 0.001$, species B is almost completely depleted and this contribution to the flux is negligible. The flux is given solely in terms of the uncharged species, A. Since A is uncharged, its mass transport is independent of potential gradients in solution. As C_{supp} decreases, $J_{\text{peak2}} - J_{\text{baseline}}$ is constant. In contrast, when K_{comp} is large species A is almost completely depleted close to the electrode and this contribution to the flux is negligible. The flux is given solely in terms of the charged species, B. Since B is negatively charged, it is repelled by the negative charge at the surface of the electrode. As C_{supp} decreases, the flux of species B at the electrode surface, and $J_{\text{peak2}} - J_{\text{baseline}}$, decreases. At very low values of C_{supp}, the system begins to tend towards a limit in which the ionic strength of the solution varies as a function of only the electroactive species present in solution and its counter ion and products, and hence is independent of C_{supp}. This is called the limit of 'self support'.[6] The comproportionation reaction is most effectively studied at, or near,

steady state because the charge on the ions close to the electrode changes with K_{comp} and leads to significant changes in the voltammetry at low support when migration is a significant form of mass transport.

6.5.3 Effect of D_{supp}

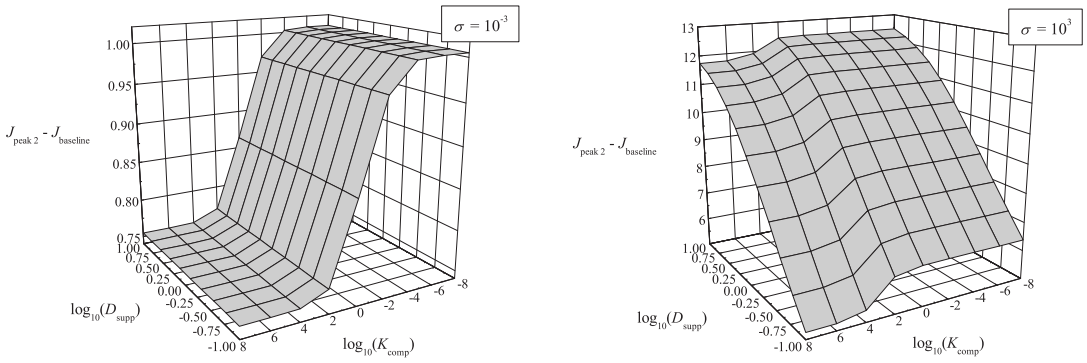

Figure 6.5.3:
$J_{\text{peak 2}} - J_{\text{baseline}}$ *as a function of* $D_{\text{supp}} = D_{\text{M}} = D_{\text{X}}$ *and* K_{comp} *for* $\sigma = 10^{-3}$ *and* 10^{3}.

Figure 6.5.3 shows $J_{\text{peak2}} - J_{\text{baseline}}$ as a function of D_{supp} ($= D_{\text{M}} = D_{\text{X}}$) and K_{comp}. The surface is drawn for a situation in which $C_{\text{supp}} = 1$. This value represents a compromise between a support ratio low enough to allow comproportionation to be observed while allowing the effect of changing D_{supp} to be probed. As explained above, $J_{\text{peak2}} - J_{\text{baseline}}$ decreases as K_{comp} increases. As D_{supp} increases, the ions of the supporting electrolyte can move more quickly and so are more effective at maintaining the electroneutrality in the solution: the proportion of migration that must occur from the electroactive species is smaller. As the scan rate increases, the time over which the ions can adapt increases and the rate at which the ions move becomes less significant. Therefore, when $\sigma = 0.001$, the voltammetry is insensitive to D_{supp}; in contrast, when $\sigma = 1000$ the value of the value of $J_{\text{peak2}} - J_{\text{baseline}}$ tends

towards the limit of full support as D_{supp} increases.

6.5.4 Effect of $D_{\text{B}}/D_{\text{A}}$ and $D_{\text{C}}/D_{\text{A}}$

It was concluded in section 6.5.2 that the effect of comproportionation is most pronounced at steady state. In this section, the value of the steady-state current is studied as a function of $D_{\text{B}}/D_{\text{A}}$ and $D_{\text{C}}/D_{\text{A}}$ at various values of C_{supp}. When $K_{\text{comp}} = 0$, the flux is given solely in terms of species A and the voltammetry is independent of $D_{\text{B}}/D_{\text{A}}$ and $D_{\text{C}}/D_{\text{A}}$. In addition, since A possesses no charge, the steady state value is independent of C_{supp}. In contrast, when $K_{\text{comp}} = 10^8$, the flux depends on upon all three electroactive species. It is therefore anticipated that the value of the steady-state current will depend upon $D_{\text{B}}/D_{\text{A}}$, $D_{\text{C}}/D_{\text{A}}$ and C_{supp}. Figure 6.5.4 shows $J_{\text{peak 2}} - J_{\text{baseline}}$ as a function of $D_{\text{B}}/D_{\text{A}}$ and $D_{\text{C}}/D_{\text{A}}$ for $\sigma = 10^{-3}$. Surfaces are drawn for several values of C_{supp}. As noted in Section 6.5.4, the value of $J_{\text{peak2}} - J_{\text{baseline}}$ increases with C_{supp}; however, the rate at which this occurs changes with $D_{\text{B}}/D_{\text{A}}$ and $D_{\text{C}}/D_{\text{A}}$. It has been observed experimentally,[12] and is shown analytically in the appendix, that at full support, the value of $J_{\text{peak 2}} - J_{\text{baseline}}$ at steady-state when $K_{\text{comp}} = 0$ is equal to that when $K_{\text{comp}} = 10^8$, regardless of the values of $D_{\text{B}}/D_{\text{A}}$ and $D_{\text{C}}/D_{\text{A}}$. Given that most mechanisms of this type have either no comproportionation or diffusion controlled comproportionation, the presence or absence of the homogeneous step can easily be verified experimentally by comparing the value of the steady-state current under weakly supported conditions with one at full support: comproportionation is absent if the two are concordant. At each support ratio, $J_{\text{peak 2}} - J_{\text{baseline}}$ increases with $D_{\text{C}}/D_{\text{A}}$. Species C travels

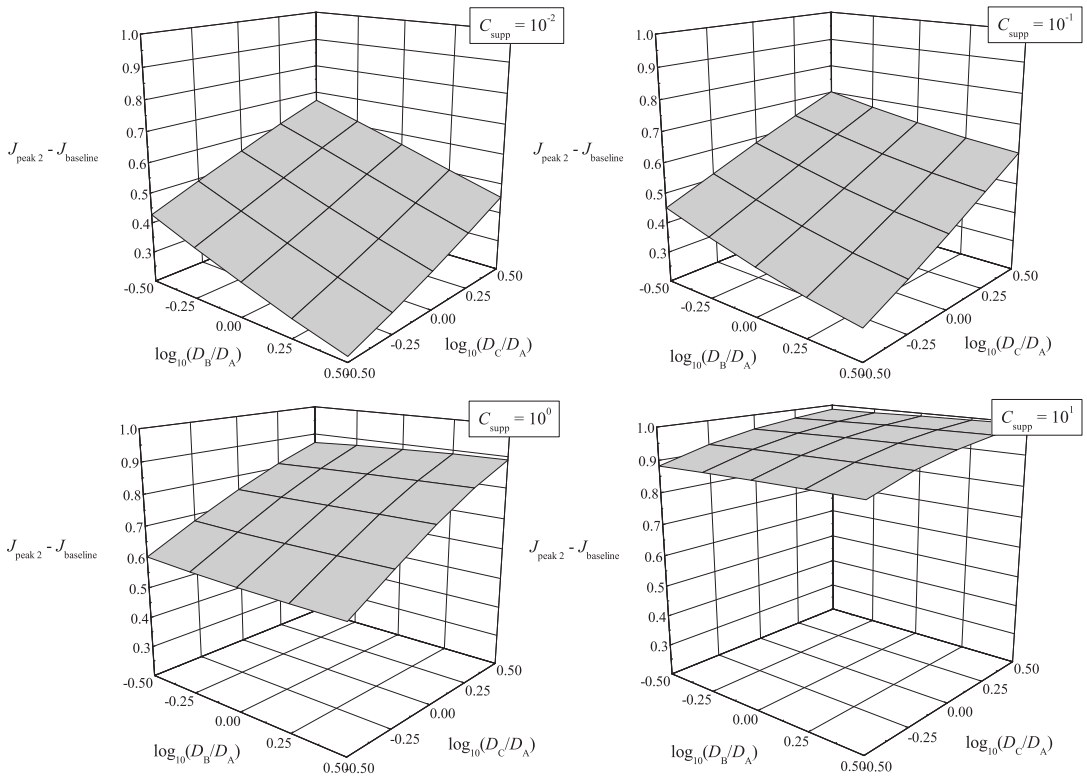

Figure 6.5.4:
$J_{\text{peak}\,2} - J_{\text{baseline}}$ *as a function of* $D_{\text{B}}/D_{\text{A}}$ *and* $D_{\text{C}}/D_{\text{A}}$ *for* $\sigma = 10^{-3}$.

away from the electrode and make no contribution to the current; however, there is a large concentration of C close to the surface of the electrode. Species C can therefore exert strong ionic strength effects. As $D_{\text{C}}/D_{\text{A}}$ increases, the C ions can respond more rapidly to changes in potential at the electrode surface. This leads to a decrease in ohmic drop and in the size of the potential at the plane of electron transfer, ϕ_{PET}. It is reasonable to assume that

$$\frac{\mathrm{d}\phi}{\mathrm{d}r} \propto -\phi_{\text{PET}} \tag{6.5.2}$$

Therefore, as $D_{\text{C}}/D_{\text{A}}$ increases, the potential gradient at the electrode surface becomes smaller. Under these conditions, negative migration of the flux determining

species, species B, is less significant and the current increases. At each support ratio, $J_{\text{peak}\,2} - J_{\text{baseline}}$ decreases with $D_{\text{B}}/D_{\text{A}}$. It follows that, from the concentration profiles shown in figure 6.3.1, the size of maximum in concentration of species B increases as $D_{\text{B}}/D_{\text{A}}$ becomes smaller. The concentration gradient between this maximum and the electrode surface increases and the diffusion term becomes more significant. This leads to an increase in the current.

6.5.5 Effect of z_{A}

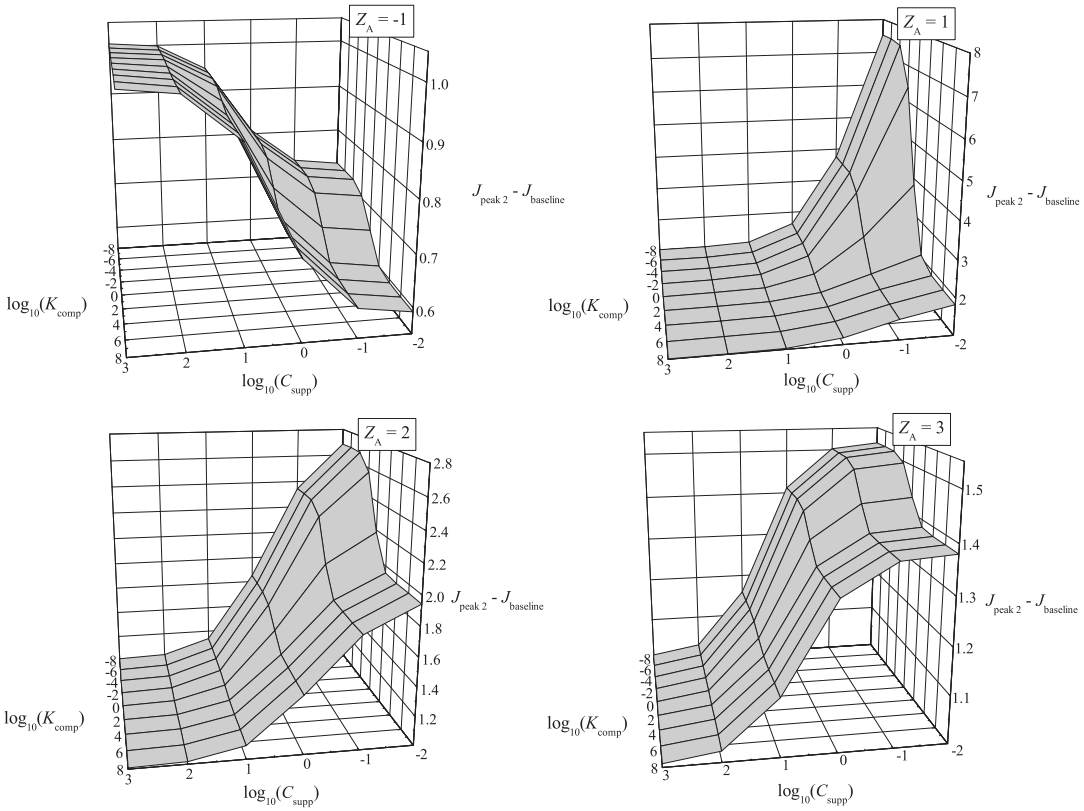

Figure 6.5.5:
$J_{\text{peak}\,2} - J_{\text{baseline}}$ as a function of C_{supp} and K_{comp} for $z_{\text{A}} = -1$, 1, 2 and 3.

As explained in section 6.5.2, when $z_{\text{A}} = 0$, the presence of comproportionation is most easily measured at low scan rates and low support ratios. This conclusion is expected to hold in other situations when $z_{\text{A}} \neq 0$. Figure 6.5.5 shows $J_{\text{peak2}} - J_{\text{baseline}}$

as a function of C_{supp} and K_{comp}. The surface is redrawn for different values of z_{A}; the case for which $z_{\text{A}} = 0$ has already been considered in section 6.5.2. Since both heterogeneous processes are one electron transfers, the charges of the other species follow directly from z_{A}. In each case, the charge on species A is balanced by a counterion of equal but opposite charge. The ionic strength of the solution, for a given C_{supp}, changes between the surfaces for z_{A}; however, it is still possible to identify meaningful trends in the z_{A} values.

In each case, when K_{comp} is close to zero, the value of $J_{\text{peak2}} - J_{\text{baseline}}$ is determined solely by the flux of species A, from eqn 6.5.1. As C_{supp} decreases, the mass transport of species A becomes increasingly dictated by the potential gradient at the electrode surface. The reaction considered is a reduction and the electrode is negatively charged. Therefore, when $z_{\text{A}} < 0$, negative migration occurs and the value of $J_{\text{peak2}} - J_{\text{baseline}}$ decreases with C_{supp}; in contrast, when $z_{\text{A}} > 0$, positive migration occurs and the value of $J_{\text{peak2}} - J_{\text{baseline}}$ increases with C_{supp}. As pointed out in section 6.5.2, when $z_{\text{A}} = 0$, migration does not occur and the value of $J_{\text{peak2}} - J_{\text{baseline}}$ does not vary with C_{supp}.

When $z_{\text{A}} = -1$ and K_{comp} is very large, both species B is negatively charged and undergo negative migration close to the surface of the electrode. The difference between $K_{\text{comp}} = 0$ and $K_{\text{comp}} = 10^8$ is relatively small because each case, the flux determining species is negatively charged and mass transport is affected by negative migration.

When $z_{\text{A}} = 1$ and K_{comp} is very large, species B is neutral and is not affected by migration close the electrode surface. The difference between $K_{\text{comp}} = 0$ and

$K_{\text{comp}} = 10^8$ is very large because in the former case, mass transport is affected by positive migration while, in the latter, mass transport is affected by positive migration. In this situation, it is even possible to voltammetrically distinguish a wide range of intermediate values of K_{comp}, between $K_{\text{comp}} = 0$ and $K_{\text{comp}} = 10^8$. The range lies approximately between $K_{\text{comp}} = 10^{-4}$ and $K_{\text{comp}} = 10^4$.

When $z_{\text{A}} = 2$ or 3, and K_{comp} is very large, species B is positively charged and is affected by positive migration towards the electrode surface. The difference between $K_{\text{comp}} = 0$ and $K_{\text{comp}} = 10^8$ is small because, in both cases, mass transport is affected by positive migration. The difference is less when $z_{\text{A}} = 3$ because the relative difference in charge between species A and B is lower.

6.6 Experimental results and discussion

All experimental work was conducted by Dr. Juan G. Limon-Peterson. The method and materials used are described in detail in Appendix B.

Parameter	Experimental Value	Reference
$\alpha_{\text{AQ/AQ}^-}$	0.5	
$\alpha_{\text{AQ}^-/\text{AQ}^{2-}}$	0.5	
D_{AQ}	2.1×10^{-9} m^2 s^{-1}	
D_{AQ^-}	1.7×10^{-9} m^2 s^{-1}	
$D_{\text{AQ}^{2-}}$	1.6×10^{-9} m^2 s^{-1}	
D_{TBA^+}	0.68×10^{-9} m^2 s^{-1}	Szymanska *et al.*[40]
D_{Cl^-}	2.35×10^{-9} m^2 s^{-1}	Szymanska *et al.*[40]
$\epsilon_{\text{r,AN}}$	37.5	Ritzoulis *et al.*[39]
$k^0_{\text{AQ/AQ}^-}$	≥ 0.001 m s^{-1}	
$k^0_{\text{AQ}^-/\text{AQ}^{2-}}$	≥ 0.001 m s^{-1}	
k_{comp}	1×10^8 m^3 mol^{-1} s^{-1}	

Table 6.1: *Experimental data for anthraquinone, AQ, in acetonitrile, AN.*

The experimental data is summarised in Table 8.1. It is reasonable to expect the

diffusion coefficients to be close to those used in the fully supported media. This occurs because the charges of the ions considered in this reaction are small and ion pairing ion pairing, which increases at low support, is unlikely to occur. This was found experimentally.

The formal potentials are not given because they vary as a function of support ratio. Changing the concentration of supporting electrolyte leads to a large change in the ionic strength of the solution. This, in turn, affects the potential of any redox couple by ionic strength effects:

$$\delta E_{\mathrm{f}}^{\ominus} = \frac{RT}{F} \ln \frac{\gamma_{\mathrm{red}}}{\gamma_{\mathrm{ox}}} \tag{6.6.1}$$

The values of γ_{red} and γ_{ox} can be obtained analytically using the Robinson Stokes equation.[41,42] However, the requisite parameters required for these calculations are not available in the literature. The ionic strength effects change peak position and, to a lesser extent, peak to peak separation; peak height, which is used as the main probe for comproportionation, is unaffected. It is therefore possible to obtain concordance between experimental and simulated data by treating $E_{\mathrm{F}}^{\ominus}$ as a variable 'fitting parameter'. The reduced species in each heterogeneous process possesses a higher charge, $\gamma_{\mathrm{red}} > \gamma_{\mathrm{ox}}$. The ionic strength effects change peak position and, to a lesser extent, peak to peak separation; peak height, which is used as the main probe for comproportionation, is unaffected. Given that activity coefficients increase with ionic strength, $E_{\mathrm{F}}^{\ominus}$ values are expected to become more negative. This was observed experimentally.

6.6.1 Fully supported conditions

When dissolved in acetonitrile, anthraquinone is known to present two, reversible, single electron reduction peaks;[43] in contrast, when dissolved in water, anthraquinone presents a complex mechanism that is pH dependent.[44] Chronoamperograms where

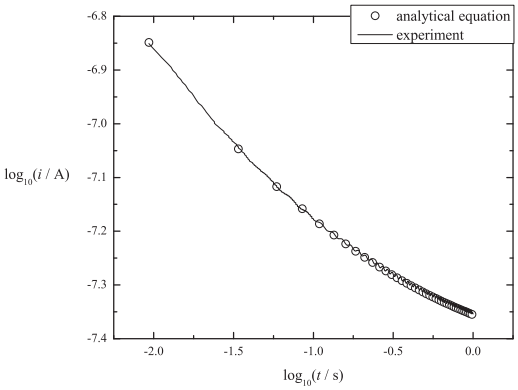

Figure 6.6.1:
Experimental chronoamperometry compared with the analytical equation ($D_{\mathrm{AQ}} = 2.1 \times 10^{-9}$ m^2 s^{-1}).

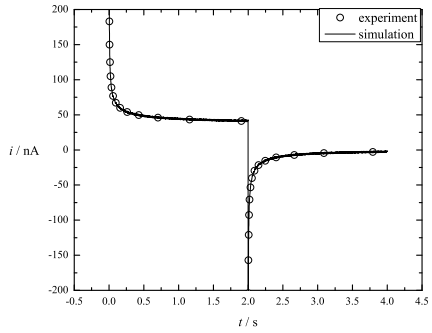

Figure 6.6.2:
Experimental double potential step chronoamperometry compared with the simulated result ($D_{\mathrm{AQ}} = 2.1 \times 10^{-9}$ m^2 s^{-1} and $D_{\mathrm{AQ^-}} = 1.7 \times 10^{-9}$ m^2 s^{-1}).

recorded in a solution containing 1.25 mM anthraquinone and 62.5 mM of TBAP, $C_{\mathrm{supp}} = 50$. Under these conditions, mass transport can be considered 'diffusion-only'. The single step chronoamperogram shown in figure 6.6.1 was obtained by applying a potential of -1 V *vs.* Ag_{wire} for two seconds. This potential lies in between the two reduction waves and therefore corresponds to rate limiting diffusion of AQ only. The value of D_{AQ} was determined by fitting the experimental transient to the analytical equation[2]

$$i = nF\pi r_{\mathrm{e}}^2 D_{\mathrm{A}} c_{\mathrm{A}}^* \left(\frac{1}{\sqrt{D_{\mathrm{A}}\pi t}} + \frac{1}{r_{\mathrm{e}}} \right) \tag{6.6.2}$$

The analytical transient shown in figure 6.6.1 was obtained using $D_{\mathrm{AQ}} = 1.2 \times 10^{-5}$ cm^2 s^{-1}.

The double potential step chronoamperogram shown in figure 6.6.2 as obtained by applying a potential of -1 V *vs.* Ag$_{wire}$ for two seconds subsequently applying -0.3 V *vs.* Ag$_{wire}$ for two seconds. The first potential lies in between the two reduction waves and therefore corresponds to rate limiting diffusion of AQ only. The second potential is more positive than either voltammetric wave and corresponds to rate limiting diffusion of AQ$^-$ only. These experimental results were compared with numerical results obtained using a program described by Klymenko *et al.*[45] Concordance between the experimental and simulated data occurred when $D_{\mathrm{AQ}} = 2.1 \pm 0.2 \times 10^{-9}$ m^2 s^{-1} and $D_{\mathrm{AQ^-}} = 1.7 \pm 0.2 \times 10^{-9}$ m^2 s^{-1}. These values are consistent with the literature data.[46] The quadruple potential step chronoamperogram shown in figure 6.6.3 as obtained by applying a potential of -1 V *vs.* Ag$_{wire}$ for two seconds, -1.6 V *vs.* Ag$_{wire}$ for two seconds, -1 V *vs.* Ag$_{wire}$ for two seconds, -0.3 V *vs.* Ag$_{wire}$ for two seconds. These potentials correspond to from

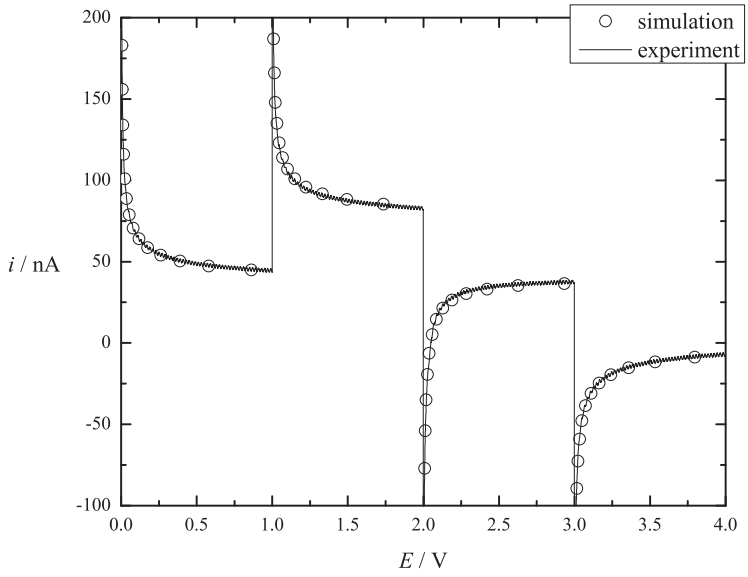

Figure 6.6.3: *Experimental quadruple potential step chronoamperometry compared with the simulated result ($D_{\mathrm{AQ}} = 2.1 \times 10^{-9}$ m^2 s^{-1}, $D_{\mathrm{AQ^-}} = 1.7 \times 10^{-9}$ m^2 s^{-1} and $D_{\mathrm{AQ^{2-}}} = 1.6 \times 10^{-9}$ m^2 s^{-1}).*

open circuit step to a potential between the first and second wave, then stepping to a potential after the second wave, after coming back to a potential between both waves and finally stepping before the first wave. These potentials correspond to rate limiting diffusion of species A, B, C and B respectively. These experimental results were compared with numerical results obtained using a program described by Wang *et al.*[47] Concordance between the experimental and simulated data occurred when $D_{\mathrm{AQ}} = 2.1 \pm 0.2 \times 10^{-9}$ m^2 s^{-1}, $D_{\mathrm{AQ^-}} = 1.7 \pm 0.2 \times 10^{-9}$ m^2 s^{-1} and $D_{\mathrm{AQ^-}} = 1.6 \pm 0.2 \times 10^{-9}$ m^2 s^{-1}. Cyclic voltammograms were recorded at

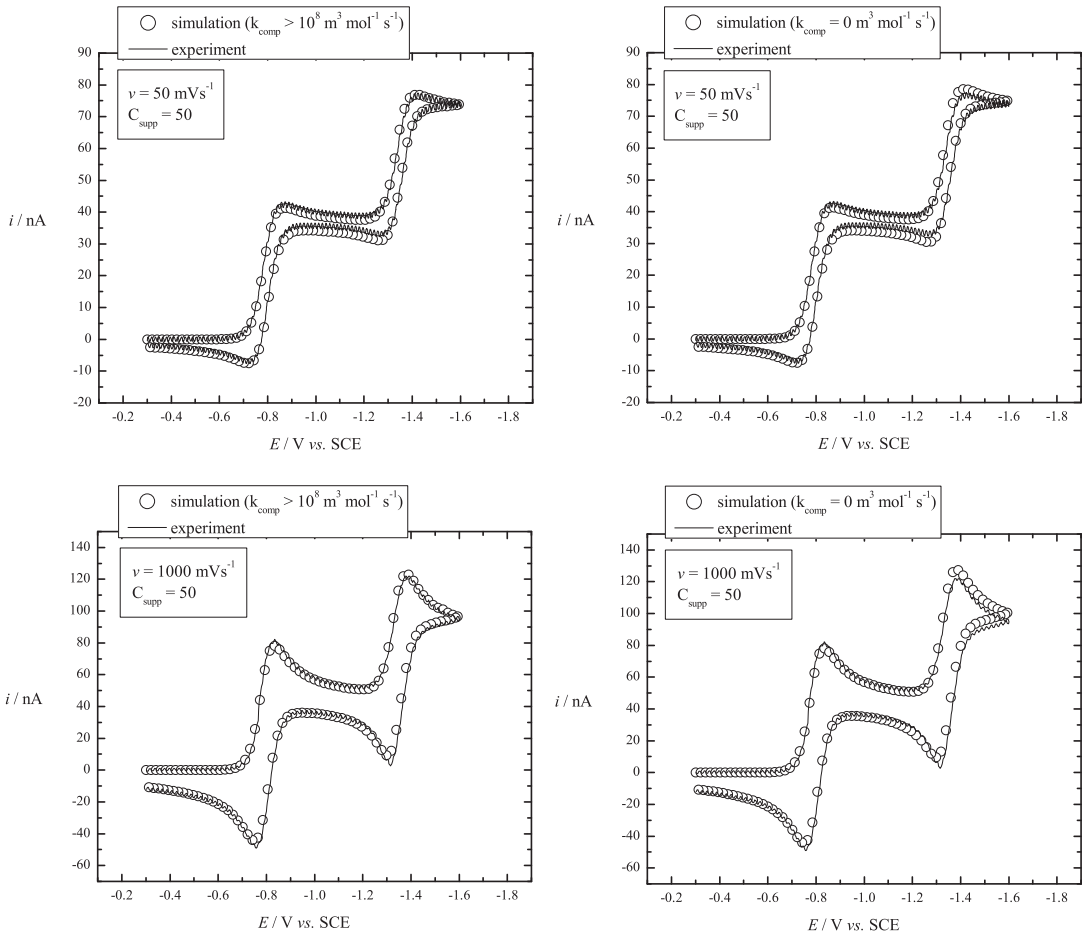

Figure 6.6.4:
Experimental cyclic voltammetry compared with simulated results when $C_{\mathrm{supp}} = 50$.

different scan rates (50, 100, 200, 500 and 1000 mV s^{-1}). The results for the

highest and lowest scan rates studied are shown in figure 6.6.4. The voltammetry was simulated as described in section 7.2. The parameters that yielded the greatest concordance between theory and experiment are given in table 8.1. Simulated voltammograms are shown in figure 6.6.4 for both $k_{\text{comp}} = 10^{11}$ dm^3 mol^{-1} s^{-1} and $k_{\text{comp}} = 0$ dm^3 mol^{-1} s^{-1}. The former corresponds to the limit of diffusion control. Both simulated voltammograms are in good agreement with the experimental results over the range of scan rates studied. This is expected because the diffusion coefficients of AQ, AQ^- and AQ^{2-} are similar.[10] Cyclic voltammetry is unable to resolve the presence of comproportionation under conditions of full support.

6.6.2 Weakly supported conditions

Cyclic voltammograms were recorded at low concentration of supporting electrolyte in a solution containing 1.25 mM of TBAP and 0.7mM of TBAP at various scan rates. The results are shown in figure 6.6.5. The peak current of the second wave decreases with support ratio due to negative migration, as explained in section 7.2. As before, cyclic voltammograms for $k_{\text{comp}} = 0$ dm^3 mol^{-1} s^{-1} and $k_{\text{comp}} = 10^{11}$ dm^3 mol^{-1} s^{-1}. Unlike the case of full support, these simulated voltammograms are distinctly different. From this data it is possible to conclude, unambiguously, that comproportionaton occurs at diffusion control. This conclusion is in accordance with Marcus theory which predicts that molecule, such as anthraquinone, that are rigid with respect to gain or los of electrons, lead to rapid rate constants for reactions, such as comproportionation, involving electron transfer.[48]

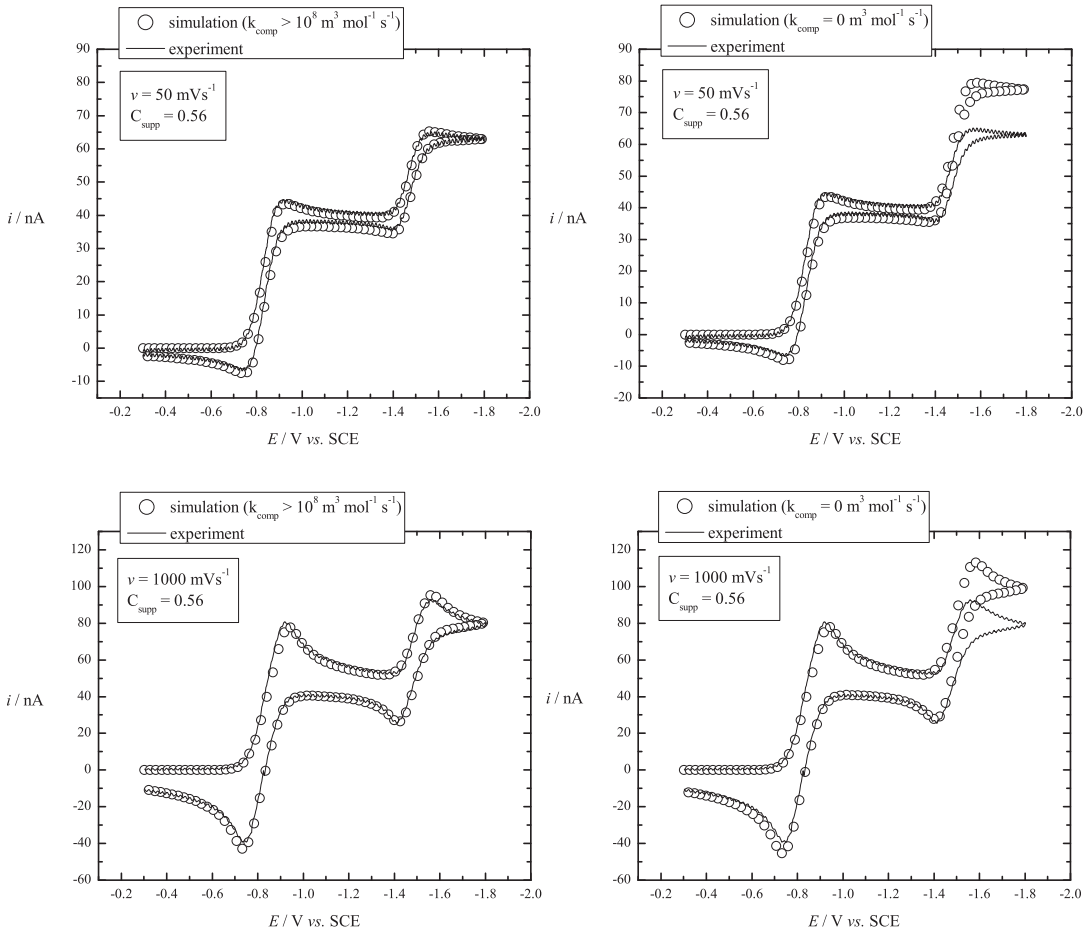

Figure 6.6.5:
Experimental cyclic voltammetry compared with simulated results when $C_{\text{supp}} = 0.56$.

6.7 Conclusion

Cyclic voltammetry, with homogeneous kinetics, can be simulated for conditions of low support. In many cases, cyclic voltammetry is unable to determine the presence or absence of diffusion-controlled comproportionation under conventional, fully supported, conditions; in contrast, under weakly supporting conditions the distinction can be unequivocal. It has been shown experimentally that, in the case of anthraquinone in acetonitrile, comproportionation is diffusionally controlled.

In the experimental study presented here, the validity of the data is improved con-

siderably by comparing theory and experiment over a range of scan rates and a range of concentrations of the supporting electrolyte. We anticipate electrochemistry in solutions of variable ionic strength is therefore likely to become widely used and is expected to greatly enhance the scope of voltammetry for detecting kinetic and thermodynamic parameters.

Bibliography

[1] Belding, S. R.; Limon-Petersen, J. G.; Dickinson, E. J. F.; Compton, R. G. *Angewandte Chemie International Edition* **2010**, *49*, 9242–9245.

[2] Compton, R. G.; Banks, C. E. *Understanding Voltammetry*; World Scientific: Singapore, 2007.

[3] Fisher, A. C. In *Electrode Dynamics*; Compton, R. G., Ed.; Oxford University Press: New York, 1996.

[4] Bard, A. J.; Faulkner, L. R. *Electrochemical Methods, Fundamentals and Applications*; John Wiley & Sons Inc.: Hoboken, 2001.

[5] Limon-Petersen, J. G.; Han, J. T.; Rees, N. V.; Dickinson, E. J. F.; Streeter, I.; Compton, R. G. *J. Phys. Chem. C* **2010**, *114*, 2227–2236.

[6] Dickinson, E. J. F.; Limon-Petersen, J. G.; Rees, N. V.; Compton, R. G. *J. Phys. Chem. C* **2009**, *113*, 11157–11171.

[7] Evans, D. H.; Lehmann, M. W. *Acta Chem. Scand.* **1999**, *53*, 765–774.

[8] Evans, D. H. *Chem. Rev. (Washington, DC, U. S.)* **2008**, *108*, 2113–2144.

[9] Andrieux, C. P.; Savéant, J. M. *J. Electroanal. Chem.* **1970**, *28*, 339–348.

[10] Belding, S. R.; Baron, R.; Dickinson, E. J. F.; Compton, R. G. *J. Phys. Chem. C* **2009**, *113*, 16042–16050.

[11] Barnes, E. O.; O'Mahony, A. M.; Belding, S. R.; Compton, R. G. *J. Chem. Eng. Data* **2010**, *55*, 2219–2224.

[12] Lehmann, M. W.; Evans, D. H. *Anal. Chem.* **1999**, *71*, 1947–1950.

[13] Amatore, C.; Deakin, M. R.; Wightman, R. *J. Electroanal. Chem.* **1987**, *225*, 49 – 63.

[14] Ciszkowska, M.; Stojek, Z. *J. Electroanal. Chem.* **1999**, *466*, 129–143.

[15] Klymenko, O. V.; Amatore, C.; Svir, I. *Anal. Chem.* **2007**, *79*, 6341–6347.

[16] Palys, M. J.; Stojek, Z. *J. Electroanal. Chem.* **2002**, *534*, 65–73.

[17] Hyk, W.; Stojek, Z. *Anal. Chem.* **2005**, *77*, 6481–6486.

[18] Bond, A. M.; Feldberg, S. W. *J. Phys. Chem. B* **1998**, *102*, 9966–9974.

[19] Rooney, M. B.; Coomber, D. C.; Bond, A. M. *Anal. Chem.* **2000**, *72*, 3486–3491.

[20] Bond, A. M.; Coomber, D. C.; Feldberg, S. W.; Oldham, K. B.; Vu, T. *Anal. Chem.* **2001**, *73*, 352–359.

[21] Streeter, I.; Compton, R. G. *J. Phys. Chem. C* **2008**, *112*, 13716–13728.

[22] Limon-Petersen, J. G.; Streeter, I.; Rees, N. V.; Compton, R. G. *J. Phys. Chem. C* **2008**, *112*, 17175–17182.

[23] Limon-Petersen, J. G.; Streeter, I.; Rees, N. V.; Compton, R. G. *J. Phys. Chem. C* **2009**, *113*, 333–337.

[24] Limon-Petersen, J. G.; Dickinson, E. J. F.; Rees, N. V.; Compton, R. G. *J. Phys. Chem. C* **2009**, *113*, 15320–15325.

[25] Norton, J. D.; Benson, W. E.; White, H. S.; Pendley, B. D.; Abruna, H. D. *Anal. Chem.* **1991**, *63*, 1909–1914.

[26] Norton, J. D.; White, H. S. *J. Electroanal. Chem.* **1992**, *325*, 341–350.

[27] Amatore, C.; Bento, M. F.; Montenegro, M. I. *Anal. Chem.* **1995**, *67*, 2800–2811.

[28] Kowski, M.; Stojek, Z.; Palys, M. J. *Electrochem. Commun.* **2009**, *11*, 905–908.

[29] Svir, I. B.; Oleinick, A. I.; Compton, R. G. *Radiotekhnika* **2001**, *116*, 114.

[30] Press, W. H., Teukolsky, S. A., Vetterling, W. T., Flannery, B. P., Eds. *Numerical Recipes: The Art of Scientific Computing*; Cambridge University Press, 2007.

[31] Rongfeng, Z.; Evans, D. H. *J. Electroanal. Chem.* **1995**, *385*, 201–207.

[32] Amatore, C.; Klymenko, O.; Svir, I. *Electrochemistry Communications* **2010**, *12*, 1170–1173.

[33] Amatore, C.; Klymenko, O.; Svir, I. *Electrochemistry Communications* **2010**, *12*, 1165–1169.

[34] Britz, D. *Digital Simulation in Electrochemistry*; Springer-Verlag: New York, 2005.

[35] Belding, S. R.; Rogers, E. I.; Compton, R. G. *J. Phys. Chem. C* **2009**, *113*, 4202–4207.

[36] Belding, S. R.; Dickinson, E. J. F.; Compton, R. G. *J. Phys. Chem. C* **2009**, *113*, 11149–11156.

[37] Belding, S. R.; Dickinson, E. J. F.; Compton, R. G. *J. Phys. Chem. C* **2009**, *113*, 11149–11156.

[38] Smith, C. P.; White, H. S. *Anal. Chem.* **1993**, *65*, 3343–53.

[39] Ritzoulis, G.; Papadopoulos, N.; Jannakoudakis, D. *J. Chem. Eng. Data* **1986**, *31*, 146–148.

[40] Szymanska, J.; Palys, M. J.; Van den Bossche, B. *Anal. Chem.* **2004**, *76*, 5937–5944.

[41] Debye, P. *Physik. Z.* **1924**, *25*, 97.

[42] Robinson, R.; Stokes, R. *Electrolyte Solutions*; Butterworths, Inc., London, 1955.

[43] Quan, M.; Sanchez, D.; Wasylkiw, M. F.; Smith, D. K. *J. Am. Chem. Soc.* **2007**, *129*, 12847–12856, PMID: 17910453.

[44] Batchelor-McAuley, C.; Li, Q.; Dapin, S. M.; Compton, R. G. *J. Phys. Chem. B* **2010**, *114*, 4094–4100.

[45] Klymenko, O. V.; Evans, R. G.; Hardacre, C.; Svir, I. B.; Compton, R. G. *J. Electroanal. Chem.* **2004**, *571*, 211–221.

[46] Rees, N. V.; Clegg, A. D.; Klymenko, O. V.; Coles, B. A.; Compton, R. G. *J. Phys. Chem. B* **2004**, *108*, 13047–13051.

[47] Wang, Y.; Rogers, E. I.; Compton, R. G. *Journal of Electroanalytical Chemistry* **2010**, *648*, 15–19.

[48] Marcus, R. A. *J. Chem. Phys.* **1956**, *24*, 966–978.

Chapter 7

Diffusion-migration voltammetry: the microdisc electrode

This chapter presents research into voltammetry at microdisc electrodes in which mass transport occurs by a combination of diffusion and migration. This chapter extends the work presented in chapters 5 and 6. This reasearch has been published as an article in *Physical Chemistry Chemical Physics*.[1]

7.1 Introduction

Over last 25 years, two types of experiment have enhanced the applicability and appeal of analytical electrochemistry: voltammetry at microdisc electrodes and voltammetry in the absence of excess supporting electrolyte. The microdisc electrode[2–6] has allowed cyclic voltammograms to be obtained with a high current density, a low capacitance and a low ohmic drop. In addition, microdiscs can be fabricated cheaply[5] and can easy be reused.[7] These unique properties have contributed to several pio-

neering papers, perhaps most notably to the ultra fast scan work of Amatore.[8–10] Voltammetry conducted in the absence of excess supporting electrolyte allows *both* diffusional and migrational modes to contribute to the overall mass transport properties of the system.[11–17] The added complexity can be used, for example, to investigate mechanistic pathways invisible to conventional, 'diffusion-only', techniques.[18,19] Despite both techniques providing useful scientific insights, the use of both simultaneously has been limited by a need for accurate theoretical methods.[20–22] In general, chemical systems are most throughly investigated by means of a combination of theoretical and experimental techniques. Most theoretical research into diffusional-migrational mass transport is based on a hemispherical electrode. Compared to the two dimensional microdisc, the one dimensional hemisphere is a much easier problem to solve: both analytically and numerically.[23] Consequently, the use of hemispherical electrodes in experimental work is also popular.[18,24,25] However, such studies are restricted because hemispheres are only easily fabricated using mercury: the electrode must be made and characterised before every experiment in order to maintain a clean surface; mercury is toxic; mercury reacts with many common ions, most notably halides and sulphides; mercury often limits the potential window of the experiment in the oxidative direction; finally, the surface tension of mercury, and its potential dependence, limits the range of radii over which the electrode is truly hemispherical. In order to strike a compromise between theoretical and experimental work, many workers rely on the so-called 'hemispherical approximation': the voltammetry obtained at a microdisc, of radius r_e, is presumed identical to that obtained at a hemisphere, of radius $\frac{2}{\pi}r_e$. That is to say, equivalence between a disc and a

hemisphere occurs when their superficial diameters are equal.[26] This approximation provides a useful way in which to quantitatively relate straight-forward experiments, involving microdiscs, to simple theory, based on hemispheres. The relationship is known to be exact for electrochemically reversible reactions, of the type $A + e^- \rightleftharpoons B$, at steady-state where surface concentrations are fixed by the Nernst equation.[26–28] Although useful in certain circumstances (i.e. voltammetry at small electrodes and at low scan rates),[29,30] this simple approximation cannot necessarily be assumed in general.[27] The only work to date was published in the early 1990s, when Verbrugge and Baker simulated potential step chronoamperometry at microdisc electrodes (including both the transient and the steady state regions) in the absence of excess supporting electrolyte using the ADI method[20,21] where the steps were to potentials corresponding to transport control leading to limiting currents indicative of the electrode potential. Steady state voltammetry measuring current as a function of the applied potential has never been simulated at a microdisc electrode, possibly owing to the high computational cost.[31]

In this chapter, the steady-state voltammetric waveshapes, for the one electron reductions, $A + e^- \rightleftharpoons B$, are studied at a microdisc electrode in the absence of excess supporting electrolyte. For the first time, this voltammetric experiment is numerically simulated for a microdisc electrode. The voltammetry is investigated as a function of two variables: the concentration of supporting electrolyte and the electrochemical rate constant. The 'hemispherical approximation' is shown to be valid under weakly supported conditions for a defined, limited, range of electrochemical rate constants. For the first time, microdisc simulations were used, in conjunction

with the, Debye-Hückel theory, to rationalise the experimental steady-state voltammetry of two aqueous redox couples as a function of the applied potential without the use of the hemispherical approximation. The couples were hexammineruthenium ($[Ru(NH_3)_6]^{3+}/[Ru(NH_3)_6]^{2+}$) and hexachloroiridate ($[IrCl_6]^{2-}/[IrCl_6]^{3-}$) (each with KCl supporting electrolyte):

$$[Ru(NH_3)_6]^{3+} + e^- \rightleftharpoons [Ru(NH_3)_6]^{2+} \tag{7.1.1}$$

$$[IrCl_6]^{2-} + e^- \rightleftharpoons [IrCl_6]^{3-} \tag{7.1.2}$$

This investigation provides evidence for ion pairing between $[IrCl_6]^{2-}/[IrCl_6]^{3-}$ and K^+ from the supporting electrolyte. No ion pairing is observed between $[Ru(NH_3)_6]^{3+}/[Ru(NH_3)_6]^{2+}$ and Cl^-.

7.2 Theory

The following reaction is studied:

$$A^{Z_A} + e^- \rightleftharpoons B^{Z_A - 1} \tag{7.2.1}$$

where species A is accompanied by a monovalent counter ion, X^-. The reaction occurs in the presence of a variable concentration of inert 1:1 supporting electrolyte, M^+X^-. It is assumed that no ion pairing occurs. The reaction with be studied at both a hemispherical shaped and a disc shaped electrode. All symbols are defined in the glossary.

7.2.1 Hemispherical electrode

In real space (r_{hemi}):

$$\begin{aligned} \nabla &= \frac{\partial}{\partial r_{\mathrm{hemi}}} \\ \nabla^2 &= \frac{\partial^2}{\partial {r_{\mathrm{hemi}}}^2} + \frac{2}{r_{\mathrm{hemi}}} \frac{\partial}{\partial r_{\mathrm{hemi}}} \end{aligned}$$

The steady-state transport equations for bulk solution are:

$$\begin{aligned} 0 &= D_{\mathrm{A}} \nabla^2 C_{\mathrm{A}} + D_{\mathrm{A}} \frac{Z_{\mathrm{A}} F}{RT} \nabla \left(C_{\mathrm{A}} \nabla \phi \right) \\ 0 &= D_{\mathrm{B}} \nabla^2 C_{\mathrm{B}} + D_{\mathrm{B}} \frac{Z_{\mathrm{B}} F}{RT} \nabla \left(C_{\mathrm{B}} \nabla \phi \right) \\ 0 &= D_{\mathrm{M}} \nabla^2 C_{\mathrm{M}} + D_{\mathrm{M}} \frac{Z_{\mathrm{M}} F}{RT} \nabla \left(C_{\mathrm{M}} \nabla \phi \right) \\ 0 &= D_{\mathrm{X}} \nabla^2 C_{\mathrm{X}} + D_{\mathrm{X}} \frac{Z_{\mathrm{X}} F}{RT} \nabla \left(C_{\mathrm{X}} \nabla \phi \right) \end{aligned}$$

The electroneutrality equation is:

$$0 = \sum_s Z_{\mathrm{s}} C_{\mathrm{s}}$$

In this chapter, the electroneutrality equation is used instead of the, more general, Poisson equation. Since these are solved under steady state conditions, this simplification is justified and can be used without loss of accuracy or computational efficiency.[32] The boundary conditions for steady state voltammetry on the electrode surface ($r_{\mathrm{hemi}} = r_{\mathrm{e}}$) are:

$$\begin{aligned} D_{\mathrm{A}} \nabla C_{\mathrm{A},0} + D_{\mathrm{A}} C_{\mathrm{A},0} \frac{Z_{\mathrm{A}} F}{RT} \nabla \Delta\phi &= C_{\mathrm{A},0}\ k^0\ \exp\left(\frac{-\alpha F (E - E_{\mathrm{f}} - \Delta\phi)}{RT} \right) \\ &\quad - C_{\mathrm{B},0}\ k^0\ \exp\left(\frac{\beta F (E - E_{\mathrm{f}} - \Delta\phi)}{RT} \right) \\ D_{\mathrm{B}} \nabla C_{\mathrm{B},0} + D_{\mathrm{B}} C_{\mathrm{B},0} \frac{Z_{\mathrm{B}} F}{RT} \nabla \Delta\phi &= -D_{\mathrm{A}} \nabla C_{\mathrm{A},0} - D_{\mathrm{A}} C_{\mathrm{A},0} \frac{Z_{\mathrm{A}} F}{RT} \nabla \Delta\phi \\ D_{\mathrm{M}} \nabla C_{\mathrm{M},0} + D_{\mathrm{M}} C_{\mathrm{M},0} \frac{Z_{\mathrm{M}} F}{RT} \nabla \Delta\phi &= 0 \\ D_{\mathrm{X}} \nabla C_{\mathrm{X},0} + D_{\mathrm{X}} C_{\mathrm{X},0} \frac{Z_{\mathrm{X}} F}{RT} \nabla \Delta\phi &= 0 \\ \sum_s Z_{\mathrm{s}} C_{\mathrm{s},0} &= 0 \end{aligned}$$

where E is the potential applied at the electrode; $E^{\ominus}_{\mathrm{f,A/B}}$ is the formal potential of the A/B redox couple. $\Delta\phi$ is the difference in potential between bulk solution and the edge of the double layer. The parameter $\Delta\phi$ is therefore the loss in 'driving force' for the reaction. Note that under conditions of full support, $\Delta\phi = 0$ V.

The problem is solved using the standard fully implicit finite difference procedure.[11]

The remaining boundary conditions are:

$$r = \infty \qquad C_{\mathrm{A}} = C^{*}_{\mathrm{A}} \qquad C_{\mathrm{B}} = 0 \qquad C_{\mathrm{M}} = C^{*}_{\mathrm{M}} \qquad C_{\mathrm{X}} = C^{*}_{\mathrm{X}} \qquad \phi = 0$$

The current is:

$$i = 2\pi r_{\mathrm{e}}^{2} F D_{\mathrm{A}} \left(\nabla C_{\mathrm{A}} + \tfrac{Z_{\mathrm{A}} F}{RT} C_{\mathrm{A}} \nabla\phi \right)$$

The problem is solved using using the following coordinate transform:

$$\eta = 1 - \tfrac{r_{\mathrm{e}}}{r}$$

The problem is then conveniently confined to finite space $0 \leq \eta \leq 1$.

7.2.2 Microdisc electrode

In real space (r_{disc}, z_{disc}):

$$\nabla = \frac{\partial}{\partial r_{\mathrm{disc}}} + \frac{\partial}{\partial z_{\mathrm{disc}}}$$

$$\nabla^{2} = \frac{\partial^{2}}{\partial {r_{\mathrm{disc}}}^{2}} + \frac{1}{r_{\mathrm{disc}}} \frac{\partial}{\partial r_{\mathrm{disc}}} + \frac{\partial^{2}}{\partial {z_{\mathrm{disc}}}^{2}}$$

The transport equations, for bulk solution, are:

$$
\begin{aligned}
0 &= D_{\mathrm{A}}\nabla^2 C_{\mathrm{A}} + D_{\mathrm{A}}\tfrac{Z_{\mathrm{A}}F}{RT}\nabla\left(C_{\mathrm{A}}\nabla\phi\right)\\
0 &= D_{\mathrm{B}}\nabla^2 C_{\mathrm{B}} + D_{\mathrm{B}}\tfrac{Z_{\mathrm{B}}F}{RT}\nabla\left(C_{\mathrm{B}}\nabla\phi\right)\\
0 &= D_{\mathrm{M}}\nabla^2 C_{\mathrm{M}} + D_{\mathrm{M}}\tfrac{Z_{\mathrm{M}}F}{RT}\nabla\left(C_{\mathrm{M}}\nabla\phi\right)\\
0 &= D_{\mathrm{X}}\nabla^2 C_{\mathrm{X}} + D_{\mathrm{X}}\tfrac{Z_{\mathrm{X}}F}{RT}\nabla\left(C_{\mathrm{X}}\nabla\phi\right)
\end{aligned}
$$

The electroneutrality equation is:

$$
0 = \sum_s Z_{\mathrm{s}}C_{\mathrm{s}}
$$

The boundary conditions on the electrode surface ($r_{\mathrm{disc}} \leq r_{\mathrm{e}}$, $z = 0$) are:

$$
\begin{aligned}
D_{\mathrm{A}}\nabla C_{\mathrm{A},0} + D_{\mathrm{A}}C_{\mathrm{A},0}\tfrac{Z_{\mathrm{A}}F}{RT}\nabla\Delta\phi &= C_{\mathrm{A},0}\ k^0\ \exp\left(\tfrac{-\alpha F(E-E_{\mathrm{f}}-\Delta\phi)}{RT}\right)\\
&\quad -C_{\mathrm{B},0}\ k^0\ \exp\left(\tfrac{\beta F(E-E_{\mathrm{f}}-\Delta\phi)}{RT}\right)\\
D_{\mathrm{B}}\nabla C_{\mathrm{B},0} + D_{\mathrm{B}}C_{\mathrm{B},0}\tfrac{Z_{\mathrm{B}}F}{RT}\nabla\Delta\phi &= -D_{\mathrm{A}}\nabla C_{\mathrm{A},0} - D_{\mathrm{A}}C_{\mathrm{A},0}\tfrac{Z_{\mathrm{A}}F}{RT}\nabla\Delta\phi\\
D_{\mathrm{M}}\nabla C_{\mathrm{M},0} + D_{\mathrm{M}}C_{\mathrm{M},0}\tfrac{Z_{\mathrm{M}}F}{RT}\nabla\Delta\phi &= 0\\
D_{\mathrm{X}}\nabla C_{\mathrm{X},0} + D_{\mathrm{X}}C_{\mathrm{X},0}\tfrac{Z_{\mathrm{X}}F}{RT}\nabla\Delta\phi &= 0\\
\sum_s Z_{\mathrm{s}}C_{\mathrm{s},0} &= 0
\end{aligned}
$$

The remaining boundary conditions are:

$r_{\mathrm{disc}} > r_{\mathrm{e}}$ and $z = 0$	$\nabla C_{\mathrm{A}} = 0$	$\nabla C_{\mathrm{B}} = 0$	$\nabla C_{\mathrm{M}} = 0$	$\nabla C_{\mathrm{X}} = 0$	$\sum_s Z_{\mathrm{s}}C_{\mathrm{s}} = 0$
$r_{\mathrm{disc}} = \infty$ and all z	$C_{\mathrm{A}} = C^*_{\mathrm{A}}$	$C_{\mathrm{B}} = 0$	$C_{\mathrm{M}} = C^*_{\mathrm{M}}$	$C_{\mathrm{X}} = C^*_{\mathrm{X}}$	$\sum_s Z_{\mathrm{s}}C_{\mathrm{s}} = 0$
all r_{disc} and $z = \infty$	$C_{\mathrm{A}} = C^*_{\mathrm{A}}$	$C_{\mathrm{B}} = 0$	$C_{\mathrm{M}} = C^*_{\mathrm{M}}$	$C_{\mathrm{X}} = C^*_{\mathrm{X}}$	$\sum_s Z_{\mathrm{s}}C_{\mathrm{s}} = 0$
$r_{\mathrm{disc}} = 0$ and all z	$\nabla C_{\mathrm{A}} = 0$	$\nabla C_{\mathrm{B}} = 0$	$\nabla C_{\mathrm{M}} = 0$	$\nabla C_{\mathrm{X}} = 0$	$\sum_s Z_{\mathrm{s}}C_{\mathrm{s}} = 0$

The current is:

$$
i = 2\pi F D_{\mathrm{A}} \int_{r_{\mathrm{disc}}=0}^{r_{\mathrm{e}}} \left(\nabla C_{\mathrm{A}} + \tfrac{z_{\mathrm{A}}F}{RT}C_{\mathrm{A}}\nabla\phi\right) r_{\mathrm{disc}}\mathrm{d}r
$$

The problem is solved using these coordinate transforms:

$$r_{\text{disc}} = r_{\text{e}} a_{\text{h}}(\xi) a_{\text{e}}(\eta)$$

$$z = r_{\text{e}} b_{\text{h}}(\xi) b_{\text{e}}(\eta)$$

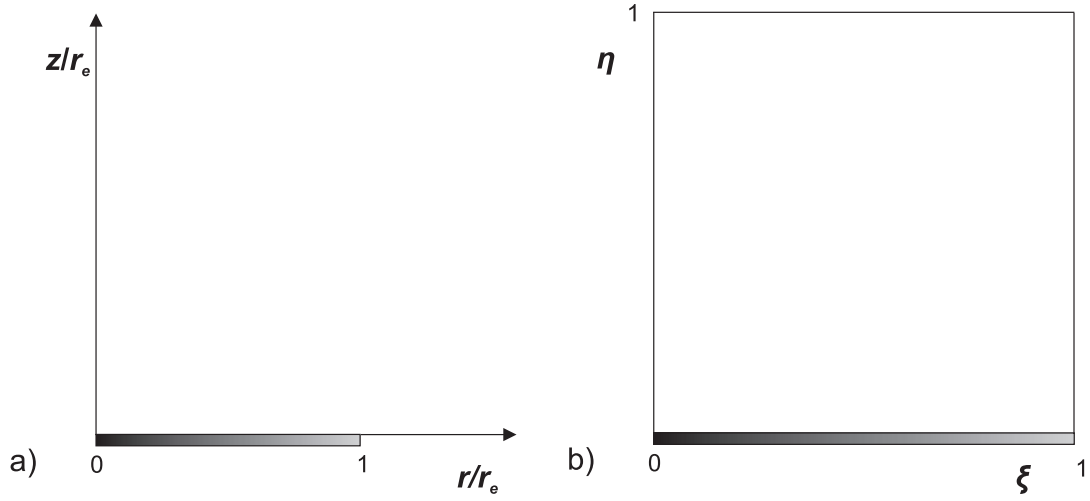

Figure 7.2.1:
a) Real Space
b) Transformed Space

The functional forms of $a_{\text{h}}(\xi)$, $a_{\text{e}}(\eta)$, $b_{\text{h}}(\xi)$ and $b_{\text{e}}(\eta)$ corresponding to the three most commonly used coordinate transforms are given in table 7.1. In each case, the transform converts the real, rectilinear, space, shown in figure 7.2.1(a), to square, conformal, space, shown in figure 7.2.1(b). The mesh arrangement corresponding to each conformal map is shown in figure 7.2.2. In each case, there are 11 points in the ζ and η directions. The conformal maps efficiently arrange the points of the spacial mesh around the singularity located at the electrode edge. Consequently, simulations conducted in conformal space (ξ, η) are considerably more efficient that those in real (r, z).

Transform Type	**Function Pairs**	
	$a_{\mathrm{e}}(\eta)$, $b_{\mathrm{e}}(\eta)$	$a_{\mathrm{h}}(\xi)$, $b_{\mathrm{h}}(\xi)$
Real space	$a_{\mathrm{e}}(\eta) = 1$	$a_{\mathrm{h}}(\xi) = \xi$
	$b_{\mathrm{e}}(\eta) = \eta$	$b_{\mathrm{h}}(\xi) = 1$
	$\eta \in [0; \infty]$	$\xi \in [0; \infty]$
Verbrugge-Baker	$a_{\mathrm{e}}(\eta) = \sec\left(\frac{\eta}{1-\eta}\right)$	$a_{\mathrm{h}}(\xi) = \cos\left(\frac{\pi}{2}(1-\xi)\right)$
	$b_{\mathrm{e}}(\eta) = \sinh\left(\frac{\eta}{1-\eta}\right)$	$b_{\mathrm{h}}(\xi) = \sin\left(\frac{\pi}{2}(1-\xi)\right)$
	$\eta \in [0; 1]$	$\xi \in [0; 1]$
Amatore-Fossett	$a_{\mathrm{e}}(\eta) = \sec\left(\frac{\pi}{2}\eta\right)$	$a_{\mathrm{h}}(\xi) = \sqrt{1-\xi^2}$
	$b_{\mathrm{e}}(\eta) = \tan\left(\frac{\pi}{2}\eta\right)$	$b_{\mathrm{h}}(\xi) = \xi$
	$\eta \in [0; 1]$	$\xi \in [0; 1]$
Oleinick-Amatore-Svir	$a_{\mathrm{e}}(\eta) = \sec\left(\frac{\pi}{2}\eta\right)$	$a_{\mathrm{h}}(\xi) = \sin\left(\frac{\pi}{2}\xi\right)$
	$b_{\mathrm{e}}(\eta) = \tan\left(\frac{\pi}{2}\eta\right)$	$b_{\mathrm{h}}(\xi) = \cos\left(\frac{\pi}{2}\xi\right)$
	$\eta \in [0; 1]$	$\xi \in [0; 1]$

Table 7.1:
Summary of common conformal maps.

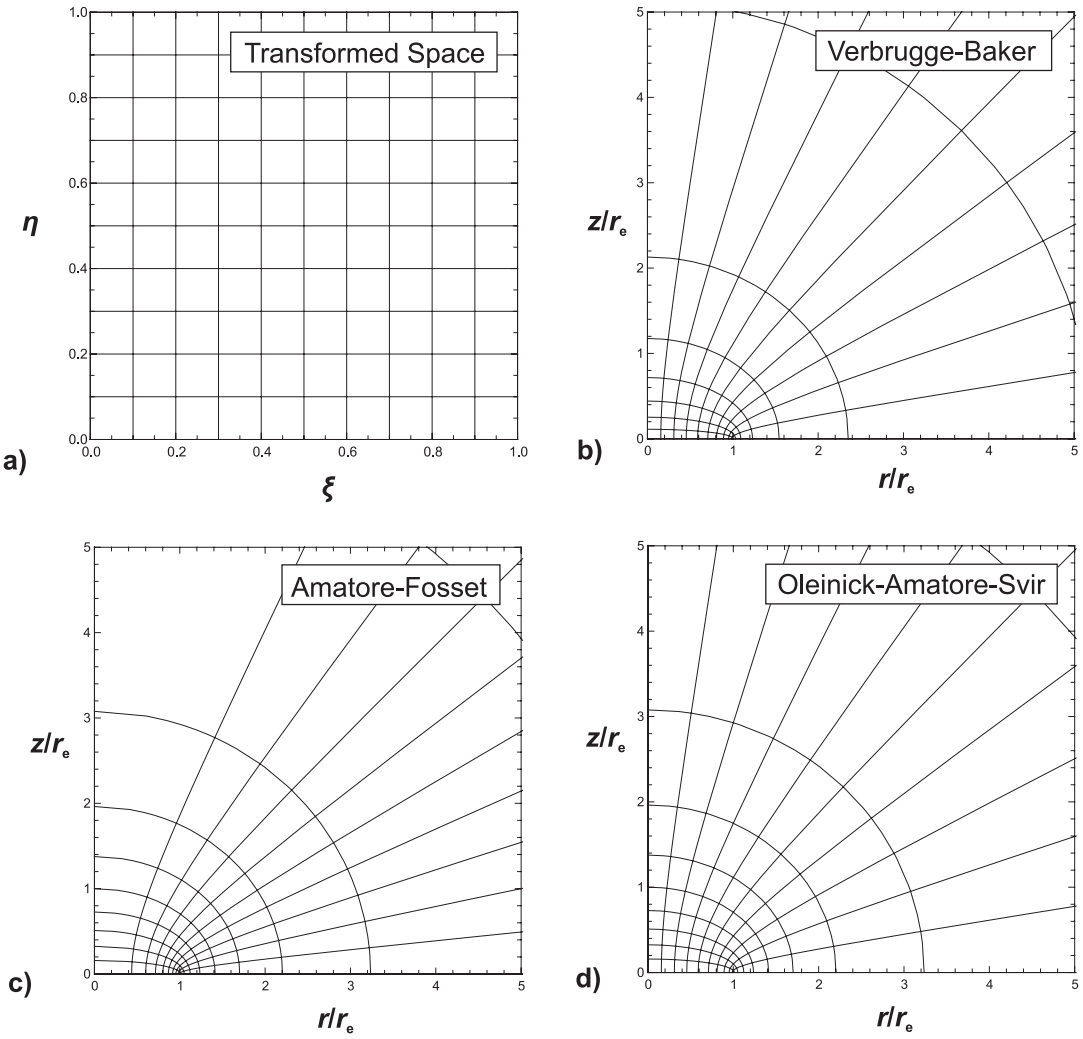

Figure 7.2.2:
a) Transformed Space
Real space corresponding to:
b) The Verbrugge-Baker transformation
c) The Amatore-Fossett transformation
d) The Oleinick-Amatore-Svir transformation

7.2.3 Microdisc-hemisphere equivalence

It is possible to transform *both* the microdisc and the hemisphere problems into any conformal space of the form shown in figure 7.2.1(b).[33,34] For *both* geometries, the transport equations, for bulk solution, are:

$$\begin{aligned}
0 &= D_{\mathrm{A}}\nabla^2 C_{\mathrm{A}} + D_{\mathrm{A}}\tfrac{z_{\mathrm{A}}F}{RT}\nabla\left(C_{\mathrm{A}}\nabla\phi\right)\\
0 &= D_{\mathrm{B}}\nabla^2 C_{\mathrm{B}} + D_{\mathrm{B}}\tfrac{z_{\mathrm{B}}F}{RT}\nabla\left(C_{\mathrm{B}}\nabla\phi\right)\\
0 &= D_{\mathrm{M}}\nabla^2 C_{\mathrm{M}} + D_{\mathrm{M}}\tfrac{z_{\mathrm{M}}F}{RT}\nabla\left(C_{\mathrm{M}}\nabla\phi\right)\\
0 &= D_{\mathrm{X}}\nabla^2 C_{\mathrm{X}} + D_{\mathrm{X}}\tfrac{z_{\mathrm{X}}F}{RT}\nabla\left(C_{\mathrm{X}}\nabla\phi\right)\\
0 &= \sum_s z_{\mathrm{s}}C_{\mathrm{s}}
\end{aligned}$$

The boundary conditions on the electrode surface (ξ, $\eta = 0$) are:

$$\begin{aligned}
C_{\mathrm{A},0} &= C_{\mathrm{B},0}\exp\left(\tfrac{F(E_{\mathrm{app}}-E_{\mathrm{f}}-\Delta\phi)}{RT}\right)\\
D_{\mathrm{B}}\nabla C_{\mathrm{B},0} &= -D_{\mathrm{A}}\nabla C_{\mathrm{A},0}\\
D_{\mathrm{M}}\nabla C_{\mathrm{M},0} &= 0\\
D_{\mathrm{X}}\nabla C_{\mathrm{X},0} &= 0\\
\sum_s z_{\mathrm{s}}C_{\mathrm{s}} &= 0
\end{aligned}$$

The remaining boundary conditions are:

$\xi = 1$ and all η	$C_{\mathrm{A}} = C_{\mathrm{A}}^*$	$C_{\mathrm{B}} = 0$	$C_{\mathrm{M}} = C_{\mathrm{M}}^*$	$C_{\mathrm{X}} = C_{\mathrm{X}}^*$	$\sum_s z_{\mathrm{s}}C_{\mathrm{s}} = 0$
$\xi = 0$ and all η	$\nabla C_{\mathrm{A}} = 0$	$\nabla C_{\mathrm{B}} = 0$	$\nabla C_{\mathrm{M}} = 0$	$\nabla C_{\mathrm{X}} = 0$	$\sum_s z_{\mathrm{s}}C_{\mathrm{s}} = 0$
all ξ and $\eta = 1$	$C_{\mathrm{A}} = C_{\mathrm{A}}^*$	$C_{\mathrm{B}} = 0$	$C_{\mathrm{M}} = C_{\mathrm{M}}^*$	$C_{\mathrm{X}} = C_{\mathrm{X}}^*$	$\sum_s z_{\mathrm{s}}C_{\mathrm{s}} = 0$

Therefore, for a given η, concentration does not vary with ξ.

The current is:

$$i = FD_{\mathrm{A}}\sigma \int_0^1 \left(\nabla C_{\mathrm{A}} + \frac{z_{\mathrm{A}}F}{RT} C_{\mathrm{A}} \nabla\phi\right) \mathrm{d}\xi$$

where σ is a parameter that is determined by the change of variables used to project the problem into the (η, ξ) space. This is the only parameter in this problem that depends on the geometry of the electrode. It can be shown[28] that $\frac{\sigma_{\mathrm{hemi}}}{\sigma_{\mathrm{disc}}} = \frac{\pi}{2}$. Therefore, for a reversible A/B reaction at steady state and at any support ratio, $i_{\mathrm{disc}} = \frac{2}{\pi} i_{\mathrm{hemi}}$. This relation is called the hemispherical approximation and is independent of the value of D_{A} and D_{B}. This relation is not exact for an irreversible couple or in the presence of homogeneous kinetics.[28]

7.2.4 Numerical methods

The problems laid out in the previous sections were transformed into a conventional set of dimensionless variables, defined in the glossary. Both discs and hemispheres were solved using the fully implicit finite difference method across an irregular grid of spatial points. The resulting collection of coupled, non-linear, simultaneous equations were discretised using the Crank-Nicholson method and solved using the iterative Newton-Raphson method.[35] All simulations were programmed in C++ and run on a desktop computer (Intel Intel Core2 Quad, 2.4 GHz, 2 GB of RAM). The simulations were converged to within < 0.5 % of the analytical steady state current corresponding to an infinitely large overpotential.[6] In the hemispherical simulation space, spacings at $\eta = 0$, Δ_{bottom}, and $\eta = 1$, Δ_{top}, were specified and the remaining spacings varied linearly between these limits. That is:

$$i = 0 \qquad \eta_0 = 0$$

$$0 < i < n_{\text{total}} \qquad \eta_i = \eta_{i-1} + i\left(\frac{\Delta\eta_{\text{top}} - \Delta\eta_{\text{bottom}}}{n_{\text{total}} - 1}\right) + \Delta\eta_{\text{bottom}}$$

In the microdisc simulation space, the grid spacings in the η and ξ directions followed the same functional form as for the hemisphere above. Three conformal maps in table 7.1[20,21,36,37] are considered and compared in the theoretical results and discussion section.

It is known that problems of this type, solved in this way, require a dense spatial grid and must exclude the case for which Z_{A} is equal to the number of transferred electrons.[31,32] This cases causes numerical instability. Figure 7.2.3 shows concentra-

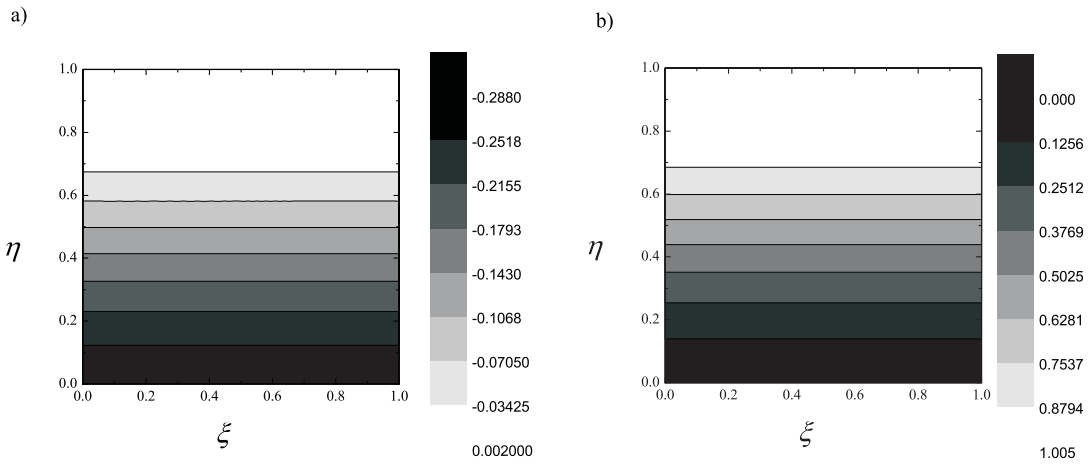

Figure 7.2.3:
Profiles takes at the top of the potential step (corresponding to the mass transport limited steady-state current). a) Potential profile b) Concentration profile of species A

tion and potential profiles for a full potential step ($E \gg E_{\text{f}}$). There is seen to be negligible flux in the ξ direction. This confirm the conformal nature of the spacial grid used.

7.3 Theoretical results and discussion

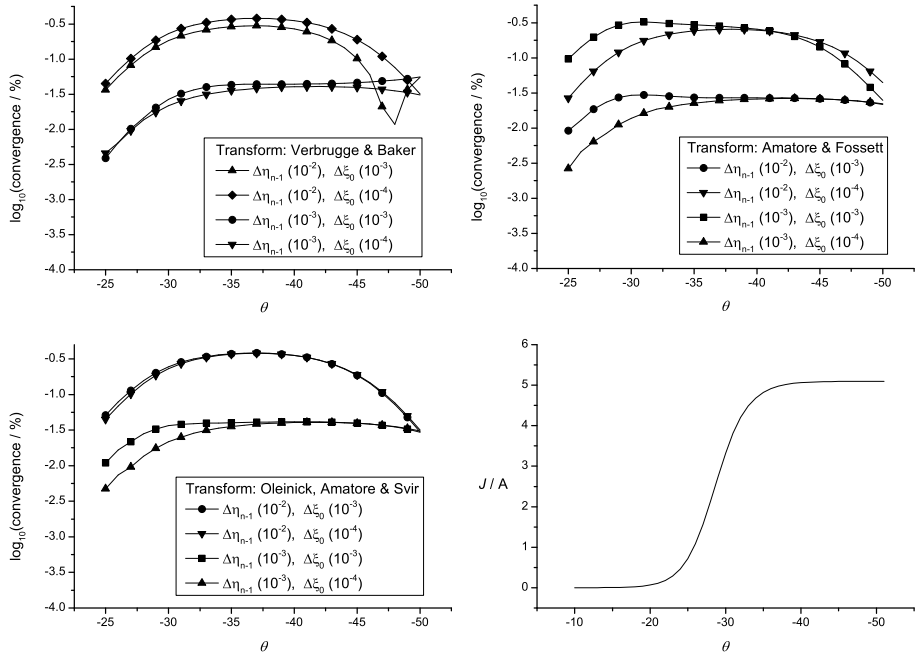

Figure 7.3.1:
Convergence plots
a) Verbrugge-Baker transformation
b) Amatore-Fossett transformation
c) Oleinick-Amatore-Svir transformation
d) Corresponding Cyclic voltammogram

Figure 7.3.1 shows convergence plots for three conformal maps: Verbrugge-Baker, Amatore-Fossett and Oleinick-Amatore-Svir. The simulations were run for the system with the lowest rate of convergence: the irreversible, self supported, redox couple $A^{2+} + e^- \rightleftharpoons B^+$. This is expected because electroactive ions of low charge, in the absence of electrolytic support, will maximise the contribution of the migrational component to the overall mass transport of the system. The migrational part is know to exhibit slow convergence characteristics.[31] In addition, irreversible

electrode kinetics lead to a non-uniform concentration distribution over the electrode surface (see figure 7.3.2). This necessitates the use of a high density of spacial

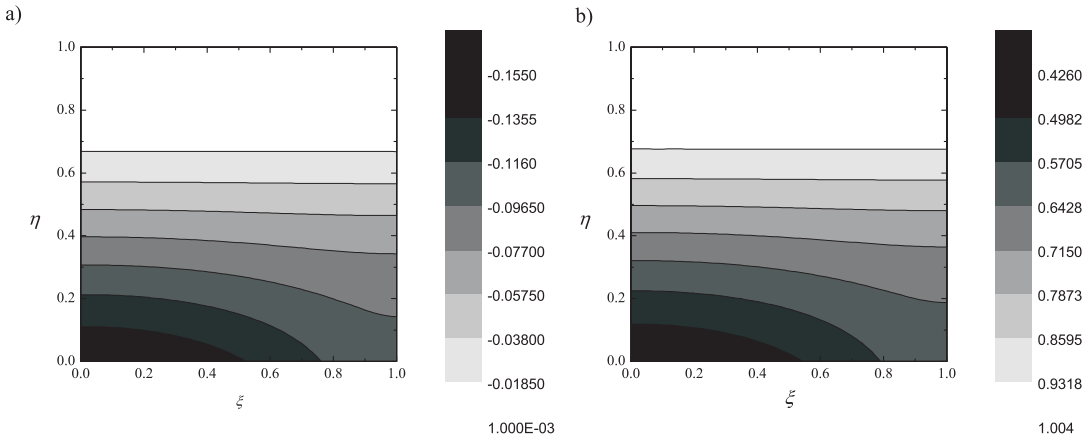

Figure 7.3.2:
Profiles takes at the half wave potential. a) Potential profile b) Concentration profile of species A

mesh points on the ξ direction. In each case, $\Delta\eta_{\text{top}} = 0.05$ and $\Delta\xi_{\text{bottom}} = 0.05$. The simulations were unchanged when these parameters were decreased by an order of magnitude: indicating that convergence is limited by $\Delta\eta_{\text{bottom}}$ and $\Delta\xi_{\text{top}}$. This region corresponds to the edge of the electrode. This is known to be the location of a spatial node[38,39] and a high mesh density is required. The simulations were compared relative to $\Delta\eta_{\text{bottom}} = 10^{-5}$ and $\Delta\xi_{\text{top}} = 10^{-4}$, i.e. an order of magnitude smaller than the values plotted on the convergence plots. Figure 7.3.1 shows the rate of convergence for a complete range of applied potentials, θ, when $\Delta\eta_{\text{bottom}}$ and $\Delta\xi_{\text{top}}$ are varied. This is necessary because the conditions for convergence at the top of the wave, where electrode kinetics are reversible, is likely to be less stringent than the region close to the half wave potential. The rate of convergence is shown to be very similar in each case and, as expected, is slowest close to the half wave poten-

tial. Similar rates of convergence are expected because, as shown in figure 7.2.2 the distribution of spacial points are very similar. For the remainder of the chapter, the Verbrugge-Baker transform is used in order to be consistent with previous work.[20,21] The concentration profiles are most easily studied in conformal space. This is because the greatest changes in concentration and in potential occur close to the electrode surface. The x axis is completely occupied by the electrode in the conformal space but is only partially occupied in real space. However, figures 7.3.3, 7.3.4, 7.3.5, and 7.3.6 are included in real space for to enable comparisons to be made with the following discussions in conformal space.

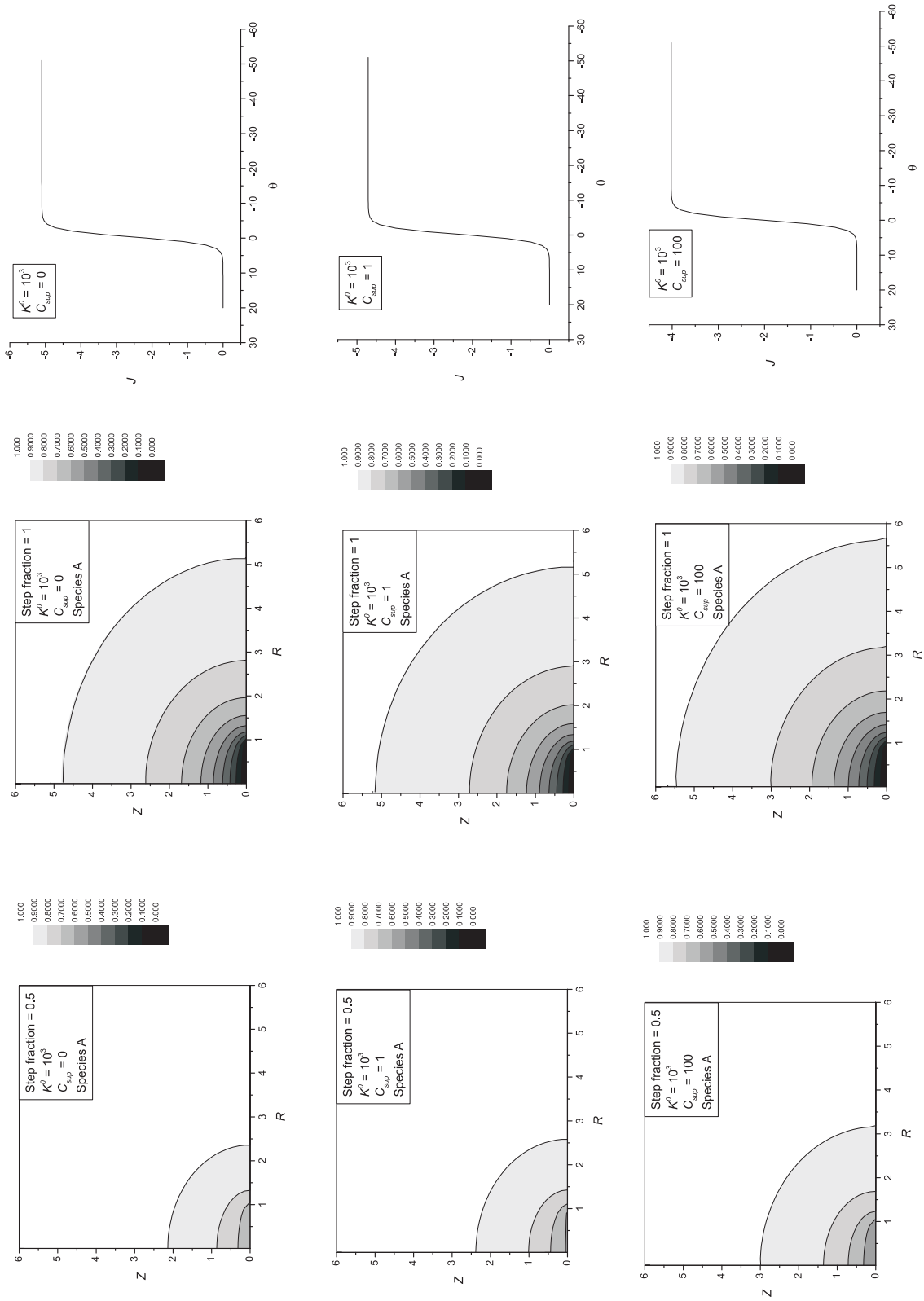

Figure 7.3.3:
Profiles for species A at the half wave and full wave potentials when $K^0 = 10^3$ *and* $c_{\text{sup}} = 0, 1,$ *are* 100.

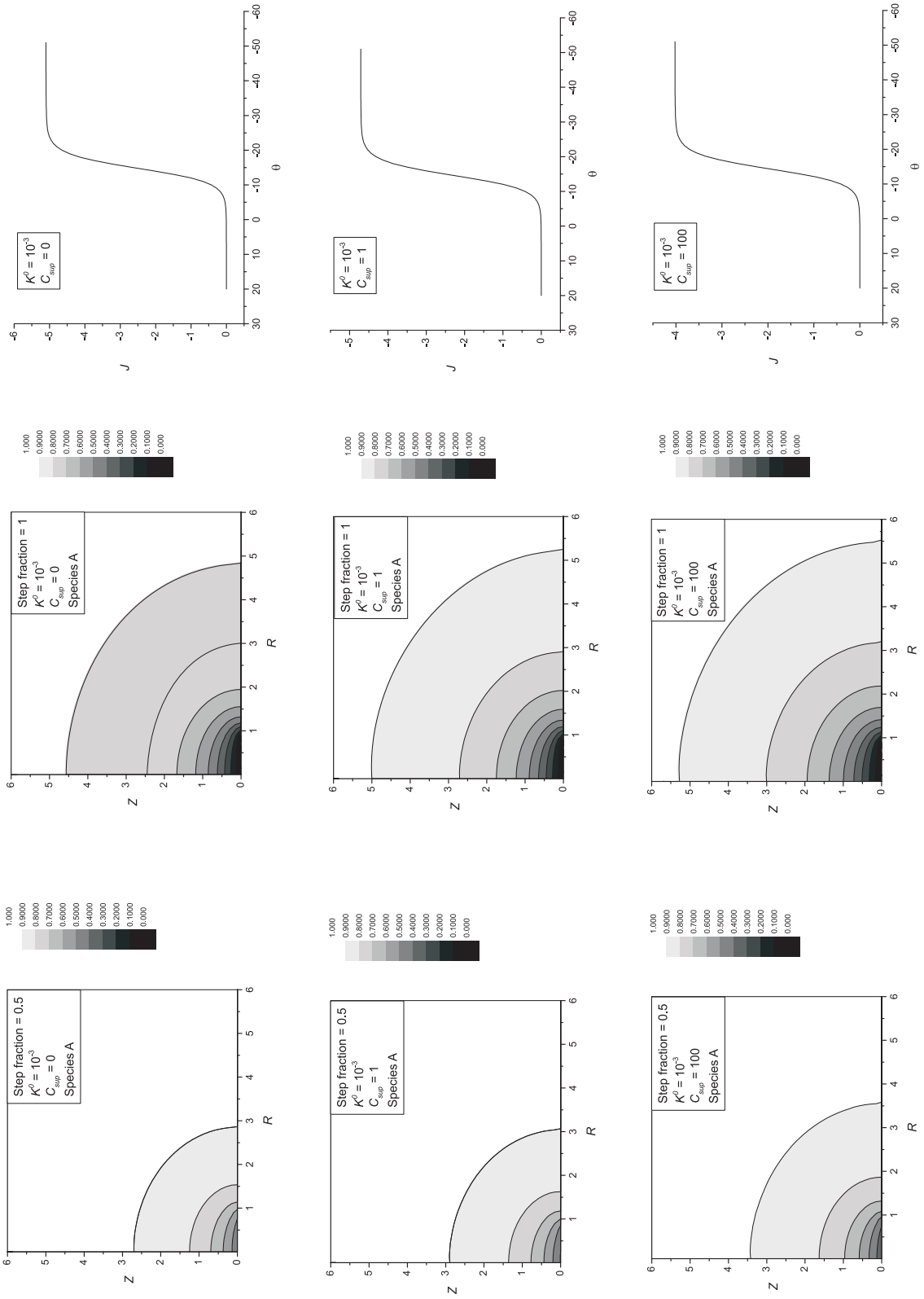

Figure 7.3.4:
Profiles for species A at the half wave and full wave potentials when $K^0 = 10^{-3}$ *and* $c_{\text{sup}} = 0, 1,$ *are* 100.

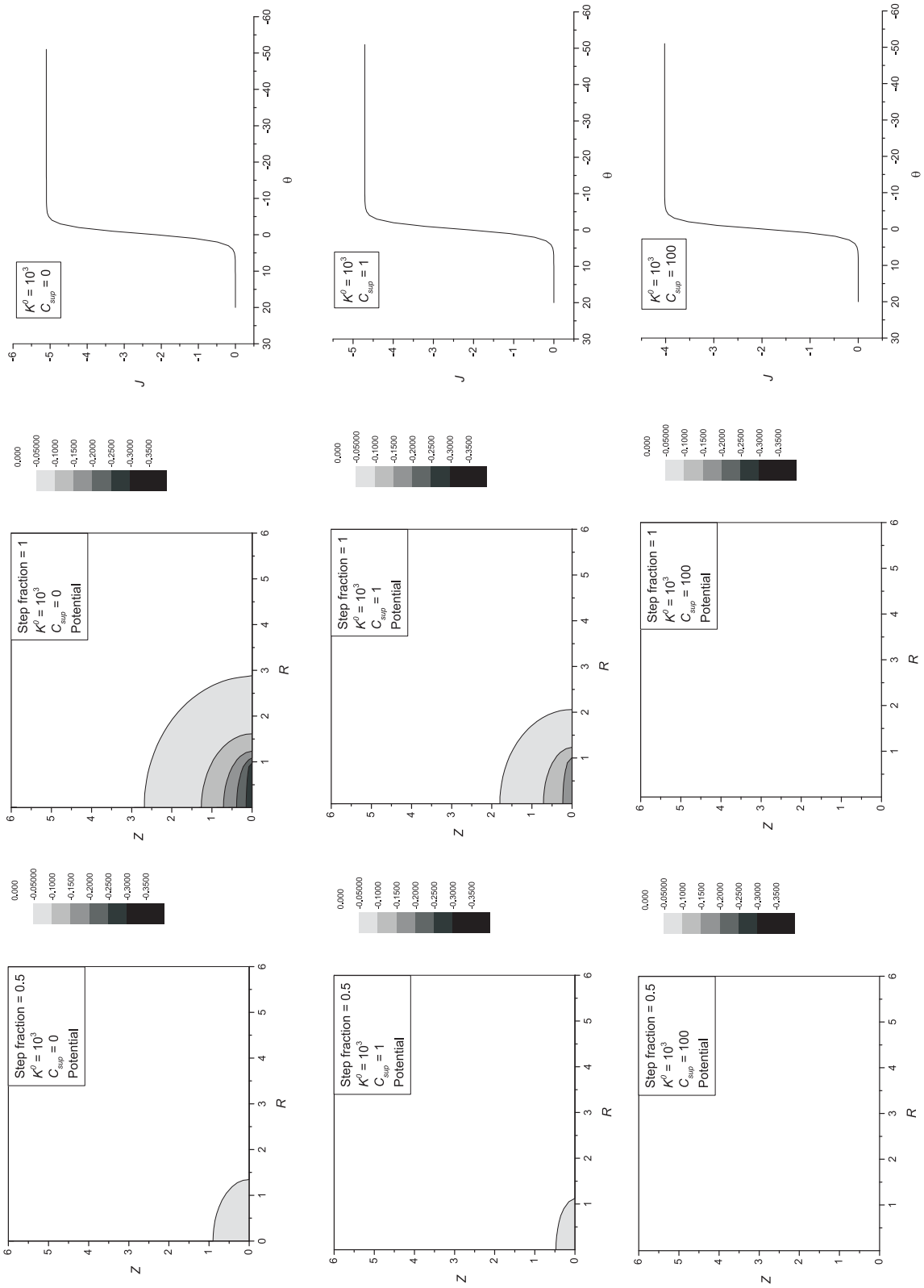

Figure 7.3.5:
Profiles for potential at the half wave and full wave potentials when $K^0 = 10^3$ *and* $c_{\text{sup}} = 0, 1,$ *are* 100.

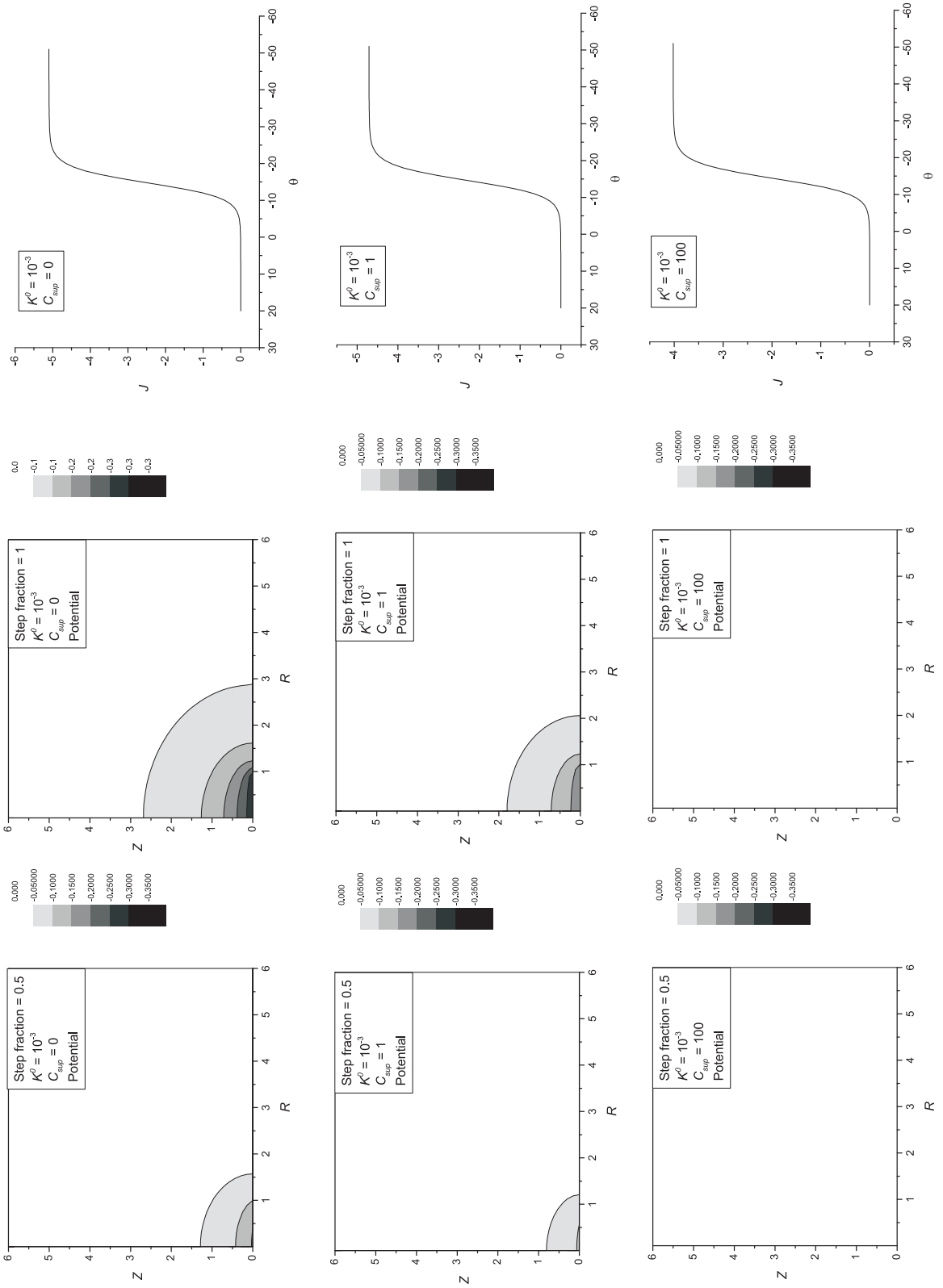

Figure 7.3.6:
Profiles for potential at the half wave and full wave potentials when $K^0 = 10^{-3}$ *and* $c_{\text{sup}} = 0, 1,$ *are* 100.

Figure 7.3.2 shows the potential (a) and concentration (b) profiles for the irreversible redox couple $A^{2+} + e^- \rightleftharpoons B^+$ at self support. The loss in potential driving force is negligible ($\theta = -0.15$ corresponds to $E \approx -3.85{\times}10^{-3}\ V$ at 298 K), as expected for voltammetry at steady-state. The concentration varies over the electrode surface. This can be explained with respect to the Butler-Volmer equation in the transformed space:

$$\begin{aligned} D'_{\mathrm{A}} \frac{\partial c_{\mathrm{A}}}{\partial \eta} &= \sin\left(\tfrac{\pi}{2}(1-\xi)\right) K^0 c_{\mathrm{A}} \exp\left(-\frac{\alpha F(E-E_{\mathrm{f}}-\Delta\phi)}{RT}\right) \\ &\quad - \sin\left(\tfrac{\pi}{2}(1-\xi)\right) K^0 c_{\mathrm{B}} \exp\left(\frac{\beta F(E-E_{\mathrm{f}}-\Delta\phi)}{RT}\right) \end{aligned}$$

Consequently, the effective rate constant over the electrode surface is:

$$K^0_{\mathrm{effective}} = \sin\left(\frac{\pi}{2}(1-\xi)\right) K^0_{\mathrm{real}} \tag{7.3.1}$$

Therefore, $K^0_{\mathrm{effective}}$ increases with decreasing ξ. Greater depletion of species A is therefore expected at the centre of the electrode, as shown in figure 7.3.2 (b).

Figure 7.2.3 shows the corresponding potential (a) and concentration (b) profiles at the top of the voltammetric wave. This corresponds to reversible electrode kinetics. Consequently, the Nernst equation is obeyed over the electrode surface and the flux is uniform. Again, the loss in the potential driving force is negligible ($\theta = -0.288$ corresponds to $E \approx -7.39{\times}10^{-3}\ V$ at 298 K), as expected for voltammetry at steady-state. Figure 7.3.7 a) shows the cyclic voltammetry at a microdisc for the redox couple $A^{2+} + e^- \rightleftharpoons B^+$ under self support as a function of the electrochemical

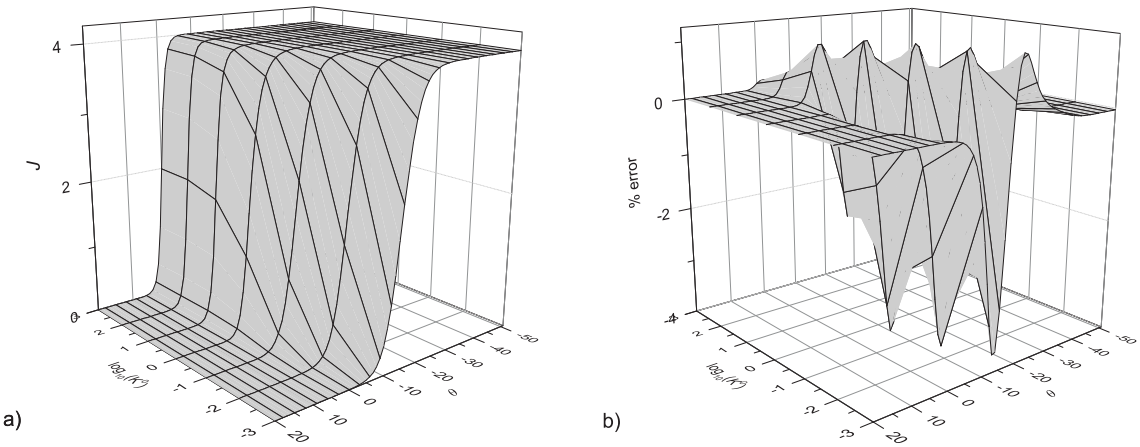

Figure 7.3.7:
a) Percentage error between microdisc and equivalent hemisphere at $c_{\mathrm{sup}} = 0$
b) Cyclic voltammograms corresponding to 'a)' (above)

rate constant, K^0. The following equivalence relation is used:

$$r_{\mathrm{e,disc}} = \frac{2}{\pi} r_{\mathrm{e,hemi}} \tag{7.3.2}$$

As explained in the theory section, this relation becomes increasingly unreliable as the electrochemical rate constant, K^0, decreases.[26,28] Figure 7.3.7 b) shows the percentage error between the simulation for a microdisc and for a hemisphere using the hemispherical approximation. The maximum error is shown to be 3.81 %: close to the error range of most experiments. The hemispherical approximation is therefore quantitatively useful when $K^0 < 10^{-3}$. Since this analysis is conducted for an extreme case, this is also valid for higher support ratios and different charges in the one electron A/B redox couple.

7.4 Experimental results and discussion

The experiments in this section were condicted by Dr. Eduardo Laborda. The experimental methods used are described in Appendix C. Figure 7.4.1 shows the

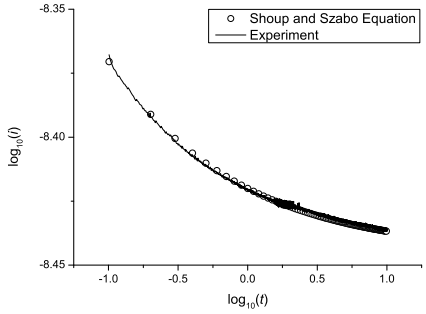

Figure 7.4.1: *Chronoamperometry for* $[Ru(NH_3)_6]^{3+}/[Ru(NH_3)_6]^{2+}$.

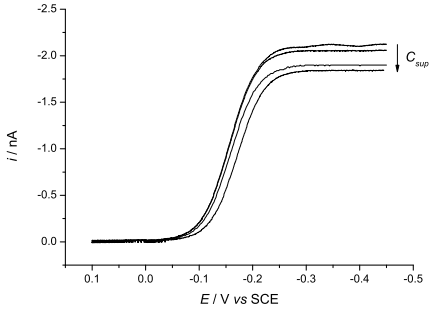

Figure 7.4.2: *Experimental cyclic voltammetry for* $[Ru(NH_3)_6]^{3+}/[Ru(NH_3)_6]^{2+}$

chronoamperometry at a microdisc at full support for the $[Ru(NH_3)_6]^{3+}/[Ru(NH_3)_6]^{2+}$ system. In order to extract the diffusion coefficient from this transient, the line was fitted using the nonlinear curve fitting function in the software package Origin 7.0 (Microcal Software Inc.) according to the following equation proposed by Shoup and Szabo:[40]

$$i = -4nFDCr_e\left(0.7854 + 0.4432\left(\frac{Dt}{{r_e}^2}\right)^{-\frac{1}{2}} + 0.2146\exp(-0.3912\left(\frac{Dt}{{r_e}^2}\right)^{-\frac{1}{2}})\right) \tag{7.4.1}$$

The value of the diffusion coefficient for $[Ru(NH_3)_6]^{3+}$ is 8.7×10^{-10} m^2 s^{-1}, in good agreement with the literature value.[41–45] Figure 7.4.2 shows experimental cyclic voltammetry for the $[Ru(NH_3)_6]^{3+}/[Ru(NH_3)_6]^{2+}$ system. The value of the diffusion coefficient for $[Ru(NH_3)_6]^{2+}$ is obtained by fitting the voltammetric current at

steady-state using the numerical simulation.[25] The value of the diffusion coefficient for $[Ru(NH_3)_6]^{2+}$ is 8.6×10^{-10} m^2 s^{-1}, in good agreement with the literature value.[41] The steady-state value becomes smaller with increasing support ratio. In this reduction reaction, negative charge is generated at the electrode surface. Positive ions must therefore migrate towards the surface in order to maintain overall electroneutrality. Since $[Ru(NH_3)_6]^{3+}$ is positively charged, any factor that decreases the contribution of this species to the maintenance of electroneutrality (e.g. increasing the support ratio) will decrease the value of the limiting current. The variation in limiting current can be simulated as shown in figures 7.4.3 and 7.4.4. However, since the loss in potential driving force is negligible, the numerical simulations do not account for the observed variation in E_f as a function of the support ratio. The trend in E_f, instead, must be explained using the extended Debye-Hückel theory:[46–48]

$$E = E_{f,real} - \Delta\phi - 2.3\frac{RT}{F}\log_{10}\left(\frac{a_B}{a_A}\right) \tag{7.4.2}$$

From the simulations, it was found that $\Delta\phi \approx 0\ V$

$$E = E_{f,real} - 2.3\frac{RT}{F}\log_{10}\left(\frac{\gamma_B C_B}{\gamma_A C_A}\right) \tag{7.4.3}$$

$$E_{f,apparent} = E_{f,real} - 2.3\frac{RT}{F}\log_{10}\left(\frac{\gamma_B}{\gamma_A}\right) \tag{7.4.4}$$

$$E_{f,apparent} = E_{f,real} - 2.3\frac{RT}{F}\left(\frac{0.51(z_A^2 - z_B^2)\sqrt{I}}{1 + 0.32a\sqrt{I}}\right) \tag{7.4.5}$$

where I is the ionic strength, $a = 3.3 \times 10^{-10}$ m is the radius of the electroactive ions (assumed equal).[49] Excellent concordance between theory and experiment is shown in figure 7.4.5. Figure 7.4.6 shows the chronoamperometry at a microdisc, at full support, for the $[IrCl_6]^{2-}/[IrCl_6]^{3-}$ system. The value of the diffusion coefficients for $[IrCl_6]^{2-}$ and $[IrCl_6]^{3-}$, obtained using the procedures described above are 7.5×10^{-10} m^2 s^{-1} and 7.2×10^{-10} m^2 s^{-1} respectively, in good agreement with the literature values.[45,50] Figure 7.4.7 shows experimental cyclic voltammetry for the $[IrCl_6]^{2-}/[IrCl_6]^{3-}$ system. The steady-state current becomes larger as the support ratio increases. In this reduction reaction, negative charge is generated at the electrode surface. Negative ions therefore migrate away from the surface in order to maintain electroneutrality. Since $[IrCl_6]^{2-}$ is negatively charged, any factor that decreases the contribution of this species to the maintenance of electroneutrality (e.g. increasing the support ratio) will increase the value of limiting current. The variation in limiting current can be simulated as shown in figures 7.4.8 and 7.4.9. However, as above, the value of E_f must be explained using the Debye-Hückel theory. The ionic radius is of 4×10^{-10} m.[51] Poor concordance between theory and experiment is illustrated in figure 7.4.10. The experimental ionic strength appears too high to match the theory. This effect is likely to be caused by ion pairing, as suggested in the literature.[51]

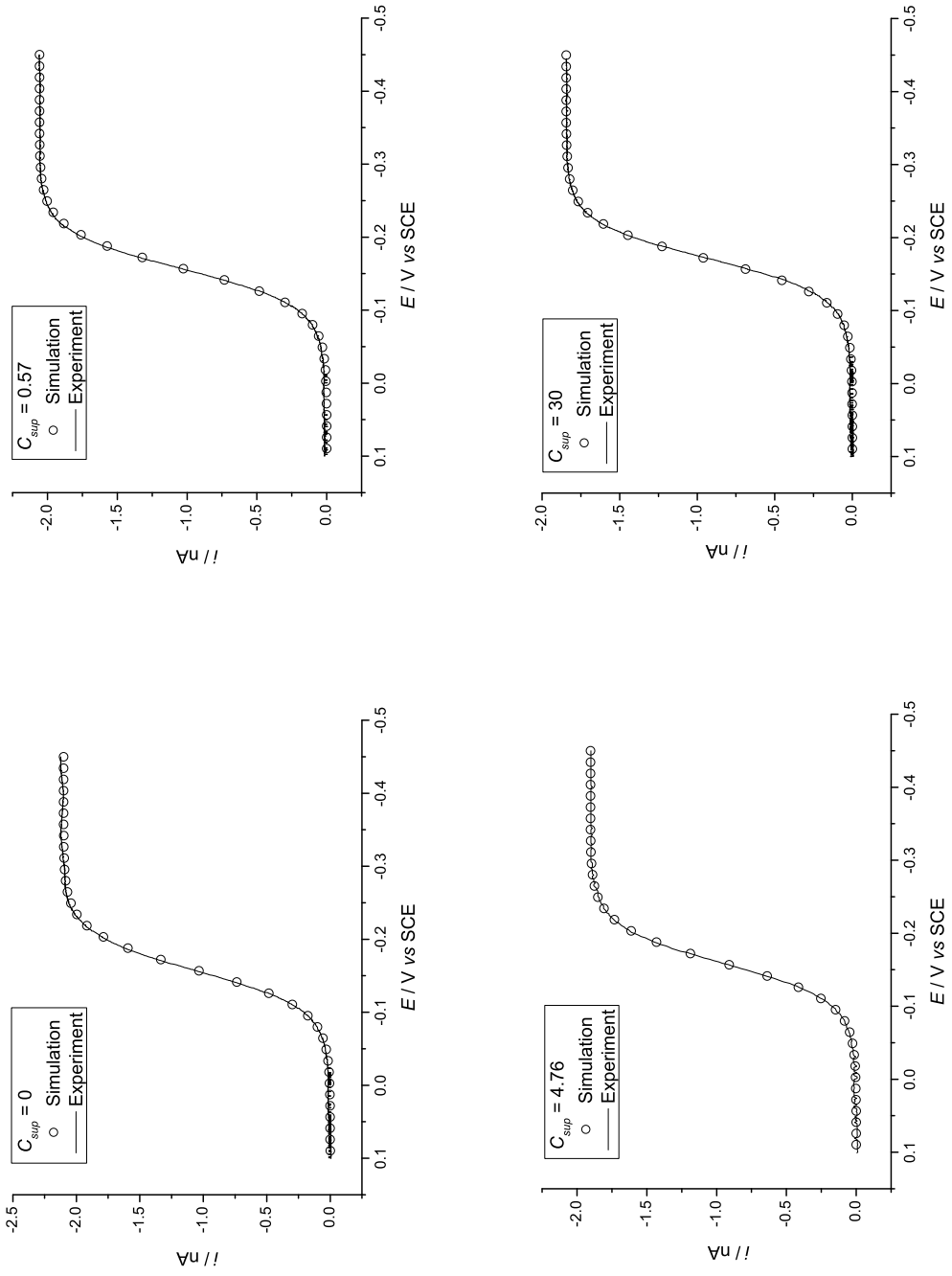

Figure 7.4.3: *Comparison between experimental and simulated cyclic voltammograms for* $[Ru(NH_3)_6]^{3+}/[Ru(NH_3)_6]^{2+}$

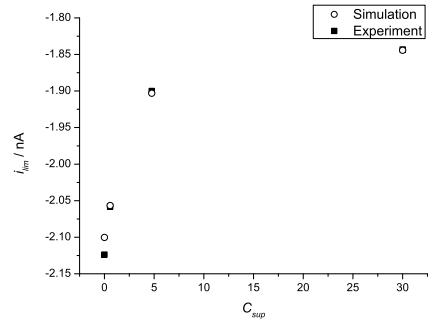

Figure 7.4.4:
Comparison between experimental and simulated limiting currents for $[Ru(NH_3)_6]^{3+}/[Ru(NH_3)_6]^{2+}$

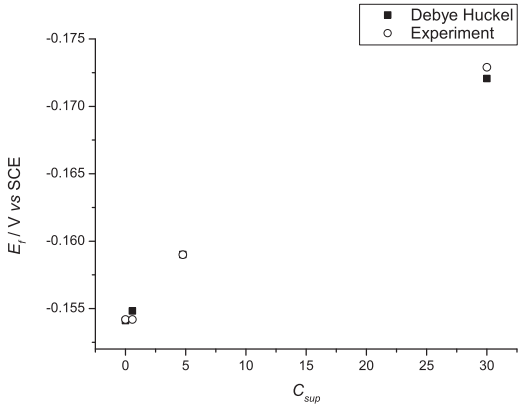

Figure 7.4.5:
Comparison between experimental and theoretical formal potentials for $[Ru(NH_3)_6]^{3+}/[Ru(NH_3)_6]^{2+}$

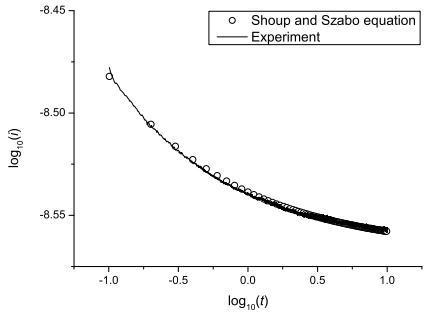

Figure 7.4.6:
Chronoamperometry for $[IrCl_6]^{2-}/[IrCl_6]^{3-}$

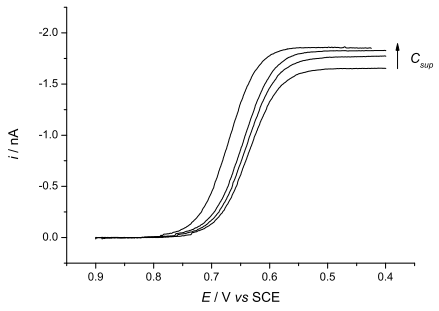

Figure 7.4.7:
Experimental cyclic voltammetry for $[IrCl_6]^{2-}/[IrCl_6]^{3-}$

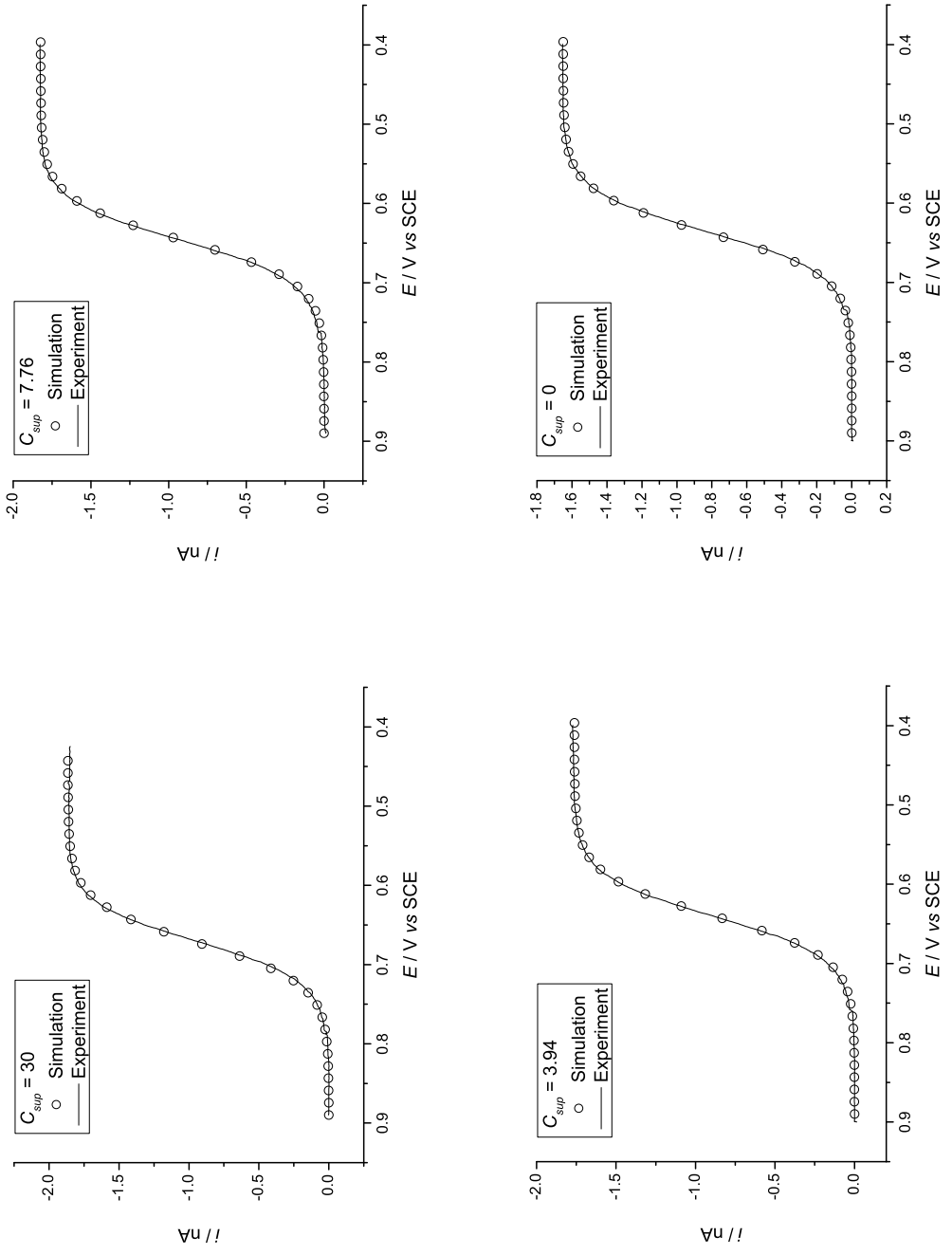

Figure 7.4.8:
Comparison between experimental and simulated cyclic voltammograms for $[IrCl_6]^{2-}/[IrCl_6]^{3-}$

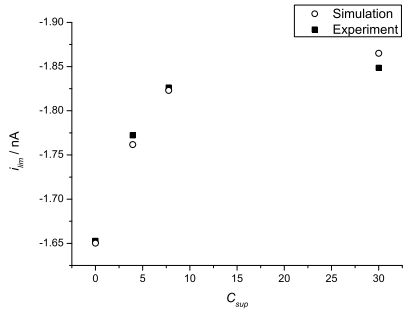

Figure 7.4.9:
Comparison between experimental and simulated limiting currents for $[IrCl_6]^{2-}/[IrCl_6]^{3-}$

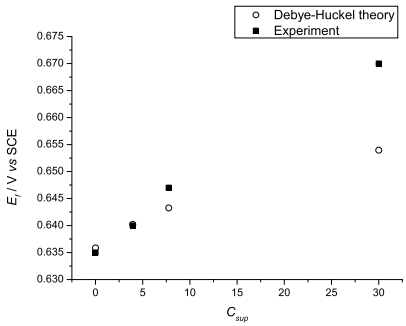

Figure 7.4.10: *Comparison between experimental and theoretical formal potentials for* $[IrCl_6]^{2-}/[IrCl_6]^{3-}$

7.5 Conclusion

Steady-state cyclic voltammetry at low support can be efficiently simulated for both reversible and irreversible electrode kinetics. It is shown, by numerical and analytical means, that the hemispherical approximation is reliable over a range of support ratios and electrochemical rate constants.

The simulations and the Debye-Hückel theory are used to analyze cyclic voltammetry obtained for two aqueous redox couples: hexammineruthenium $[Ru(NH_3)_6]^{3+}/[Ru(NH_3)_6]^{2+}$ and hexachloroiridate $[IrCl_6]^{2-}/[IrCl_6]^{3-}$. The data indicates the occurrence of ion pairing in the latter but not in the former.

Bibliography

[1] Belding, S. R.; Laborda, E.; Compton, R. G. *Phys. Chem. Chem. Phys.* **2012**, *14*, 14635–14649.

[2] Bond, A. M. *Analyst* **1994**, *119*, 1R–21R.

[3] Bard, A. J.; Faulkner, L. R. *Electrochemical Methods, Fundamentals and Applications*, 2nd ed.; John Wiley & Sons Inc.: Hoboken, NJ, 2001.

[4] Compton, R. G.; Banks, C. E. *Understanding Voltammetry*, 2nd ed.; World Scientific, 2011.

[5] Heinze, J. *Angew. Chem. Int. Ed.* **1993**, *32*, 1268–1288.

[6] Myland, J. C.; Oldham, K. B. *J. Electroanal. Chem.* **1993**, *347*, 49–91.

[7] Wightman, R.; Wipf, D. In *Electroanalytical Chemistry*, 1st edition ed.; Bard, A. J., Ed.; Marcel Dekker: New York, 1988; Vol. 15; p 267.

[8] Amatore, C.; Maisonhaute, E.; Simonneau, G. *Electrochem. Commun.* **2000**, *2*, 81–84.

[9] Amatore, C.; Farsang, G.; Maisonhaute, E.; Simon, P. *J. Electroanal. Chem.* **1999**, *462*, 55–62.

[10] Amatore, C.; Maisonhaute, E.; Simonneau, G. *J. Electroanal. Chem.* **2000**, *486*, 141–155.

[11] Streeter, I.; Compton, R. G. *J. Phys. Chem. C* **2008**, *112*, 13716–13728.

[12] Bond, A.; Fleischmann, M.; Robinson, J. *J. Electroanal. Chem.* **1984**, *172*, 11–25.

[13] Palys, M. J.; Stojek, Z.; Bos, M.; van der Linden, W. E. *J. Electroanal. Chem.* **1995**, *383*, 105–117.

[14] Oldham, K. B. *J. Electroanal. Chem.* **1988**, *250*, 1–21.

[15] Ciszkowska, M.; Stojek, Z. *J. Electroanal. Chem.* **1999**, *466*, 129–143.

[16] Amatore, C.; Deakin, M. R.; Wightman, R. *J. Electroanal. Chem.* **1987**, *225*, 49 – 63.

[17] Myland, J. C.; Oldham, K. B.; Zhu, G. *Anal. Chem.* **1988**, *60*, 1610–1621.

[18] Belding, S. R.; Limon-Petersen, J. G.; Dickinson, E. J. F.; Compton, R. G. *Angew. Chem. Int. Ed.* **2010**, *49*, 9242–9245.

[19] Barnes, E. O.; Wang, Y.; Belding, S. R.; Compton, R. G. *ChemPhysChem* **2012**, *13*, 92–95.

[20] Baker, D. R.; Verbrugge, M. W.; Newman, J. *J. Electroanal. Chem.* **1991**, *314*, 23–44.

[21] Verbrugge, M. W.; Baker, D. R. *J. Phys. Chem.* **1992**, *96*, 4572–4580.

[22] Bond, A. M.; Oldham, K. B.; Zoski, C. G. *J. Electroanal. Chem.* **1988**, *245*, 71–104.

[23] Oldham, K. B. *J. Electroanal. Chem.* **1992**, *337*, 91–126.

[24] Limon-Petersen, J. G.; Streeter, I.; Rees, N. V.; Compton, R. G. *J. Phys. Chem. C* **2009**, *113*, 333–337.

[25] Palys, M. J.; Stojek, Z. *J. Electroanal. Chem.* **2002**, *534*, 65–73.

[26] Oldham, K. B.; Zoski, C. G. *J. Electroanal. Chem.* **1988**, *256*, 11–19.

[27] Alden, J. A.; Hutchinson, F.; Compton, R. G. *J. Phys. Chem. B* **1997**, *101*, 949–958.

[28] Amatore, C.; Fosset, B. *Anal. Chem.* **1996**, *68*, 4377–4388.

[29] Belding, S. R.; Rees, N. V.; Aldous, L.; Hardacre, C.; Compton, R. G. *J. Phys. Chem. C* **2008**, *112*, 1650–1657.

[30] Robertson, R. T.; Pendley, B. D. *J. Electroanal. Chem.* **1994**, *374*, 173–177.

[31] Klymenko, O. V.; Amatore, C.; Svir, I. *Anal. Chem.* **2007**, *79*, 6341–6347.

[32] Dickinson, E. J.; Limon-Petersen, J. G.; Compton, R. G. *J. Solid State Electrochem.* **2011**, *15*, 1335–1345.

[33] Amatore, C. A.; Fosset, B.; Deakin, M. R.; Wightman, R. M. *J. Electroanal. Chem.* **1987**, *225*, 33 – 48.

[34] Amatore, C.; Deakin, M. R.; Wightman, M. *J. Electroanal. Chem.* **1986**, *206*, 23 – 36.

[35] Press, W. H., Teukolsky, S. A., Vetterling, W. T., Flannery, B. P., Eds. *Numerical Recipes: The Art of Scientific Computing*; Cambridge University Press, 2007.

[36] Oleinick, A.; Amatore, C.; Svir, I. *Electrochem. Commun.* **2004**, *6*, 588 – 594.

[37] Amatore, C.; Fosset, B. *J. Electroanal. Chem.* **1992**, *328*, 21–32.

[38] Gavaghan, D. J. *J. Electroanal. Chem.* **1997**, *420*, 147–158.

[39] Gavaghan, D. J. *J. Electroanal. Chem.* **1998**, *456*, 25–35.

[40] Shoup, D.; Szabo, A. *J. Electroanal. Chem.* **1982**, *140*, 237–245.

[41] Wang, Y.; Limon-Petersen, J. G.; Compton, R. G. *J. Electroanal. Chem.* **2011**, *652*, 13 – 17.

[42] Ferreira, T. L.; Paixão, T. R. L. C.; Richter, E. M.; El Seoud, O. A.; Bertotti, M. *J. Phys. Chem. B* **2007**, *111*, 12478–12484.

[43] Laborda, E.; Rogers, E. I.; Martinez-Ortiz, F.; Limon-Petersen, J. G.; Rees, N. V.; Molina, A.; Compton, R. G. *J. Electroanal. Chem.* **2009**, *634*, 1–10.

[44] Licht, S.; Cammarata, V.; Wrighton, M. S. *J. Phys. Chem.* **1990**, *94*, 6133–6140.

[45] Beriet, C.; Pletcher, D. *J. Electroanal. Chem.* **1994**, *375*, 213–218.

[46] Compton, R. G.; Sanders, G. H. W. In *Electrode Potentials*; Compton, R. G., Ed.; OUP, 1996.

[47] Rieger, P. H. *Electrochemistry*; Chapman & Hall, 1994.

[48] Debye, P.; Hückel, E. *Physikalische Zeitschrift* **1923**, *24*, 185206.

[49] Brown, G. M.; Sutin, N. *J. Am. Chem. Soc.* **1979**, *101*, 883–892.

[50] Macpherson, J. V.; Jones, C. E.; Unwin, P. R. *J. Phys. Chem. B* **1998**, *102*, 9891–9897.

[51] Watkins, J. J.; White, H. S. *Langmuir* **2004**, *20*, 5474–5483.

Chapter 8

Cyclic voltammetry in room temperature ionic liquids: the comproportionation mechanism

Increasingly, ionic liquids are being used as electrochemical solvents. This chapter explains this trend and presents recent research using these solvents in voltammetry. This chapter complements the previous three because ionic liquids must necessarily yield fully supported voltammetry. In particular, the same mechanistic problem encountered in chapter 6 is solved in a different way. The work presented in this chapter has been published in The Journal of Chemical and Engineering Data.[1] The experimental work discussed here was preformed by Dr. Aoife M. O'Mahoney and Edward O. Barnes.

8.1 Introduction

Room temperature ionic liquids (RTILs) have led to substantial synthetic innovations in both academic[2–4] and industrial[5] contexts. Advantages such as of solvent tunability,[6] greenness,[7] recyclability and negligible volatility are seen over conventional non-aqueous solvents. However, unlike reactions in the latter media, the measurement of reaction parameters, both kinetic and thermodynamic, has lagged and comparatively less data is available to guide the planning and interpretation of chemistry in the RTIL environment.

Voltammetry, at least in principle, offers an experimentally simple yet accurate route into the quantitative measurement of both kinetic and thermodynamic data. For example, in the case of an arbitrary species, A, which can undergo oxidation to species B and C:

$$\mathrm{A} - \mathrm{e}^- \rightleftharpoons \mathrm{B} \quad (E^{\ominus}_{\mathrm{f,A/B}}) \tag{8.1.1}$$

$$\mathrm{B} - \mathrm{e}^- \rightleftharpoons \mathrm{C} \quad (E^{\ominus}_{\mathrm{f,B/C}}) \tag{8.1.2}$$

if two separate voltammetric features are attributable to these processes then their analysis can give information about the comproportionation reaction:[8]

$$\mathrm{A} + \mathrm{C} \rightleftharpoons 2\mathrm{B} \tag{8.1.3}$$

where, specifically, the formal potentials $E^{\ominus}_{\mathrm{f,A/B}}$ and $E^{\ominus}_{\mathrm{f,B/C}}$ will provide information

about the equilibrium constant:

$$K_{\mathrm{eqm}} = \frac{[\mathrm{B}]^2}{[\mathrm{A}][\mathrm{C}]} \tag{8.1.4}$$

and $\Delta G^{\ominus}$ for reaction 8.1.3:

$$\Delta G^{\ominus} = -RT\ln(K_{\mathrm{eqm}}) = -F(E^{\ominus}_{\mathrm{f,B/C}} - E^{\ominus}_{\mathrm{f,A/B}}) \tag{8.1.5}$$

The kinetics of reaction 8.1.3 may sometimes be discernible from the precise voltammetric waveshapes and their separation.[9] However, in the context of voltammetry using large planar electrodes ('macroelectrodes'), Savéant has shown, in a paper long regarded as a classic,[10] that if species A, B and C have identical diffusion coefficients, D_{A}, D_{B} and D_{C}, then the voltammetry is completely insensitive to the rate of comproportionation. The same is true of voltammetry recorded under diffusional modes other than linear.[8] Only if there is an appreciable disparity in the diffusion coefficients can the kinetics of reaction 8.1.3 become apparent in the voltammetry. Accordingly, voltammetry has been relatively little used in the context of measuring comproportionation kinetics except in so far that it has been coupled to spectroscopic methods, such as ESR[10] and UV/visible spectroscopy.[11] At the heart of this neglect is the fact that, in most aqueous and non-aqueous systems, species A, B and C often have closely similar diffusion coefficients unless they are structurally very dissimilar.

As electrochemical research using RTILs as solvents[12–18] has matured it has become apparent that, unlike conventional solvents such as DMF, DMSO and ace-

tonitrile, the difference in diffusion coefficients between structurally similar species in a redox couple is not always insignificant. An extreme example, discovered by Buzzeo,[19] is that of the oxygen/superoxide (O_2/O_2^-) couple in which the anion has a diffusion coefficient *ca* 30 times smaller than the neutral parent in the RTIL *n*-hexyltriethylammonium bis(trifluoromethanesulfonyl)imide ($[N_{6222}][N(Tf)_2]$). Work by Evans[13] and by Hapiot[20] have shown that even for aromatic molecules, such as N,N,N',N'-tetramethyl-para-phenylenediamine, the diffusion coefficients differ significantly between the neutral parent and the corresponding radical cation and dication despite close structural similarity. Analyte ions of higher charge typically diffuse less rapidly due to electrostatic interaction with the ions in the solvent. As a consequence it can be anticipated that, in ionic liquids, voltammetric analysis can be used as a means of obtaining information about the rate of comproportionation in solution. In this chapter we consider the oxidation of N,N-dimethyl-p-phenylenediamine, DMPD (Figure 8.1.1(a)), in the ionic liquid 1-butyl-3-methylimidazolium tetrafluoroborate, $[C_4mim][BF_4]$ (Figure 8.1.1(b)), using a microdisc electrode. It is shown that comparison between experimental and simulated data can be used to extract both kinetic and thermodynamic data including information about comproportionation. Also noted is the value of double potential step chronoamperometry in elucidating the diffusion coefficients of DMPD and $DMPD^+$.[15]

8.2 Theory

We consider an EE reaction at a microdisc electrode (Figure 8.2.1), as defined by eqs 8.1.1 and 8.1.2, where we additionally allow for comproportionation (eq 8.1.3). The

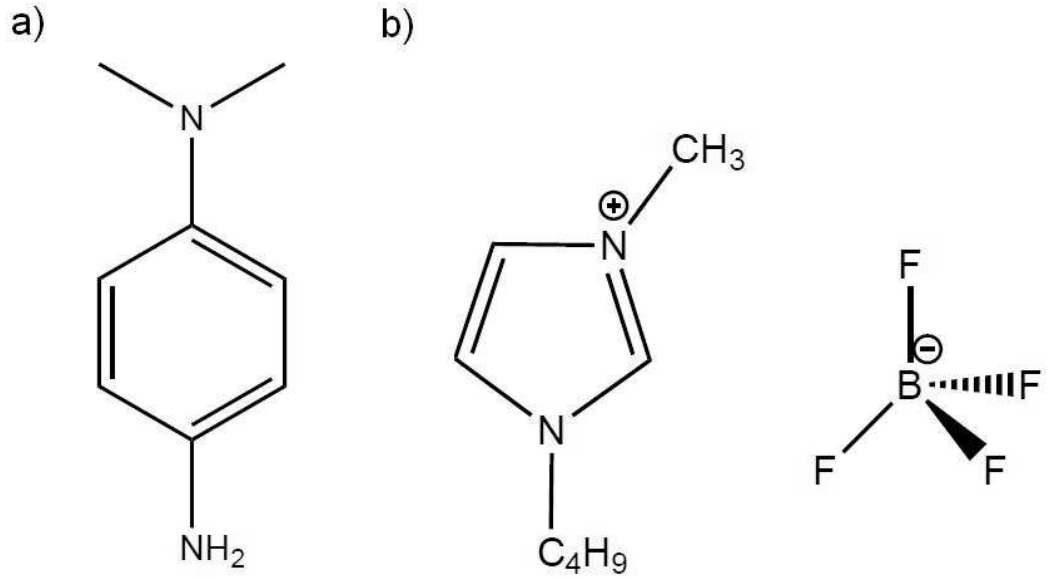

Figure 8.1.1:
a) Structure of N,N-dimethyl-p-phenylenediamine (DMPD)
b) Structure of the ionic liquid 1-butyl-3-methylimidazolium tetrafluoroborate ([C_4 mim][BF_4])

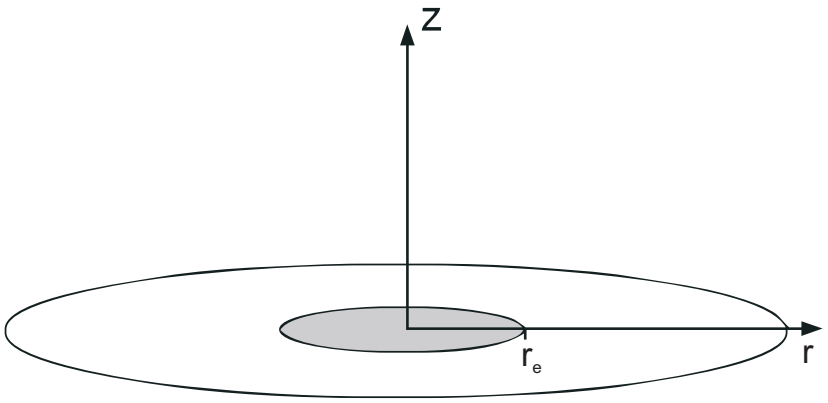

Figure 8.2.1:
Circular disc electrode inlaid on an insulating support.

heterogeneous rate constants for the first two steps are $k^0_{\mathrm{A/B}}$ and $k^0_{\mathrm{B/C}}$ respectively. The homogeneous rate constant for comproportionation is k_{comp} and for disproportionation is k_{disp}. The equilibrium constant for eq 8.1.3 is therefore $K_{\mathrm{eqm}} = \frac{k_{\mathrm{comp}}}{k_{\mathrm{disp}}}$. Specifically we consider the case of cyclic voltammetry.

$$\frac{\partial c_{\mathrm{A}}}{\partial t} = D_{\mathrm{A}}\left(\frac{\partial^2 c_{\mathrm{A}}}{\partial r^2} + \frac{1}{r}\frac{\partial c_{\mathrm{A}}}{\partial r} + \frac{\partial^2 c_{\mathrm{A}}}{\partial z^2}\right) + k_{\mathrm{disp}}{c_{\mathrm{B}}}^2 - k_{\mathrm{comp}}c_{\mathrm{A}}c_{\mathrm{C}} \tag{8.2.1}$$

$$\frac{\partial c_{\mathrm{B}}}{\partial t} = D_{\mathrm{B}}\left(\frac{\partial^2 c_{\mathrm{B}}}{\partial r^2} + \frac{1}{r}\frac{\partial c_{\mathrm{B}}}{\partial r} + \frac{\partial^2 c_{\mathrm{B}}}{\partial z^2}\right) - 2\left(k_{\mathrm{disp}}{c_{\mathrm{B}}}^2 - k_{\mathrm{comp}}c_{\mathrm{A}}c_{\mathrm{C}}\right) \tag{8.2.2}$$

$$\frac{\partial c_{\mathrm{C}}}{\partial t} = D_{\mathrm{C}}\left(\frac{\partial^2 c_{\mathrm{C}}}{\partial r^2} + \frac{1}{r}\frac{\partial c_{\mathrm{C}}}{\partial r} + \frac{\partial^2 c_{\mathrm{C}}}{\partial z^2}\right) + k_{\mathrm{disp}}{c_{\mathrm{B}}}^2 - k_{\mathrm{comp}}c_{\mathrm{A}}c_{\mathrm{C}} \tag{8.2.3}$$

where all symbols are defined in the glossary.

8.2.1 Cyclic voltammetry

In the cyclic voltammetry experiment, the applied potential, E, is swept from an initial value, E_{i}, to a more oxidising value, E_{f}, and then back to the initial value. The value of E is therefore calculated at any time on the forward sweep using eq 8.2.4 and on the reverse sweep using eq 8.2.5, where v is the voltage scan-rate and t is the time:

$$E_{\mathrm{forward}} = E_{\mathrm{i}} + vt \tag{8.2.4}$$

$$E_{\mathrm{reverse}} = 2E_{\mathrm{f}} + E_{\mathrm{i}} - vt \tag{8.2.5}$$

When $t > 0$, $z = 0$ and $r \leq r_{\mathrm{e}}$, the boundary conditions are the Butler-Volmer conditions describing species A and C and conservation of mass for species B:

$$
\begin{aligned}
-D_{\mathrm{A}}\left(\tfrac{\partial c_{\mathrm{A}}}{\partial z}\right)_0 = \quad & k^0_{\mathrm{A/B}} c_{\mathrm{A},0} \exp\left(-\alpha_{\mathrm{A/B}} \tfrac{F(E-E^{\ominus}_{\mathrm{f,A/B}})}{RT}\right) \\
& -k^0_{\mathrm{A/B}} c_{\mathrm{B},0} \exp\left((1-\alpha_{\mathrm{A/B}}) \tfrac{F(E-E^{\ominus}_{\mathrm{f,A/B}})}{RT}\right) \\
-D_{\mathrm{B}}\left(\tfrac{\partial c_{\mathrm{B}}}{\partial z}\right)_0 = \quad & -D_{\mathrm{A}}\left(\tfrac{\partial c_{\mathrm{A}}}{\partial z}\right)_0 - D_{\mathrm{C}}\left(\tfrac{\partial c_{\mathrm{C}}}{\partial z}\right)_0 \\
-D_{\mathrm{C}}\left(\tfrac{\partial c_{\mathrm{C}}}{\partial z}\right)_0 = \quad & -k^0_{\mathrm{B/C}} c_{\mathrm{B},0} \exp\left(-\alpha_{\mathrm{B/C}} \tfrac{F(E-E^{\ominus}_{\mathrm{f,B/C}})}{RT}\right) \\
& +k^0_{\mathrm{B/C}} c_{\mathrm{C},0} \exp\left((1-\alpha_{\mathrm{B/C}}) \tfrac{F(E-E^{\ominus}_{\mathrm{f,B/C}})}{RT}\right)
\end{aligned}
$$

The remaining boundary conditions are:

$t = 0$, all r, all z	$c_{\mathrm{A}} = c^*_{\mathrm{A}}$	$c_{\mathrm{B}} = 0$	$c_{\mathrm{C}} = 0$
$t > 0$, $r > r_{\mathrm{e}}$, $z = 0$	$\frac{\partial c_{\mathrm{A}}}{\partial z} = 0$	$\frac{\partial c_{\mathrm{B}}}{\partial z} = 0$	$\frac{\partial c_{\mathrm{C}}}{\partial z} = 0$
$t > 0$, all r, $z \to \infty$	$\frac{\partial c_{\mathrm{A}}}{\partial z} = 0$	$\frac{\partial c_{\mathrm{B}}}{\partial z} = 0$	$\frac{\partial c_{\mathrm{C}}}{\partial z} = 0$
$t > 0$, $r \to \infty$, all z	$\frac{\partial c_{\mathrm{A}}}{\partial r} = 0$	$\frac{\partial c_{\mathrm{B}}}{\partial r} = 0$	$\frac{\partial c_{\mathrm{C}}}{\partial r} = 0$
$t > 0$, $r = 0$, all z	$\frac{\partial c_{\mathrm{A}}}{\partial r} = 0$	$\frac{\partial c_{\mathrm{B}}}{\partial r} = 0$	$\frac{\partial c_{\mathrm{C}}}{\partial r} = 0$

8.2.2 Computational details

The problem is generalised by means of a transformation into non-dimensional form using a conventional set of normalised parameters. The resulting set of normalised diffusion equations were derived by Belding et al.[8] The problem is then discretised using the Alternating Direct Implicit method[21,22](ADI) and solved numerically using the iterative Newton-Raphson scheme.[23] The discretised spatial mesh is analogous to that reported by Gavaghan[24](Figure 8.2.2) and converged to within 0.1 %. Each temporal increment is optimised during runtime such that convergence to within 0.01 % is obtained. All programs were written in C++ and compiled using a Borland

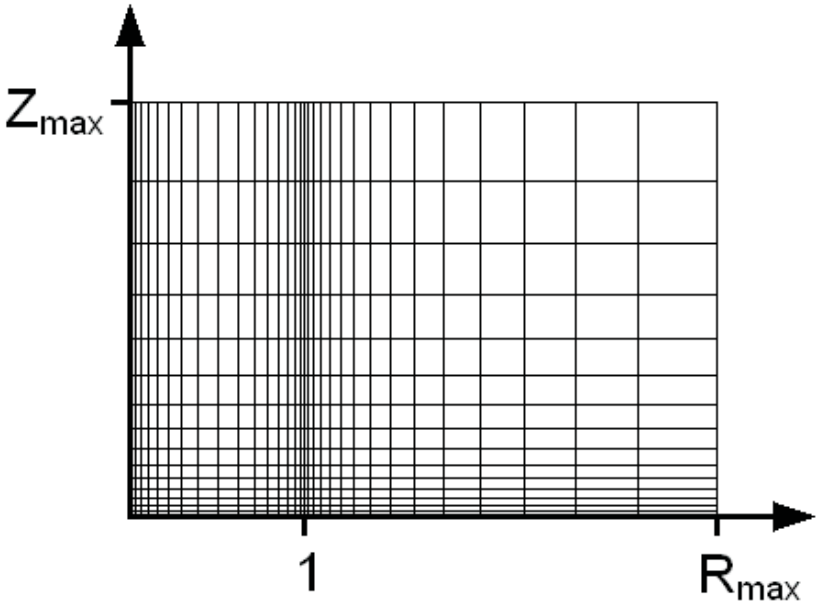

Figure 8.2.2: *Discretised grid used in the simulations (some points have been removed for clarity).*

compiler. The simulations were run on a desktop PC with a processor speed of $\approx$ 3 GHz. Approximately 20 min of CPU time were required to simulate a single voltammogram.

8.2.3 Results and discussion

The experimental work presented in this section was conducted by Edward O. Barnes and Dr. Aoife M. O'Mahony. The details are included in Appendix D on page 258.

Chronoamperometry

Double potential step chronoamperometric transients at the platinum electrode (10 μm diameter) were achieved using a sample time of 0.01 s. A solution of approximately 20 mM DMPD in $[C_4mim][BF_4]$ was pretreated by holding the potential at a point of zero current for 20 s, after which the potential was stepped to a position after the oxidative peak for DMPD corresponding to transport controlled diffusion, and the current measured for 5 s. The potential was then stepped to a position af-

ter the reductive peak for $DMPD^+$ corresponding to transport controlled diffusion, and the current response measured for a further 5 s. In order to extract diffusion coefficients and solubility data from these transients, the first potential step was fitted using the nonlinear curve fitting function in the software package Origin 7.0 (Microcal Software Inc.) according to the following equations proposed by Shoup and Szabo:[25]

$$i = -4nFD_{\mathrm{DMPD}}c_{\mathrm{DMPD}}r_{\mathrm{e}}f(\tau) \tag{8.2.6}$$

$$f(\tau) = 0.7854 + 0.4432\tau^{-\frac{1}{2}} + 0.2146\exp(-0.3912\tau^{-\frac{1}{2}}) \tag{8.2.7}$$

$$\tau = \frac{D_{\mathrm{DMPD}}t}{{r_{\mathrm{e}}}^2} \tag{8.2.8}$$

where n is the number of electrons transferred, F is the Faraday constant, D_{DMPD} is the diffusion coefficient, c_{DMPD} is the initial concentration of parent species, r_{e} is the radius of the disc electrode, t is the time and $f(\tau)$ is a function describing the slope of the transient. The equations used in this approximation are sufficient to give D_{DMPD} and c_{DMPD} within an uncertainty of ± 0.6 %. The value of the parameter $D_{\mathrm{DMPD^+}}$ was elucidated by fitting the transient for the second potential step using simulation software developed by Klymenko *et al.*[15] The fitted transient is shown in Figure 8.2.3 and the corresponding values of c_{DMPD}, D_{DMPD} and $D_{\mathrm{DMPD^+}}$ recorded in Table 8.1. It is important to note the value of $c_{\mathrm{DMPD}} = 19.5$ mM obtained from fitting the chronoamperometric transient to the Shoup and Szabo equation is in good agreement with the value of $c_{\mathrm{DMPD}} \approx 20$ mM used in the experiment. As noted in

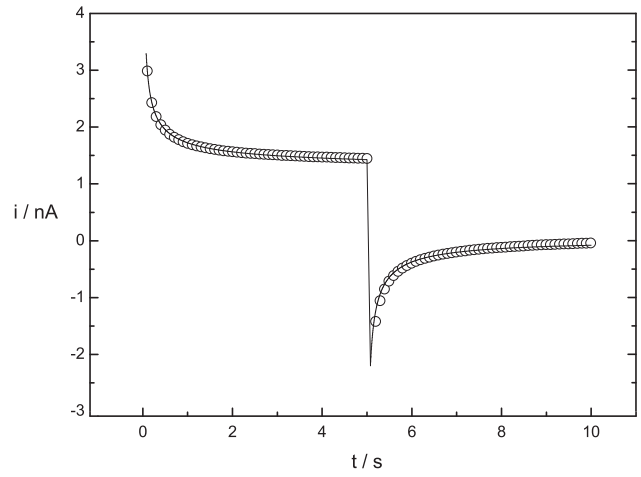

Figure 8.2.3:
Chronoamperometric fit: —, experiment; ∘, simulation.

other situations,[19] despite structural similarity between DMPD and $DMPD^+$, the discrepancy in diffusion coefficients is not insignificant. It is important to note that the potentials applied over the course of the double-step experiment are not sufficient to bring about transfer of a second electron ($DMPD^+ - e^- \rightleftharpoons DMPD^{2+}$). The concentration of $D_{DMPD^{2+}}$ in solution is negligible and, consequently, comproportionation cannot occur: Figure 8.2.3 is independent of the effects of comproportionation regardless of the values of D_{DMPD}, D_{DMPD^+} and $D_{DMPD^{2+}}$.

Parameter	**Experimental Value**
$\alpha_{DMPD/DMPD^+}$	(0.5 ± 0.1)
$\alpha_{DMPD^+/DMPD^{2+}}$	(0.5 ± 0.1)
c_{DMPD}	(19.5 ± 1.0) mM
$E^{\ominus}_{f,DMPD/DMPD^+}$	$(0.205 \pm 0.01$ V *vs* Pt
$E^{\ominus}_{f,DMPD^+/DMPD^{2+}}$	(0.745 ± 0.01) V *vs* Pt
$k^0_{DMPD/DMPD^+}$	≥ 0.01 cm s^{-1}
$k^0_{DMPD^+/DMPD^{2+}}$	(0.001 ± 0.002) cm s^{-1}
D_{DMPD}	$(2.0 \pm 0.1) \times 10^{-7}$ cm^2 s^{-1}
D_{DMPD^+}	$(1.1 \pm 1) \times 10^{-7}$ cm^2 s^{-1}
$D_{DMPD^{2+}}$	$(7 \pm 0.1) \times 10^{-8}$ cm^2 s^{-1}
k_{comp}	(250 ± 150) dm^3 mol^{-1} s^{-1}
$\Delta G^{\ominus}_{comp}$	-52.1 kJ mol^{-1}

Table 8.1:
Fitted data for DMPD in [C_4 mim][BF_4].

Cyclic voltammetry

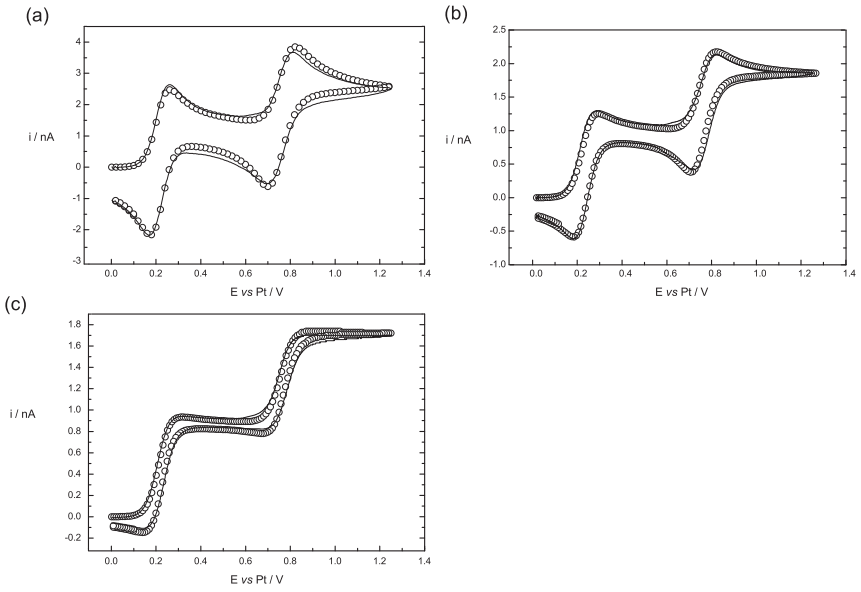

Figure 8.2.4:
Voltammetric fits: —, experiment; ∘, simulation ($k_{\mathrm{comp}} = 250$ dm^3 mol^{-1} s^{-1}).
(a) 1000 mV s^{-1}
(b) 100 mV s^{-1}
(c) 10 mV s^{-1}.

The kinetic and thermodynamic parameters of the two redox couples were elucidated by means of cyclic voltammetry. The oxidation of DMPD was examined in $[C_4\mathrm{mim}][BF_4]$. Cyclic voltammetry for the oxidation of 20 mM DMPD was carried out on a Pt microelectrode (diameter 10μm) at scan rates ranging from 10 mV s^{-1} to 1 V s^{-1}. The voltammograms are typically scanned from 0 V to 1.5 V *vs.* a Pt quasi-reference electrode. Two oxidation peaks were observed for scan rates 10 mV s^{-1} to 1 V s^{-1}, shown in Figure 8.2.4 at potentials 0.4 V and 0.9 V. These correspond, respectively, to the oxidation of DMPD to $DMPD^+$ and $DMPD^{2+}$. Both electron transfers are chemically reversible as indicated by the presence of two back peaks. The reliability of the fitting procedure was ensured by fitting the voltammograms

over a wide range of scan-rates (2 orders of magnitude). The fitted voltammograms are shown in Figure 8.2.4 and the corresponding data quoted in Table 8.1.

The onset of electrochemical reversibility occurs in RTILs at much lower values of the electrochemical rate constant compared to other non-aqueous solvents. For example, in a classic paper by Amatore,[26] electrochemical rate constants as high as 4 cm s^{-1} could be distinguished voltammetrically in acetonitrile. The reason for this discrepancy lies in the high viscosity of ionic liquid solvents (e.g. $\mu_{[C_{4mim}][BF_4]} = 112$ mPas at 25°C[27]) compared to other non-aqueous solvents (e.g. $\mu_{\text{acetonitrile}} = 34$ mPas at 25°C[28]). Mass transport is more likely to be rate limiting in solvents of greater viscosity. The rate constant for the first electron transfer ($DMPD - e^- \rightleftharpoons DMPD^+$) is electrochemically reversible on the voltammetric timescale ($k^0_{DMPD/DMPD^+} \geq 0.01$ cm s^{-1}) while the second ($DMPD^+ - e^- \rightleftharpoons DMPD^{2+}$) is quasi-reversible ($k^0_{DMPD^+/DMPD^{2+}} = (0.001 \pm 0.002)$ cm s^{-1}).

The comproportionation of DMPD and $DMPD^{2+}$ to form $DMPD^+$ is thermodynamically downhill. Using eq 8.1.5 and the data in Table 8.1, $\Delta G^{\ominus} = -52.1$ kJ mol^{-1}. However, from the Table 8.1, comproportionation is slow on the voltammetric timescale ($k_{comp} = 250$ dm^3 mol^{-1} s^{-1}). When DMPD is oxidised, the lone electron pair on each nitrogen atom makes an increased contribution to the resonance within the aromatic ring: the double bond character of each C-N bonds increases. The rearrangement energy for the electron transfer is substantial and leads to a small value of the rate constant as predicted by Marcus theory.[29,30]

In a recent paper[8] it was shown that, in the limit of electrochemical reversibility, the presence of diffusionally controlled comproportionation can be discerned only

at high scan-rates when the diffusion coefficients of the species (D_{DMPD}, $D_{\mathrm{DMPD^+}}$ and $D_{\mathrm{DMPD^{2+}}}$) are significantly different such that $D_{\mathrm{DMPD^+}}/D_{\mathrm{DMPD}} > 1.5$ and $D_{\mathrm{DMPD^{2+}}}/D_{\mathrm{DMPD}} > 1.5$ or $D_{\mathrm{DMPD^+}}/D_{\mathrm{DMPD}} < 0.75$ and $D_{\mathrm{DMPD^{2+}}}/D_{\mathrm{DMPD}} < 0.75$. It is important to note that this conclusion refers to a comparison between $k_{\mathrm{comp}} = 0$ dm^3 mol^{-1} s^{-1} and *diffusion control*. For an arbitrary value of k_{comp} the aforementioned conditions for the observation of comproportionation are neither necessary nor sufficient. Figure 8.2.5 shows a comparison between the experimental voltam-

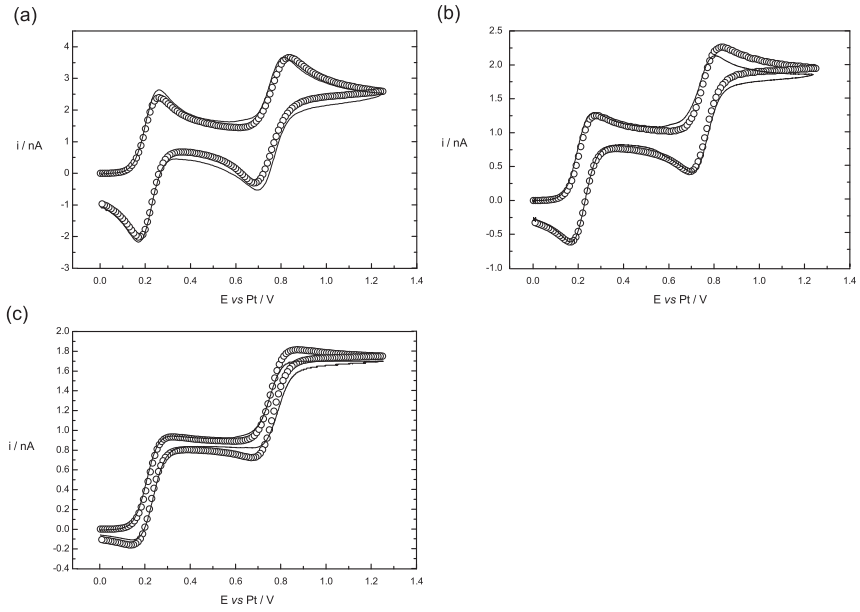

Figure 8.2.5:
Voltammetric fits: —, experiment; ∘, simulation ($k_{\mathrm{comp}} = 0$ dm^3 mol^{-1} s^{-1}).
(a) 1000 mV s^{-1}
(b) 100 mV s^{-1}
(c) 10 mV s^{-1}

mograms at a range of scan rates and the simulated transients corresponding to the data in Table 8.1 with $k_{\mathrm{comp}} = 0$ dm^3 mol^{-1} s^{-1}. It is clear that, for the present system, the occurrence of comproportionation *can* be identified voltammetrically and the discrepancy between $k_{\mathrm{comp}} = 0$ dm^3 mol^{-1} s^{-1} and $k_{\mathrm{comp}} = 250$ dm^3 mol^{-1} s^{-1}

increases with decreasing scan-rate. At low scan-rates a steady-state voltammetric response is obtained while at high scan-rates comproportionation is outrun on the voltammetric timescale. Therefore, in each case, the presence of comproportionation cannot be discerned from the voltammetry. For DMPD in [C_4 mim][BF_4], the effect of comproportionation is not expected to be apparent in the limit of very low scan-rates.

8.3 Conclusion

In this chapter, simulation studies have been used to show that comproportionation, in which DMPD reacts homogeneously with $DMPD^+$ ($DMPD + DMPD^{2+} \rightleftharpoons 2DMPD^+$), can be discerned for the 2 electron oxidation of DMPD in the ionic liquid [C_4 mim][BF_4]. In addition, the kinetic and thermodynamic parameters of the reaction were elucidated by means of double potential step chronoamperometry and cyclic voltammetry.

Bibliography

[1] Barnes, E. O.; O'Mahony, A. M.; Belding, S. R.; Compton, R. G. *J. Chem. Eng. Data* **2010**, *55*, 2219–2224.

[2] Wang, Y.; Sun, Y.; Yu, L.; Zeng, Z. *Shenyang Yaoke Daxue Xuebao* **2006**, *23*, 432–434.

[3] Mallakpour, S.; Kolahdoozan, M. *Polym. J. (Tokyo, Jpn.)* **2008**, *40*, 513–519.

[4] Silvester, D. S.; Compton, R. G. *Z. Phys. Chem.* **2006**, *220*, 1247–1274.

[5] Ignat'ev, N. V.; Welz-Biermann, U.; Kucheryna, A.; Bissky, G.; Willner, H. *Journal of Fluorine Chemistry* **2005**, *126*, 1150 – 1159.

[6] Camper, D.; Bara, J. E.; Gin, D. L.; Noble, R. D. *Ind. Eng. Chem. Res.* **2008**, *47*, 8496–8498.

[7] Zhu, S.; Chen, R.; Wu, Y.; Chen, Q.; Zhang, X.; Yu, Z. *Chem. Biochem. Eng. Q.* **2009**, *23*, 207–211.

[8] Belding, S. R.; Baron, R.; Dickinson, E. J. F.; Compton, R. G. *J. Phys. Chem. C* **2009**, *113*, 16042–16050.

[9] Barnes, A. S.; Rogers, E. I.; Streeter, I.; Aldous, L.; Hardacre, C.; Compton, R. G. *J. Phys. Chem. B* **2008**, *112*, 7560–7565.

[10] Andrieux, C. P.; Savéant, J. M. *J. Electroanal. Chem.* **1970**, *28*, 339–348.

[11] Amatore, C.; Bonhomme, F.; Bruneel, J.-L.; Servant, L.; Thouin, L. *J. Electroanal. Chem.* **2000**, *484*, 1–17.

[12] Belding, S. R.; Rogers, E. I.; Compton, R. G. *J. Phys. Chem. C* **2009**, *113*, 4202–4207.

[13] Evans, R. G.; Klymenko, O. V.; Price, P. D.; Davies, S. G.; Hardacre, C.; Compton, R. G. *ChemPhysChem* **2005**, *6*, 526–533.

[14] Paddon, C. A.; Silvester, D. S.; Bhatti, F. L.; Donohoe, T. J.; Compton, R. G. *Electroanalysis* **2007**, *19*, 11–22.

[15] Klymenko, O. V.; Evans, R. G.; Hardacre, C.; Svir, I. B.; Compton, R. G. *J. Electroanal. Chem.* **2004**, *571*, 211–221.

[16] Zigah, D.; Ghilane, J.; Lagrost, C.; Hapiot, P. *J. Phys. Chem. B* **2008**, *112*, 14952–14958.

[17] Endres, F.; Zein El Abedin, S. *Phys Chem Chem Phys* **2006**, *8*, 2101–2116.

[18] Hapiot, P.; Lagrost, C. *Chem. Rev. (Washington, DC, U. S.)* **2008**, *108*, 2238–2264.

[19] Buzzeo, M. C.; Klymenko, O. V.; Wadhawan, J. D.; Hardacre, C.; Seddon, K. R.; Compton, R. G. *J. Phys. Chem. A* **2003**, *107*, 8872–8878.

[20] Ghilane, J.; Lagrost, C.; Hapiot, P. *Anal Chem* **2007**, *79*, 7383–7391.

[21] Britz, D. *Digital Simulation in Electrochemistry*; Springer-Verlag: New York, 2005.

[22] Heinze, J. *J. Electroanal. Chem.* **1981**, *124*, 73–86.

[23] Press, W. H., Teukolsky, S. A., Vetterling, W. T., Flannery, B. P., Eds. *Numerical Recipes: The Art of Scientific Computing*; Cambridge University Press, 2007.

[24] Gavaghan, D. J. *J. Electroanal. Chem.* **1998**, *456*, 1–12.

[25] Shoup, D.; Szabo, A. *J. Electroanal. Chem.* **1982**, *140*, 237–245.

[26] Amatore, C.; Maisonhaute, E.; Simonneau, G. *Electrochem. Commun.* **2000**, *2*, 81–84.

[27] Okoturo, O. O.; VanderNoot, T. J. *J. Electroanal. Chem.* **2004**, *568*, 167 – 181.

[28] Cunningham, G. P.; Vidulich, G. A.; Kay, R. L. *J. Chem. Eng. Data* **1967**, *12*, 336–337.

[29] Compton, R. G.; Banks, C. E. *Understanding Voltammetry*; World Scientific: Singapore, 2007.

[30] Marcus, R. A. *J. Chem. Phys.* **1956**, *24*, 966–978.

Chapter 9

Conclusions

Almost any attempt to study a process electrochemically must include two parts: an electrode and a solvent. The work presented in this thesis has further extended the applicability of both. The final conclusions of this thesis are summarised below.

In chapter 3, it was show that, in almost all cases, the voltammetric response from a nanoparticle modified electrode is substantially different from that expected from a macroelectrode. Discrepancies occur due to a combination of electrode kinetics and mass transport. Using computer simulations, it is possible to deconvolute these factors and obtain useful experimental information regarding the nanoparticle specific effects.

In chapter 4, diffusional chronoamperometry and cyclic voltammetry at a random array of nanoparticles was simulated efficiently and rationalised in terms of four categories which define different extents of diffusion layer overlap. The cyclic voltammetry in the Category 3/4 region was been shown to be morphology dependent for voltammetry that was not electrochemically reversible. The reduction Cr^{3+} to

Cr^{2+} was carried out experimentally on an array of silver nanoparticles (80-120 nm diameter). A clear relationship was shown to exist between the degree of surface coverage (θ) and the nature of the voltammetry. Increasing the coverage resulted in an increase in the apparent reversibility of the process as well as an increased current due to the greater surface area available for the reaction to take place. This was due to the transition from convergent diffusion to linear diffusion with increasing surface coverage. By increasing the nanoparticle density the electrode kinetics tended towards those of a macro-disk electrode.

In chapter 5, the cyclic voltammetry of the E reduction, $A^{Z_A} + ne^- \rightleftharpoons B^{Z_B}$, was studied using numerical simulations. The effect of adding different concentrations of supporting electrolyte was studied as a function of the scan rate, the diffusion coefficient of species B, the diffusion coefficients of the ions in the supporting electrolyte and the charges of the analyte ions. The minimum support ratio required observe quantitative diffusion-only cyclic voltammetry was shown to vary as a function of the scan rate, σ, the diffusion coefficients of the supporting electrolyte, D'_M and D'_X, and the charge of the analyte ion, Z_A. The diffusion coefficient of species B was show to have no effect on the peak to peak separation close to the diffusion-only limit (although it did change the peak position).

In chapter 6, cyclic voltammetry, with homogeneous kinetics, was simulated for conditions of low support. In many cases, cyclic voltammetry is unable to determine the presence or absence of diffusion-controlled comproportionation under conventional, fully supported, conditions; in contrast, under weakly supporting conditions the distinction was shown to be unequivocal. It was shown experimentally that, in the case

of anthraquinone in acetonitrile, comproportionation is diffusionally controlled.

In chapter 7, steady-state cyclic voltammetry at low support was efficiently simulated for both reversible and irreversible electrode kinetics. It was shown, by numerical and analytical means, that the hemispherical approximation is reliable over a range of support ratios and electrochemical rate constants. Simulations and the Debye-Hückel theory are used to analyze cyclic voltammetry obtained for two aqueous redox couples: hexammineruthenium $[Ru(NH_3)_6]^{3+}/[Ru(NH_3)_6]^{2+}$ and hexachloroiridate $[IrCl_6]^{2-}/[IrCl_6]^{3-}$. The data indicated the occurrence of ion pairing in the latter but not in the former.

In chapter 8, simulation studies were used to show that comproportionation, in which the molecule N,N-dimethyl-p-phenylenediamine (DMPD) reacts homogeneously with $DMPD^+$ ($DMPD + DMPD^{2+} \rightleftharpoons 2DMPD^+$), can be discerned for the 2 electron oxidation of DMPD in the ionic liquid [C_4 mim][BF_4]. In addition, the kinetic and thermodynamic parameters of the reaction were elucidated by means of double potential step chronoamperometry and cyclic voltammetry.

Appendix A

Numerical simulation of nanoparticle arrays

A.1 Experimental

The experimental work was performed by Dr. Fallyn W. Campbell and Ms. Yige Zhou.

A.1.1 Chemical and reagents

All chemicals and reagents were used as received without further purification. All solutions were prepared with Millipore deionized water, with a resistivity no less than 18.2 MΩcm at 25 °C (Vivendi Water Systems, UK). All glassware was cleaned with a 'piranha' solution (4:1 H_2SO_4 and H_2O_2) prior to use. Silver nitrate salt (99%, AgNO3) was supplied by BHD and trisodium citrate (99%, $C_6H_5Na_3O_7$) supplied by Sigma-Aldrich. Chromium (III) chloride (99%, $CrCl_3{\cdot}6H_2O$) and sodium perchlorate

(98-102%, $NaClO_4$) were supplied by Sigma-Aldrich. Hydrochloric acid (37%, Fisher Scientific) was added to 1 M $NaClO_4$ solutions to achieve a pH of 2.0.

Colloidal silver nanoparticles (AgNPs) of 80-120 nm diameter were synthesised by a seed-mediated citrate reduction of $AgNO_3$. This method was adapted from syntheses by Pyatenko[1,2] and has been outlined in detail in our previous publications.[3–5] These AgNPs were subsequently used to modify a basal plane pyrolytic graphite (BPPG, Le Carbone Ltd., Sussex, UK) electrode by drying a volume of the suspension on the electrode surface. The loading could be increased or decreased with volume of colloidal suspension.

A.1.2 Instrumentation

The electrochemical cell used was a standard 3-electrode set-up using saturated calomel (SCE) reference electrode and a carbon rod as the counter electrode. The working electrode was a silver macro-disk (0.5 mm diameter) or a AgNP-modified BPPG electrode (5 mm diameter). All electrochemical measurements were performed using an Eco Chemie PGSTAT20 potentiostat connected to a desktop computer.

A.1.3 Experiments

These electrodes (Ag_{macro}/AgNP-BPPG) were then applied to the reduction of Cr^{3+}. Experiments were performed for Cr^{3+} (10 mM) in $NaClO_4$ (1 M, pH of 2) electrolyte solutions. AgNP-BPPG electrodes with surface coverage ranging from 0 percent to 20 percent, were employed. The potential was scanned negatively from 0 to -0.9 V

(*vs.* SCE) at 50 mV s^{-1}. In the case of the AgNP-BPPG electrodes, silver loading was then quantified by stripping from the surface in $NaClO_4$ (0.1 M), by scanning positively from 0.1 to 1.0 V (*vs.* SCE).[6]

Bibliography

[1] Pyatenko, A.; Yamaguchi, M.; Suzuki, M. *J. Phys. Chem. C* **2007**, *111*, 7910.

[2] Pyatenko, A.; Yamaguchi, M.; Suzuki, M. *J. Phys. Chem. B* **2005**, *109*, 21608.

[3] Campbell, F. W.; Belding, S. R.; Baron, R.; Compton, R. G. *J. Phys. Chem. C* **2009**, *113*, 14852.

[4] Campbell, F. W.; Belding, S. R.; Compton, R. G. *ChemPhysChem* **2010**, *11*, 2820.

[5] Campbell, F. W.; Belding, S. R.; Baron, R.; Compton, R. G. *J. Phys. Chem. C* **2009**, *113*, 9053.

[6] Ward-Jones, S. E.; Campbell, F. W.; Baron, R.; Xiao, L.; Compton, R. G. *J. Phys. Chem. C* **2008**, *112*, 17820.

Appendix B

Diffusion-migration voltammetry: extra kinetic and mechanistic insights

B.1 Chemicals and equipment

All experimental work was conducted by Dr. Juan G. Limon-Peterson.

All solutions were made with acetonitrile solvent (MeCN, HPLC grade, Fisher Scientific). Anthraquinone (>97%, Strem Chemicals) was used as the electroactive species, with tetra-*n*-butylammonium perchlorate (TBAP, ≥99%,Fluka) as supporting electrolyte. A three electrode cell was used: a 25 micron radius platinum disk or a 25 micron radius mercury hemispherical electrode was used as a working electrode. The latter was prepared by electrodepositing mercury on a platinum disk, and the size was controlled by passing the necessary amount of current to form a

hemisphere, using the procedure stated in Bard *et al.*[1] and Limon-Petersen *et al.*[2] The size of the electrode minimised the effect of ohmic drop in the solution. The geometry of the electrode ensured that the potential and concentration profiles were of the same geometry at all times. A silver wire was used as a reference electrode to avoid leaking of ionic impurities in the solution.

Note that voltammograms were recorded using a PG-STAT12 potentiostat (Autolab, Netherlands) without the 'ohmic drop correction' used or theorised in some early studies of weak support,[3,4] so as to permit a clear comparison of theory and experiment.

All solutions were thoroughly degassed with N_2 before each experiment, and an inert atmosphere was maintained during the experiments.

Bibliography

[1] Mauzeroll, J.; Hueske, E. A.; Bard, A. J. *Anal. Chem.* **2003**, *75*, 3880–3889.

[2] Limon-Petersen, J. G.; Rees, N. V.; Streeter, I.; Molina, A.; Compton, R. G. *J. Electroanal. Chem.* **2008**, *623*, 165–169.

[3] Bond, A. M.; Feldberg, S. W. *J. Phys. Chem. B* **1998**, *102*, 9966–9974.

[4] Bond, A. M.; Coomber, D. C.; Feldberg, S. W.; Oldham, K. B.; Vu, T. *Anal. Chem.* **2001**, *73*, 352–359.

Appendix C

Diffusion-migration voltammetry: the microdisc electrode

C.1 Experimental methods

The experiments in this section were condicted by Dr. Eduardo Laborda.

C.1.1 Chemical reagents

Potassium chloride (KCl, Sigma-Aldrich, 99.0-100.5%), hexaammineruthenium(III) chloride ($[Ru(NH_3)_6]Cl_3$, Aldrich, 98%), potassium hexachloroiridate(IV) (K_2IrCl_6, Aldrich, 99.99%), acetonitrile (MeCN, Fischer Scientific, dried and distilled, 99%), ferrocene ($Fe(C_5H_5)_2$, Aldrich, 98%) and tetra-n-butylammonium perchlorate (TBAP, Fluka, Puriss electrochemical grade, 99%) were all used as received without further purification.

C.1.2 Instrumentation and solutions

A computer-controlled μ-Autolab potentiostat Type II (Eco-Chemie, Netherlands) was employed to undertake the experiments. A three-electrode set-up was employed, with homemade platinum microelectrode as the working electrode,[1] a platinum mesh as the counter electrode and a Saturated Calomel Electrode (SCE, Radiometer, Denmark) as the reference electrode. Before each experiment, the working electrode was polished by using 1.0, 0.3 and 0.05 μm alumina-water slurry on soft lapping pads (Buehler, Illinois) and subsequently sonicated in deionised water.

The calibration of the size of the working electrodes was performed electrochemically from the steady state limiting current of the reduction of a 2.0 mM solution of ferrocene in acetonitrile containing 0.1 M TBAP, adopting a value of the diffusion coefficient of ferrocene in MeCN of $D = 2.43 \times 10^{-5}$ cm^2s^{-1} at 298 K.[2]

For the cyclic voltammetry and chronoamperometry experiments, 2.0 mM $[Ru(NH_3)_6]Cl_3$ or K_2IrCl_6 solutions in ultrapure water with resistivity > 18.2 $M\Omega\,cm^{-1}$ (20 °C) were prepared, at different concentrations of the supporting electrolyte, KCl. Solutions were outgassed with N_2 before experiments and a positive pressure of N_2 was maintained throughout.

All measurements were carried out at 25 °C by thermal control of the electrochemical cell through the use of an air heater-controller system fabricated in-house.

Bibliography

[1] Heinze, J. *Angew. Chem. Int. Ed.* **1993**, *32*, 1268–1288.

[2] Wang, Y.; Rogers, E. I.; Compton, R. G. *J. Electroanal. Chem.* **2010**, *648*, 15–19.

Appendix D

Cyclic voltammetry in room temperature ionic liquids: the comproportionation mechanism

D.1 Experimental methods

The experiments in this section were condicted by Dr. Aoife M. O'Mahoney and Edward O. Barnes.

D.1.1 Chemical reagents

1-butyl-3-methylimidazolium tetrafluoroborate ($[C_4mim][BF_4]$) was kindly donated by Merck KGaA. N,N-dimethyl-1,4-phenylenediamine (DMPD, Aldrich, >97%), ferrocene (Aldrich, 98%), tetrabutylammonium perchlorate (TBAP, Fluka, Puriss electrochemical grade, >99.99%) and acetonitrile (Fischer Scientific, dried and distilled,

>99.99%) were used as received without further purification.

D.1.2 Instrumental

Electrochemical experiments were performed using a computer controlled μ-Autolab potentiostat (Eco-Chemie, Netherlands). A conventional two-electrode system was used, typically with a platinum electrode (10 μm diameter) as the working electrode, and a 0.3 mm diameter platinum wire as a quasi-reference electrode. The platinum microdisc working electrode was polished on soft lapping pads (Kemet Ltd., U.K.) using alumina powder (Buehler, IL) of size (5.0, 1.0 and 0.3) μm. The electrode diameter was calibrated electrochemically by analyzing the steady-state voltammetry of a 2 mM solution of ferrocene in acetonitrile containing 0.1 M TBAP, with a diffusion coefficient for ferrocene of 2.3×10^{-5} cm^2 s^{-1} at 293 K.[1] The electrodes were housed in a glass cell "T-cell" designed for investigating microsamples of ionic liquids under a controlled atmosphere[2](Figure A.1). RTILs are sensitive to water,[2,3] the presence of water can alter the viscosity of the ionic liquid and reduce the electrochemical window, therefore the samples are purged under vacuum before voltammetry is carried out. In addition, this procedure removes electroactive oxygen from solution.[4] The working electrode was modified with a section of disposable micropipette tip to create a small cavity above the disc into which a drop (20 μL) of ionic liquid was placed. DMPD was directly dissolved in [C_4mim][BF_4] at concentration 20 mM. Prior to voltammetric scanning, the RTIL solution was purged under vacuum (Edwards High Vacuum Pump, Model ES 50) for *ca*. 90 min, which served to remove trace atmospheric moisture naturally present in the RTIL.

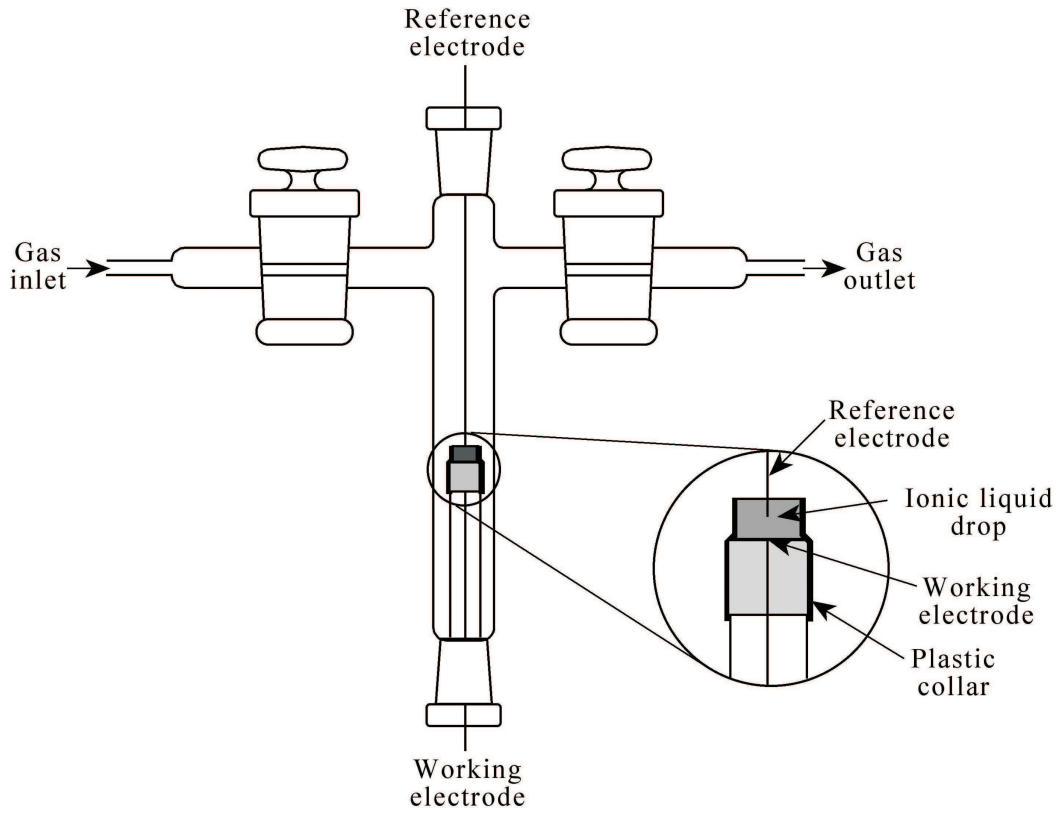

Figure A.1:
Cross section of the T-cell used to perform chronoamperometry.

All experiments were performed inside a fume cupboard, in a thermostatted box (previously described by Evans *et al.*)[5] which also functioned as a Faraday cage. The temperature was maintained at (298±1.0) K.

Bibliography

[1] Sharp, M. *Electrochim. Acta* **1983**, *28*, 301–308.

[2] Schroder, U.; Wadhawan, J. D.; Compton, R. G.; Marken, F.; Suarez, P. A. Z.; Consorti, C. S.; de Souza, R. F.; Dupont, J. *New J. Chem.* **2000**, *24*, 1009–1015.

[3] O'Mahony, A. M.; Silvester, D. S.; Aldous, L.; Hardacre, C.; Compton, R. G. *J. Chem. Eng. Data* **2008**, *53*, 2884–2891.

[4] Evans, R. G.; Klymenko, O. V.; Saddoughi, S. A.; Hardacre, C.; Compton, R. G. *J. Phys. Chem. B* **2004**, *108*, 7878–7886.

[5] Evans, R. G.; Klymenko, O. V.; Price, P. D.; Davies, S. G.; Hardacre, C.; Compton, R. G. *ChemPhysChem* **2005**, *6*, 526–533.